Design and Simulation of a Microwave Kinetic Inductance Detector Spectrograph for Astronomy

VOLKAN BENEDICT HOFMANN

Design and Simulation of a Microwave Kinetic Inductance Detector Spectrograph for Astronomy

Volkan Benedict Hofmann

A thesis presented for the degree of

Doctor of Philosophy

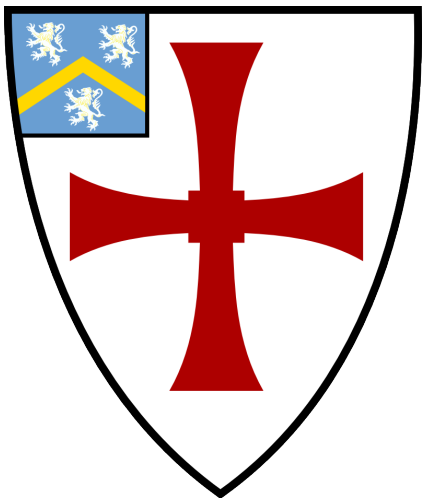

Centre for Advanced Instrumentation

The University of Durham

United Kingdom

March 2024

For Opa,

Ich lege meine neben deine.

Design and Simulation of a Microwave Kinetic Inductance Detector Spectrograph for Astronomy

Volkan Benedict Hofmann

Abstract

This thesis presents a Microwave Kinetic Inductance Detector (MKID) spectrograph concept, the Kinetic Inductance Detector Spectrometer (KIDSpec). MKIDs are superconducting photon-counting detectors that can resolve the energy of incoming photons and their time of arrival.

KIDSpec will use these detectors to separate incoming spectral orders from a grating, thereby not requiring a cross-disperser. In Chapter 3, a simulation tool is presented for assessing KIDSpec's potential performance upon construction to optimise a given design. This simulation tool is the KIDSpec Simulator (KSIM), a Python package designed to simulate various KIDSpec and observation parameters. A range of astrophysical objects is simulated, including stellar objects, an SDSS-observed galaxy, a Seyfert galaxy, and a mock galaxy spectrum from the JAGUAR catalogue. Multiple medium spectral resolution designs for KIDSpec are simulated. The possible impact of MKID energy resolution variance and dead pixels is also simulated, with observed impacts on KIDSpec performance assessed using the Reduced Chi-Squared (RCS) value. Using dead pixel percentages from current instruments, the RCS result was found to increase to only 1.21 at worst for one of the designs simulated. SNR comparisons of object simulations between KSIM and X-Shooter's ETC were also performed. KIDSpec demonstrates a particular improvement over X-Shooter for short and faint observations. For a Seyfert galaxy ($m_R = 21$) simulation with a 180s exposure, KIDSpec achieved an average SNR of 4.8, compared to 1.5 for X-Shooter. By using KSIM, the design of KIDSpec can be optimised to further enhance the instrument.

Chapter 4 presents the Superconducting Spectrograph for Medium resolution in an Array of Telescopes (SuperSmart). This concept would utilise an array of small ($\leq$1m diameter) telescopes, each with a KIDSpec-style instrument connected optically with a fibre. A key benefit of this would be the use of MKIDs,

which would allow these smaller telescopes to bin the photons they observe together, effectively becoming the equivalent of a larger-class telescope, such as a 4m-class telescope. The concept and a design for the array is presented, with KSIM simulations used to predict the performance of both individual telescopes and the array as a whole. The simulations include limiting magnitudes, a set of survey objects from GAIA, and LISA calibration sources. If enough 0.6m diameter telescopes are used to reach a total equivalent telescope diameter of 4m, SuperSmart would need 190 nights to observe 100,000 objects of $m_V < 19$. This assumes that each telescope can act independently and does not require the rest of the array to finish an observation before moving to a new object. If this independence is not considered, the required nights more than doubled to 477 nights. From KSIM simulations, SuperSmart could characterise important gravitational wave sources for LISA. To halve the standard error on the radial velocity semi-amplitude of ZTF J1539+5027, SuperSmart would utilise the time resolution and lack of read noise. This would involve using exposures of 9s throughout the ≈ 414s period and improving the signal-to-noise ratio in these time bins over 15 hours of observation.

An important part of MKID operation is the analysis of the data received from the MKID. Initially, this involves characterising the MKID before analysing the data stream for photon events. Chapter 5 describes the methods used for this. Chapter 6 presents the KIDSpec Prototype. The Prototype is a fibre-fed spectrograph, with the camera affixed on an arm articulating from the grating. The MKID, which is fibre-fed from the output of the camera, then separates the spectral orders that the camera observes. The concept, design, and assembly are presented, along with data taken from calibration lamps and the Sun. Full spectra of the bandpass $\approx 300 - 1500$nm are observed from the calibration lamps; however, a solar spectrum was not achieved due to poor weather with intermittent clouds in Durham, UK. Nevertheless, photons were observed and separated between the orders, demonstrating the MKID's capability for spectrographs.

Supervisors: Dr Kieran S. O'Brien and Prof Chris Done

Acknowledgements

I have to first mention the pandemic. The height of the pandemic was an incredibly difficult and gut wrenching time for us all. But, a vaccine was produced. I thank both the NHS and everyone around the world who worked tirelessly to protect us as much as possible from COVID-19, and for getting us back to where we are now.

An admission I have to make is that, much like the thesis, I had no idea how to start this. Getting to this point has been quite the experience, with plenty of challenges and successes along the way. These successes would not have happened without the help of those around me.

Without my supervisor Kieran O'Brien, none of this would have been possible. Your advice and guidance over the years was invaluable, and always lead to great science. In particular I have to thank you for reading what feels like countless pages of my writing, and always helping me to make it better.

To all the members of CfAI, your answers to my never ending, seemingly random, questions is incredibly appreciated. You all made me feel like a firm part of the department, and I'll certainly miss the Vic trips too.

Thank you to all my family, who have never stopped supporting and loving me. The 'writer's retreats' back home were always just what I needed to keep motivation and progress high, and when I wasn't there with you, the messages/calls of support always put a smile on my face. Love you all.

Next, my friends, both new and old. Every single one of you mean so much to me, and I cannot thank you enough for being there for me over the years. From badminton, pubs (and crawls), picnics, games, and coffees, I hope we get to either continue doing them or will get a chance to again.

Finally of course, the MVP, my incredible wife. Tilly, you have been nothing short of amazing. Your love, patience, and banter helped me more than you know through what was some difficult times for me. You have made me a stronger and

happier man, and for that I couldn't be more grateful. I hope you enjoy reading this thesis, because I owe as much of it to you, as I do to me.

V. B. H.

September 2023

Contents

Declaration

The work in this thesis is based on research carried out at the Centre for Advanced Instrumentation, Department of Physics, University of Durham, England. No part of this thesis has been submitted elsewhere for any other degree or qualification, and it is the sole work of the author unless referenced to the contrary in the text.

The COVID-19 pandemic was a terrible event that affected the globe and its population. Alongside the hardship faced by all it did also impact the research throughout this Thesis. The construction of the laboratory used for this research was delayed by a year, the following semiconductor shortage slowed the acquisition of new components, and the majority of the first two years of the Degree was completed remotely. This did cause the progress which was possible to be reduced.

Some of the work presented in this thesis has been published in journals and conference proceedings - the relevant publications are listed below.

Publications

Chapter 3, excluding Section 3.6, research paper published in RASTI: Hofmann and O'Brien (2023)
Chapter 3, Section 3.6, SPIE conference proceedings: Hofmann et al. (2022)

List of Figures

List of Tables

Nomenclature

MKID Microwave Kinetic Inductance Detector

PTS Photon Time Stream

HEMT High Electron Mobility Transistor

DR Dilution Refrigerator

ADR Adiabatic Demagnetisation Refrigerator

PDF Probability Density Function

R_E Energy Resolution

R_{var} R_E variance

VCRO Vera C. Rubin Observatory

NIR Near-Infrared

PV Peculiar Velocity

SNR Signal to Noise Ratio

VLT Very Large Telescope

ELT Extremely Large Telescope

UCB Ultra-Compact Binary

KIDSpec Kinetic Inductance Detector Spectrometer

KSIM KIDSpec SIMulator

SuperSmart Superconducting Spectrograph for Medium resolution in an Array of Telescopes

OAP Off-Axis Parabola

NA Numerical Aperture

IFU Integral Field Unit

MOS Multi-Object Spectroscopy

FSR Free Spectral Range

CCD Charge Coupled Device

EMCCD Electron-Multiplying Charge Coupled Device

QE Quantum Efficiency

CMOS Complementary Metal Oxide Semiconductor

SAPHIRA Selex Avalanche Photodiode for HgCdTe InfraRed Array

MUSE Multi Unit Spectroscopic Explorer

FLAMES Fibre Large Array Multi Element Spectrograph

FOS Faint Object Spectrograph

FoV Field of View

ARCONS Array Camera for Optical to Near-IR Spectrophotometry

DARKNESS DARK-speckle Near-infrared Energy-resolving Superconducting Spectrophotometer

MEC MKID Exoplanet Camera

DAC Digital-to-Analogue Converter

ADC Analogue-to-Digital Converter

LO Local Oscillator

STJ Superconducting Tunnel Junction

TES Transition Edge Sensor

SDSS Sloan Digital Sky Survey

LSST Legacy Survey of Space and Time

RCS Reduced Chi-Squared

Chapter 1

Introduction

In 1666, Isaac Newton observed a beam of light from the Sun that entered a darkened room through a 'slit,' which was, in fact, a hole in his window curtains. Placed approximately 22 feet away from the slit was a glass prism, which he used to observe the beam become separated into five colours: red, yellow, green, blue, and violet (Newton, 1672). This groundbreaking experiment marked the first recorded demonstration of astronomical spectroscopy (Hearnshaw, 2009), during which he observed five solar lines.

Spectroscopy, as we know it today, involves the study of an object's intensity depending on the wavelength of the electromagnetic radiation emanating from that object. The resulting spectrum of an object provides significant insight into its characteristics and properties. The applications of this powerful technique are numerous and diverse, including the study of atomic structure (Cowan, 1981), improving drug effectiveness (McLoughlin et al., 2009), and understanding the human body itself (Hamaoka et al., 2011). Another field where spectroscopy remains a primary method of data acquisition, and is the topic of this work, is astronomical spectroscopy.

In this field, spectroscopy allows us to study our Universe and its fundamental constituents. For instance, it facilitates the determination of elemental abundances within stars (Hamann and Ferland, 1999) and offers a means to peer into the past.

When we observe astronomical objects moving away from Earth, the wavelength of incoming light becomes 'stretched' or increased, a phenomenon known as redshift. The extent of this redshift in the light provides information about when the light was originally emitted by the astronomical object, as redshift depends on the distance between the observer and the object. By measuring the distance of the object from Earth, we can ascertain the time period during the Universe's existence when the light originated (Kaiser, 2014).

Studying the Universe and its makeup through spectroscopy enables us to answer fundamental questions about both the Universe's origins and our own. It offers insights into the evolution and composition of cosmic objects, shedding light on the processes that have shaped our cosmic history.

1.1 Astronomical Spectrographic Instruments

In the approximately 360 years since Isaac Newton's groundbreaking demonstration, astronomical spectroscopy has advanced significantly. Nowadays, an astronomical spectrograph typically consists of five key components: the slit, collimator, grating, camera, and detector. The instrument is optically connected to an astronomical telescope, which focuses the light onto the instrument's slit or fibre, as is the case for the instrument under study in this thesis. These advancements in astronomical spectroscopy include increased spectral resolution, which refers to how small a difference in wavelength the spectroscope can separate. Additionally, the use of larger telescopes has enabled the observation of fainter objects in the night sky.

For instance, almost 100 years ago, the Palomar Hale Dome was unveiled, housing a large telescope with a diameter of 200 inches (5.1 meters). Since then, many large telescopes have been built, such as the 8.2-meter-diameter Very Large Telescope (VLT) and the 10-meter-diameter Keck telescope. Currently, the construction of the 40-meter-diameter Extremely Large Telescope (ELT) is underway, with an

expected first light in 2027 (Tamai et al., 2020). This will be the largest telescope ever constructed, opening up new opportunities for groundbreaking astronomical observations.

A modern spectrograph of note used on the VLT is X-Shooter (Vernet et al., 2011), a single-target medium spectral resolution spectrograph in use on the VLT. X-Shooter has a wide bandpass of 300-2500 nm, high efficiency, and offers spectral resolving powers of 4000-17000. To achieve such a wide bandpass, X-Shooter is separated into three spectral arms: UV, visible, and NIR. X-Shooter has contributed significantly to various science cases, such as extreme star evolution (Martayan et al., 2011), providing new insights into the outflows of high-redshift red quasars (Zakamska et al., 2016), advancing our understanding of red supergiant physics (Davies et al., 2013), and playing a role in epoch of reionisation studies. The epoch of reionisation was studied with z>6 Lyα galaxies (Caruana et al., 2014) (Sobral et al., 2015), quasars (Schindler et al., 2020), and the objects that potentially played major roles in this epoch were studied in (Naidu et al., 2021).

Recent developments in astronomical spectroscopy have introduced new types of spectroscopes that go beyond single-target spectroscopy, such as integral field units (Integral Field Units (IFUs)), which enable 2D spectroscopy. In 2D spectroscopy, both spectral and spatial information are captured, providing a spectrum for each spatial pixel observed in the sky. The concept of an IFU was initially proposed in a paper by Courtes (1982). This proposal suggested using a microlens array to separate the image field, potentially in conjunction with a fibre bundle to direct incoming light to the spectrograph(s). However, the first realisation of this concept took place with the TIGER instrument (Bacon et al., 1988) in 1987. TIGER did not follow the original route proposed by Courtes (1982); instead, it directly fed light from the microlens array into a grism spectrograph. TIGER achieved a spectral resolving power of 220-2200, depending on the grism used, with a bandpass spanning approximately 380-850 nm. This advancement allowed for the study of galaxy dynamics and chemical composition, as demonstrated in Bacon et al. (1988).

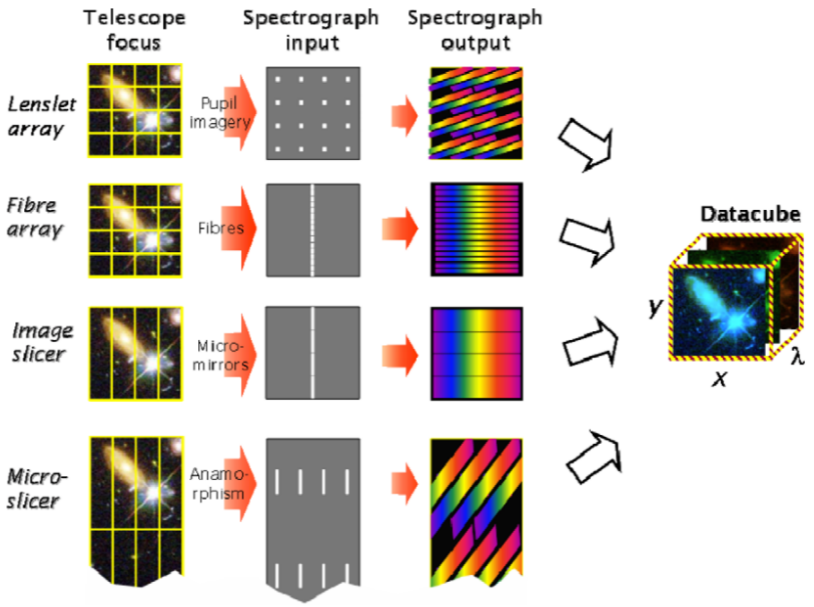

Figure 1.1: A summary of the different methods used for IFU instruments to separate the FoV into spatial pixels each with spectra. Shown from Allington-Smith (2006).

More recent IFU instruments employ alternative methods, such as image slicers, which are utilised in instruments like Multi Unit Spectroscopic Explorer (MUSE) (Bacon et al., 2010). Figure 1.1 provides a summary of the different methods used for field separation in IFUs.

Unlike TIGER, MUSE employs a Mini-Lens Array to separate the field from the telescope. Further separation of these fields is achieved using an image slicer (Henault et al., 2003). This image slicer consists of a reflective surface with differently angled 'slices', effectively dividing the image into sub-fields (Content, 1997), which are then directed to individual spectrographs. A summary of this is provided in Figure 1.2.

In contrast to TIGER, which achieved a highest spatial resolution of 0.6" upon construction, MUSE significantly enhances spatial resolution, achieving an impressive 0.2". This improvement has enabled in-depth studies of galaxy physics, including investigations into the relationships between galaxies and their central supermassive black holes (Henault et al., 2003). MUSE also offers a generous bandpass

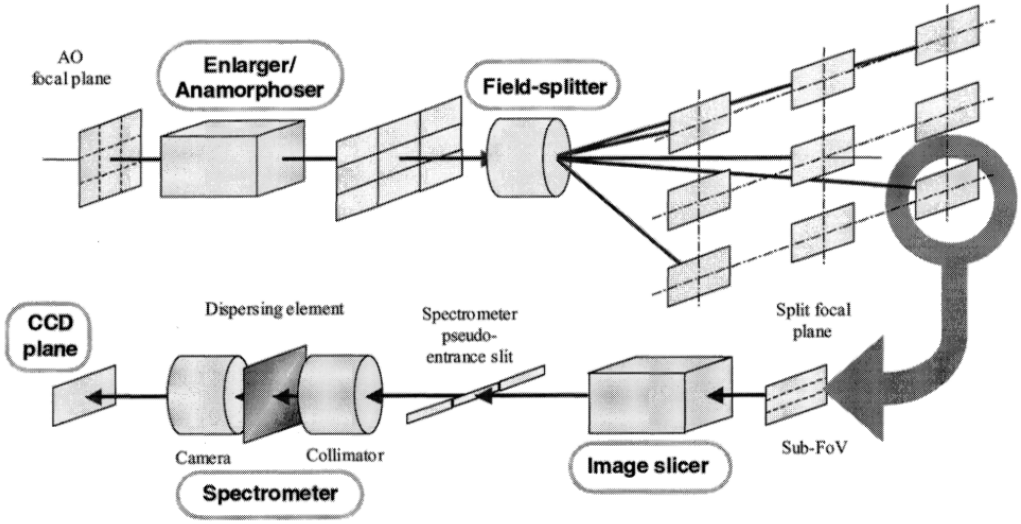

Figure 1.2: The schematic view of the MUSE instrument where it splits the incoming field. Shown from Henault et al. (2003).

of 475–935 nm, with spectral resolving powers ranging from 1750 to 7500. This spectral capability makes it well-suited for tasks like separating the OII doublet for galaxy redshift estimation (Urrutia et al., 2019).

Thanks to its remarkable spectral and spatial resolution, MUSE is particularly well-suited for survey observations, allowing for the characterisation of numerous galaxies, even those at redshifts exceeding $z > 6$. MUSE has impressively observed approximately 10,000 objects up to redshifts around $z \approx 6.6$, providing valuable data for further scientific investigations (Hashimoto et al., 2017).

Current Multi-Object Spectroscopy (MOS) instruments, such as FLAMES (Pasquini et al., 2002), boast nearly 200 fibres across their Field of View (FoV) and are optically connected to two instruments. GIRAFFE operates within the range of 370-950 nm with spectral resolving powers ranging from 6000 to 33,000. The UVES Red Arm offers a resolving power of 47,000, with three possible setups featuring central wavelengths of 520, 560, and 860 nm. This extensive range enables observations spanning from 420 to 1100 nm. GIRAFFE utilises 162 fibres, while UVES employs 8 fibres. Notably, the number of fibres will increase with upcoming instruments like MOONS (Cirasuolo and Consortium, 2020), which will harness a thousand fibres

within its observing field, enabling simultaneous observations of numerous objects. Each fibre is optically linked to a spectrograph, providing a spectral resolving power of 4000-7000 within the wavelength range of 645-1800 nm.

Another notable MOS instrument pertinent to this thesis is FORS (Appenzeller et al., 1998), which employs a slit mask to observe multiple objects in a single observation. Nevertheless, FORS can also operate in a single-object mode. The instrument boasts a spectral resolving power of up to 5000, contingent on various instrument parameters, and offers a bandpass spanning from 330 to 1100 nm. FORS' versatility in observing modes, coupled with its capacity to observe faint objects, facilitated the execution of a survey known as the FORS Deep Field (Noll et al., 2004). In this field, objects up to redshift $z \approx 5$ were observed using both imaging and spectroscopy, significantly advancing our comprehension of galaxy evolution (Heidt et al., 2001). One of the primary advantages of the FORS Deep Field Survey was its larger field of view compared to earlier faint measurements conducted with the Hubble Space Telescope. Some of these measurements were performed using the Faint Object Spectrograph (FOS), an instrument operating in the wavelength range of 115-700 nm and offering resolving powers ranging from 100 to 1000 (Harms et al., 1979).

1.2 Instrument Detectors

A vital component for all instruments, not just those listed in the previous Section, is the detector used at the camera of the spectrograph. In this section, a selection of both relevant and important detectors that have been used for these instruments will be discussed.

There are many detectors used for instruments in astronomical spectroscopy. Here, the focus will be on detectors relevant to the optical and near-infrared regimes of electromagnetic radiation, as well as detectors relevant to the work conducted throughout this thesis.

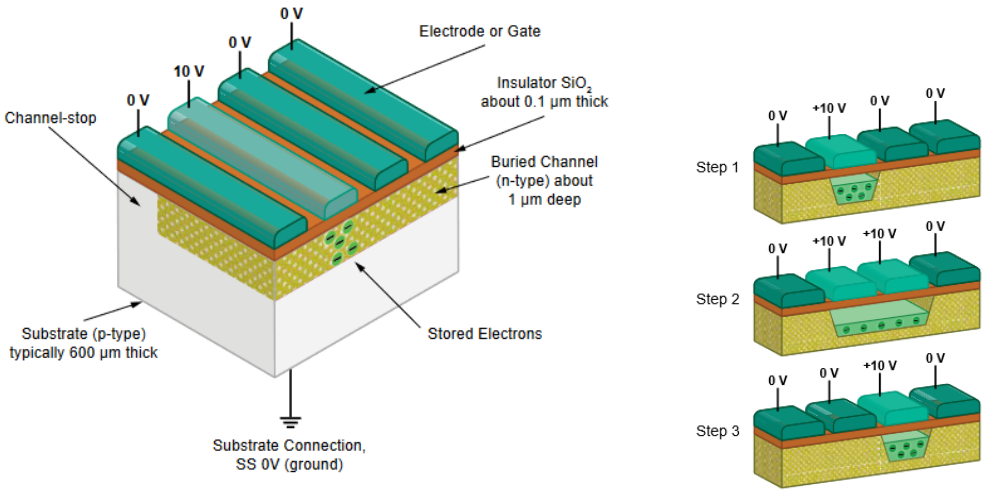

Figure 1.3: **Left** shows a basic diagram of a CCD, made by Teledyne Imaging. Incoming photons strike the Buried Channel (or epitaxial layer) and create electrons by the photoelectric effect. These photons are then stored using a biased Gate above this layer. **Right** shows a step diagram of the readout process of a CCD. Gates are procedurally biased to move the collected charge through the array to the output amplifiers where the analogue-to-digital conversion takes place.

1.2.1 Charge-Coupled Devices

Arguably, in the visible, the most common detector used for astronomy is the CCD. It is favoured for its high quantum efficiency in the range of approximately 400-1000 nm and its ability to have a large number of pixels, reaching up to 80 million in a single array* for off-the-shelf arrays. Specialist arrays of CCDs have reached 1.4 billion pixels, which was the array used for the Pan-STARRS facility (Kaiser et al., 2010). A diagram of a CCD is shown in Fig. 1.3, provided by Teledyne Imaging†.

The CCD structure consists of a silicon substrate with an epitaxial layer above it, also made of silicon but doped with other elements. This epitaxial layer, labelled as the "Buried Channel" in Fig. 1.3, is where electrons are generated through the photoelectric effect in response to incoming photons.

*https://www.teledyneimaging.com/en/aerospace-and-defense/products/ccds-for-space/

†https://www.teledyneimaging.com/media/1300/2020-01-22_e2v_how-a-charge-coupled-device-works_web.pdf

These generated electrons are then held in place with the biased Gate, which is separated from the buried channel by an insulating layer. As photons strike the CCD, more electrons are created and stored in the channel, accumulating more charge depending on the number of photons that arrived.

To convert this collected charge into usable data, the readout process is initiated. As shown in the right panel of Fig. 1.3, also from *, the gate's biases are procedurally altered to shift the collected electrons out of the CCD array. The collected charge is then read out row by row, one pixel at a time, to output amplifiers that convert the charge into a voltage.

While simple, CCDs introduce some added noise sources, as discussed in Dussault and Hoess (2004), such as readout noise. This noise is caused by electrons being either left behind or jumping ahead during the charge transfer process due to the electron circuitry used in the device. Readout noise also includes output amplifier and quantisation noise. The quantisation noise occurs as a result of the analog-to-digital conversion of the continuous CCD "image" to a digital image, which is a collection of integer values (Merchant and Castleman, 2022).

Another factor affecting CCD measurements is dark current, which is caused by thermally generated electrons in the CCD silicon substrate. However, the effect of this dark current can be reduced with dark field subtraction.

Despite these noise sources, CCDs have been successfully used in many astronomical instruments, such as X-Shooter (Vernet et al., 2011) on the VLT.

1.2.2 Electron-Multiplying CCDs

A variation of CCD technology that has garnered interest is the Electron-Multiplying Charge Coupled Device (EMCCD), and has been used in instruments such as ULTRASPEC (Dhillon et al., 2008). As described in Tulloch and Dhillon (2011), EM-

*https://www.teledyneimaging.com/media/1300/2020-01-22_e2v_how-a-charge-coupled-device-works_web.pdf

CCDs address two significant issues associated with standard CCDs: slow readout times and read noise. To improve readout times, EMCCDs employ a frame transfer design. This design includes both an 'Image' section and a 'Storage' section, both of the same size in pixels. After an exposure is completed in the 'Image' section, the charge is automatically transferred to the 'Storage' section, following the same process described earlier in this section. While the 'Storage' section is being read out, a new exposure can already begin in the 'Image' section.

Regarding the readout noise, before the collected charge reaches the output amplifier, it passes through an additional multi-stage register. In this stage, the collected electrons are multiplied using a high voltage clock, creating potential wells to which the electrons are moved. When the electrons fall into the potential well, they can be multiplied through the impact ionisation effect. This effect occurs when an electron with enough energy impacts the crystal lattice and creates extra electron-hole pairs through ionisation, generating the amplification of the collected charge (Ives et al., 2008).

Due to the multiplied charge, and given that the readout noise is independent of the incoming charge, the readout noise is now negligible in comparison to the multiplied charge. However, EMCCDs then suffer from multiplication noise, which arises from the fact that a single electron passing through the multi-stage register can cause a wide range of output amplification. According to Tulloch and Dhillon (2011), this has the effect of doubling the variance of the incoming signal, which is statistically equivalent to halving the Quantum Efficiency (QE). This means that in a photon noise-limited regime, a standard CCD will actually outperform an EMCCD (Tulloch and Dhillon, 2011). Additionally, EMCCD detectors do not offer the array sizes available to their typical CCD counterparts, with the largest available at the time of Tulloch and Dhillon (2011) being a 1k x 1k EMCCD, much smaller than a typical CCD.

1.2.3 Complementary Metal Oxide Semiconductor

Complementary Metal Oxide Semiconductor (CMOS) detectors have been widely used for near-infrared and infrared astronomy, in the form of HgCdTe detectors, for example, on X-Shooter (Vernet et al., 2011). CMOS and CCD detectors share some similarity in operation. Electrons are generated in both as a result of incoming photons in the HgCdTe photodiode, but for the CMOS readout, this charge is then converted straight to a voltage at the individual pixel by pairing the photodiode and readout amplifier together (Rogalski, 2019). This allows for knowing how much flux each specific individual pixel observes. However, these detectors primarily suffer from thermal, dark current, and 'reset' noise. Reset noise arises from the temperature and capacitance of the CMOS circuit. However, due to the use of HgCdTe, the effective wavelength range can be tuned by altering the individual elemental compositions, granting usability up to 2μm and beyond (Magnan, 2003), hence its use in the NIR arm of X-Shooter.

1.2.4 Selex Avalanche Photodiode for HgCdTe InfraRed Array

Selex Avalanche Photodiode for HgCdTe InfraRed Array (SAPHIRA) detectors are HgCdTe electron avalanche photodiodes. These detectors were developed with the aim of reducing the observation time by reaching photon limited performance for smaller photon counts than those of other detectors operating in the $0.8 - 2.5\mu$m range (Baker et al., 2016). An incoming electron strikes a HgCdTe layer on the detector, which creates electron-hole pairs in the layer. These electrons are then drawn through the detector, as shown in Fig. 1.4, shown from Baker et al. (2016). Because of this these detectors are low read and dark noise, and can have enhanced frame rates by reading out particular subarrays of the detector, rather than the entire detector (Goebel et al., 2018). From this SAPHIRA detectors have been used at the Suburu Telescope on SCExAO, the NASA Infrared Telescope Facility, the KECK II AO system, and GRAVITY, but the list extends beyond these (Goebel

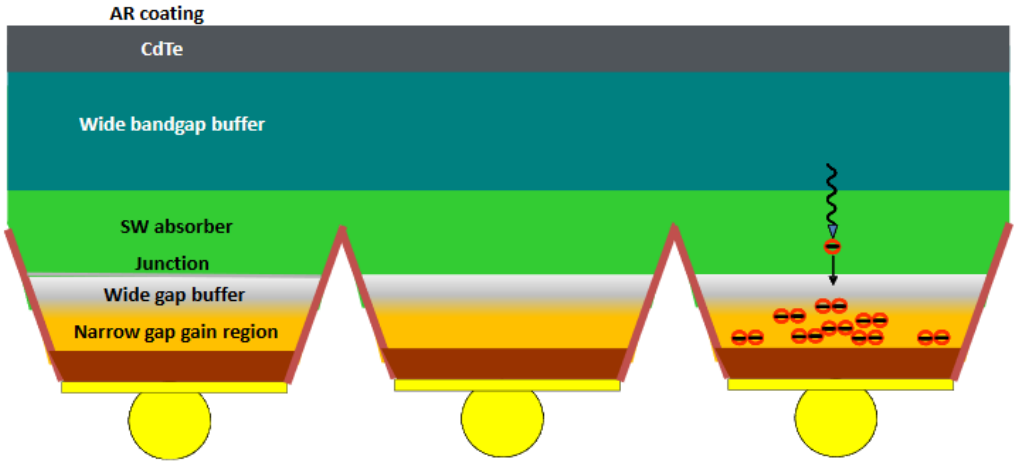

Figure 1.4: The schematic view of an HgCdTe e-APD array which the SAPHIRA detector is based on, shown from Baker et al. (2016).

et al., 2018). However while reduced, these detectors still suffer from read and dark current noise (Baker et al., 2016), and the maximum reduction of noise can only be achieved with the trade off of a longer pixel reset time (Goebel et al., 2018).

1.2.5 Microwave Kinetic Inductance Detectors

The next stage of astronomical spectroscopy is positioned to incorporate the benefits of the detectors and instruments listed here, while minimising their disadvantages. This detector is the Microwave Kinetic Inductance Detector (MKID) (Day et al., 2003), a superconducting detector. MKIDs are energy-resolving photon-counting detectors and, therefore, do not suffer from read noise like CCDs (Mazin, 2020). Their energy-resolving capabilities enable new spectrograph designs that can improve the optical system's throughput. Moreover, the absence of read noise allows for spectral rebinning without any penalty, eliminating the need for pre-defined spectral resolutions with instruments using these detectors (O'Brien et al., 2014). They have an effective wavelength range from the visible to near-infrared (De Visser et al., 2021; Zobrist et al., 2022) without requiring three spectrographs, as is the case with X-Shooter. Additionally, throughout their effective wavelength range, MKIDs do not suffer from increased readout noise or dark current at near-

infrared wavelengths, as observed in CMOS detectors (Mazin, 2020). MKIDs can also achieve photon arrival time resolutions on the order of microseconds (Mazin et al., 2013), and they do not exhibit a relative loss in performance in either photon noise-limited or read noise-limited regimes. These features can be harnessed for a new astronomical spectrograph that offers a wide bandpass, time resolution, high throughput, and exceptional performance in low SNR regimes.

Chapter 2

MKID Principles and Use

The overall structure of an MKID is an LC resonant circuit, composed of a capacitor and inductor (Day et al., 2003). An image of an example MKID is shown in Fig. 2.1. For a brief overview of the operating principle: when an incoming photon strikes the inductor portion of the MKID, Cooper pairs are broken, generating quasiparticles. Due to the energy gap of the superconducting materials used for these detectors, many Cooper pairs are broken, creating numerous quasiparticles. To read out the information about the photon impact, a microwave signal is propagated through the MKID circuit. Depending on the number of quasiparticles created, the phase and amplitude of the signal are altered. Because this alteration depends on the number of quasiparticles generated, which is in turn dependent on the energy of the incoming photon, this grants the MKID energy-resolving capabilities. Due to the form of the readout information, photon events can be both individually counted and observed to a μs (Mazin et al., 2010). However, due to the superconducting requirement of the MKID, they must be cryogenically cooled to temperatures of the order of ≈ 100 mK. The operation and readout will be discussed in more detail in Sec. 2.1 and Chapter 5.

It should be noted that MKIDs are not the only detectors in the superconducting category; others include Superconducting Tunnel Junctions (STJs) (Kurakado, 1992) and Transition Edge Sensors (TESs) (Irwin et al., 2005). Compared to these

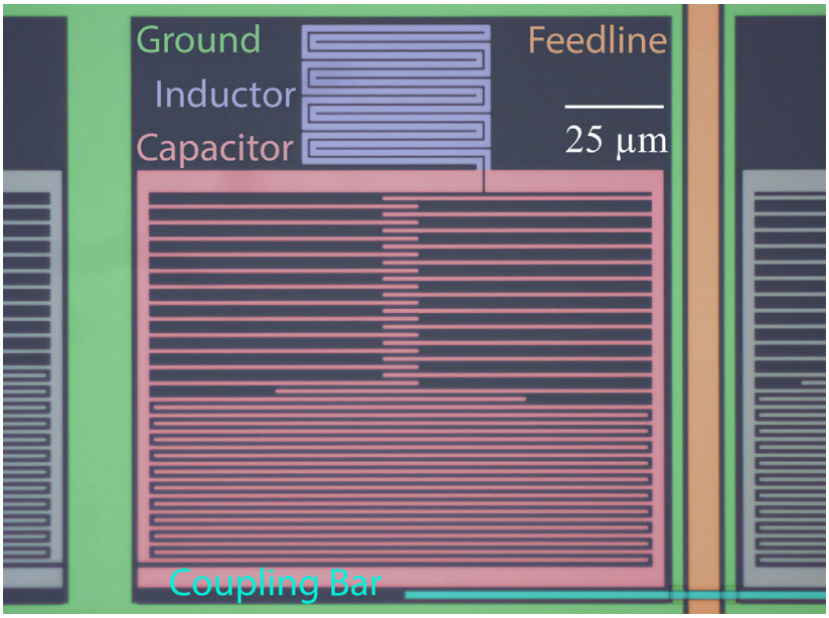

Figure 2.1: Image shown from Zobrist et al. (2022). A hafnium MKID coupled to a coplanar waveguide. An approximate scale bar was included for reference. False colours were added for labelling purposes. The dark area surrounding the capacitor and inductor is bare sapphire substrate. During operation, light is focused onto the inductor portion of the device using a microlens.

other detectors, MKIDs are a newer technology, but they offer several advantages over other cryogenic detectors.

For example, MKIDs can be fabricated into larger pixel arrays than STJs and TESs. This is because these two detectors require each pixel to have its own signal processing electronics and subsequently wiring, which presents limitations in hardware and thermal noise. However, this is only the case for when the units are simply grouped into an array. Alternatively, for STJs, a matrix readout can be used, which involves reading out the base and top film of the units separately in a 'base' and 'top' array in a line. After readout, a coincidence technique is utilised to match base and top film signals. This method reduces the processing and wiring required from N1xN2 to N1+N2, where N1 and N2 are the number of pixels. The drawbacks to this option for STJs are that count rates larger than 1000/s are more difficult to process for the electronics, and IR suppression is also made more difficult (Verhoeve et al., 2000). The IR suppression issue is a result of

IR flux seen by each unit (and therefore line here) being recorded as noise, which will be much higher than the simple array setup (Martin et al., 2000). However it should be noted MKIDs also suffer from issues of having a maximum photon rate and more difficult IR suppression. These will be discussed more in Chapter 3 and 5 TESs typically employ the use of Superconducting QUantum Interference Devices (SQUIDs), which also allows the TESs to be multiplexed. The use of SQUIDs, though, involves extra wires between the SQUID and TESs, requiring a complex heat management system for the thermal load (Irwin et al., 2005).

2.1 Theory of Operation

Following from Sec. 1.2.5, a KID (and MKID) is essentially made up of a resonant circuit containing a capacitor and an inductor. The circuit is also capacitively coupled to a coplanar waveguide for excitation and readout, shown in Fig. 2.1. Included as an example of the use of MKIDs, Fig. 2.2 shows images of the MKID array used for DARKNESS (Meeker et al., 2018). In this resonant circuit, a superconductor is used as the inductor, and its complex impedance is measured through the circuit. The surface impedance of the superconductor is given by Eq. 2.1,

$$Z_s = R_s + i\omega L_s \tag{2.1}$$

where L_s is the surface inductance, R_s the surface resistance, and ω is angular frequency.

The use of a superconductor allows for no resistance for DC electrical currents, but this is not the case for AC electrical currents, where the impedance is non-zero. The current through the system is carried by Cooper pairs, which are pairs of loosely bound electrons bonded via the electron-phonon interaction. When an AC electric field is applied near the surface of the superconductor, it causes the Cooper pairs to accelerate, applying kinetic energy to these pairs (Day et al., 2003). This, if

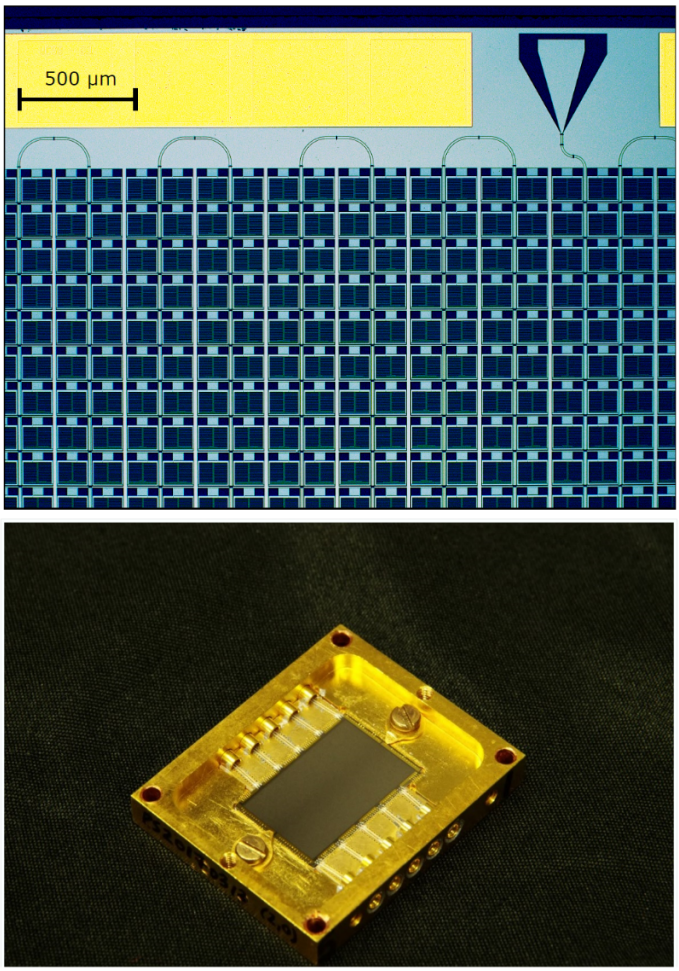

Figure 2.2: (**Top**) is a microscopic image of the DARKNESS MKID array after fabrication. (**Bottom**) shows the DARKNESS array after being mounted in their sample boxes and wire bond connections made. The DARKNESS array contains 10,000 MKIDS. Figure shown from Szypryt et al. (2017).

measured, results in extra inductance caused by the extraction of the kinetic energy of the Cooper pairs. To do this, the field direction must be reversed. Measurement of this can then be done by placing the superconductor within a lithographed resonator (Mazin et al., 2012). This change in inductance then causes a change in impedance from Eq. 2.1. The change of impedance can be described using Eq. 2.2 below, which is fully derived in Mazin (2004),

$$\frac{\delta Z_s}{Z_s} = -\frac{1}{3}\frac{\delta\sigma}{\sigma} \tag{2.2}$$

where σ is the complex conductivity. For the case of an incoming photon with greater energy than the band gap of the superconductor, if the incoming photon is absorbed it will break one or more Cooper pairs depending on its energy. As a result of this a cascade of interacting quasiparticles is formed with a population of excess quasiparticles described by Eq. 2.3 (Day et al., 2003),

$$N_{qp} \approx \frac{\eta h\nu}{\Delta}. \tag{2.3}$$

In Eq. 2.3 $\eta \approx 0.57$ is the efficiency of the photon energy conversion to quasiparticles (Mazin, 2004). The band gap parameter is represented by Δ, and $h\nu$ describes the energy of the incoming photon by Planck's constant and frequency respectively. These generated quasiparticles have a average lifetime of τ_{qp}, during which two quasiparticles meet, emit a phonon, and recombine into a Cooper pair. For the devices used in this thesis, this lifetime is on the order of hundreds of μs. During the time where there are excess quasiparticles however, this causes a change in the superconductor similar to a change in temperature. A change in temperature causes a change in conductivity which, from Eq. 2.2, causes a change in surface impedance Z_s (Mazin, 2004). The change in Z_s depending on the change in density of thermally excited quasiparticles n_{qp} can be described by,

$$\delta Z_s = \delta n_{qp} \frac{\partial Z_s}{\partial n_{qp}} \tag{2.4}$$

which can be approximated to,

$$\frac{\delta Z_s}{Z_s} \approx \frac{\delta n_{qp}}{2N_0\Delta} \tag{2.5}$$

where N_0 is the single-spin density of electron states at the Fermi energy of the superconductor material. The approximation made between Eq. 2.4 and 2.5 arises from the expectation that the fraction of Cooper pairs broken is comparable to the fractional change in surface impedance (Mazin, 2004).

This change δZ_s can be measured then using a resonant circuit. When the surface resistance R_s increases as a result of quasiparticle generation, the width of the resonance dip increases and becomes shallower. The result of this increase in R_s is the inductor becomes slightly lossy and adds a series resistance. At resonance the coplanar waveguide through line is loaded by the LC circuit, which causes a transmission dip. Also when quasiparticles are produced the surface inductance L_s increases, increasing the total inductance L, and lowering the frequency. These effects combine to alter the amplitude and phase (the definition of which is described below) of a microwave signal transferred through the circuit, used to excite the detector. The amplitude change specifically causes a power change δP (Day et al., 2003). Shown in Fig. 2.3 is a general overview of the photon detection process that is described here, shown from Day et al. (2003).

After the microwave signal is transmitted through the MKID device, a broadband cryogenic High Electron Mobility Transistor (HEMT) amplifies it. Next, an in-phase-quadrature (IQ) mixer measures the phase and amplitude of the signal as a function of time. The I portion is a sine wave at the resonant frequency of the MKID (I=in-phase), and the Q is a similar wave shifted -90 degrees out of phase (Q=quadrature) (McHugh et al., 2012). In the IQ plane, the resonance as a function of frequency can be shown and generates a circle, with different frequencies representing a different point on the circle. Fig. 2.4 shows an example loop. The phase angle θ is then calculated after using the centre of the circle as a reference to translate the circle to the origin. As the resonant frequency changes as a result of photons, the phase angle will change as well. The higher the number of quasiparticles generated, the higher the phase angle change (Day et al., 2003). When this phase angle is plotted with time, it is referred to in this work as a phase time stream. When an MKID is exposed to a monochromatic source, the phase angle change experienced by the MKID will vary, even though the wavelength of the incoming photons is approximately equal. This is the result of many factors, such as phonon losses, signal to noise ratio, and quasiparticle diffusion. The limit

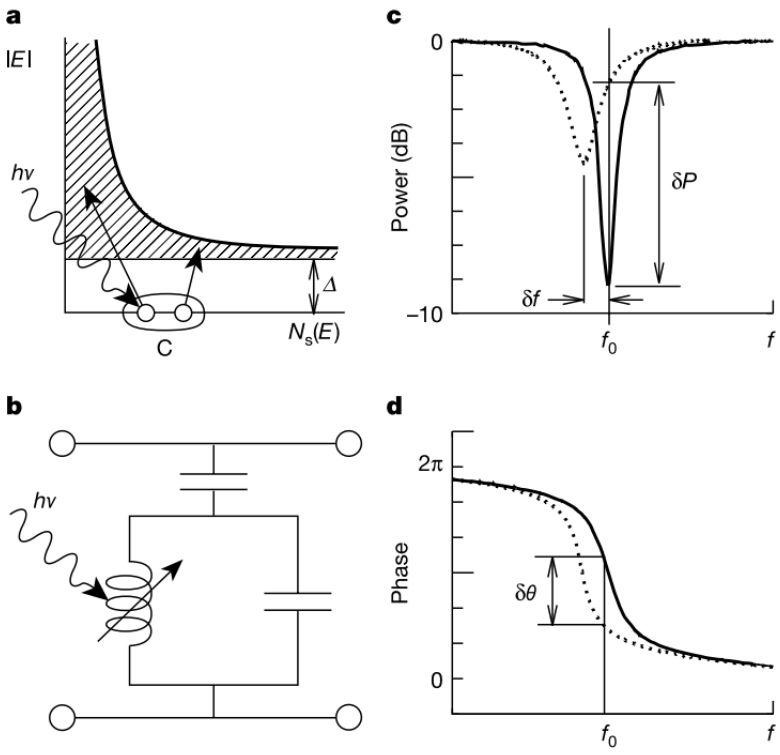

Figure 2.3: Figure shown from Day et al. (2003). (**a**) shows absorption of photons with energy $h\nu > 2\Delta$ by a superconductor(typically a film) cooled to $T << T_c$, causing Cooper pairs to be broken and quasiparticles to be generated. Here $N_s(E)$ represents the density of states for quasiparticles, and the shaded region as a function of energy of the quasiparticle. A Cooper pair at the Fermi level is represented by C. (**b**) describes the impact of the incoming photon on the LC circuit, namely changing Z_s of the superconducting film. The circuit is shown here as a parallel LC circuit capacitively coupled to a CPW through line. (**c**) presents the power change δP dip change, which occurs as a result of the generated quasiparticles increasing L_s and R_s, lowering the resonant frequency, and making the dip smaller and broader, shown by the dotted line. Finally (**d**) includes the data actually measured, the phase angle θ, with the change to phase as a result of quasiparticle generation shown by the dotted line.

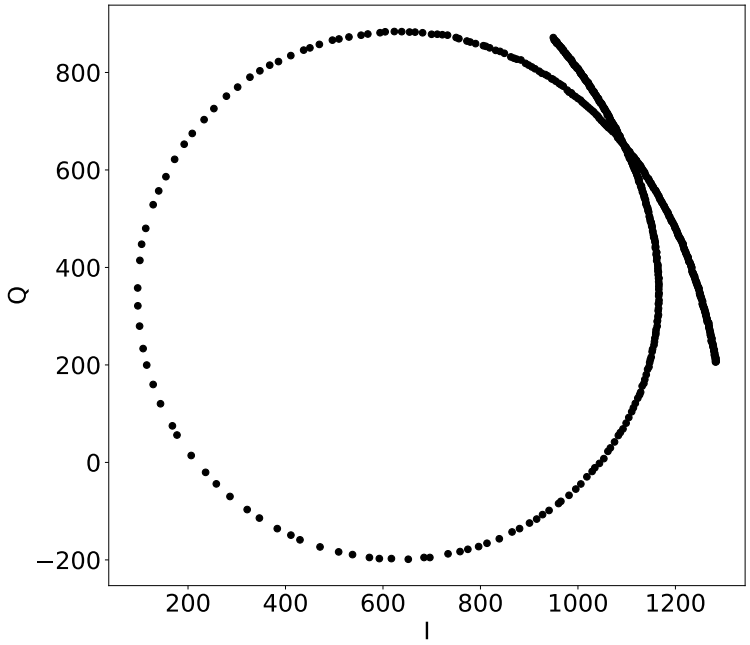

Figure 2.4: An IQ loop of an Al MKID, with the probe signal sweeping in frequency from $\approx 4.29 - 4.31$ GHz. Each point represents a frequency in this range. At each frequency 256 readings of I and Q are taken, and then mean averaged.

of the resolving power of an MKID is due to the initial photon energy conversion to quasiparticles, which occurs through a number of electron-electron and electron-phonon interactions (De Visser et al., 2021). The range of this variation can be described by,

2.2 Energy Resolution

Importantly for this thesis is the Energy Resolution (R_E) of MKIDs, which essentially is how well an MKID can discern different energy photons as a result of quasiparticle generation. Energy resolution in MKIDs can be defined as,

$$R_E = \frac{E}{E_{FWHM}} = \frac{1}{2.355}\sqrt{\frac{\eta h\nu}{F\Delta}} \tag{2.6}$$

where E is energy, η is the conversion of energy into quasiparticles efficiency ($\approx$0.57), $h\nu$ is photon energy, Δ is bandgap energy, and F is the Fano factor ($\approx$0.2) (Kozorezov et al., 2008; Mazin et al., 2019). Eq. 2.6 is for the case where the resolving power is governed by Fano statistics, which is where the incoming photon's energy is entirely kept inside the detector after the initial impact of the photon (De Visser et al., 2021) which results in $R_E \propto \lambda^{-1}$. This is the limit for the MKID R_E, caused by the variation in quasiparticle generation by each photon. Due to higher energy (and as such, shorter wavelengths), photons generate more quasiparticles, and energy resolution falls as a result of increasing wavelength. To determine R_E, though, the FWHM of the pulse height distribution is measured. When a photon interacts with the MKID and generates quasiparticles, causing a change in phase, it appears as a peak in a phase time stream. However, the height of the peak is not the same with every photon of the same energy, because of the quasiparticle generation variation and current detectors are unable to trap all the energy from the incoming photons. For example through phonon losses after the initial photon arrival.

There are a number of intrinsic and external factors that influence the height of the peak, such as the amplifier noise, Fano noise, and the generation recombination noise (Yates et al., 2011; Mazin et al., 2013), which can be seen as phase stream noise in Fig. 2.5. The Fano noise represents the variance in number of generated quasiparticles from a photon event. The generation recombination noise represents the fluctuation of the kinetic inductance of the superconductor, as a result of random generation and recombination of the thermal quasiparticles also in the superconductor (Mazin, 2004). There is also additional noise introduced from the electronics used for the readout of the detector, such as the previously mentioned amplifier noise.

Because of these factors, if a monochromatic source is exposed onto an MKID the pulse heights will not all be equal. The R_E value of an MKID can be determined by the full width half maximum (FWHM) of the phase heights distribution, when

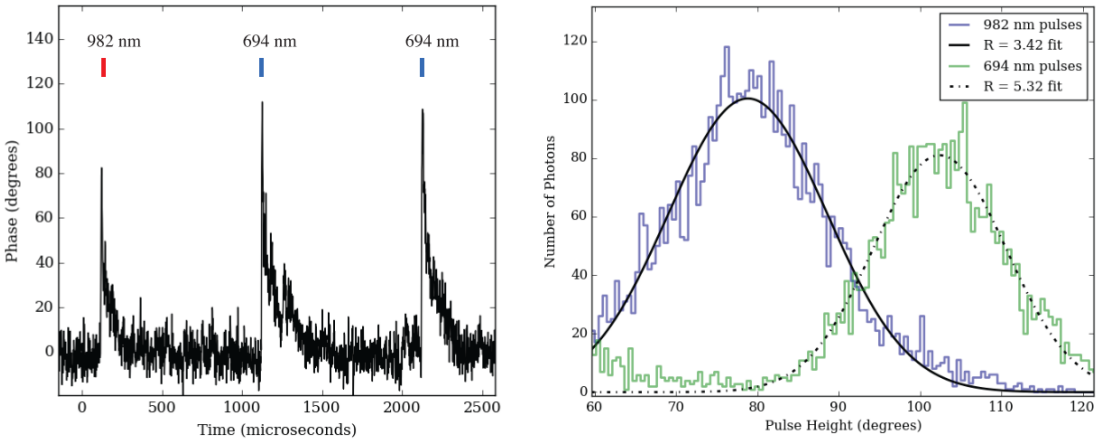

Figure 2.5: (**Left**) Pulses in the phase time stream of an MKID pixel resulting from 694nm and 982nm photons. The height of these pulses is defined as the maximum phase change (in degrees), which has been measured by the microwave probe signal fed through the pixel. As seen in this panel, lower wavelengths result in higher pulse peaks. (**Right**) The energy resolution R_E at a particular wavelength can be determined by measuring the FWHM of the pulse height distribution after exposure to monochromatic light. Here, for 694 nm, $R_E \approx 5$, and for 982 nm, $R_E \approx 3$. Figure shown from Meeker et al. (2015).

the MKID has been exposed to monochromatic light (Meeker et al., 2015). This phase height distribution can be approximated as a Gaussian-like trend, as shown in Fig. 2.5. If R_E were infinite, the resulting Gaussian would actually be a delta function, and the MKID would be able to separate every photon of differing energy from each other. The impact of R_E for a MKID instrument will be explored in Chapter 3.

Additionally the R_E of MKIDs can be affected by the choice of material, such as previously mentioned PtSi, or Al. These materials are used as a superconducting film deposited on the device for the superconducting resonator, consisting of the inductor and capacitor portions of the device (Szypryt et al., 2017), shown in Fig. 2.1. The PtSi devices achieved R_E values of 5.8-8.1 at 1310-808nm respectively (Szypryt et al., 2017), whereas the Al devices achieved 19-52 at 1545-402nm (De Visser et al., 2021). For aluminium this is in comparison to a maximum theoretical value of 94 at 400nm (Mazin, 2004). However the designs of the devices were also different, contributing to these results. The Al devices from De Visser

et al. (2021) had a focus on reducing various noise sources, at the cost of a lower photon absorption efficiency due to the aluminium being more reflective in the optical wavelength range.

The R_E of MKIDs can also be affected by fabrication effects. One such fabrication effect that can potentially affect observations with MKIDs is R_E variance (R_{var}) Meeker et al. (2018). When an MKID array is fabricated, the R_E of the MKID pixels may not all be equal to each other. Meeker et al. (2018) showed that in an array of PtSi MKIDs, the R_E values had a normal distribution with a FWHM of approximately 3. This variance may have been the result of the resonator etching process for the inductor, where 300nm wide features were fabricated. With 10,000 MKIDs to fabricate on a single array, some etches may not have been completed and caused varying results and resonator properties (Szypryt et al., 2017). The effects of this fabrication effect, in addition to the dead pixel fraction, are explored in Sec. 3.4.2.

2.3 Cryogenic Refrigerators

Due to the superconducting nature of the MKIDs, to avoid thermal excitations, they must be operated below the critical temperature, at temperatures of $T \approx 10^{-1}$K, thereby requiring a cryogenic refrigerator. Aluminium MKID devices have been operated at 120mK (De Visser et al., 2021), and PtSi devices have been operated at a temperature of 100mK (Meeker et al., 2018). To do this cryostats are used, which does impose added constraints and requirements on instrument design. Two choices of cryogenic refrigerators are Dilution Refrigerators (DRs) and Adiabatic Demagnetisation Refrigerators (ADRs).

DRs use a mixture of ^{3}He and ^{4}He pumped through a system for heat absorption to achieve mK temperatures. The ^{3}He leaves a still and begins by being cooled initially with the use of liquid nitrogen followed then by a bath of ^{4}He at 4.2K. Next a 1K vacuum pumped ^{4}He bath liquefies the ^{3}He. The ^{3}He is afterwards directed

to the mixing chamber. Here the ^{3}He removes heat from the mixing chamber and as such cools the desired device. After leaving the mixing chamber the ^{3}He returns to the still before continuing the cycle (Martin et al., 2010).

ADRs on the other hand exploit salts. Salt molecules have particularly large internal magnetic fields in comparison to other molecules. When these molecules are exposed to an external magnetic field the molecules will align themselves with this magnetic field. However the random thermal motions of the molecules have the opposite effect causing the molecules to de-align, with a greater temperature causing a greater de-alignment. These salt molecules are contained inside a salt pill in the ADR, thermally connected to the device which is to be cooled. When this salt pill is subjected to a strong magnetic field the molecules align with the field, until the strength of the field is decreased and the thermal motions of the molecules begin to de-align them. This process of de-aligning requires energy, which comes from the thermal motion and heat from the surroundings. The result of this is the thermal energy is transformed into magnetic energy which cools the salt pill and as a result the device to be cooled (Hagmann and Richards, 1995).

DRs tend to be smaller and lighter due to not having the added magnets requirements (Martin et al., 2010) and can be kept at milliKelvin temperatures much longer than ADRs, but ADRs have a lower base temperature, higher efficiency, and do not require gravity to function (Shirron et al., 1999).

2.4 MKID instruments

At the time of writing this work, MKIDs' unique properties have been exploited in an increasing number of optical/NIR instruments, such as the Array Camera for Optical to Near-IR Spectrophotometry (ARCONS; Mazin et al., 2013), the DARK-speckle Near-infrared Energy-resolving Superconducting Spectrophotometer (DARKNESS; Meeker et al., 2018), and the MKID Exoplanet Camera

(MEC; Walter et al., 2020). More instruments are also planned to take advantage of these superconducting detectors.

ARCONS was an imaging spectrophotometer deployed on the Palomar 200-inch and Lick 120-inch telescopes in 2010. It utilised TiN MKIDs to create images of the night sky, with each MKID capable of resolving a spectrum with R$\approx$ 10 at 400nm. Initially, 1024 MKIDs arranged in a 32x32 grid were used, providing a FoV of 10x10 arcseconds (Mazin et al., 2010). In 2013, an upgrade increased the number of MKIDs to 2024, expanding the FoV to 20x20 arcseconds. The decision to employ MKIDs was motivated by their advantages, including a simple optical design, improved throughput, μs time resolution, a wide detector bandpass without the need for extra spectral arms, no loss of observing time due to readout, precise photon arrival time recording, and the absence of read noise or dark current (Mazin et al., 2013).

Thanks to their energy-resolving capability, MKIDs eliminate the need for additional optics to separate incoming wavelengths, a requirement for CCDs. MKIDs can perform this task independently, with spectral resolution determined by their specific capabilities. Moreover, the precise recording of photon arrival times enhances cosmic ray removal, as cosmic rays affect only a few-microsecond time bins, unlike CCDs, where they impact the entire exposure.

ARCONS, deployed on 24 observing nights at Palomar Observatory, capitalised on these MKID advantages. During its observations of celestial objects, ARCONS revealed a connection between enhanced optical flux and giant radio pulses, registering an increase of $11.3 \pm 2.5\%$ in the presence of a radio pulse (Strader et al., 2013). ARCONS also studied SDSS J0926+3624, placing constraints on its orbital period rate of change at $(3.07 \pm 0.56) \times 10^{-13}$ days per cycle. This finding indicated orbital expansion, shedding light on the system's formation history. These discoveries were made possible by MKIDs, particularly their time and energy resolution (Szypryt et al., 2014). These features facilitated data timing for comparison with radio observations and enabled tracking of spectral variability from blue to infrared

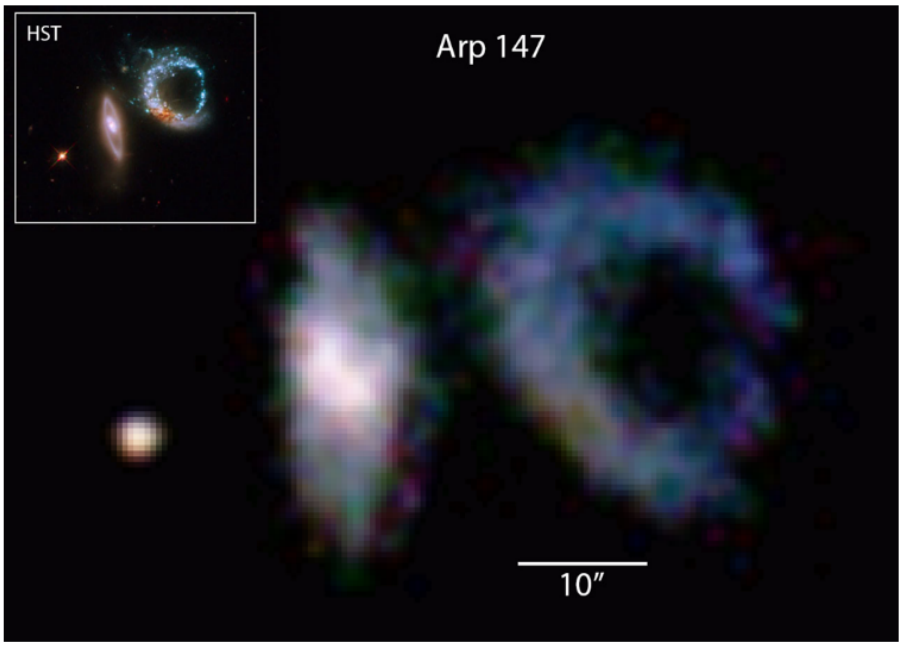

Figure 2.6: Shown in Mazin et al. (2013), this image was taken by ARCONS on the Palomar 200-inch telescope, capturing the interacting galaxies Arp 147. The observation was made with 36 pointings, each lasting 1 minute. The false colours in the image were created by separating the ARCONS MKID data into three bands: red, green, and blue. The inset figure in the top right corner shows a processed Hubble Space Telescope image of the same galaxy system.

wavelengths by observing in multiple bands, as illustrated in Fig. 2.6 from Mazin et al. (2013). This marked a significant milestone in the application of MKID instruments (Meeker et al., 2018).

The next MKID instrument commissioned in 2017 at the Palomar Observatory was DARKNESS. When undergoing exoplanet imaging, a significant issue encountered are speckles. These speckles are particular patterns that resemble faint companions to the host star. They occur within the adaptive optics of the instrument due to residual wavelength and non-common path aberrations between the wavefront sensor and science camera, which allow some light from the host star to escape the coronagraph (Meeker et al., 2018). Speckles can also arise from the optics of the instrument or residual atmospheric aberrations. These atmospheric aberration speckles have decorrelation times of the order of milliseconds to seconds. To overcome this issue, fast, low-noise detectors in the NIR are needed. DARKNESS was

constructed precisely to fulfil this requirement.

DARKNESS employs PtSi MKIDs in an 80x125 (10,000) array, representing a substantial increase over ARCONS. The selection of PtSi material for MKIDs in DARKNESS resulted from a performance comparison, demonstrating that PtSi devices performed as well as or even better than TiN devices. This superiority was particularly noticeable in terms of the uniformity of the fabricated array and photometric stability. The instrument's bandpass ranged from 800 to 1400 nm. The MKIDs used in DARKNESS offered a resolution of approximately 7 at 800 nm, which decreased to 5 at 1400 nm.

As illustrated in Meeker et al. (2018), during the observation of 32 Peg Ab, DARKNESS effectively suppressed fast speckles. This was achieved by leveraging the MKID's microsecond time resolution to discern differences in intensity over time, as compared to an actual companion object.

Building upon the successes of DARKNESS, MEC (as described in Walter et al., 2020) was developed as the first permanently deployed NIR MKID instrument. It operates at the Subaru telescope, serving dual roles as an Integral Field Unit (IFU) and a focal plane wavefront sensor for the adaptive optics system at SCExAO. MEC shares several similarities with DARKNESS, including the same bandpass, MKID devices, and readout electronics. However, MEC's MKID array is larger, with dimensions of 140x146 (20,440), approximately double the size of DARKNESS. As of the time of writing this thesis, MEC boasts the largest active MKID array in the optical/NIR domain.

Chapter 3

KIDSpec Simulation

3.1 Kinetic Inductance Detector Spectrometer

As discussed in the previous Chapter, MKID usage in the optical/NIR range is growing. In the future, a new instrument that could take advantage of these detectors is Kinetic Inductance Detector Spectrometer (KIDSpec), which is the focus of this thesis. KIDSpec is a conceptual medium-resolution optical through near-IR MKID echelle spectrograph (O'Brien, 2020). In this instrument, MKIDs will enable medium-resolution spectroscopy instead of the spectro-imaging applications of previous instruments.

MKID technology presents exciting opportunities for low-SNR spectroscopy, which remains in high demand. MKIDs are well-suited for this purpose due to their absence of read noise and dark current (Mazin et al., 2018), and their inherent energy resolving capabilities. The improvements in SNR provided by MKIDs can be observed from the standard SNR equation,

$$SNR = \frac{N_{Obj}}{\sqrt{N_{Obj} + N_{Sky} + RON^2 + N_{Dark}t}} \tag{3.1}$$

where N_{Obj} represents the target object signal, N_{Sky} is the sky background signal, RON is the readout noise contribution, N_{Dark} is the dark current contribution,

and t is exposure time in seconds. The absence of read noise and dark current components for MKIDs allows for higher SNR at shorter exposures compared to typical semiconductor detectors. MKIDs also offer greater flexibility than typical semiconductor detectors, as it is possible to rebin the spectrum to a lower spectral resolution post-observation without adding additional readout noise.

KIDSpec will provide low-noise spectroscopy, particularly suitable for studying faint sources such as high redshift galaxies. Examples of these faint sources in relation to KIDSpec are explored further in Sec. 3.5.2 and 3.5.3. These sources are of great importance as they provide crucial information on the different stages of the universe's evolution and enable studies of the stellar content of these galaxies. MKIDs' lack of read noise and dark current will support these studies, while their time resolution will allow for other features such as excellent cosmic ray removal.

The time-resolving capabilities of MKIDs will also facilitate observations of short-period binary systems, such as eclipsing double white dwarf binaries (Burdge et al., 2019). Furthermore, the MKID's ability to take real-time simultaneous sky background data using an extra spatial pixel will improve sky subtraction. This will be possible by utilising the energy and time resolving capabilities of the MKIDs to track sky emission throughout an observation (Mazin et al., 2010).

KIDSpec is intended to have similar capabilities to the VLT instrument X-Shooter (Vernet et al., 2011), which is currently one of the most oversubscribed instruments on the VLT and utilises CCDs for the visible wavelength range. KIDSpec aims to fulfil similar goals as X-Shooter and then more with additional functionality due to KIDSpec's use of MKIDs. This key difference in the instruments leads to alterations in design, one of which is the use of a cross-disperser for order resolving. CCDs require the use of a cross-disperser to separate the orders of incoming diffracted light since CCDs lack energy-resolving capabilities and cannot differentiate different orders (Vernet et al., 2011; Tull et al., 2019). The complex optical layout of the NIR arm of X-Shooter, as a result of this requirement, is shown in Fig. 3.1. As stated in the X-Shooter User Manual, the NIR arm optical system has 29 surfaces.

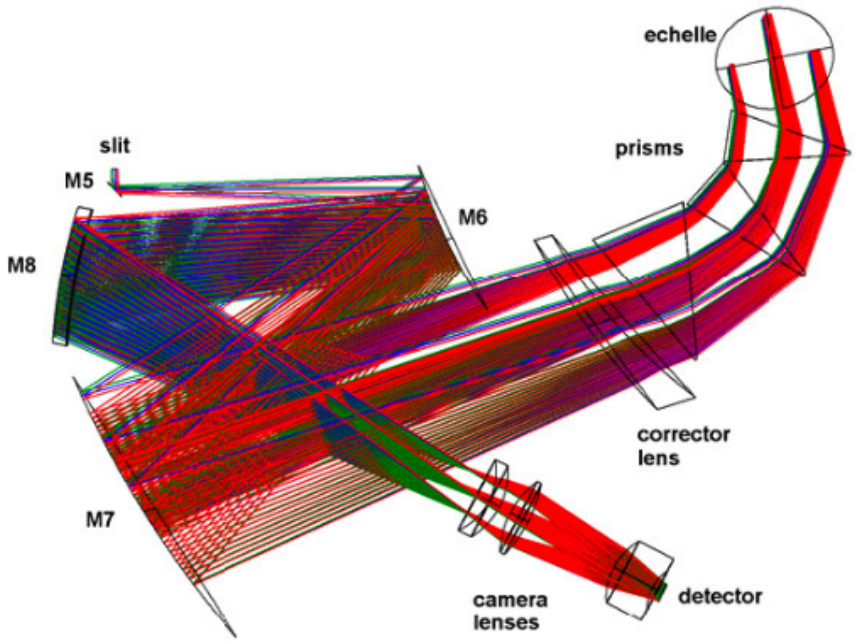

Figure 3.1: Shown from Vernet et al. (2011), the optical layout of the NIR arm of X-Shooter.

KIDSpec would not need this many surfaces due to the lack of a need for a cross-disperser, improving its throughput in comparison. Since the MKIDs can separate between orders through their energy-resolving capability, the cross-disperser is not needed. Potential designs of KIDSpec will be explored in this Chapter.

3.2 KIDSpec Design

KIDSpec will be a single object spectrograph with sufficient spectral resolution to resolve background sky lines for their subtraction, with a bandpass of $0.35 - 1.8\mu m$ in this work. The grating which would be used would be an echelle grating, which is a ruled grating with a low groove density and high blaze angle in comparison to standard ruled gratings. The use of an echelle grating would allow for more orders to be exposed onto an MKID from the higher orders accessible with an echelle grating, allowing higher spectral resolutions.

The use of MKIDs will allow KIDSpec to photon count with μs time resolution.

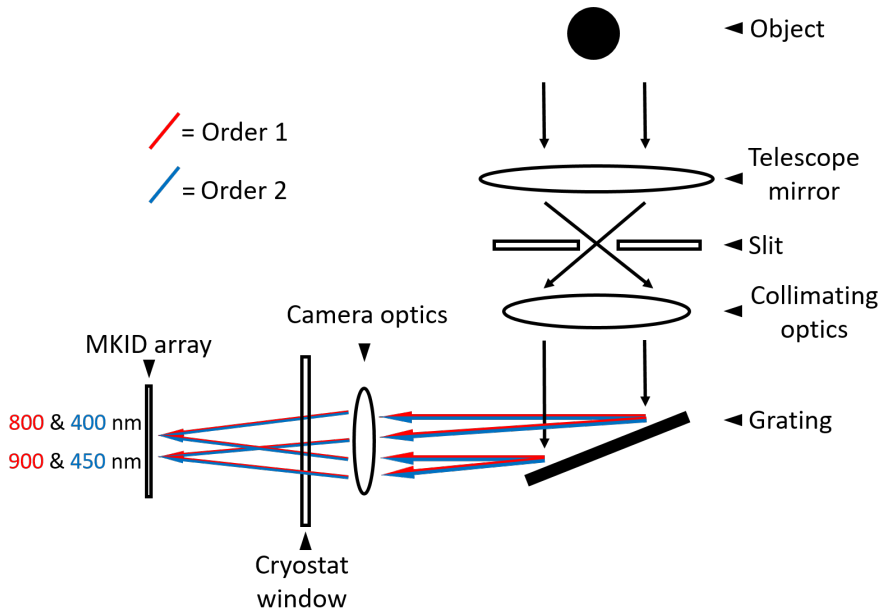

Figure 3.2: Conceptual optical layout of KIDSpec. Note that a cross disperser is not required. Shown after the grating are the first and second orders, arbitrarily chosen to show an example of separate order wavelengths which are incident on the MKIDs. Each set of wavelengths from the orders shown are exposed onto a single MKID, which can then separate the different orders. In practice many orders, and hence wavelengths, would be exposed onto a single MKID.

These features and the MKIDs low-noise capabilities makes KIDSpec an exciting instrument for many science cases, especially those which require short and/or faint exposures with a wide bandpass. Fig. 3.2 shows a conceptual optical layout for KIDSpec.

This design is based on a slit spectrograph where each spatial resolution element is dispersed onto a linear array of MKIDs. The slit could be formed by a mask, or a fibre, or even an integral field unit (IFU). A KIDSpec design with multiple spatial elements would require additional MKID pixels but would deliver additional information such as a simultaneous sky measurements or spatial information on the source. We have chosen to keep the geometry here as simple as possible to demonstrate KIDSpec's and KSIM's functionality, but more complex spaxel geometries could also be simulated in a similar manner.

A key parameter of MKIDs, and thereby KIDSpec is how accurately they can

determine the energy of a photon, their energy resolution (R_E). This R_E allows KIDSpec to discern the incoming orders from the echelle grating, thereby not requiring a cross-disperser. The highest R_E achieved for MKIDs in the optical/NIR regime is 55 at 402nm (de Visser et al., 2020). This is sufficient for KIDSpec but is still 2-3 times lower than the theoretical maximum for MKID energy resolution (Mazin et al., 2010).

To separate the incoming orders, each MKID pixel within KIDSpec would see a particular wavelength bin from each order exposed onto it, depending on the pixel's position in the linear array. The R_E then determines the number of orders which can be separated, since a higher R_E results in a smaller FWHM for the phase height Gaussians of each order. This is shown in Fig. 3.3, with example grating orders of 8, 9, and 10, with the R_E for each order determined. Essentially, the higher the R_E is of an MKID, the more orders can be resolved by the device. Conversely, as the R_E lowers, the order Gaussians overlap more, and in a wider wavelength range it becomes unclear to which order an individual photon belongs, and it could be misidentified. From the top panel of Fig. 3.3, if a photon event appears as ≈475nm to the MKID, there is a finite probability that it could belong to any of the orders shown. Probability distributions using the Scipy Stats Python module were generated of the dataset shown in the top panel of Fig. 3.3. A 475nm photon would have a 20% likelihood to be from order 10, 74% likelihood to belong to order 9, and a 6% likelihood to belong to order 8. Here this photon would be sorted into order 9, due to it having the highest probability, but it may have been incorrectly placed.

In the bottom panel of Fig. 3.3, a $3 \times m$ separation between the orders is shown, where m is the order number. For equal height Gaussians, the orders are fully separated when $R_E \geq 3m$. The R_E of the MKIDs in an array hence defines the highest grating order which can be resolved with this separation. However, by using a separation factor of 2 instead, this would reduce the number of MKIDs required for the same spectral resolution. The lower separation requirement means

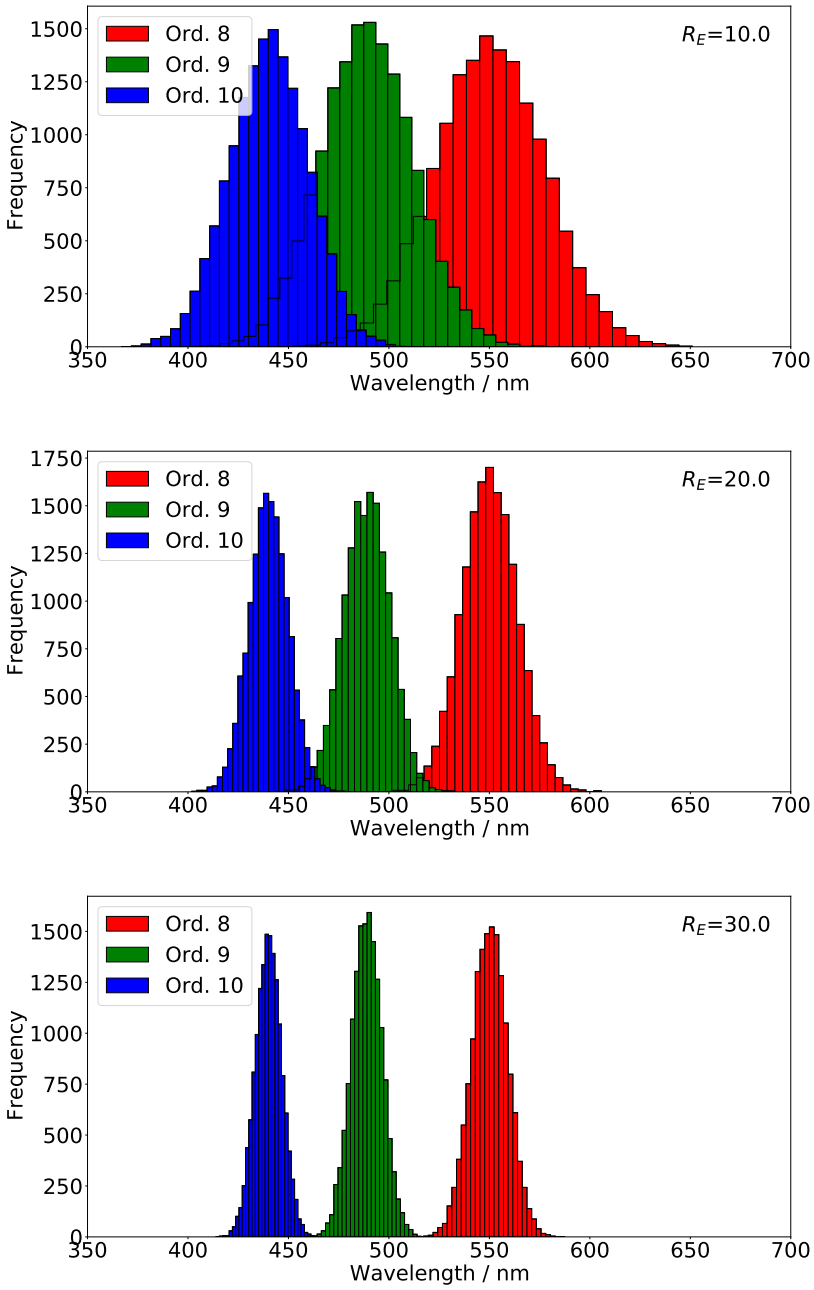

Figure 3.3: Three adjacent order Gaussians for orders 8, 9, and 10 with wavelengths 550, 489, and 440 nm at varying R_E. Values used here for R_E are 10, 20, and 30 at the centre of Order 10, which are equal to the order number m, $2m$, and $3m$, where $m = 10$ is the order number. Note that if the R_E was higher, the MKID could resolve higher order numbers. The Gaussians were generated using the photon time stream simulation outlined in Sec. 3.3.5 and exhibit the spread of wavelengths of the incoming photons as seen by the MKID because of its R_E, which is determined for each order. The percentage of photons falling in an overlapping region for an R_E of 10, 20, and 30 were approximately 97%, 38%, and 0% respectively.

a higher maximum grating order, increasing the number of spectral orders exposed onto the MKID. However, this increases the overlap between order Gaussians as seen in Fig. 3.3.

To prevent photon misidentification issues in this scenario, these Gaussians could be fitted with probability density functions to determine what photons are sorted into which order. This function would be used to determine the probability of the photon belonging to each spectral, similarly to the probabilities presented in the previous paragraph. Whereas with a separation factor of 3, a range of wavelengths would be assigned to each order and the incoming photons can simply be sorted into which order they have originated from. Therefore reducing the separation factor does complicate the analysis of incoming photons, and also requires enough incoming photons to create the fits for the orders. For simplicity hereafter, a separation factor of 3 is used.

Variance in the R_E of the MKIDs will also affect how well each individual MKID can separate incoming wavelengths, meaning the width of the Gaussians shown in Fig. 3.3 will vary between MKID pixels in the array. We define this variance as R_{var} which will also affect KIDSpec. This fabrication effect in addition to the dead pixel fraction are explored in Sec. 3.4.2.

To develop the design and establish the limitations of KIDSpec, a simulation tool has been created to test various design and observational parameters, for a range of science cases. This is the KIDSpec SIMulator (KSIM). For the remainder of this Chapter we outline KSIM and its current features, and include simulations of a selection of KIDSpec's science cases to showcase the instrument's potential, and limitations, upon construction.

3.3 KIDSpec Simulator

KSIM aims to give a performance prediction of what KIDSpec could achieve on sky. A key motivation for KSIM is flexibility, to be able to simulate a range of

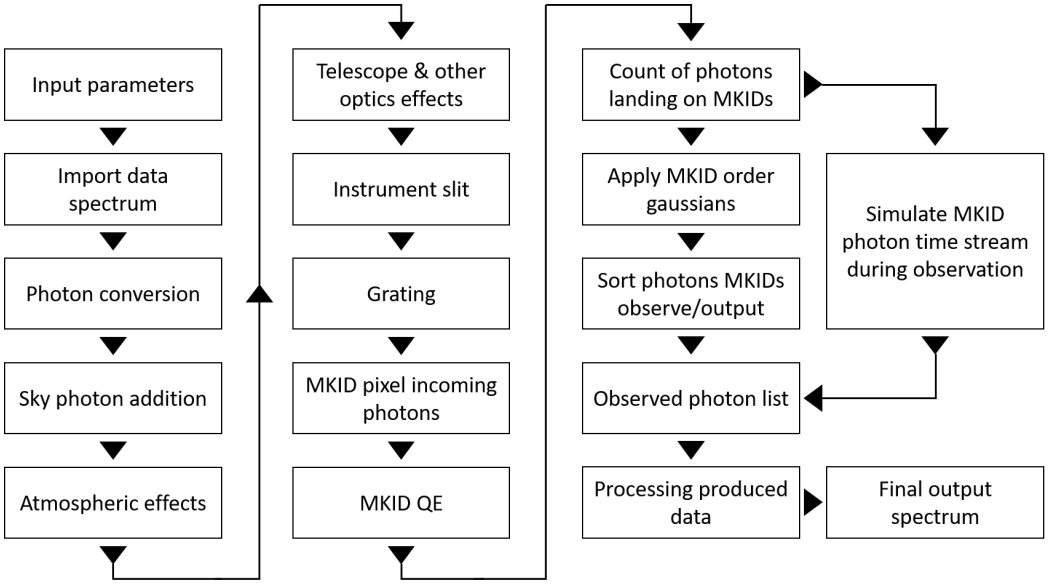

Figure 3.4: Flowchart depicting an overview of KSIM during the simulation of an object spectrum. The split in the directional arrows in the top right corner of the diagram indicates a choice of two methods for processing the MKID response to the incoming photons, the order Gaussians and photon time stream method, more details in Sec. 3.3.4 and 3.3.5.

potential KIDSpec instruments, to give an overview simulation of what science those potential instruments could be used for. Fig. 3.4 shows a flowchart of KSIM. A parameter text file is read in, which includes aspects such as the grating parameters, telescope information, and atmospheric parameters. The full list of KSIM parameters are included in Sec. 3.8. All steps in KSIM are modular and so can be modified easily. Within KSIM, spectral pixels are defined as the number of MKID pixels used to make up an individual 1D spectrum. The effective number of MKID pixels is the total MKID pixels multiplied by the number of orders each MKID observes, more details in Sec. 3.3.3 and 3.3.4.

The simulation initially reads in the data spectrum of the object to be simulated. As the simulation progresses, various processes are accounted for such as atmosphere and telescope transmission.

3.3.1 Atmospheric effects, photon conversion, and telescope effects

Transmission data for the atmosphere was acquired from the GEMINI Observatory* in Cerro Pachon, Chile. The optical (OPT) extinction, and the near-infrared (NIR) atmospheric transmission† data were utilised. This transmission data was used instead of potential data from Paranal because the GEMINI data is publicly available. Paranal data that could be sourced was used, such as the sky emission used later in this Chapter. The OPT extinction data was converted to the OPT transmission of the atmosphere using Eq. 3.2,

$$\frac{I_2}{I_1} = \mathrm{OPT}_{\mathrm{Transmission}} = e^{-\frac{A_{\mathrm{atmos}} x}{2.5}} \tag{3.2}$$

where I_1 and I_2 are the intensity before and after atmospheric transmission respectively, A_{atmos} is the atmospheric extinction values from GEMINI, and x is airmass. The computed OPT transmission data and GEMINI NIR transmission data are then applied to the spectrum. For flux to photon conversion Eq. 3.3 is used which assumes flux F in units of erg cm^{-2} s^{-1} Å^{-1},

$$N_{\mathrm{photons}} = \left(\frac{F\ \Delta\lambda\ A_{\mathrm{mirror}}\ t_{\mathrm{exposure}}}{E_{\mathrm{photon}}} \right) \times T_{tel} \times T_{ins} \tag{3.3}$$

where $\Delta\lambda$ is the size of the wavelength bins in the spectrum, A_{mirror} is the area of the telescope mirror, t_{exposure} is the exposure time, N_{photons} is the number of photons arriving within $\Delta\lambda$ with wavelength λ, energy of the photon is defined as $E_{\mathrm{photon}} = hc/\lambda$, T_{tel} is the telescope transmission, and T_{ins} is the optics transmission of the instrument. Telescope and optics reflectance are separately modelled using material reflectivity values as a function of wavelength. For the telescope mirrors and optical

*https://www.gemini.edu/

†https://www.gemini.edu/observing/telescopes-and-sites/sites#Transmission

surfaces transmission, freshly recoated silver mirror transmission data is used from the GEMINI telescopes*.

3.3.2 Instrument slit and MKID QE

This section of KSIM is where the effects of the incoming light propagating through the slit are simulated. A transmissions file is used containing transmission factors with respect to wavelength, which can be generated within KSIM.

A Gaussian distribution is used to model the point spread function of the incoming point source object flux, over the desired slit parameters. To create one of the transmission files the standard deviation of this Gaussian is calculated. An example of this Gaussian distribution is shown in Fig. 3.5. This method is well documented within the ESO ETCs and in van den Ancker et al. (2016), and is used in KSIM because many of the simulations that will be done with KSIM will not involve individually simulating each incoming photon. Rather, the final result of the exposure will be determined, similar to the ESO ETC simulations. It should be noted then, that effects due to speckles and short exposure PSF distortion are not considered for the photon stream simulations later in this Chapter. However the purpose of the photon stream is more focused on the performance of the MKIDs themselves rather than an entire exposure, particularly due to the computing time required, as discussed later.

The standard deviation is dependant on the wavelength of the incoming photons and is also the result of atmospheric effects, i.e. seeing in units of arcseconds. The simulation calculates the standard deviation value by finding the FWHM using a method outlined in van den Ancker et al. (2016) and is also used in the X-Shooter Exposure Time Calculator†. To determine the FWHM of the Gaussian, the Image Quality (IQ) using Eq. 3.4 is found,

*`http://www.gemini.edu/observing/telescopes-and-sites/telescopes`

†`https://www.eso.org/observing/etc/bin/gen/form?INS.NAME=X-SHOOTER+INS.MODE=spectro`

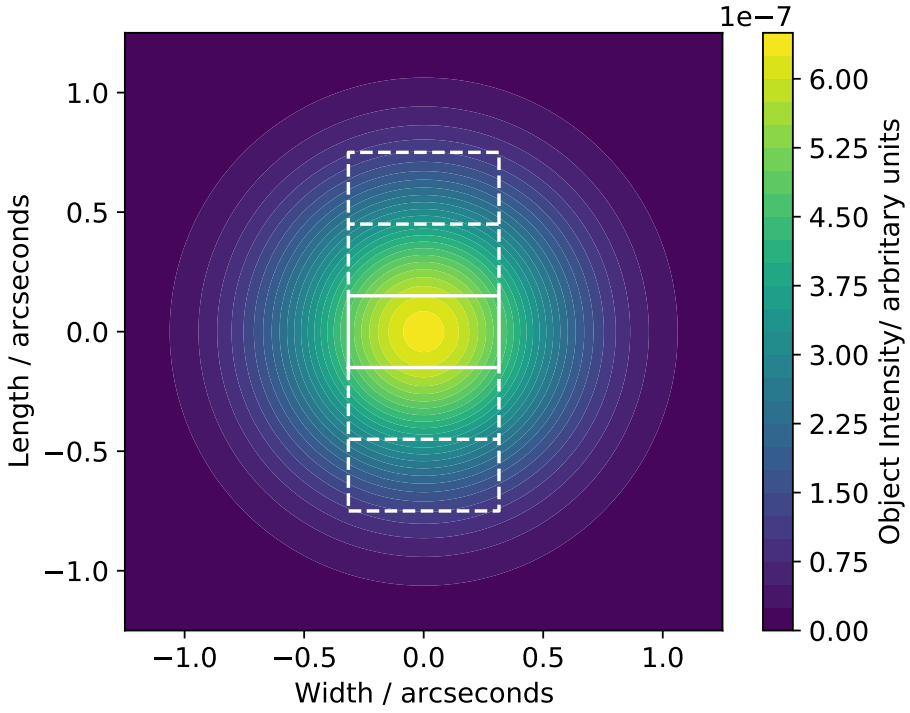

Figure 3.5: Gaussian distribution of a stellar object because of simulated atmosphere. Parameters were; seeing set to 0.8", airmass 1.5, slit width 0.63" and length 2.7", pixel scale of 0.3", and at a wavelength of 534nm. The solid box shows the spaxel used in this work. The dashed boxes represent a potential spatial geometry using additional spaxels, e.g. for simultaneous sky measurement.

$$\mathrm{IQ} = \sqrt{\mathrm{FWHM}^2_{\mathrm{atm}}(s, X, \lambda) + \mathrm{FWHM}^2_{\mathrm{tel}}(D, \lambda) + \mathrm{FWHM}^2_{\mathrm{ins}}} \tag{3.4}$$

where s is seeing in arcseconds, x airmass, λ wavelength in nm, and D telescope diameter in metres. The value of $\mathrm{FWHM}_{\mathrm{ins}}$ is a constant adopted from van den Ancker et al. (2016) as an estimate for KIDSpec also. $\mathrm{FWHM}_{\mathrm{tel}}$ is calculated as shown in Eq. 3.5 (van den Ancker et al., 2016) which is the FWHM of the Airy disc with the same units as Eq. 3.4,

$$\mathrm{FWHM}_{\mathrm{tel}}(D, \lambda) = 0.000212 \frac{\lambda}{D}. \tag{3.5}$$

Finally,

$$\mathrm{FWHM}_{\mathrm{atm}}(s,x,\lambda) = s \times x^{0.6} \times \frac{\lambda}{500nm}^{-0.2} \times \frac{}{\sqrt{1 + F_{\mathrm{Kolb}} \times 2.183 \times (r_0/L_0)^{0.356}}} \tag{3.6}$$

where L_0 is the wavefront outer scale, F_{Kolb} is the Kolb factor, and r_0 is the Fried parameter defined in Eq. 3.7 (van den Ancker et al., 2016). When L_0 is approached to or exceeded by the telescope's diameter, the optical turbulence effects change. For example tip and tilt aberration power is reduced (Ziad, 2016). The Fried parameter is described in Eq. 3.7 at a particular wavelength and airmass,

$$r_0 = 0.101 \times s^{-1} \times \frac{\lambda}{500.0}^{1.2} \times x^{-0.6}. \tag{3.7}$$

The Kolb factor is defined as follows,

$$F_{\mathrm{Kolb}} = \frac{1}{1 + 300 \times D/L_0} - 1 \tag{3.8}$$

with the same definitions as above (van den Ancker et al., 2016). When the standard deviation is calculated and applied to a Gaussian distribution in a 2D plane, it results in images similar to Fig. 3.5. This image shows the spread of a point source's incoming flux to ground observatories as a result of atmospheric effects. These Gaussian fields are used to find the object intensity transmission through the user-set slit, depending on wavelength.

At this point in the simulation the sky background is added, using data generated from the ESO SKYCALC Sky Model Calculator*. A separate sky-only simulation is computed simultaneously from this point, for sky subtraction in the final steps of KSIM. This assumes the same slit geometry as the science observation. In practice, this could be taken by offsetting the telescope at the expense of additional telescope time, or a simultaneous sky exposure could be taken using additional MKIDs as described in Sec. 3.2.

*`http://www.eso.org/observing/etc/bin/gen/form?INS.MODE=swspectr+INS.NAME=SKYCALC`

The QE of the MKIDs is also applied here to simplify the software at later stages. The QE value used is either a constant value of 0.75 (Marsden et al., 2013), or a value between 0.73 at 200nm reducing to 0.22 at 3000nm, as shown in Mazin et al. (2010). However, more recent work has begun to improve this to >80% absorption from 400 to 1500nm (Kouwenhoven et al., 2021), using a method shown in Dai et al. (2019) where efficiencies $\geq 90\%$ were demonstrated at 1550nm. The use of a microlens array to focus incoming light onto the sensitive portion of the detector is assumed in KSIM. This is to ensure a nearly 100% factor (Mazin et al., 2010).

3.3.3 Grating

KIDSpec will use an echelle grating for multiple orders to be exposed onto the MKID array. The grating of the instrument and its efficiency is simulated using a method outlined in Casini and Nelson (2014).

This section of the simulation is split into three parts; calculating the relevant orders and efficiency of the grating setup, assigning the pixels that the spectrum photons fall onto by their wavelength, and distributing the photons which arrive to the instrument. For the first part the simulation calculates each order's wavelengths up to a chosen order number. While the light from all orders will land onto the MKIDs, only orders with wavelengths within the bandpass are considered. The wavelengths KIDSpec will observe in KSIM are calculated using the grating equation,

$$\lambda = \frac{d\left(\sin(\beta) + \sin(\alpha)\right)}{m} \tag{3.9}$$

where λ is wavelength, d the groove spacing, m the order number, α the incidence angle, and β the angle of diffraction. The orders which have values of λ within the bandpass are extracted.

The efficiency of the grating is found using Eq. 3.10,

$$I(\beta) = \mathrm{sinc}^2\left(m\pi \frac{\cos(\alpha)}{\cos(\alpha-\phi)} \frac{\sin(\alpha-\phi)+\sin(\beta-\phi)}{\sin(\alpha)+\sin(\beta)}\right) \tag{3.10}$$

where ϕ is the blaze angle and all other variables have the same definition as Eq. 3.9 (Casini and Nelson, 2014). Fig. 3.6 shows an example of how Eq. 3.10 is used within KSIM. The calculated wavelengths (from Eq. 3.9) and efficiencies are mapped to the MKIDs, depending on their position in the array. The number of wavelengths a spectral pixel (an MKID) will observe is the number of orders passing the grating calculations. For the third part of this section, the majority of input data spectra used will have a different spectral resolution than what KSIM can produce. This is because of a large number of effective MKID pixels; the data spectrum can be interpolated if necessary.

Starting with the data spectrum, each wavelength is binned onto a KIDSpec grid of effective MKID pixel bins using Eq. 3.9. The grating efficiency for each bin in the order is applied. In the cases where photons with a wavelength which falls within a region of order overlap, the grating efficiency of each order distributes the photons into the different grating orders. A Poisson distribution is used to simulate the photon shot noise for each bin. In an MKID array there are a typically a number of unresponsive (or dead) pixels due to current fabrication processes (Walter et al., 2020). These can be included in the simulation and distributed randomly in position in the array.

3.3.4 MKID Order Gaussians

The MKID pixel response to each order incident on it is applied in this section of the simulation tool, examples of which are shown in Fig. 3.3. Each MKID has a single wavelength incident on it from each order, defined here as the order wavelength. However incoming photons of the same wavelength cause a range of responses by the MKID, resulting in a range of measured wavelengths for each order, as discussed in Sec. 3.2. The size of this range is dependant on the R_E. To represent this range

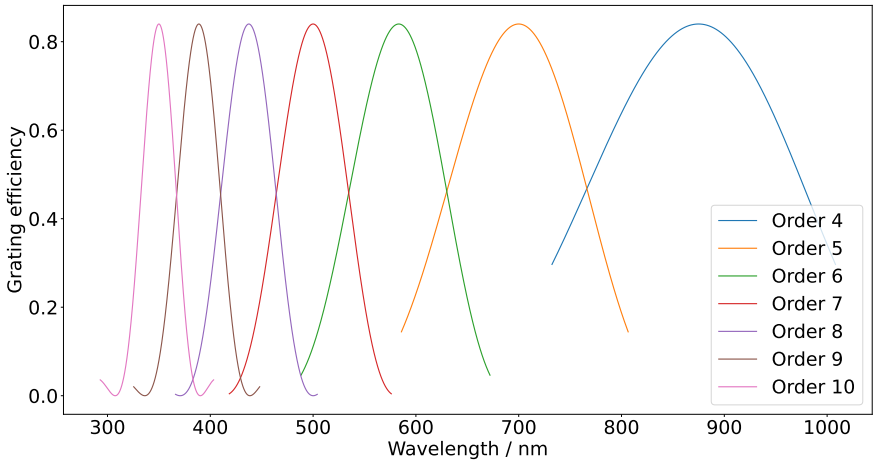

Figure 3.6: Grating efficiency plot calculated using Eq. 3.10. For this a grating with 241 grooves/mm, a blaze angle of 25 degrees, and a reflected angle angle of 16.9 degrees was used. This grating is only used here as an example to show how the grating efficiencies are calculated later in KSIM, using a method shown in Casini and Nelson (2014).

of wavelengths, each order observed by the MKID is assigned a random Gaussian distribution. The mean of this order Gaussian is the order wavelength incident on that MKID. The standard deviation value of the order Gaussian distribution is calculated using Eq. 3.11, used from Marsden et al. (2013) with the FWHM term defined as in Sec. 3.2,

$$1\sigma = \frac{\mu_\lambda}{R_E \times 2\sqrt{2\log(2)}} \tag{3.11}$$

with R_E and the mean wavelength μ_λ. R_E in the MKID array reduces as the wavelength increases, owing to them breaking fewer Cooper pairs, which also causes the fast rise heights to drop closer to the phase stream noise. In the simulation the R_E drops from the value set in the parameters, decreasing linearly with increasing wavelength (O'Brien et al., 2014) instead of decreasing as the square root. This is because the condition of retaining all of the photon's energy within the detector was assumed to not be met here, following MKID detectors constructed at the time of writing this thesis (De Visser et al., 2021; Szypryt et al., 2017). R_{var} is

implemented here if desired, and will vary each MKID pixel's R_E following an approximately Gaussian trend (Meeker et al., 2018) centred on the set R_E in the KSIM parameters. The scale of R_{var} can be set by the user.

Order overlap within the simulation is defined as when the Gaussians calculated above, overlap in wavelength as seen in Fig. 3.3. The order of a photon within an overlapping region of wavelength, is determined by the order with the highest probability for that particular wavelength. After the overlap is calculated, the photons are sorted into their highest probability orders using the description above. A list of photon counts seen by the MKID from each order is then produced. A non-trivial scenario which can be seen with KSIM is when the Gaussians are not all equal height, which can negatively impact the percentage of photons misidentified. An example of this is bright sky lines which could cause this difference in heights to occur during observations.

For the bottom panel of Fig. 3.3 where the R_E was 30 at 400nm, the misidentified photon percentage was 0.2, 0.2, and 0.1 % for orders 8, 9, and 10 respectively. When the incoming photon count of order 9 was increased to be 100 times the counts of the other orders, orders 8, 9, and 10 had misidentified photon percentages of 5.8, 0.1, and 7.1% – a decrease in misidentified photons for the more intense order 9, and an increase for the adjacent two orders.

The impact of the unequal Gaussian heights can be reduced by careful design of the MKID arrays and optics used for KIDSpec. For example, in a constructed KIDSpec there will be MKID pixels which will fall outside of multiple spectral order's Free Spectral Ranges (FSRs), and as such will receive less flux from these orders. This will occur for MKIDs on the ends of the linear array. If these MKID pixels with fewer orders are where the bright sky lines are exposed then the sky lines will impact fewer orders than if it was exposed onto a central MKID which had wavelengths from all order's FSR.

3.3.5 Photon Time Stream

An alternative, more computationally expensive method to Sec. 3.3.4, is to simulate the photon time stream (PTS) which each MKID would observe in an exposure. This represents an actual MKID observation more closely than Sec. 3.3.4. This method provides more output information of an object simulation, such as number of potentially saturated time bins. A saturated time bin has had two photons arrive in the same microsecond time bin.

The PTS method produces time bins from an exposure, rather than using only the total photon count in wavelength bins, as described in Sec. 3.3.4. The number of time bins is determined by the exposure time, time resolution of the MKIDs, and any coincidence rejection time the user wishes to incorporate. This coincidence rejection time is incorporated because of the 'cool-off' tail of a fast rise in a phase time stream, owing to a photon arrival. This tail can be seen in Fig. 2.5. If a photon then arrives during this tail, the height of the rise will have the tail's height included within it, which makes it non-trivial to find the incoming photon's true fast rise height. Because of this, a duration of time bins following a photon detection are rejected in software. For an example of a time bin calculation, an MKID with time resolution $1\mu s$, used for an exposure of 50s, with a coincidence rejection time of $200\mu s$, would result in a minimum of 250,000 time bins. This $200\mu s$ rejection time is a conservative figure, as analysis of MKID data improves this can be reduced to effectively zero, and currently on MEC a $10\mu s$ rejection time is used (Walter et al., 2020). The photons arriving at each MKID are then assigned randomly into the time stream bins. Each order the MKID observes receives its own time stream. The total MKID response for each time bin is determined by summing the energies of the photons which arrived in that time bin.

R_E of the MKIDs at each order is calculated in the same way as in Sec. 3.3.4, and similarly used in a random Gaussian distribution with the order wavelength as the mean. After the PTS has been generated, the total response of each time

bin is taken and KSIM attempts to assign the correct order wavelength to the result of that time bin. A Gaussian probability density function is created for each order, using the order wavelength and previously calculated 1σ as the mean and standard deviation respectively. The order distribution which produces the highest probability is assumed to be the order of the photon which arrived in that time bin.

A maximum of one photon per time bin is allowed here; any additional photons saturate the time bin and have the potential to cause misidentifications in the assignments of wavelengths to these photons. In the PTS the time bins of the following $\approx 100\mu$s after a photon event are not used because of the 'cool-off' tail following the fast rise event. It should be noted that the method used here aims to be conservative in its simulation.

As R_E increases with MKID development, more orders will also be able to be resolved, lowering the required MKIDs in an array as discussed in Sec. 3.2. The potential misidentification issues will also be reduced in the future as the readout technology continues to be developed, and is not an issue with the MKIDs themselves.

3.3.6 Simulation Output

Here a grid of the MKID's responses to the simulated observation is produced. This response grid is in dimensions of order number vs pixel, and has a wavelength counterpart. Sky subtraction is applied here using the sky only response grid, which has been run through the simulation tool simultaneously. Using the sky subtracted and sky only grids the SNR is determined.

Orders are merged using these response grids by rebinning the response grids onto a larger grid to form a 1D spectrum. From the rebinning a raw photon spectrum is produced, before having a set of standard star weights applied to the wavelength bins. The observed photon counts are not discarded however and can be retrieved.

These standard star weights are calculated by simulating a standard star spectrum, GD71 (V=13.032), with the simulation tool. This spectrum was obtained from the ESO Archive and simulated using KSIM with an exposure time of one hour. The resulting spectrum of the standard star simulation is divided by the original standard star spectrum, to produce factors with respect to wavelength to account for the instrument, atmosphere and telescope response, similarly to Modigliani et al. (2010). This method assumes a bright enough comparison star can be found that will mean the SNR of the object will dominate instrument performance.

Instead of using the known values of the various responses in KSIM, the standard star weights are used to represent an observation using KIDSpec where these responses may not be known. The weighted spectrum is then converted back to units of flux in $erg\,cm^{-2}\,s^{-1}\,\AA^{-1}$.

3.4 Simulations

In this section we optimise potential designs of a medium resolution KIDSpec and show the impacts MKID fabrication effects may have on observations. Consistent simulation parameters are shown in Table 3.1.

3.4.1 KSIM to influence KIDSpec's design

When designing KIDSpec the wavelength coverage must be carefully chosen to maximise the use of the MKIDs, covering as wide a desired bandpass as possible. To find the optimal use of a KIDSpec design, a scoring script was used which determined the optimal grating order placements, considering the sky background and atmospheric transmission. The orders were placed using a method from Cropper et al. (2003). The scorer varied the position of the highest order and number of MKID pixels required given a set spectral resolution and R_E. Given a certain spectral resolution, the wavelengths in each order were then sampled in the scorer with

Table 3.1: Consistent parameters and astronomical objects for simulations shown in this Chapter. These parameters were used for each of the three setups described in Sec. 3.4.1, which were used to simulate the cases in this Chapter, unless stated otherwise. The QE used was from Mazin et al. (2010), and the fill factor of the MKIDs was assumed to be incorporated in these QE results.

Parameter	Value
Seeing (arcsec)	0.8
Airmass	1.5
Slit width (arcsec)	0.63
Pixel FOV (arcsec)	0.3
Incidence angle (deg)	25
Blaze angle (deg)	25
Telescope diameter (m)	8
Effective area (m^2)	50
QE/Fill Factor	0.73-0.22/1.0
SDSS J003948.20+000814 (V=16) exposure time (seconds)	60
SDSS J003948.20+000814 (V=22) exposure time (seconds)	180
Mrk 348 (R=14) exposure time (seconds)	60
Mrk 348 (R=21) exposure time (seconds)	180
JAGUAR mock galaxy (R=20) exposure time (seconds)	180 & 1800
HD212442 (R=7) exposure time (seconds)	60

score gained for the wavelength residing in an area of high atmospheric transmission and low sky background. For the atmospheric transmission score, values were given by the transmission values themselves, with score also gained from orders missing areas of low transmission. For the sky background the values were normalised, and then the inverse was used to calculate the score. The results for these calculations for each individual wavelength bin were then summed to form the final score of the setup. Two spectral resolving powers were chosen here, 5000 and 8500 to coincide with X-Shooter spectral resolving powers (Vernet et al., 2011). A range of R_E between 25 and 40 inclusive at approximately 400nm were also selected.

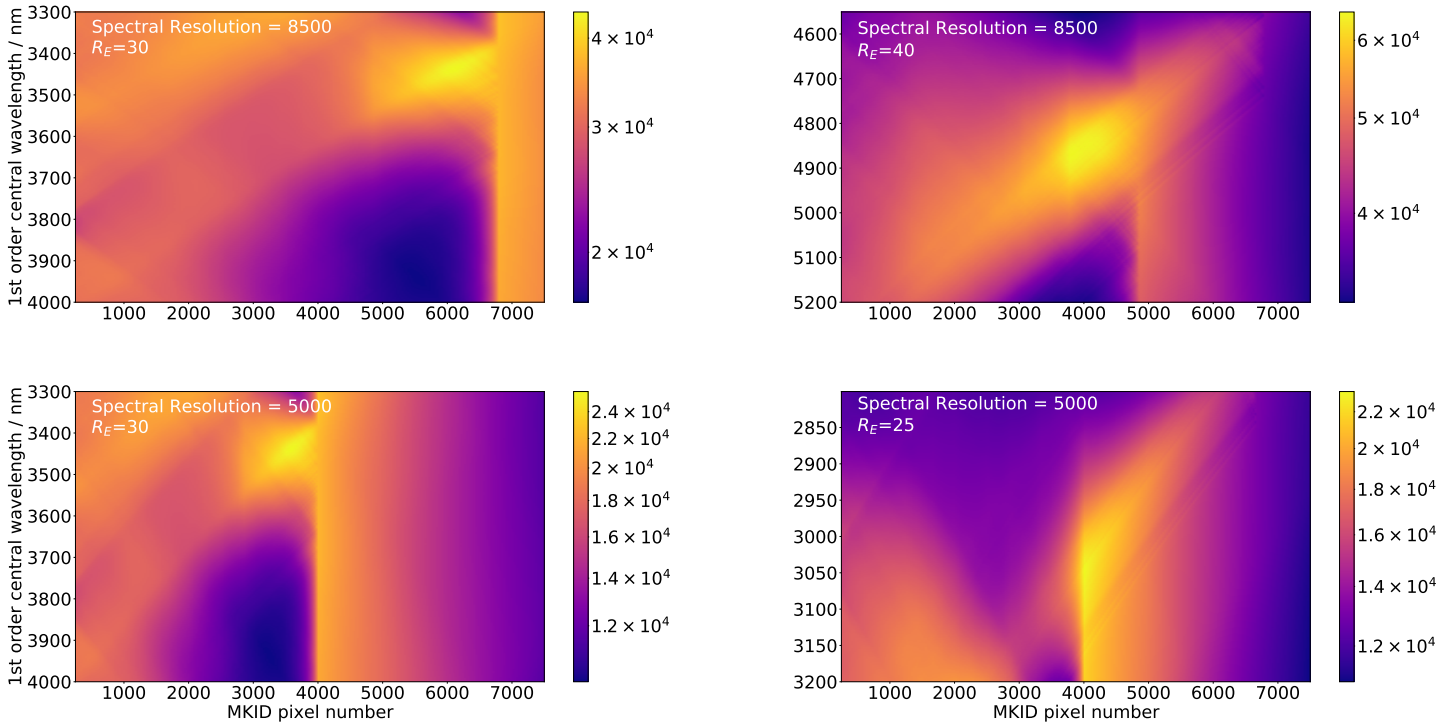

Figure 3.7: Grating order placement optimiser maps for a KIDSpec with spectral resolving powers of 8500 at R_E values of 30 (**Top Left**) and 40 (**Top Right**) and 5000 at R_E values of 30 (**Bottom Left**) and 25 (**Bottom Right**). Sampled were the first order central wavelength and number of MKIDs required. Score, indicated by colour in these plots, was gained by having wavelength coverage in areas of low sky brightness and high atmospheric transmission, while maximising coverage. Common to all plots is a vertical line which signifies the point where adding MKIDs no longer improves the bandpass coverage and there is unnecessary bandpass overlap in the orders. The large area of low score for the (**Top Left**) plot in the area of $\approx$ 5000 MKIDs is the result of the positions of the orders being in poor areas of the bandpass and experiencing more overlap. Similarly for (**Bottom Left**) plot which has the same R_E.

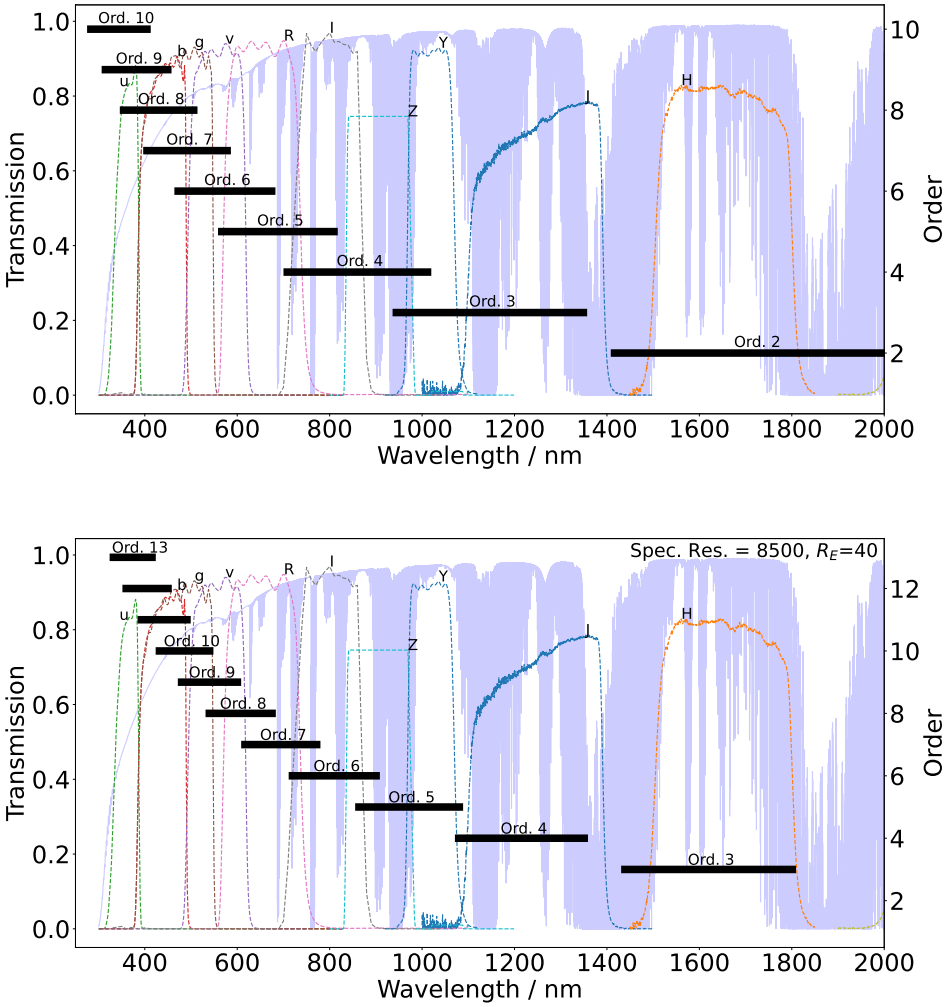

Figure 3.8: Grating order placement optimiser results for a KIDSpec with a spectral resolving powers of 8500 at R_E values of 30 (**Top**) and 40 (**Bottom**). Plotted for all are the grating order wavelength ranges observed by the MKIDs in bold black bars. The free spectral range for each order is represented by the thinner black lines and arrows pointing inwards. Magnitude bands from ESO used for ETC simulations are also plotted, with the GEMINI atmospheric transmission data.

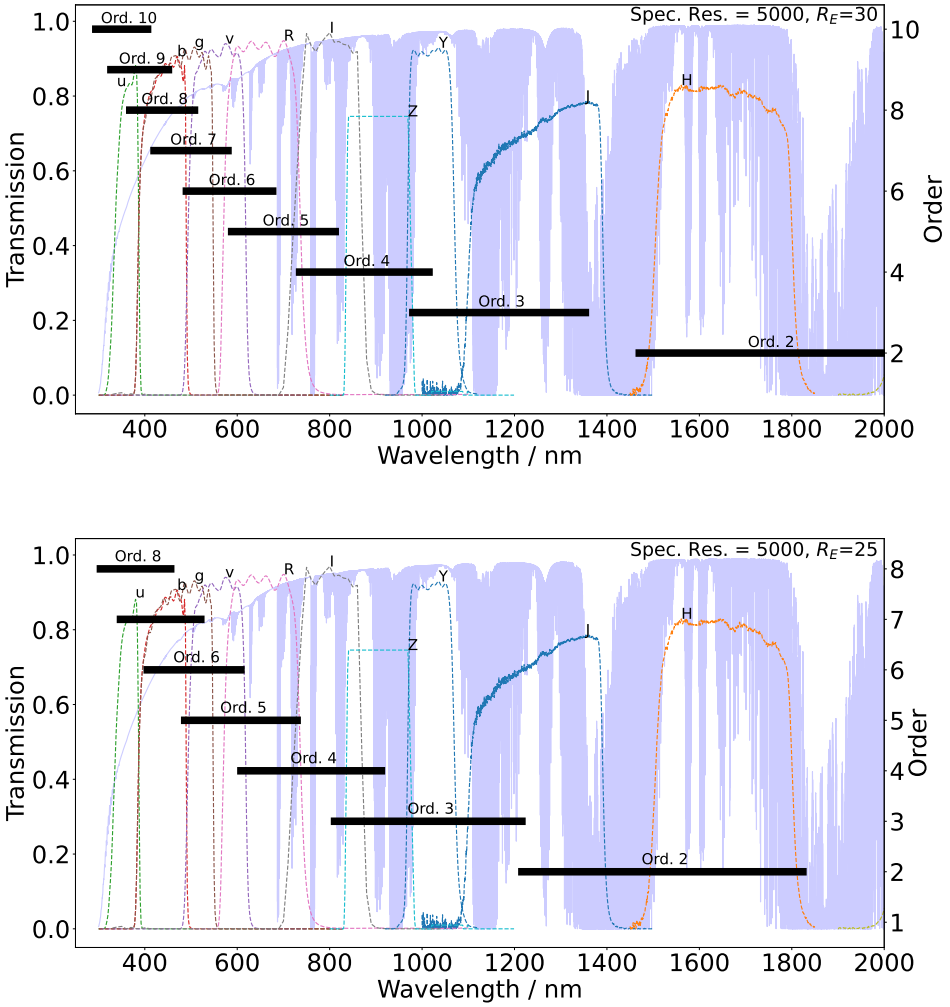

Figure 3.9: Grating order placement optimiser results for a KIDSpec with a spectral resolving power of 5000 at R_E values of 30 (**Top**) and 25 (**Bottom**). Plotted for both are the grating order wavelength ranges observed by the MKIDs in bold black bars. The free spectral range for each order is represented by the thinner black lines and arrows pointing inwards. Magnitude bands from ESO used for ETC simulations are also plotted, with the GEMINI atmospheric transmission data.

The optimiser's results for the parameter space which was sampled is shown in Fig 3.7. For the 8500 spectral resolving power setup, two R_E values were used, 30 and 40. These optimisations resulted in a 1st order central wavelength of 3.44 and 4.86μm respectively. The number of pixels determined were 6000 and 3800 respectively. The difference in number of pixels between the two were the result of the $R_E = 40$ setup observing more grating orders with a 3σ separation as discussed in Sec. 3.2. The gaps in coverage for these setups were optimised by the scorer to contain the large dips in atmospheric transmission, rather than add extra MKIDs to get full bandpass coverage at this resolving power. For the 5000 spectral resolving power setup R_E values of 25 and 30 were used. This gave a 1st order central wavelength of 3.04 and 3.50 μm respectively, with 4000 and 3200 MKID pixels. Shown in Fig. 3.8 and 3.9 are the scorer's chosen grating order placements for a spectral resolving power of both 8500 and 5000 at various R_E values. Magnitude bands from ESO* used for ETC simulations are also plotted in Fig. 3.8 and 3.9, with the GEMINI atmospheric transmission data. The $R_E = 30$ results demonstrate a trade off between spectral resolving power and number of MKID pixels, to achieve similar grating order placement. This trade off is shown by the 8500 spectral resolving power results for $R_E = 30$ having a number of MKID pixels that was higher, than that for the 5000 spectral resolving power. Additionally from Fig. 3.8 and 3.9 with the results using the same spectral resolving power, a higher R_E allows for a reduction in the number of MKID pixels required for an optimised coverage in the range $\approx 400 - 2000$nm. This is understandable, owing to a higher R_E meaning more orders can be separated and so more order wavelengths can be observed on a single MKID.

For all of these KIDSpec setups, limiting magnitudes were predicted using KSIM. The AB magnitudes of each order's blaze wavelength were simulated, for varying exposures on a 8m class telescope, at the point where SNR>10, given a 30s exposure, without the R_E variation effects. This demonstrates KIDSpec's potential for

*https://www.eso.org/observing/etc/doc/formulabook/node12.html

short exposure science. A one hour exposure for SNR>10 was also done, to match the X-Shooter limiting magnitudes setup in Vernet et al. (2011). Table 3.2 contains the results of the predictions. From Table 3.2 KIDSpec could, for exposures of only 30 seconds for an SNR>10, achieve magnitudes of up to ≈ 17.7 for a spectral resolving power of 8500, and ≈ 18.0 for 5000. This increases to up to ≈ 21.7 and ≈ 21.8 for the two spectral resolving powers respectively, for an exposure of one hour. The results for the exposure time of 3600s are plotted in Fig. 3.10. All the plots show the same general trend as seen in Kaper et al. (2008) as a result of atmospheric absorption. An interesting result is the spectral resolution of 5000 and R_E of 30 at $\approx$ 1100nm which has a sudden brighter magnitude. This is due to this wavelength region being within an area of atmospheric absorption that is high and happened to correspond with this results wavelength bin, which can be seen in Fig. 3.8 and 3.9, which then caused the poorer performance here.

KIDSpec's spectral resolving power can be lowered post observation with rebinning and no detriment, owing to the lack of readout noise. The 5000 spectral resolving power performs similarly to the 8500 spectral resolving power setup towards the H band. This is the result of the low atmospheric transmission areas contained inside these orders as seen in Fig. 3.8 and 3.9. For the two spectral resolving power setups with $R_E = 30$, as expected, the lower spectral resolving power had fainter magnitudes, except for the $\approx$ 1200nm result where the two are very similar. This is because of this wavelength being in a low atmosphere transmission region in the J band. These results demonstrate that KIDSpec has the potential to make a large impact, while still having the flexibility in post observation rebinning and low-noise capabilities of the MKID devices.

These varying simulated KIDSpec setups demonstrate KSIM's potential to simulate a variety of design choices for KIDSpec and will therefore help finalise a KIDSpec design.

In the rest of this work, we utilise the two 5000 spectral resolving power setups, and the 8500 spectral resolving power setup with $R_E = 40$. The $R_E = 30$ setup is

Table 3.2: Predicted limiting magnitude results for a KIDSpec with spectral resolving powers of 8500 at R_E values of 30 and 40, and 5000 at R_E values of 30 and 25 all at $\approx$ 400nm. The wavelengths shown are the blaze wavelengths for each spectral order, this method was chosen to follow the the ESO X-Shooter ETC. An exposure of 3600s and 30s on an 8m diameter telescope were used for these simulations with a SNR>10 threshold. In the AB magnitude columns the exposure times are separated in the form of 3600s/30s. The GEMINI atmospheric transmission, ESO SKYCALC, and GEMINI freshly recoated silver mirror transmission data was used for these simulations.

Spectral Res. 8500				Spectral Res. 5000			
Energy Res. 40		Energy Res. 30		Energy Res. 30		Energy Res. 25	
Wavelength/nm	AB mag.	Wavelength/nm	AB mag.	Wavelength/nm	AB mag.	Wavelength/nm	AB mag.
1617	19.0/15.8	1742	19.5/15.9	1741	19.8/16.4	1507	19.0/15.9
1212	20.2/16.5	1161	20.0/16.2	1160	19.6/15.8	1005	20.9/17.5
970	21.0/17.3	871	21.3/17.6	870	21.8/18.2	753	21.6/17.9
808	21.5/17.7	697	21.4/17.5	696	21.7/18.0	603	21.4/17.6
693	21.7/17.7	581	21.0/17.1	580	21.3/17.5	502	21.6/17.6
606	21.1/17.2	498	20.8/16.5	497	21.4/17.3	431	20.8/16.3
539	20.8/16.6	435	20.3/15.8	435	20.6/16.3	377	17.7/12.8
485	21.0/16.8	387	18.1/13.1	387	18.6/13.7		
441	20.2/15.8						
404	18.9/14.1						
373	16.8/11.6						

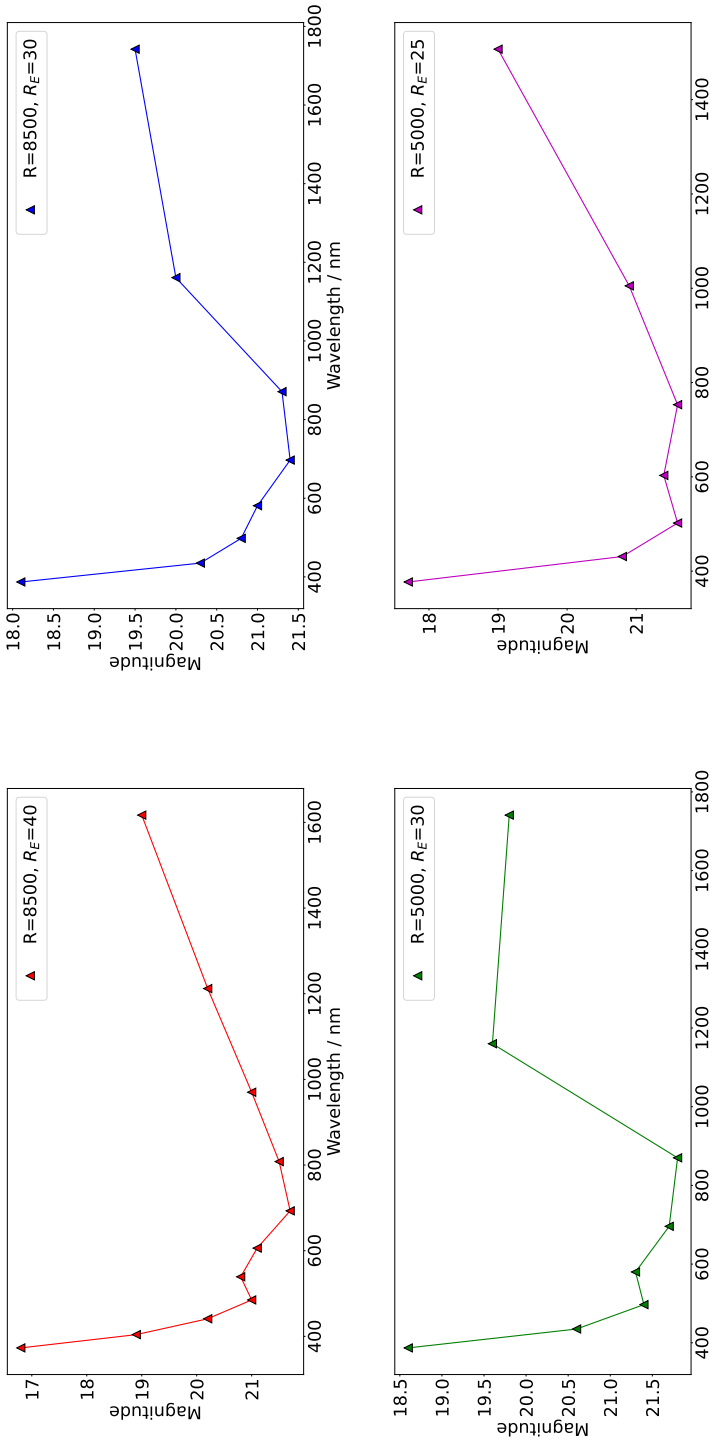

Figure 3.10: Limiting AB magnitudes using the data shown in Table 3.2 for each spectral resolution and MKID energy resolution. These plots are for an exposure time of 3600s on an 8m diameter telescope were used for these simulations with a SNR>10 threshold. The wavelengths shown are the blaze wavelengths for each spectral order.

omitted, because of it having similar grating order placements as its 5000 spectral resolving power counterpart.

3.4.2 MKID Fabrication Effects

To observe the potential impact of MKID effects such as dead pixels and varying R_E, KSIM can include these effects in a simulation.

Here the impact of combinations of dead pixels and R_{var} are explored. The dead pixel proportion was allowed to vary up to 22%, similar to the yield from Walter et al. (2020), with the dead pixels randomly assigned. Other dead pixel proportions included are; 1% a yield from a Hawaii 2RG detector currently conducting observations*, and 3% from the yield of a avalanche photodiode array (Atkinson et al., 2017). Other instrument avalanche photodiode arrays have reported yields of 5%†. Meeker et al. (2018) showed a R_{var} that occurred in an array of MKIDs for DARKNESS. This variance had an approximately Gaussian form with a standard deviation of 3, centred on 8. To investigate the impact this variance could have on KIDSpec, it is simulated using KSIM. As described in Sec. 3.3.4, R_E of the MKIDs were randomly chosen using a normal distribution with varying standard deviations, up to 10. This is a similar ratio to central R_E as was observed in Meeker et al. (2018), owing to the R_E here being higher. It should be noted that these values used for the dead pixels and R_{var} are an upper limit, and are from earlier MKID instruments. Current MKID technology is expected to improve on these values.

The object used for these simulations was a $m_R = 20$ mock star-forming galaxy spectrum at redshift $z = 2$, from the JAGUAR mock catalogue (Williams et al., 2018), chosen for the wide wavelength range which covers the KIDSpec bandpass in these simulations. An example of this simulation is included in Fig. 3.11 for

*https://www.eso.org/sci/facilities/paranal/instruments/crires/doc/CRIRES_User_Manual_P108_Phase2.pdf

†https://www.eso.org/observing/dfo/quality/PIONIER/reports/HEALTH/trend_report_BADPIX_HC.html

the 8500 spectral resolving power design. The ESO SKYCALC tool was used here for the sky background, with the assumption of a second MKID array observing a similar patch of sky simultaneously during the observation. The rebinning of this spectrum from a spectral resolution of 8500 to 4000 would also have reduced the appearance of sky features from the background. The section between ≈1300 to ≈1500 nm falls directly in a region of poor atmospheric transmission, which could result in a poorer recreation of the galaxy spectrum. This setup however has omitted this area of atmospheric transmission owing to the optimiser which gives the gap seen in their respective figures. The region of $\approx 350 - 370$nm has poor results here also because of the atmospheric transmission reducing quickly from $\approx$ 400nm as can be seen in Fig. 3.8 and 3.9. This transmission resulted in very low numbers of photons reaching the detector stage of the simulation causing this wide spread of flux for this region. The sharp line noise at $\approx$ 1100nm is also the result of low atmospheric transmission and bright sky lines in this region.

To understand how these MKID effects may impact observations, different combinations of these effects were tested for the spectral resolving powers of 8500 with $R_E = 40$, and both 5000 KIDSpec setups. An exposure time of 1800s is used on an 8m diameter telescope. To track KIDSpec performance in observing this spectrum, a Reduced Chi-Squared (RCS) value between the JAGUAR spectrum and the KIDSpec spectrum was used.

Fig. 3.12 contains the results for each combination. All had multiple simulation results averaged, to reduce the impact of photon shot noise. Of the two effects tested, the dead pixels had the largest impact on the RCS value. For no dead pixels, the R_{var} caused a change of 0.09, 0.34, and 0.30 in the RCS value, from standard deviation values of 0-10 for the $R_E = 40$, 30, and 25 setups respectively. Whereas for no variance, the dead pixels caused a change of 1.66, 1.43, and 1.37 in RCS value from 0-22% dead pixels, for the $R_E = 40$, 30, and 25 setups respectively. Generally for all plots, a trend of increasing RCS occurs diagonally, following increasing dead pixels and R_{var}. Outliers such as the 6% dead pixels and R_E standard deviation of

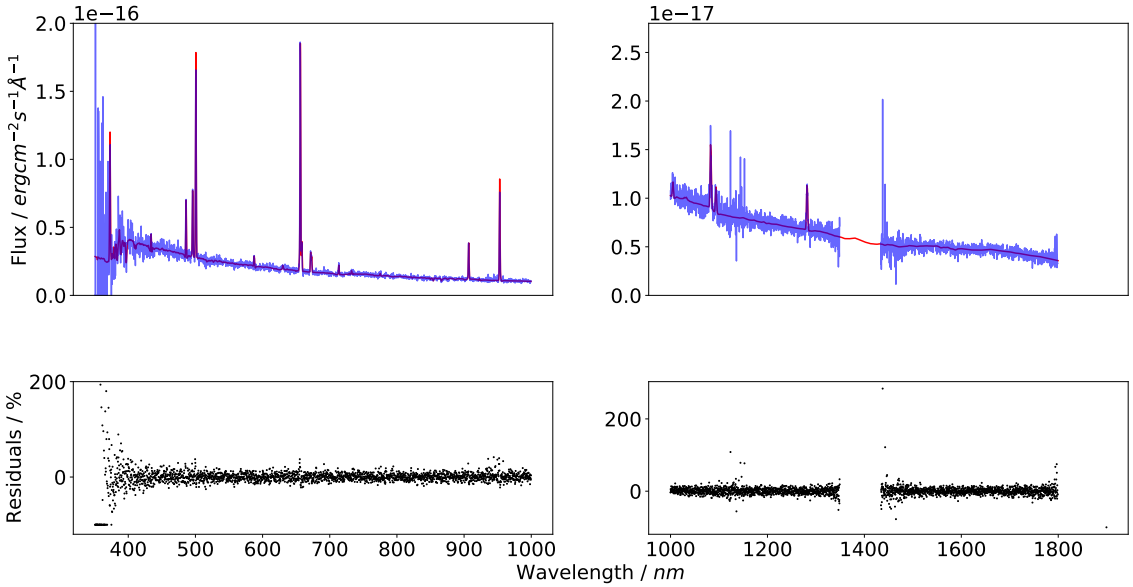

Figure 3.11: Simulations of a JAGUAR mock spectrum ($m_R = 20$) for 1800s on a 8m telescope using the consistent parameters in Table 3.1. Shown is the result for the KIDSpec setup with a spectral resolving power of 8500, rebinned to a spectral resolving power of ≈ 4000, the original resolving power of the JAGUAR spectra. In the upper segment of the Figure the blue represents the KSIM result, and the red the input spectrum. The percentage residuals for their respective simulations are included in the bottom segment of the Figure. The result from KSIM has been split into two plots because of the lower flux at wavelengths higher than 1000nm, this was simulated for a KIDSpec design with bandpass $0.35 - 1.8\mu m$.

10 tile, in the $R_E = 25$ simulations are the results of particularly unfortunate dead or low R_E MKIDs. Here these MKIDs have had brighter portions of the JAGUAR spectrum incident on them, and then are dead, have a lower R_E, or both.

As mentioned above, for the two 5000 spectral resolving power setups, R_{var} had a greater impact than for the higher R_E 8500 spectral resolving power setup. All R_E standard deviations of 10 had higher RCS values for the $R_E = 25$ and 30 setup than the $R_E = 40$ simulations. This is expected since the value of the standard deviations used across the setup simulations was the same. But this demonstrates that as the R_E continues to improve alongside the fabrication, the effect of the R_E variation will be mitigated. The dead pixel percentages which follow currently active instruments also did not greatly impact the RCS value. The 1% dead pixel

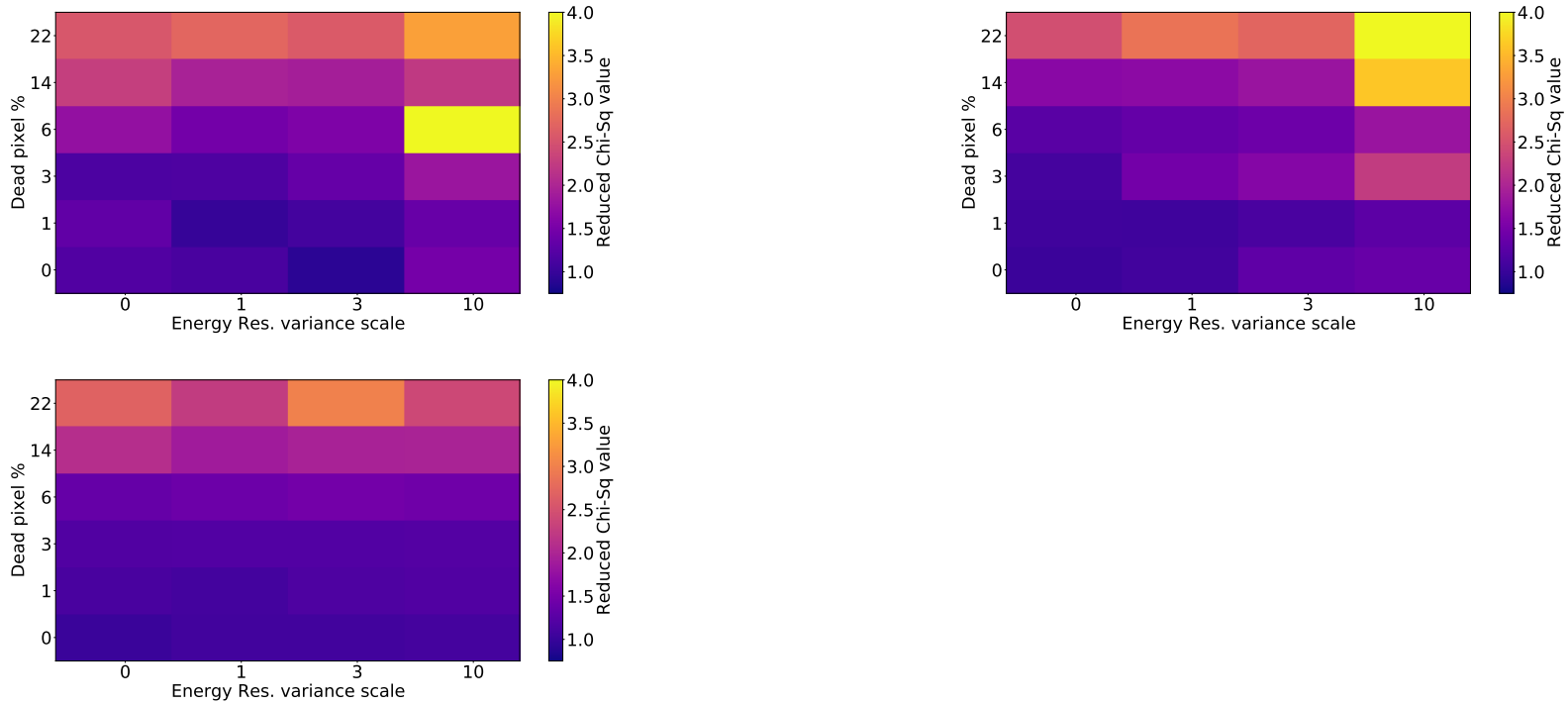

Figure 3.12: Reduced-Chi Squared results for varying MKID R_{var} and dead pixel percentage, with the Reduced-Chi Squared values representing the colour of the tiles. Simulated using the 8500 spectral resolving power KIDSpec setup with $R_E = 40$, and the two 5000 spectral resolving power setups. **Top Left** is the spectral resolving power of 5000 with $R_E = 25$ setup. **Top Right** is the spectral resolving power of 5000 with $R_E = 30$ setup. **Bottom** is the spectral resolving power of 8500 with $R_E = 40$ setup. All grid tiles were averaged over 10 1800s exposures, owing to the photon shot noise.

simulations had average RCS values of only 1.15, 1.11, and 1.21 across the $R_E = 40$, 30, and 25 simulations respectively. For the 3% dead pixel simulations, the average RCS values were 1.21, 1.55, and 1.26. In particular for the $R_E = 40$ simulations these effects did not cause a large increase in RCS.

To mitigate the impact these effects will have on an observation with KIDSpec, any dead pixels, with their locations, and the R_E values of the MKID array will be known when the MKID array has been fabricated. This knowledge could be used to dither or nod the telescope to manoeuvre objects of interest away from being exposed onto dead pixels. This would therefore reduce their impact on a final observation. Additionally because of the lack of read noise, rebinning can be used here with no penalty. For example, if a dead pixel would happen to have a part of a line feature incident on it. With KIDSpec the spectrum could be rebinned, removing that dead bin and only leaving the reduction to the overall SNR. Additionally for both effects, as fabrication methods improve these effects will reduce, further lowering their impact.

3.5 Science Examples

3.5.1 Stellar Spectra

HD212442, a B9 type star of $m_R = 7$, is simulated here to act as a comparison object between the PTS and Order Gaussian methods of simulating the MKID response. The HD212442 spectrum is used from the ESO Archive Library. Parameters used for these simulations are shown in Table 3.1, with exposure time and telescope primary mirror diameter being set to 60 seconds and 0.5 metres respectively. This exposure is chosen here owing to this being the exposure time taken of HD212442 by X-Shooter to gain this data. Here KIDSpec was simulated on a 0.5m diameter telescope, to coincide with the many smaller robotic telescopes currently active in the world, for examples see Jehin et al. (2011), Williams et al. (2008), Steeghs et al.

(2022), Roelfsema et al. (2016) and Boer et al. (2003).

This comparison of the resulting HD212442 spectrum, between the Order Gaussian and PTS methods gave a R value of 0.964, implying strong positive correlation. Here a value of 1 or -1 implies the two spectra are entirely positively or negatively correlated respectively, greater than 0.5 implies strong positive correlation, and 0 implies entirely no relationship between the two datasets. Additionally the Hα feature at $\approx$ 656nm for both was fitted, as shown in Fig. 3.13. A Lorentzian fitted to this feature gave a width which, both matched each other and the original data spectrum of HD212442 used, with the Order Gaussian method having a width of 1.513$\pm$0.040 nm and the PTS method had 1.505$\pm$0.038 nm. The original data spectrum of HD212442 had a $H\alpha$ width of 1.483$\pm$0.007 nm, meaning KSIM successfully retrieved this feature across both methods of MKID simulation. From these results we assume the two methods act generally consistently. To observe how faint KIDSpec could still fit this feature for a 60 second exposure on a 0.5m diameter telescope, the magnitude of HD212442 was reduced and simulated using the Order Gaussian method. This was also measured using the Pearson R correlation coefficient value between the KSIM spectrum and the HD212442 spectrum. Fig. 3.14 shows the results of this as HD212442's magnitude was progressively reduced. From Fig. 3.14 KIDSpec could successfully retrieve the $H\alpha$ line to $m_R \approx 14$ on a 0.5m diameter telescope for a 60s exposure. Extending this to a 3600s exposure, the $H\alpha$ line could be retrieved down to $m_R \approx 18$, with a fit of 1.420$\pm$0.141 with a R value of 0.50. This gain in magnitude is greater than what would be expected when just considering the SNR, which is $\sqrt{(}60)$ or $\approx 2.2mag$. However the fitter was being used on a known line and therefore the wavelength region is known to the fitter. This allowed it to fit beyond the SNR dropoff.

The theoretical brightness limit for this particular simulation on a 0.5m diameter telescope can also be determined with KSIM. Using the MKID's μs time resolution and the chosen coincidence rejection time, a maximum number of possible photons per second can be calculated. The same coincidence rejection times discussed in

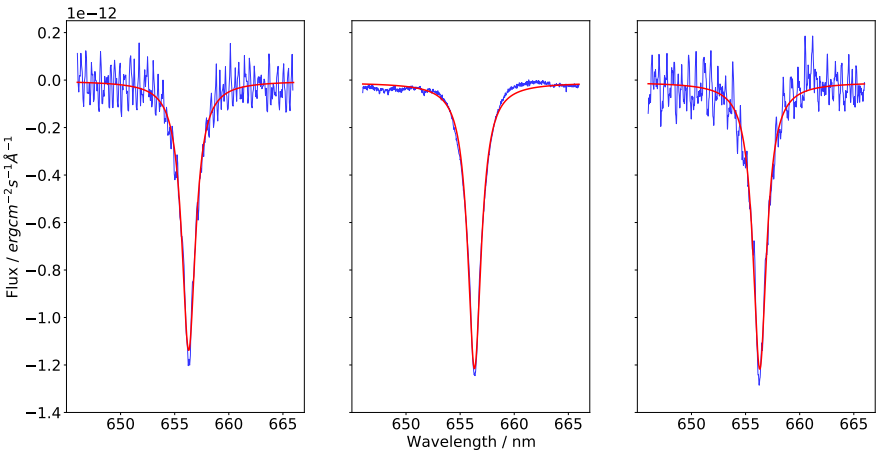

Figure 3.13: Lorentzian fits of the $H\alpha$ line for the PTS method of KSIM **(Left)**, the input data spectrum of HD212442 **(Middle)**, and the Order Gaussian method of KSIM **(Right)**. The blue spectrum indicates the spectrum used for fitting, and the red line is the resulting fit. These fits respectively gave a FWHM of the $H\alpha$ feature of 1.505±0.038, 1.483±0.007, and 1.513±0.040 nm. Both methods were simulated using the KIDSpec setup with $R_E = 30$, and a spectral resolving power of 5000. The R value comparing the two MKID simulation methods was 0.964. Both methods were simulated using the parameters in Table 3.1 and for 60s on a 0.5m telescope.

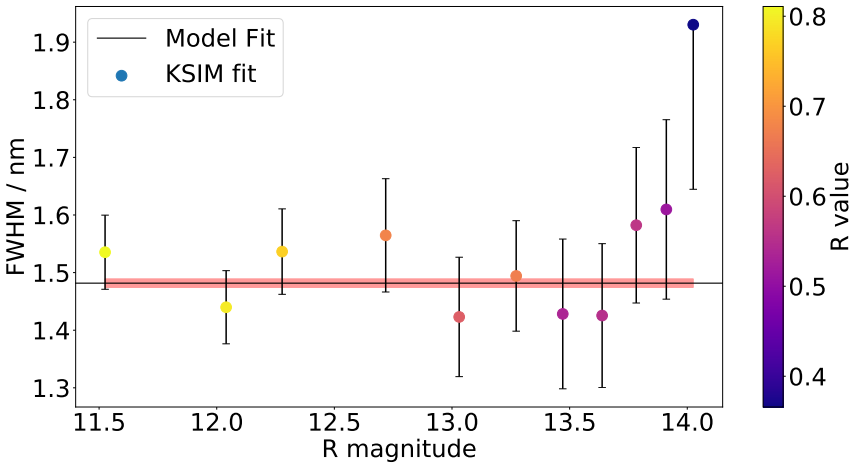

Figure 3.14: Fit results of KSIM simulations of the magnitude reduced spectrum of HD212442, simulated on a 0.5m telescope for 60s using the spectral resolving power of 5000 and energy resolution of 30. The bold black horizontal line is the fit to the input spectrum, and the red bar is the error in this fit. The circular points are the KSIM data fit and the errorbars are included for each fit. At $m_R \approx 14$ the R value of the resulting fit reduces to 0.48, below the 0.5 threshold for the fit and data to be strongly correlated.

Sec. 3.3.5, 200 and 10 μs, are used here. Considering the $H\alpha$ line again from the HD212442 spectrum, it could be observed to $m_R \approx 0.5$ for a coincidence rejection time of 200 μs. For 10 μs, the line could be observed up to $m_R \approx -2.4$, with a range then of down to $m_R \approx 18$, as described above.

3.5.2 SDSS J003948.20+000814.6

KIDSpec has the potential to be able to observe many galaxy emission lines. As an example of this is the $m_V = 16$ star forming galaxy SDSS J003948.20+000814.6 was simulated in KSIM. The data for this galaxy was used from the Sloan Digital Sky Survey's (SDSS's) 16th Data Release (DR) (Ahumada et al., 2020). In Table 3.1 are the parameters used for the simulation of this target, with telescope diameter and exposure time set to 8m and 60s respectively. These simulations gave an average blaze wavelength SNR of 24.1, 29.2, and 32.8 for the 8500, 5000 ($R_E = 25$), and 5000 ($R_E = 30$) spectral resolving power setups respectively. These results are in line with expectations, because an improvement in SNR of $\sqrt{8500/5000}$ would be expected. Here that is $24.2 \times \sqrt{8500/5000} = 30.9$, which is approximately the two $R = 5000$ SNR results.

One of the key advantages KIDSpec would have over typical CCD detectors is the lack of read noise and dark current, particularly aiding faint source spectroscopy. To illustrate this, X-Shooter's ETC was used to calculate the predicted SNR for an observation and compare with KIDSpec's. This instrument was chosen because X-Shooter is an optical to NIR spectrograph with comparable spectral resolution. For this comparison a $m_V = 22$ spectrum of SDSS J003948.20+000814.6 was simulated, for a 180s exposure on an 8m telescope. The mean SNR was taken from the blaze wavelength SNRs from X-Shooter's ETC for this spectrum observation, and the same was done for KSIM's result. Results are shown in Table 3.3. The average SNR for KIDSpec in this comparison was 1.66 and 1.71 for the two spectral resolving power of 5000 setups, with R_E 25 and 30 respectively. The spectral resolving power

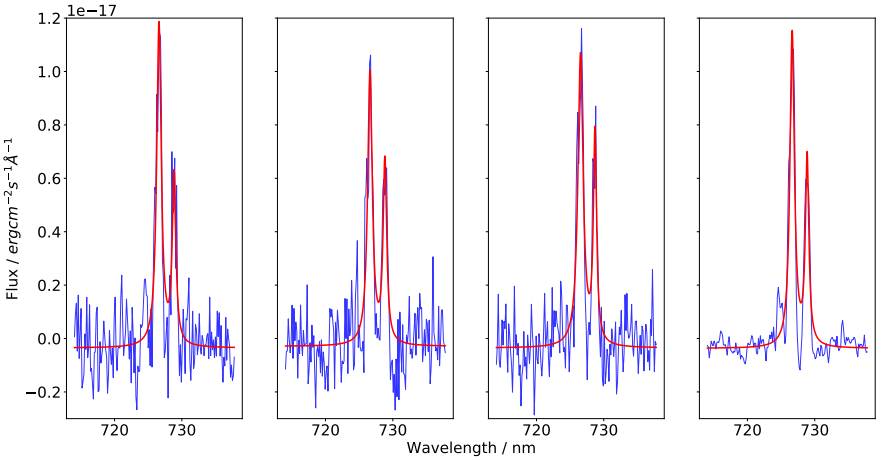

Figure 3.15: KSIM simulation of SDSS J003948.20+000814.6 ($m_V = 22$), with an exposure of 180s on an 8m class telescope. Shown are the Lorentzian fit results for the KIDSpec setup with spectral resolving power 8500 and $R_E = 40$ (**Left**), spectral resolving power 5000 and $R_E = 30$ (**Middle Left**), spectral resolving power 5000 and $R_E = 25$ (**Middle Right**), and the original spectral resolving power $\approx$ 2000 data spectrum (**Right**). Included here is the Lorentzian fit of the $H\alpha$ and NII line located at $\approx$726 and 729nm to determine its FWHM. For the $H\alpha$ line this gave 0.792$\pm$0.052nm for the input data spectrum from the SDSS DR, and 0.809$\pm$0.084, 0.815$\pm$0.100nm, and 0.927$\pm$0.096nm for the 8500, 5000 ($R_E = 30$), and 5000 ($R_E = 25$) spectral resolving power setups respectively. For the NII line this gave 0.614$\pm$0.076nm for the input data spectrum from the SDSS DR, and 0.634$\pm$0.142nm, 0.640$\pm$0.130nm, and 0.568$\pm$0.101nm for the 8500, 5000 ($R_E = 30$), and 5000 ($R_E = 25$) spectral resolving power setups respectively.

of 8500 had a average SNR of 1.44. For X-Shooter the average SNRs were 1.10 and 0.83 respectively for the spectral resolving power options of 5000 and 8900.

Using its MKIDs, KIDSpec would also be able to flexibly rebin down to lower spectral resolving powers, because the detectors do not suffer from read noise. By rebinning down to a spectral resolving power of $\approx$ 2000, features can be extracted from faint objects and short exposures. This resolving power is the approximate spectral resolving power used to originally observe SDSS J003948.20+000814.6. The rebinning which was computed was including bright sky lines, and the wavelength bins were calculated using the desired spectral resolution across the bandpass of the simulation. This simple method was chosen to demonstrate the benefit of rebinning KIDSpec observations without adding complexity to the data analysis.

The Lorentzian fitter was used to find the width of the $H\alpha$ and NII lines, located at ≈726 and 729nm respectively. For the $H\alpha$ line, this gave 0.792±0.052 nm for the input data spectrum from the SDSS DR, and 0.809±0.084, 0.815±0.100, and 0.927±0.096 nm for the 8500, 5000 (R_E = 30), and 5000 (R_E = 25) spectral resolving power setups respectively. For the NII line, this gave 0.614±0.076 nm for the input data spectrum from the SDSS DR. KIDSpec achieved 0.634±0.142, 0.640±0.130, and 0.568±0.101 nm for the 8500, 5000 ($R_E = 30$), and 5000 ($R_E = 25$) spectral resolving power setups respectively. Results are shown in Fig. 3.15. These results demonstrate the potential for KIDSpec to reach higher SNRs with set exposure times, using its lack of read noise and dark current. This is particularly so for these short observations, where KIDSpec still successfully recreates spectral lines.

3.5.3 Mrk 348

A NIR spectrum of Mrk 348 (m_R = 14) was simulated using KSIM, with the parameters used for the simulation in Table 3.1. The data of Mrk 348 shown in Ramos Almeida et al. (2009), were shared by the author for use in KSIM. Exposure time and telescope diameter was set to 60s and 8m respectively. The average SNR values for these simulations were 82.5, 105, and 102 for the 8500, 5000 ($R_E = 25$), and 5000 ($R_E = 30$) spectral resolving power setups respectively. The larger difference between the SNR results for the R_E of 40 and 30 is expected here also. This is due to the R_E =30 and 25 setups having a lower spectral resolution of 5000 than the R_E=40 spectral resolution of 8500. The expected SNR for the $R = 5000$ setup would be $82.5 \times \sqrt{8500/5000} = 107.3$. The SNR results for the $R = 5000$ setups are in line with this, with the difference here being acceptable due to the photon shot noise simulated in these results.

To push KIDSpec to more extreme parameters, the m_R magnitude of this spectrum was reduced to 21, and simulated with an exposure time of 180s. Results are shown in Fig. 3.16. These simulations had average SNR values of 3.63, 4.60, and 4.79

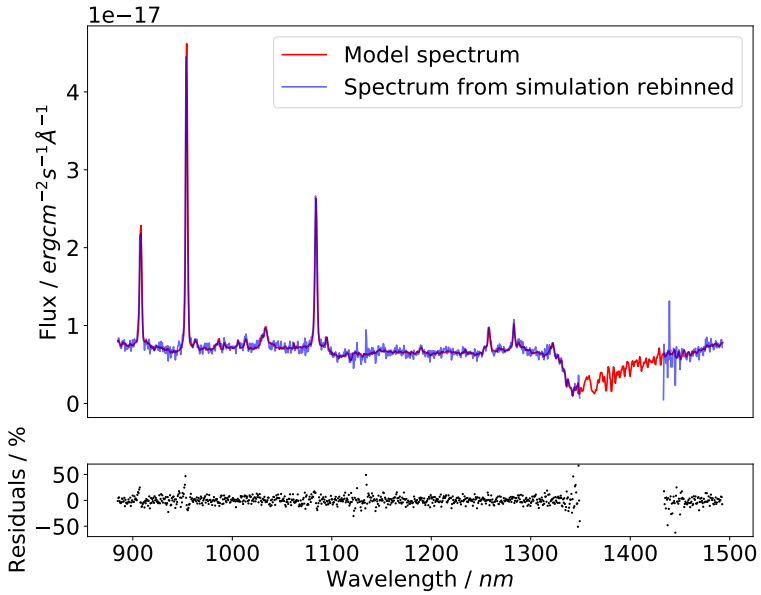

Figure 3.16: Simulation of Mrk 348 ($m_R = 21$) for 180s on a 8m telescope using the parameters in Table 3.1. Shown is the result for the KIDSpec setup with a spectral resolving power of 8500. The percentage residuals are included in the bottom segment of the Figure. The section between ≈1300 to ≈1500 nm falls directly in a region of poor atmospheric transmission, which results in a poorer recreation of the galaxy spectrum. This setup however has omitted this area of atmospheric transmission, owing to the optimiser which gives the gap seen in this wavelength range.

for the 8500, 5000 ($R_E = 25$), and 5000 ($R_E = 30$) spectral resolving power setups respectively. It is noted that the region of $\approx 1300 - 1500$nm had low flux results for the $R_E = 25$ setup, which was because this region has poor atmospheric transmission. For this reason the optimiser in Sec. 3.4.1 omitted this region for the other two setups shown in this Chapter, which can be seen in Fig. 3.16. This poor transmission area can also be seen in Fig. 3.8 and 3.9.

From this, as done in Sec. 3.5.2, an SNR comparison was done with the X-Shooter ETC. In the NIR KIDSpec is expected to improve over conventional NIR detectors, such as those used for X-Shooter, owing to the MKID's lower noise capabilities described in Sec. 2.1. As in Sec. 3.5.2, the setups from the ETC were chosen to match KIDSpec's spectral resolving power setups in KSIM. Table 3.3 shows the result for this comparison, with X-Shooter having average SNRs of 1.47 and 1.16

for a spectral resolving power of 5000 and 8100 respectively. Here, KIDSpec more than doubles these with 3.63, 4.60, and 4.79 for the 8500, 5000 ($R_E = 25$), and 5000 ($R_E = 30$) spectral resolving power setups respectively.

In Sec. 3.1, the MKID's improved sky subtraction was discussed, namely by utilising a simultaneous sky subtraction with the MKID's time resolving capabilities. To illustrate the impact a simultaneous sky subtraction has in comparison to not, Mrk 348 at $m_Z = 20$ was simulated with both for 1800s. The simultaneous sky subtraction resulted in an R value of 0.964. The sky spectrum from this exposure was then used for the sky subtraction in a repeated simulation, to replicate a separate sky exposure in an observation. This had an R value of 0.794. When repeated for an exposure of 900s, the simultaneous sky exposure had an R value of 0.960. Whereas the separate sky subtraction had an R value of 0.444, passing the threshold of 0.5 making the result no longer strongly correlated. Additionally, KIDSpec's time resolving capability gives the potential to be able to track variation in the sky lines with photon counting (Mazin et al., 2010). The logistics of using simultaneous sky subtraction could be approached with multiple methods. Some examples would be using a separate MKID array for KIDSpec, or 'nodding' the telescope on sky. These aspects could improve KIDSpec's performance particularly in shorter exposures, where KIDSpec has scientific interests.

3.6 Short Period Binary systems

The Vera Rubin Observatory is predicted to detect tens of millions of eclipsing binary systems during its survey, and Gaia was predicted to observe 30 million non-single stars and 8 million spectroscopic binaries. So when short period systems are found, typical CCD detectors will struggle to characterise these systems due to the very short exposures required, causing errors as large as the estimated parameter itself (Burdge et al., 2019) . These systems are also of great interest as they are LISA verification sources (Kupfer et al., 2018; Amaro-Seoane et al., 2017) . It was

Table 3.3: This contains SNR results for objects simulated in this Chapter for KIDSpec, also simulated using X-Shooter's ETC. SNRs below are calculated by taking the mean average of the order blaze wavelength SNRs for those which fall within the object's bandpass. For the instrument comparisons the SNR value included is the average total SNR across the bandpass from the simulations in this Chapter for the simulated object spectrum. The X-S SNR column represents the X-Shooter ETC results. Results included for the JAGUAR mock galaxy are for the simulations without the MKID effects discussed in Sec. 3.4.2.

Object	Spec. Res.	Energy Res.	Exp. time (s)	Tel. diameter (m)	SNR	
					KIDSpec	X-S
SDSS J003948.20+000814.6 (V=16)	8500	40	60	8.0	24.1	23.8
SDSS J003948.20+000814.6 (V=16)	5000	25	60	8.0	29.2	30.2
SDSS J003948.20+000814.6 (V=16)	5000	30	60	8.0	32.8	30.2
SDSS J003948.20+000814.6 (V=22)	8500	40	180	8.0	1.44	0.83
SDSS J003948.20+000814.6 (V=22)	5000	25	180	8.0	1.66	1.10
SDSS J003948.20+000814.6 (V=22)	5000	30	180	8.0	1.71	1.10
Mrk 348 (R=14)	8500	40	60	8.0	82.5	57.8
Mrk 348 (R=14)	5000	25	60	8.0	105	87.0
Mrk 348 (R=14)	5000	30	60	8.0	102	87.0
Mrk 348 (R=21)	8500	40	180	8.0	3.63	1.16
Mrk 348 (R=21)	5000	25	180	8.0	4.60	1.47
Mrk 348 (R=21)	5000	30	180	8.0	4.79	1.47
JAGUAR mock galaxy (R=20)	8500	40	180	8.0	3.06	1.56
JAGUAR mock galaxy (R=20)	5000	25	180	8.0	3.82	1.86
JAGUAR mock galaxy (R=20)	5000	30	180	8.0	4.00	1.86

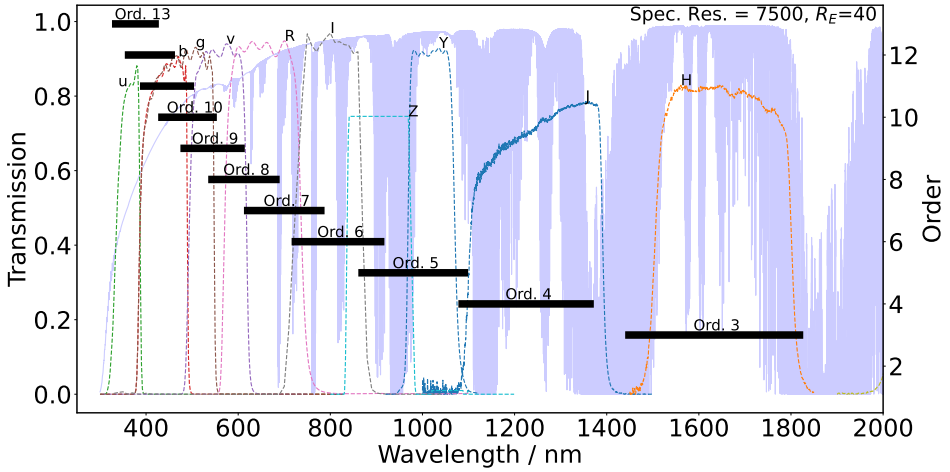

Figure 3.17: Optimiser grating parameters for a R_E of 40 with spectral resolving power 7500. Plotted are the grating order wavelength ranges observed by the MKIDs in bold black bars. The free spectral range for each order is represented by the thinner black lines and arrows pointing inwards. Magnitude bands from ESO used for ETC simulations are also plotted. The GEMINI atmospheric transmission data is plotted here at a sampling of 0.01nm, to illustrate the atmospheric transmission across the bandpass. This gave a central first order wavelength of $4.9\mu m$ with 3400 MKIDs in the linear array. In the region of $\approx 1.4\mu m$, the optimiser has excluded this region due to the poor atmospheric transmission.

predicted that LSST would be able to find these systems up to a magnitude of ≈ 24 (Korol et al., 2017) , but spectroscopic follow up will be non-trivial with typical CCDs. KIDSpec however, using its low noise detectors present a solution to this issue.

3.6.1 KIDSpec Design and Simulation

To determine a KIDSpec design for this, an optimiser was used to assign grating parameters for the instrument. This optimiser takes in a desired R_E and spectral resolving power to find the most suitable grating order placements with respect to wavelength. Accounted for is the atmospheric transmission and sky brightness. Atmospheric data is used from GEMINI* and the ESO SKYCALC Sky Model

*http://www.gemini.edu/observing/telescopes-and-sites/telescopes

Calculator* is used for the sky. A R_E of 40 was chosen as this would allow enough orders to be separated for a spectral resolving power of 7500, which is high enough to track spectral lines in a variety of astrophysical objects (D'Odorico et al., 2004) , particularly for an instrument with a wide bandpass such as KIDSpec. The result of the optimiser for the grating orders is shown in Fig. 3.17, giving a central first order wavelength of $4.9\mu m$ with 3400 MKIDs in the linear array. This design for KIDSpec was then simulated in this work using the KIDSpec Simulator (KSIM), a end-to-end simulator to estimate how KIDSpec designs could perform on sky.

3.6.2 Simulation Results

3.6.2.1 8m telescope

To demonstrate the gains KIDSpec could make over conventional detectors, its performance using KSIM was compared to FORS' using its ESO ETC. Both were simulated on an 8m diameter telescope. Simulated was a spectrum of ZTFJ1539 + 5027 like system, the binary observed in Burdge et al. (2019) . This system has a magnitude of ≈ 19 and a period of 7 minutes. The setup chosen for FORS was a spectral resolving power of 1420, due to this being closest to the ≈ 1600 spectral resolving power used for the original observations with LRIS. Through the lack of read noise of the MKIDs, it is possible for KIDSpec's original resolving power of 7500 exposure to be flexibly rebinned down to 1420, without requiring different gratings or setups. Additionally since KIDSpec would not need to be readout like a typical CCD detector, this would give more time on sky observing the object rather than reading out during a night on a telescope. This is considered here, with the setup used for FORS this would require a readout time of 39s†. Here this would mean KIDSpec would be observing for an extra 39s on top of the original exposure time, the total hereafter in this Chapter named the cycle time. The ZTFJ1539 +

*http://www.eso.org/observing/etc/bin/gen/form?INS.MODE=swspectr+INS.NAME=SKYCALC

†https://www.eso.org/sci/facilities/paranal/instruments/fors/doc/VLT-MAN-ESO-13100-1543_P07.pdf

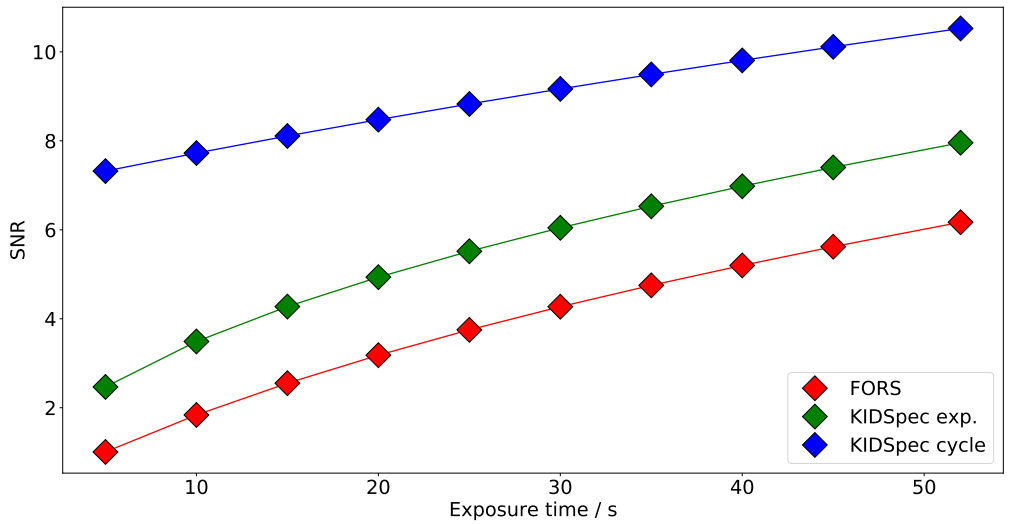

Figure 3.18: SNR results at 452nm for simulating a ZTFJ1539 + 5027 like system at various exposures. Also simulated were the cycle times for these FORS exposures. SNR taken at a spectral resolving power of 1420, to align with the ≈ 1600 spectral resolving power setup used by LRIS for the original observations of ZTFJ1539 + 5027.

5027 like system was simulated for both instruments at varying exposure times, and the SNR at FORS' central wavelength of 452nm was taken. The same wavelength bin was used for the KIDSpec result. Results are shown in Fig. 3.18.

From Fig. 3.18 at the shorter exposures such as 10s, KIDSpec at an SNR of 3.5 almost doubles the SNR of FORS at 1.8. This is as expected due to KIDSpec's MKIDs not suffering from read noise and dark current counts. When the cycle time is considered, for a FORS exposure of 10s at 1.8 SNR KIDSpec had an SNR of 7.7, a four times increase over the FORS result. As the exposure time increases the gains KIDSpec makes reduces, down to 1.3 times the FORS SNR of 6.2. This is expected as the exposure time increases since the impact of the read noise reduces with longer exposures where you are no longer read noise dominated.

3.6.2.2 40m telescope

Since there are gains to made using KIDSpec with its MKIDs, the potential of KIDSpec on an ELT class telescope of diameter 39.3m was simulated using KSIM. The ELT's transmission for M1-6 were considered, and parameters for the atmospheric conditions from ESO were also used (Clénet et al., 2015). The ZTFJ1539 + 5027 (Burdge et al., 2019) like system was simulated here with reduced magnitudes to find the limit for KIDSpec on the ELT. The threshold for this limit was 5, as this was the likely target for the original LRIS observations, since the FORS ETC simulations resulted in SNRs of ≈ 5 when replicating the original observations in Burdge et al. (2019). The SNR was taken in the same way as Sec. 3.6.2.1. Also as in Sec. 3.6.2.1, the KSIM 7500 spectral resolving power result was rebinned to 1420. KIDSpec using its MKIDs would not be limited by requiring a readout, so in addition to using the MKIDs time resolution, signal in a particular time bin can be built up with a continuous long observation. In Burdge et al. (2019) 317 52s exposures were used, so with readout time this may have been a nights worth of observations. Several observation times for this object were simulated; one 10s time bin in the period as done in Sec. 3.6.2.1, one hour of observation, and 10 hours of observation.

Fig. 3.19 contains the results for the magnitude limits of these exposures. With a spectral resolving power of 7500, KIDSpec could potentially reach $m_V \approx 19.9$ for one orbital period which the approximate magnitude of ZTFJ1539 + 5027. When rebinned to 1420 resolving power this increases to $m_V \approx 21.3$. Extending this to an hour of observation would allow KIDSpec to reach $m_V \approx 22.9$, and finally with 10 hours achieving $m_V \approx 24.3$. This improvement in magnitude is expected, since increasing the exposure time from one hour to ten hours an improvement of ≈ 1.25 magnitudes would be predicted. With a night of observation then on a 40m diameter telescope KIDSpec could spectroscopically follow up on any LISA verification sources LSST photometrically finds in the sky.

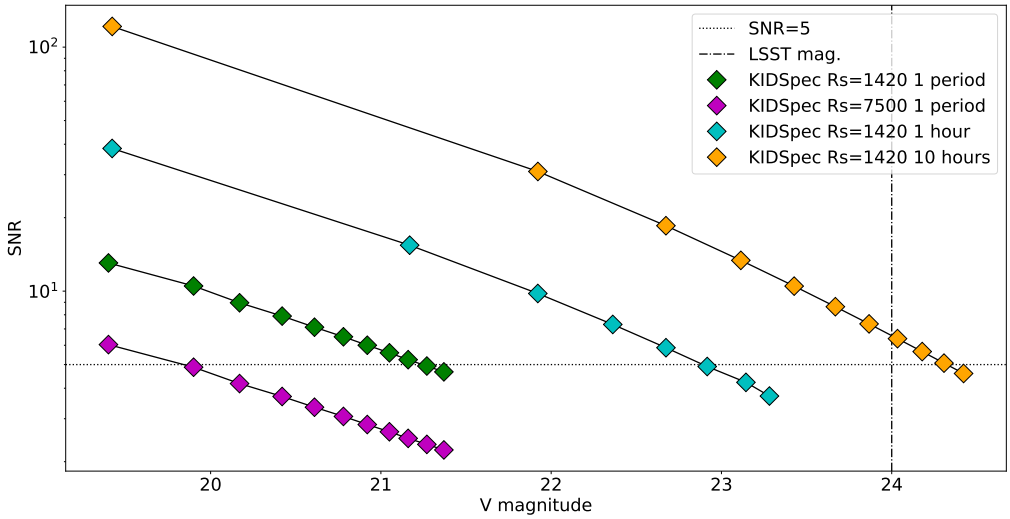

Figure 3.19: Magnitude limits for various exposures observing ZTFJ1539 + 5027 with an SNR of 5. With a spectral resolving power of 7500, KIDSpec could potentially reach $m_V \approx 19.9$ for one period which the approximate magnitude of ZTFJ1539 + 5027. When rebinned to 1420 resolving power this increases to $m_V \approx 21.3$. Extending this to an hour of observation would allow KIDSpec to reach $m_V \approx 22.9$, and finally with 10 hours achieving $m_V \approx 24.3$. This passes the magnitude of 24 threshold from LSST for these LISA verification sources.

The limiting magnitudes of this design of KIDSpec across its bandpass on the ELT were also found for an hour and 30s exposure, with a threshold of an SNR of 10. Each grating order's blaze wavelength SNR was measure here. Fig. 3.20 contains these results. The large peak at $\approx$ 1000nm is the result of an unfortunate bright sky line at this wavelength which reduced the limiting magnitude at this order's blaze wavelength. The 30s exposure limiting magnitudes at $\approx 400 - 500$nm again approach the 19 magnitude of ZTFJ1539 + 5027, which would allow KIDSpec to take more phase bins of the period. For 3600s KIDSpec could reach a magnitude of ≈ 23.8 and ≈ 20.5 for 30s.

However the state of MKID research when the ELT construction is complete can also be considered, as this is still quite some time away, at least the second half of the 2020s (Tamai et al., 2020). In 2013 ARCONS (Mazin et al., 2013) had 2024 MKIDs at an average R_E of 8. MEC (Walter et al., 2020) in 2020 had an

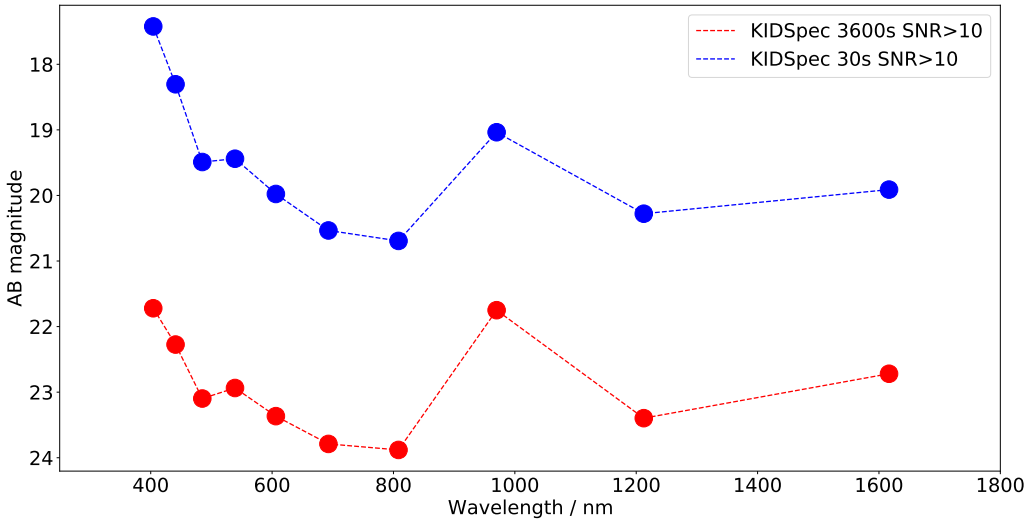

Figure 3.20: Limiting magnitudes for the 7500 spectral resolving power design used in this work. Each grating order's blaze wavelength SNR was taken with a threshold of SNR>10. Two exposure times were considered, 3600s and 30s. The large peak at $\approx$ 1000nm is the result of an unfortunate bright sky line at this wavelength which reduced the limiting magnitude at this order's blaze wavelength. The 30s exposure limiting magnitudes at $\approx 400 - 500$nm again approach the 19 magnitude of ZTFJ1539 + 5027, which would allow KIDSpec to take more phase bins of the period.

average R_E of 10 with 20,440 MKIDs. One of the focuses for MKID research in the OPT/NIR in the 2020s will be to improve the energy resolution of the detectors (Mazin et al., 2019).

3.7 Discussion

As shown in this Chapter, KIDSpec will have the ability to observe a variety of astronomical targets, and contribute to a wide range of science areas. The spectra of stars carry important information about them; abundance of elements, effective temperature, and gravity for example (Szczerba et al., 2020). Galaxy observations also present opportunities for many different science areas. High redshift star forming galaxies and their emission lines can provide information on the stages of evolution of the universe, such as the epoch of reionisation (Onodera et al., 2020).

Emission line galaxies at medium to high redshifts can aid in testing the cosmological dark energy model and constrain it (Gao and Jing, 2020). The central phase of reionisation of hydrogen in the universe can be investigated using Lyα emitter galaxies, because of the resonant scattering of Lyα photons being responsive to the neutral hydrogen in the intergalactic medium (Yang et al., 2019). KIDSpec's relevant features for this are that MKIDs do not suffer from readout noise, and KIDSpec would have superb cosmic ray removal owing to the MKID's time resolution (Mazin et al., 2013). In an MKID, the cosmic ray event lasts a few hundred microseconds and can be easily removed from the phase time-stream because of its amplitude. This will result in the loss of a small fraction of an exposure. In a semiconductor detector, all of the charge from the cosmic ray is stored until the readout, affecting the whole exposure time (O'Brien, 2020).

Also as discussed in Sec. 3.5.2, because of the MKID's lack of readout noise, the resulting spectrum can be rebinned flexibly to a lower spectral resolution.

Active galactic nuclei can be spectrally identified using observed emission lines and from this, information on their stellar populations can be gained. NIR spectroscopy is well suited to this as it is in a less extinct wavelength range when compared to the optical. NIR spectroscopy is not dominated by nonstellar emission, allowing for the study of the stellar content of the galaxy, and the search for signatures of intense star formation (Ramos Almeida et al., 2009).

Other science areas of interest to KIDSpec include spectrally time resolved studies such as orbits of compact binaries. These observations are currently limited, especially ahead of the launch of the Laser Interferometer Space Antenna (LISA) (Amaro-Seoane et al., 2017). LISA will aim to detect tens of thousands of these systems (Burdge et al., 2019). For short period binaries, ≈ 15 minutes, one limitation of CCDs is their read noise. A sufficiently long exposure must be taken to reduce the read noise's impact, which limits the number of phase bins of the binary's period to constrain its parameters. The effect of this is an increase in error on the parameters, possibly even to similar values to the found feature (Burdge

et al., 2019). Additionally, smearing of spectral features for systems with high radial velocity make long exposures also unsuitable, as the spectral line would not be resolvable. MKIDs however, are not limited by exposure time owing to a lack of read noise, and therefore can use more phase bins, i.e. shorter exposures, and hence result in more constrained parameters. The LRIS instrument (Oke et al., 1995) was used for spectroscopic observations of the system in Burdge et al. (2019). LRIS can have a spectral resolving power between 300 and 5000 with a bandpass of 320 to 1000 nm, making the 5000 spectral resolving power KIDSpec setup described here an appropriate option. The magnitudes for 30s exposures with an SNR ≥ 10, calculated in Sec. 3.4.1, at a spectral resolving power of 5000 approach the $\approx$ 19 AB magnitude of the system observed in Burdge et al. (2019). Using KIDSpec would allow for more phase bins during an observation of these systems, reducing the final error on the parameters. Additionally KIDSpec could take a continuous exposure and the observation can be separated afterwards because of the time resolving capabilities of the MKIDs. This makes KIDSpec suited to observing short period binaries, such as the systems LISA will observe.

Another field of interest is fast time variability systems such as pulsars, magnetic white dwarfs, and other binary systems (Mazin, 2004). For pulsars and magnetic white dwarfs, optical data alongside simultaneous radio and gamma ray observations, will aid testing of high-energy emission models (Mazin et al., 2010). KIDSpec will also be able to constrain parameters of various types of binaries (O'Brien, 2020). In the Bowen region of 463 to 466 nm, there are narrow high excitation emission lines, and these lines appear to move during the period of the binary system. Using the movement of these lines the semi amplitude of the radial velocity and mass function can be constrained (Cornelisse et al., 2008). Discussed here are just a selection of KIDSpec's science cases, which continues to grow.

3.8 KSIM Parameter List

Table 3.4 contains all variable parameters for KSIM, with units and formats.

Table 3.4: All parameters which can be altered for a astronomical target object observation simulation using KSIM. Where appropriate, a requirement or range for the value of the parameter is also included.

Parameter	Description
object_name	Name of astronomical target object being simulated within KSIM.
object_file	Name of file containing spectrum of astronomical target object, structured in the form of two columns with wavelength (nm) and flux ($ergcm^{-2}s^{-1}\text{Å}^{-1}$).
binstep	The size in nm of the bins in the Object File spectrum.
mirr_diam	Diameter in cm of the primary mirror of the telescope.
central_obscuration	Percentage obscuration to the primary mirror of the telescope.
seeing	Value of the atmospheric seeing, in arcseconds.
exposure_t	Exposure time of simulated observation in seconds.

tele_file	Text file containing two columns, wavelength in nm and percentage reflectance of telescope mirror material.
lambda_low_val	Minimum wavelength for simulated KIDSpec bandpass. Minimum value of 350nm and maximum value of 2999nm.
lambda_high_val	Maximum wavelength for simulated KIDspec bandpass. Minimum value of 351nm and maximum value of 3000nm.
n_pixels	Number of MKID pixels in linear array for KIDSpec. Minimum value greater than zero.
alpha_val	Incidence angle of incoming light to grating in degrees.
phi_val	Reflected central angle of incoming light to grating in degrees.
refl_deg	Reflected angle range of incoming light passed to MKIDs in degrees.
grooves	Number of grooves on grating per mm.
norders	Number of grating orders to test for incoming wavelengths.
number_optical_surfaces	Number of optical surfaces in KIDSpec instrument between primary mirror and MKIDs. The GEMINI silver mirrors reflectance is used here.

folder_dir	Folder path where all other files can be found and where results are saved to.
fudicial_energy_res	Energy resolution used to calculate energy resolution at all other wavelengths.
fudicial_wavelength	Wavelength used to calculate energy resolution at all other wavelengths.
coincidence_rejection_time	The coincidence rejection time, in μs, used for MKID saturation calculations for both the PTS and Order Gaussian methods.
raw_sky_file	FITS file containing the sky background, can be generated using ESO SKYCALC.
slit_width	Width of slit in arcseconds.
pixel_fov	FoV of MKID pixels in arcseconds.
off_centre	Sets the distance target object is from the centre of the slit in arcseconds. Can be set to zero or greater.
airmass	Airmass of atmosphere.
dead_pixel_perc	Percentage of MKIDs which are considered dead. Value can be set in the range 0-100.
R_E_spread	Standard deviation value of normal distribution used to generate spread of R_E. Can be set to zero or greater.
redshift	Desired redshift of target object.
redshift_orig	Original redshift of target object.

mag_reduce	Factor which reduces incoming flux from simulated target. Can be set to <1 for an increase in flux.
generate_sky_seeing_eff	Generates transmission file, containing transmission of sky spectrum though slit.
sky_seeing_eff_file_save_or_load	Name of sky seeing transmission file to either save or load.
generate_model_seeing_eff	Generates transmission file, containing transmission of target object spectrum though slit
model_seeing_eff_file_save_or_load	Name of target object seeing transmission file to either save or load.
generate_additional_plots	Plots additional steps throughout KSIM, including photon spectra at various stages such as atmosphere, telescope, and grating orders.
generate_standard_star_factors	Generates standard star spectral weights as described in Sec. 3.3.6.
stand_star_run_filename_details	Name of standard star spectral weights to either save or load.
fwhm_fitter	Option to use a Lorentzian shape fitter for spectral features, up to two features at once.
fwhm_fitter_central_wavelength	Central wavelength of a Lorentzian shaped line.

fwhm_fitter_central_wavelength_2	Central wavelength of a second Lorentzian shaped line.
double_fitter	If two lines are to be fitted then this is set to True.
continuum_removal_use_polynomial	If True a polynomial will be fitted to the spectrum to remove the spectrum continuum. If False a linear fit is used.
reset_R_E_spread_array	When True generates new energy resolution spreads.
reset_dead_pixel_array	When True generates dead pixel spreads.

Chapter 4

SuperSmart

4.1 Concept

The benefits of using an instrument like KIDSpec in the optical/near-infrared can also be harnessed with an array of small robotic telescopes. This setup would enable the features described in Chapter 3, such as the absence of read noise for short exposures, while providing flexibility in observations. All telescopes could operate independently, and the MKIDs used could incoherently combine their exposures. Additionally, this approach would not necessitate large-scale construction projects like those required for 2m and larger-class telescopes.

Some examples of small telescopes or telescope arrays include Tarot-S (Boer et al., 2003), LOTIS (Williams et al., 2008), TRAPPIST (Jehin et al., 2011), MINERVA (Swift et al., 2014), BlackGEM (Roelfsema et al., 2016), and GOTO (Steeghs et al., 2022). A brief summary of these telescopes is provided in Table 4.1.

These telescopes were all originally designed for photometry in scientific areas such as gamma-ray burst optical follow-up (Boer et al., 2003), exoplanet discovery (Jehin et al., 2011), and gravitational wave event optical follow-up (Roelfsema et al., 2016; Steeghs et al., 2022). By employing photometry, they were able to observe fainter objects while using telescopes with diameters of less than 1 meter. However, this concept will focus on spectroscopy with small telescopes.

Table 4.1: Brief summary of a selection of small telescopes or telescope arrays. All facilities shown conduct observations using photometry, but MINERVA also conducts high resolution spectroscopy. *T.* is Telescopes, and *D.* is Diameter. The telescope number shown for GOTO is a planned upgrade for the facility, Steeghs et al. (2022) demonstrated a 4 telescope prototype.

Name	No. *T.*	*T. D.* (cm)	CCD array
GOTO	32	40	8304x6220
BlackGEM	3	65	111 Megapixel
MINERVA	4	70	2048x2048
NGTS	12	20	2048x2048
TRAPPIST	1	60	2048x2048
LOTIS	1	60	2048x2048
Tarot-S	1	25	2048x2048

KIDSpec, using MKIDs, would function as a photon-counting, read-noise-free, high-throughput spectrograph, allowing flexible rebinning without any penalty. With these capabilities, once photons are identified, they can be incoherently combined, even if they were detected on different MKID arrays. Using separate arrays of MKIDs could of course add additional complexity such as varying energy resolutions between arrays, which could limit the resulting spectral resolving power. Here however the focus is on the initial design.

For instance, if 100,000 MKIDs were deployed and organised into 20 linear arrays of 5,000 MKIDs each, each linear array could be paired with a 0.8m diameter telescope. These 20 0.8m telescopes could be utilised independently, or the photons detected by their linear MKID arrays could be combined, effectively simulating a larger single telescope without any drawbacks. Combining all 20 MKID linear arrays from their respective 0.8m telescopes would be equivalent to a single 3.6m telescope. This telescope array concept is known as Superconducting Spectrograph for Medium resolution in an Array of Telescopes (SuperSmart). Figure 4.1 illustrates a diagram of the SuperSmart concept. This chapter explores potential SuperSmart designs, including the limiting magnitudes of various SuperSmart setups.

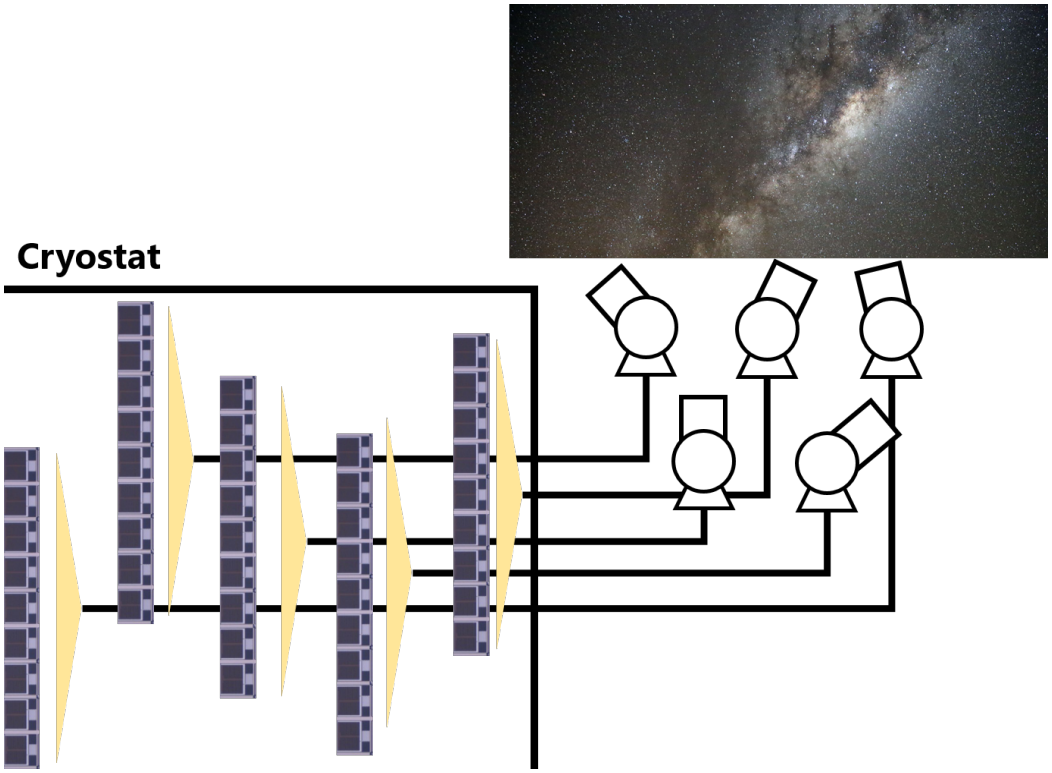

Figure 4.1: Diagram of the SuperSmart concept. Each individual telescope in the array would be optically linked to an MKID linear array by an optical fibre. The telescopes would be able to act independently or observe the same object, with all the MKID array's observed photons incoherently combined to improve the signal-to-noise ratio (SNR). Image of night sky shown from `https://cs.astronomy.com/asy/b/daves-universe/archive/2014/06/02/adventures-in-the-atacama-desert.aspx`.

4.2 Science Motivation

SuperSmart would contribute to a wide variety of science cases through its use of MKIDs and multiple telescopes. A selection are considered here, with more also being discussed previously in Chapter 3.

4.2.1 GAIA

For instance, during the GAIA survey, there were approximately 100,000 stars down to magnitude $m_V = 19$ in the Milky Way that required follow-up spectroscopy. These stars were primarily located in the local thin Disk of the Milky Way, but

stars were also sampled from the Bulge and thick Disc of the Milky Way. This follow-up was accomplished using FLAMES (Pasquini et al., 2002) on the VLT over 300 nights (Gilmore et al., 2012).

4.2.2 Vera C. Rubin Observatory

Currently, the Vera C. Rubin Observatory (VCRO) (Ivezić et al., 2019) is expected to complete construction by the end of 2024 Claver et al. (2022) and commence its planned 10-year survey, the Legacy Survey of Space and Time (LSST). The survey is anticipated to observe an enormous number of objects, many of which will require follow-up spectroscopy. It is projected that LSST will observe approximately 20 billion Milky Way stars with magnitudes exceeding $m_r = 20$ and several billion galaxies (Ivezić et al., 2019). These objects will contribute to a wide range of scientific investigations, including the analysis of the intricate and dynamic structure of our home, the Milky Way Galaxy (Bond et al., 2010), the study of variable star populations such as cataclysmic variables (Sesar et al., 2007), and the exploration of dark energy and dark matter.

4.2.2.1 Dark Energy and Matter

The nature of dark energy remains unknown, but it can be explored by studying the relationship between redshift and distance, which reveals its influence on the expansion rate of the Universe. Additionally, investigating the clustering rate of matter provides insights into the energy contents of the Universe (Ivezić et al., 2019). This approach allows for testing general relativity and the ΛCDM cosmological model, as modifying the large-scale behaviour of gravity could help us understand the nature of dark energy and matter (Howlett et al., 2017a).

The LSST is expected to observe approximately 400,000 photometrically classified Type Ia supernovae (SNe Ia), which can significantly contribute to these investigations, particularly when both light curves and spectroscopic redshifts are utilised.

Achieving a maximum spectral resolving power of approximately 2700 would be required for these studies (Da Cunha et al., 2017). Additionally, Howlett et al. (2017a) previously used a predicted SNe Ia sample to be observed by LSST with $m_i < 18.1$. Howlett et al. (2017a) also noted the importance of a future survey sample with J<19.0, pushing the wavelength range of interest up to $\approx$ 1500nm from the UV/visible.

Using these measured redshifts, the redshift distance can be determined, and the difference between the redshift distance and the true distance of the galaxy can be used to obtain the Peculiar Velocity (PV) of the host galaxy (Howlett et al., 2017b). The PV can then be employed to calculate the linear growth rate, denoted as f, of the universe. According to general relativity, the linear growth rate is predicted as $f(z) \approx \Omega_m(z)^\gamma$, where $\gamma \approx 0.55$, z represents the redshift, and Ω_m denotes the matter density fraction (Linder and Cahn, 2007). If the measured linear growth rate deviates from this prediction, it would indicate the need to modify the theoretical behaviour of gravity on large scales.

4.2.2.2 Milky Way structure

The structure of the Milky Way can be described using nine dimensions: three spatial coordinates, three velocity components, luminosity, effective temperature, and metallicity. The velocity components of the Milky Way can be constrained by studying the star sample observed by the LSST. Medium-resolution spectra of these stars can be compared to stellar templates to determine their spectral type, radial velocity, and radial velocity error (Bond et al., 2010). The templates which can be used for this are the ELODIE templates with a wavelength range of $410 - 680$nm (Prugniel and Soubiran, 2001).

Analysis of a set of these objects of interest was conducted in Bond et al. (2010) using the Sloan Digital Sky Survey (SDSS) spectroscopic survey, with a spectral resolving power of $\approx$ 1800 (Castander et al., 2001), $m_r < 20$, and the ELODIE

templates. LSST will extend the sample used here, and therefore will require more spectroscopic followup. Depending whether a higher spectral resolving power is required, spectral resolving power of >1800 exposure can be taken with SuperSmart, subtracted for sky background at that resolving power, and subsequently rebinned down to a lower spectral resolving power to improve sky subtraction (O'Brien, 2020). This approach would enhance the accuracy of spectrum matching to templates.

By utilising the radial velocity in conjunction with the star's location, all three velocity components can be calculated (Bond et al., 2010). Increasing the number of suitable stars in different stellar categories will constrain these parameters of the Milky Way. Similarly, as mentioned earlier, SuperSmart would efficiently observe these objects with each telescope operating independently. The rate at which SuperSmart can observe objects is explored in Section 4.4.

4.2.2.3 Gravitational Waves

50 million variable stars will also possibly be observed by the LSST, enabling studies of the systems where these objects reside. This includes the potential identification of LISA sources in the form of Ultra-Compact Binarys (UCBs) (Kupfer et al., 2018), as described in Section 3.6. Spectroscopic observations of these systems will assist in characterising them prior to the launch of LISA, particularly for short periods of approximately 15 minutes or less, where parameter constraints have exhibited errors as large as the actual parameter itself (Burdge et al., 2019).

A time resolution of 34 seconds was used in post-processing of LRIS (Oke et al., 1995) data, providing 12 phase bins for the ZTF J1539 + 5027 system. This was done to determine the radial velocity semi-amplitudes of the two stars, which are essential parameters for spectroscopically constraining the masses of the stars. As discussed in Sec. 3.6, the radial velocity semi-amplitudes can be constrained by characterising the 'movement' of spectral features or lines during the period of the

binary system (Cornelisse et al., 2008).

To improve this, a time resolution on the order of seconds would be needed to reduce the error found by Burdge et al. (2019). To estimate the required timing, we can use the standard error equation: $SE = \sigma_{N-1}/\sqrt{N}$, where N is the number of data points, and σ_{N-1} is the standard deviation of the data set. From this equation, we can see that the standard error is inversely proportional to $1/\sqrt{N}$. For 12 points, this would result in a $1/\sqrt{N} = 0.3$ standard error. To reduce this factor to 0.15, approximately 47 data points would be needed.

The period of ZTF J1539 + 5027 is 414 seconds, so for 47 data points, each exposure would need to be 9 seconds. Another UCB system with a short period is HM Cnc, which has a period of 5.4 minutes (Roelofs et al., 2010). To observe HM Cnc with 47 data points in its period, exposures of 7 seconds each would be required.

According to Kupfer et al. (2018), LSST is projected to discover at least 100 LISA sources with orbital periods below 10 minutes and magnitudes below 24. UCB characteristics will be crucial for predicting the gravitational wave strength emitted by these sources, enabling testing of the LISA instruments and maximising the scientific output of the mission. These characteristics include the distance, masses, and orbital inclination of the systems. The masses can be constrained by fitting optical spectroscopy and photometry (Copperwheat et al., 2010). The inclination can be determined from ellipsoidal variations in time-resolved photometry (Brown et al., 2011). Finally, the distance can be constrained using parallax measurements from either space or the ground; the Hubble Space Telescope has been used for this purpose (Kupfer et al., 2018).

Additionally, SuperSmart could make significant contributions to other areas of gravitational wave science. Following the binary neutron star merger event GW170817, emissions were observed across the electromagnetic spectrum. A gamma-ray burst was detected approximately 1.7 seconds after the merger event, and optical observations revealed a redward evolution over a span of 10 days. Initial observations, as

early as 11 hours after the merger event, were conducted using telescopes as small as 40cm in diameter. These observations unveiled a featureless blue emission that rapidly dimmed over the course of days, while the NIR emission grew brighter, ultimately culminating in broad spectral features. Optical spectrographs were crucial within 24 hours to determine the likelihood of a coincidental occurrence between the observed gravitational wave, gamma-ray burst, and optical transient originating from the host galaxy (Abbott et al., 2017). In Pian et al. (2017) GW170817 was spectroscopically followed up on using many instruments, for example X-Shooter with a spectral resolving power of ≈ 6000, and FORS2 with a spectral resolving power of ≈ 1000. The wavelength ranges used here to observe GW170817's aftermath stretched from $\approx 350 - 2400$nm, with the lower limit of the NIR observations being $\approx$ 1600nm. From this a range of at least 350-1600nm would be needed to contribute to these follow up observations.

In this context, SuperSmart could rapidly respond to the call for observations immediately after the detection of a merger event and continuously track the event's evolution without interruptions, except when the object is no longer visible in the sky. This capability stems from having multiple fast-moving smaller telescopes and utilising MKIDs, which do not require readouts like CCDs.

Other examples include studying gamma-ray and X-ray binaries to advance the understanding of particle acceleration, magnetised relativistic outflows, and accretion-ejection physics, as well as enabling other tests of general relativity (Dubus, 2013). These observations require a minimum spectral resolving power of ≈ 2000, with SuperSmart providing the added benefit of time resolution for these sources.

These are just a selection of the scientific possibilities that could be explored with SuperSmart. The capabilities of a photon counting, time-resolving, wide-bandpass, medium spectral resolving power spectrograph open up numerous other science cases beyond those mentioned.

4.3 Design

The choices for telescopes to be considered for possible SuperSmart designs were selected from the Astrosysteme* catalogue. This was because this provider has a range of diameters for their small telescopes ranging from 0.6-2.5m, with publicly available specifications for each. The telescope sizes under consideration were 60 cm, 80 cm, and 100 cm. A single telescope with a smaller diameter would not be able to fully utilise the MKID arrays due to a low number of photons, rendering it impractical for the array. On the other hand, larger telescope diameters were excluded as the number of telescopes that could be accommodated decreased significantly due to their higher cost.

The spectral resolving powers simulated was 6000, chosen from the upper limit of the science cases listed in Sec. 4.2, and some science cases for LSST follow-up may require this slightly higher spectral resolving power (Ivezić et al., 2019). All other spectral resolving powers can be reached by rebinning this higher spectral resolving power to the desired spectral resolving power.

The optimiser used in Section 3.4.1 was also employed here to determine the optimal first-order central wavelengths and the number of MKID pixels required for a linear array. The values of R_E used were 30 and 40 at approximately 400 nm, which are similar to the values discussed in Section 3.4.1. Additionally, Zobrist et al. (2022) demonstrated a hafnium/indium bilayer design for an MKID with $R_E = 33$ at 406 nm. This design, while having a lower R_E than membrane devices (De Visser et al., 2021), is less complex to fabricate, making it more suitable for large arrays of MKIDs.

A wavelength range of approximately 350-1800 nm was investigated, similar to the range in Section 3.4.1. A separation factor of 3 was considered, and by using the relation $R_E \geq 3m$ described in Section 3.2, it would allow for the separation of

*`https://www.astrosysteme.com/products/`

Table 4.2: Summary of requirements used for simulations in this Chapter. The spectral resolving power requirement originates from the gravitational waves science cases, but can be rebinned with no penalty to the resolutions discussed in Sec. 4.2.2.1 & 4.2.2.2. The values used for the energy resolution are a result of recent advancements in upcoming MKID detectors, discussed in Sec. 4.3.1. The wavelength range is also set by the gravitational wave science but due to its width also includes the other science cases discussed in Sec. 4.2. The time resolution requirement is because of the short period binary systems discussed in Sec. 4.2.2.3, and the need for phase resolved spectroscopy to characterise these systems.

Parameter	Value
Spectral resolving power	6000
Telescope Diameters (cm)	60, 80, 100
Energy Resolution	30 & 40
Wavelength Range (nm)	$\approx 350 - 1800$
Minimum Exposure Time (s)	≈ 7
SNe Ia magnitude limit	$m_i < 18.1$
Milky Way stellar sample mag. limit	$m_r < 20$
LISA gravitational wave sources mag. limit	<24

10 and 13 orders for R_E values of 30 and 40, respectively. Table 4.2 contains a summary of the requirements simulated here.

4.3.1 Spectral Order Optimiser

The results of the optimisation process are depicted in Figure 4.2. It should be noted that this stage represents a conceptual phase for SuperSmart, and various aspects of the physical design could be modified in future implementations of the array. Figure 4.3 depict the optimised grating order placements. The magnitude bands from ESO* used for ETC simulations are also plotted in Figure 4.3, along with the GEMINI atmospheric transmission data.

For a spectral resolving power of 6000 and $R_E = 30$, the optimised values were 4.86 μm and 2670, respectively, while for $R_E = 40$, the values were 4.87 μm and 2670, respectively.

*https://www.eso.org/observing/etc/doc/formulabook/node12.html

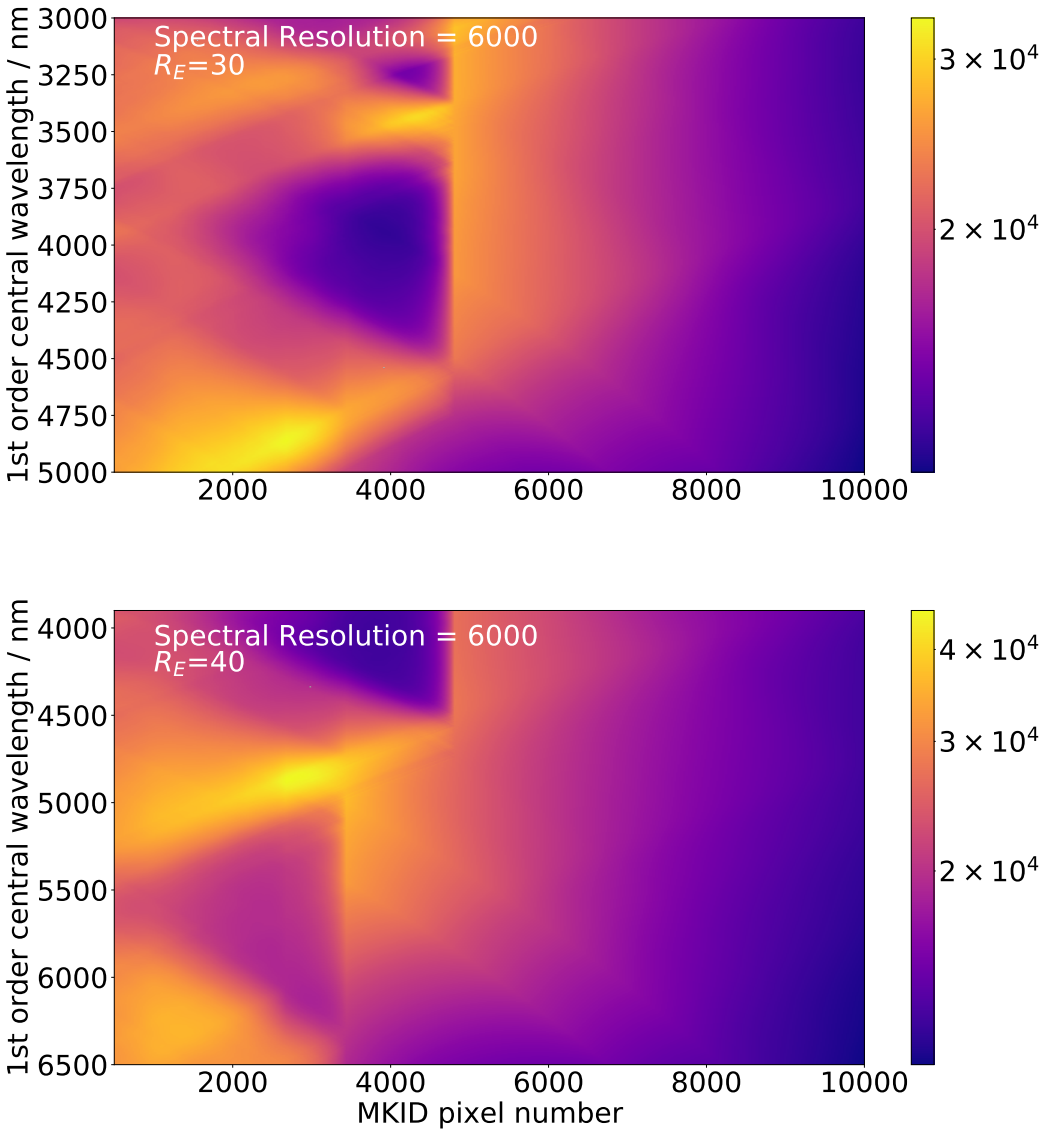

Figure 4.2: Optimiser score heatmaps for grating order placements with a spectral resolving power of 6000, and R_E values of 30 (**Top**) and 40 (**Bottom**). The score increased by positioning grating orders within regions of high atmospheric transmission and low sky brightness. The spectral resolving power of 6000 found for $R_E = 30$, the optimiser identified a first-order wavelength of 4.86 μm and determined that 2670 MKID pixels were required. For $R_E = 40$, the optimiser determined a first-order wavelength of 4.87 μm and a requirement of 2670 MKID pixels.

There was not a significant change in the number of MKID pixels required between the two R_E values. From Figure 4.3, the trade-off between the two R_E values lies in the width of the bandpass. By using the same number of MKID pixels, the $R_E = 40$ setup achieves bandpass coverage that extends to a central order wavelength of 373 nm with a maximum order of 13, while the $R_E = 30$ setup reaches 486 nm with its maximum order of 10. These maximum orders originate from the separation requirement of the order Gaussians the MKIDs are required to separate. Higher orders will be more complex to separate, as discussed in Sec. 3.2. Photons from higher orders will still potentially be exposed onto the MKID but can be minimised with the use of filters. Additionally, the drop in atmospheric transmission below ≈400nm and the high transmission in the H-band, resulted in the optimiser placing the orders for the two setups in similar positions.

The placement of orders as preferred by the optimiser is clearly influenced by the positioning of regions with low atmospheric transmission in relation to the orders. Due to the atmospheric transmission the results from the comparison between the two energy resolutions demonstrate that an R_E of 30 would be sufficient for optimised coverage of the bandpass $\approx 400 - 1800$nm. The extra orders granted by the $R_E = 40$ setup would not bring additional benefits such as a reduced MKID pixel number. Orders placed at wavelengths lower than $\approx$ 450nm would result in poor atmospheric transmission, thereby reducing their score. In both panels of Figure 4.2, triangular regions with low scores can be observed. These triangles are formed as the orders traverse areas of the bandpass with low atmospheric transmission, thereby placing the gaps between the orders in regions of high transmission.

But, this observable bandpass may not pose an issue because the atmospheric transmission begins to rapidly decrease around the wavelength where the coverage of the $R_E = 30$ setup ends, at approximately 400nm. However spectral features such as the Balmer jump at approximately 364nm (Knigge et al., 1998) would be out of reach of this design.

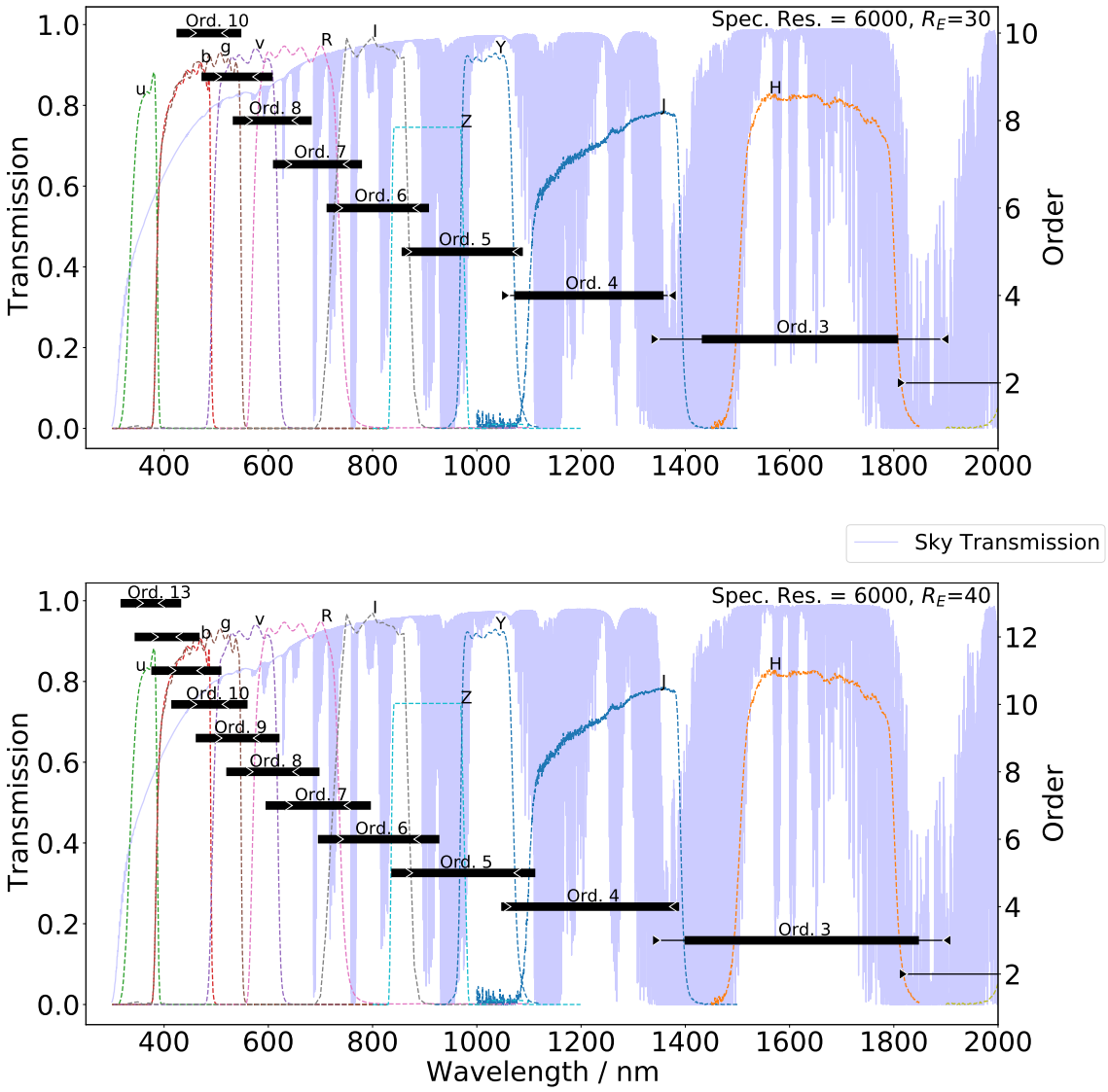

Figure 4.3: Grating order placements from the optimiser results shown in Fig. 4.2, with spectral resolving power 6000, and R_E values of 30 (**Top**) and 40 (**Bottom**). Bold black bars represent the wavelength ranges observed by the MKIDs for each grating order. The thinner black lines with inward-pointing arrows indicate the free spectral range for each order. Magnitude bands from ESO, used for ETC simulations, are also included, along with the GEMINI atmospheric transmission data.

4.3.2 Telescopes

The determined number of MKID pixels for the optimised setups can now be utilised to calculate the number of telescopes that can be employed in SuperSmart. For each telescope, it is assumed that 3 linear MKID arrays are required: one for science, one for sky subtraction, and one for a comparison object. These can be setup on the telescopes by using a pick-off fibre taking a portion of the FoV, or by attaching a spotter scope, such as the Celestron C90 MAK*, to the telescope allowing for more flexibility in pointing. Using a separate spotter scope would place requirements on a bright enough comparison star to facilitate a comparison observation in the same exposure as the target object, and increase the complexity of the software needed for this instrument. However using a separate fibre to observe a portion of the FoV would have more sky coverage than the spotter scope, not require more overheads on a separate comparison star observation, and not have the requirements on the comparison star brightness. The comparison star would not need to be brighter than what the telescope itself can observe. The FoV would be slightly obscured however. An example of a pick-off system that could be used to feed a fibre is presented but not utilised in Dhillon et al. (2021). In this work a fibre pick-off system is assumed. An estimated maximum of 100,000 MKID pixels is considered here, which could potentially correspond to several arrays of MEC number of MKID pixels (Walter et al., 2020) with an alternative aspect ratio, in a sufficiently large cryostat.

BlueFors' most popular fridge is the LD dilution refrigerator†, which provides a total of approximately 77 coax RF ports‡. Each MKID feedline requires two of these ports: one for propagating the microwave signal to the MKID and another for the return of the signal, allowing for approximately 38 feedlines. However, with the development of new coaxial cables, such as the high-density flexible coax from

*https://www.celestron.com/products/c90-mak-spotting-scope
†https://bluefors.com/products/ld-dilution-refrigerator/
‡https://bluefors.com/products/coaxial-wiring/

Delft Circuits, the number of possible feedlines will increase. More details on the MKID readout are included in Chapter 5.

Assuming a maximum number of 50 feedlines in the cryostat with a custom LD refrigerator from BlueFors, with each feedline capable of accommodating 2000 MKID pixels (Walter et al., 2020), the upper limit for a single cryostat is also 100,000 MKID pixels. However, multiple cryostats could be utilised.

From Section 4.3.1, the number of MKID pixels required per linear array is approximately 2670 for a spectral resolving power of 6000. This would allow for a maximum of 12 telescopes from a single cryostat, when considering three sets of 2670 MKIDs for a single telescope. The additional sets would be for observing both a companion star and sky data simultaneously to an observation.

As discussed previously, Astrosysteme telescopes* could be used for the SuperSmart array. A summary is included here of their telescopes which were considered, for their smaller size. The following prices include a driver mount, but no enclosure or other general construction which would influence the cost of SuperSmart. The RC600† is a 60cm diameter telescope with a price of €102,000. With 12 telescopes, this would cost a total of €1,224,000. The 80cm diameter telescope is the RC800‡, costing €227,000. This would be a total of €2,724,000 for 12 telescopes. For a 100cm diameter telescope this would be the AZ1000§, costing €549,000, costing €6,588,000 for 12 telescopes.

The RC600 telescopes have a central obscuration of 40%, resulting in an effective collection area of 1809 cm^2 out of a total area of 2827 cm^2. Therefore, they have an effective diameter of 48 cm. The RC800 and AZ1000 telescopes have central obscurations of 41% and 40%, respectively, leading to effective collecting areas of 3277 cm^2 and 5027 cm^2, respectively. This corresponds to effective diameters of 65 cm and 80 cm, respectively. Considering the total collecting area of 12 RC600,

*https://www.astrosysteme.com/
†https://www.astrosysteme.com/products/rc600_1/
‡https://www.astrosysteme.com/products/rc800_5/
§https://www.astrosysteme.com/products/asa-az1000/

RC800, and AZ1000 telescopes each, they are equivalent to a single telescope with diameters of 1.7 m, 2.2 m, and 2.8 m, respectively with no central obscuration. With a central obscuration of 41%, which is Astrosysteme's 2.5m telescope's obscuration, these telescopes would be equivalent to 2.2m, 2.9m, and 3.7m telescopes respectively.

Alternatively, instead of maximising the number of telescopes per cryostat, one might prefer to achieve an equivalent single telescope effective diameter, such as 2m. In this case, it would require either 18 RC600 telescopes, 10 RC800 telescopes, or 7 AZ1000 telescopes.

4.4 KSIM Simulations

4.4.1 Limiting Magnitudes

Using the telescopes discussed in Section 4.3.2 and the grating order placements determined in Section 4.3.1, sets of KSIM simulations were conducted to determine limiting magnitudes. These simulations involved calculating the AB magnitudes at the blaze wavelengths of each order. Varying exposures were conducted at the point where the SNR>5. Specifically, we simulated two exposure times: 60 seconds and 1 hour. The choice of 1 hour aligns with other limiting magnitude determinations, such as those in the X-Shooter User Manual*, and similar instruments discussed below. Furthermore, results were included for 2m and 4m class telescopes to demonstrate the potential performance of combining the setups determined in Section 4.3.1 into larger telescopes. The results cover spectral resolving powers of 6000, 1000, and 100, showcasing the flexible rebinning capability of the MKIDs. The simulations were run using 2 pixels per spectral resolution element, and the magnitudes shown are per spectral resolution element. The specific results of the simulations are included in Tables 4.3 to 4.5.

*https://www.eso.org/sci/facilities/paranal/instruments/xshooter/doc.html

Table 4.3: The predicted limiting magnitude results for SuperSmart with a spectral resolving power of 6000 at R_E values of 30 and 40 are presented. The displayed wavelengths correspond to the blaze wavelengths for each spectral order. The simulations were conducted using exposure times of 3600s and 60s on telescopes with diameters of 0.6m, 0.8m, 1m, 2m, and 4m, with a SNR threshold of >5. In the AB magnitude columns, the exposure times are indicated in the format of 3600s/60s. The wavelength is denoted by 'WL'.

Spectral Res. 6000												
	$R_E = 30$						$R_E = 40$					
WL/nm	0.6m	0.8m	1m	2m	4m		WL/nm	0.6m	0.8m	1m	2m	4m
1614	17.2/13.5	17.6/14.1	18.0/15.0	19.0/16.0	19.7/17.1		1617	17.2/13.5	17.6/14.1	18.0/15.0	18.8/16.0	19.7/17.1
1210	18.2/14.1	18.7/14.9	19.1/15.3	20.1/16.8	20.9/18.1		1213	18.2/14.1	18.7/15.0	19.1/14.9	20.1/16.7	20.9/18.0
968	18.1/14.1	18.6/14.9	19.0/15.4	19.9/16.7	20.7/17.9		970	18.2/14.6	18.8/14.9	19.0/14.9	20.0/16.7	20.8/18.0
807	18.6/14.4	19.0/15.0	19.3/15.5	20.3/16.9	21.2/18.2		808	18.6/14.4	19.0/15.2	19.3/15.0	20.3/16.9	21.2/18.2
692	18.5/14.5	19.1/15.0	19.4/15.5	20.4/16.9	21.4/18.4		693	18.5/14.5	19.1/14.8	19.4/15.0	20.4/17.0	21.4/18.4
605	18.8/14.5	19.2/15.2	19.5/15.7	20.7/17.1	21.5/18.5		606	18.7/14.5	19.1/15.1	19.5/15.2	20.7/17.0	21.5/18.5
538	18.8/14.5	19.3/15.2	19.7/15.7	20.7/17.1	21.6/18.5		539	18.8/14.5	19.3/15.1	19.7/15.2	20.7/17.1	21.6/18.5
484	18.2/13.9	18.8/14.7	19.1/15.0	20.2/16.5	21.1/17.9		485	18.3/14.2	18.8/14.6	19.2/14.7	20.4/16.6	21.2/18.1
							441	18.2/13.9	18.8/14.7	19.2/15.0	20.4/16.5	21.4/18.1
							404	16.5/12.2	17.1/14.7	17.6/13.3	18.9/14.8	20.0/16.4
							373	14.9/10.4	15.5/12.9	16.0/11.6	17.5/13.3	18.8/14.6

Table 4.4: The predicted limiting magnitude results for SuperSmart with a spectral resolving power of 1000 at R_E values of 30 and 40 are presented. The displayed wavelengths correspond to the blaze wavelengths for each spectral order. The simulations were conducted using exposure times of 3600s and 60s on telescopes with diameters of 0.6m, 0.8m, 1m, 2m, and 4m, with a SNR threshold of >5. In the AB magnitude columns, the exposure times are indicated in the format of 3600s/60s. The wavelength is denoted by 'WL'.

Spectral Res. 1000											
	$R_E = 30$						$R_E = 40$				
WL/nm	0.6m	0.8m	1m	2m	4m	WL/nm	0.6m	0.8m	1m	2m	4m
1616	18.3/15.4	18.7/15.8	19.0/16.2	19.8/17.2	20.7/18.2	1619	16.3/15.4	16.5/15.6	16.7/16.1	17.5/17.6	18.2/18.2
1212	16.9/14.9	17.3/14.9	17.5/15.3	18.3/16.1	19.1/16.9	1214	19.5/15.7	19.9/16.2	20.2/17.0	21.1/17.8	21.9/18.6
970	18.2/15.6	18.6/16.1	18.9/16.3	19.6/17.2	20.4/18.1	971	18.8/16.6	19.2/16.6	19.4/17.1	20.2/18.2	21.1/19.1
808	19.8/16.1	20.2/16.7	20.5/17.1	21.3/18.6	22.2/19.6	809	19.5/16.5	19.9/16.9	20.2/16.9	21.2/18.5	21.8/19.3
693	19.8/16.0	20.2/16.7	20.5/17.1	21.4/18.5	22.2/19.6	694	19.6/16.3	20.0/17.1	20.3/17.5	21.1/18.7	21.9/19.6
606	20.0/16.2	20.4/16.8	20.7/17.2	21.6/18.7	22.4/19.8	607	20.0/16.3	20.4/17.1	20.7/17.3	21.6/18.7	22.4/19.8
539	20.0/16.2	20.7/16.9	20.9/17.3	21.8/18.8	22.6/29.9	540	20.2/16.7	20.7/16.7	20.9/17.5	21.8/18.7	22.6/19.7
485	19.6/15.6	20.1/16.2	20.4/16.7	21.3/18.2	22.1/19.3	486	19.5/15.9	19.9/16.7	20.4/16.7	21.2/18.2	22.0/19.2
						441	19.6/15.9	20.0/15.9	20.4/16.7	21.4/18.1	22.3/19.1
						405	18.2/13.9	18.8/15.0	19.1/15.0	20.1/16.7	21.0/17.9
						374	16.6/12.6	17.3/13.0	17.7/13.3	19.1/15.0	20.2/16.4

Table 4.5: The predicted limiting magnitude results for SuperSmart with a spectral resolving power of 100 at R_E values of 30 and 40 are presented. The displayed wavelengths correspond to the blaze wavelengths for each spectral order. The simulations were conducted using exposure times of 3600s and 60s on telescopes with diameters of 0.6m, 0.8m, 1m, 2m, and 4m, with a SNR threshold of >5. In the AB magnitude columns, the exposure times are indicated in the format of 3600s/60s. The wavelength is denoted by 'WL'.

Spectral Res. 100											
	$R_E = 30$						$R_E = 40$				
WL/nm	0.6m	0.8m	1m	2m	4m	WL/nm	0.6m	0.8m	1m	2m	4m
1616	18.1/15.8	18.3/16.0	18.6/16.3	19.4/17.1	20.2/17.9	1619	18.1/15.8	18.4/16.2	18.7/16.4	19.5/17.2	20.2/18.0
1212	19.3/16.9	19.5/17.2	19.8/17.5	20.6/18.3	21.5/19.1	1214	19.4/17.0	19.7/17.4	20.0/17.7	20.8/18.5	21.7/19.3
970	20.1/17.6	20.5/18.0	20.7/18.3	21.5/19.2	22.2/19.9	971	20.6/17.9	21.1/18.4	21.3/18.8	22.1/19.6	22.8/20.5
808	21.2/18.4	21.5/18.9	21.7/19.1	22.5/20.1	23.3/21.0	809	21.1/18.4	21.6/18.9	21.8/19.2	22.6/20.1	23.3/21.1
693	21.2/18.4	21.6/18.9	21.9/19.2	22.7/20.2	23.4/21.1	694	21.2/18.4	21.6/18.9	21.9/19.2	22.7/20.2	23.4/21.1
606	21.5/18.5	21.9/19.1	22.1/19.4	22.9/20.4	23.7/21.4	607	21.5/18.5	21.9/19.0	22.1/19.4	22.9/20.4	23.6/21.4
539	21.7/18.7	22.0/19.2	22.3/19.5	23.1/20.7	23.9/21.5	540	21.7/18.7	22.0/19.2	22.3/19.5	23.1/20.7	23.9/21.5
485	21.2/17.9	21.5/18.5	21.8/18.9	22.5/20.0	23.3/20.9	486	21.2/18.1	21.6/18.6	21.9/19.0	22.7/20.1	23.4/21.1
						441	21.4/18.1	21.7/18.6	22.0/19.0	22.8/20.2	23.7/21.2
						405	20.0/16.4	20.4/17.1	20.8/17.5	21.5/18.8	22.4/19.9
						374	19.1/14.8	19.7/15.5	20.0/15.9	20.9/17.4	21.8/18.8

Table 4.3 shows that SuperSmart, with an effective diameter of 4m, can achieve magnitudes of approximately 21.7 at a spectral resolving power of 6000 with 3600-second exposures, maintaining an SNR > 5. Similarly, the AAOmega spectrograph on the 4m Anglo-Australian Telescope can reach an SNR of 4.1 within an hour at $m_V = 22$, offering a spectral resolving power of approximately 5000 (Saunders et al., 2004). The under-construction WEAVE instrument (Dalton et al., 2012) is also expected to reach $m_V = 21$ with an SNR of 7.2 in a one-hour exposure, with a spectral resolving power of 5000*. For 60-second exposures, the faintest magnitude achievable with SuperSmart is approximately 18.5. Therefore, SuperSmart can perform a wide range of observations at varying resolving powers and exposure times while maintaining limiting magnitudes comparable to other instruments on 4m telescopes.

Across Tables 4.3 to 4.5, the results for R_E values of 30 and 40 were largely similar in terms of wavelength placement, which is expected because the optimiser placed the orders in similar positions. The main difference between these two setups lies in the bandpass wavelength range, with the $R_E = 40$ configuration having an additional $\approx$ 100nm coverage from the higher orders which satisfy the separation condition of 3.

Other expected trends were also observed. For larger telescope diameters or lower spectral resolving powers, the limiting magnitudes became fainter. Additionally, all sets of limiting magnitudes exhibited their faintest magnitudes around 500nm, with the magnitudes then increasing with longer wavelengths. This is expected as the sky becomes brighter at longer wavelengths in this regime, and the atmosphere's transmission begins to decline at shorter wavelengths. A similar trend can be seen in Kaper et al. (2008) for X-Shooter's limiting magnitudes.

An unexpected trend was observed for two $\approx$ 1600nm and $\approx$ 1200nm results across the spectral resolving powers of 100 to 1000. Here the 100 set of results at these wavelengths had a lower magnitude result than the spectral resolving power of 1000

*`https://www.ing.iac.es/Astronomy/instruments/weave/weaveinst.html`

for the 2m diameter telescope. From Fig. 4.3 there are regions of low transmission in the J and H bands, which correspond to the wavelengths shown in these limiting magnitude results. These results being limited to only some of the results for these wavelengths and not consistently suggest these anomalous results are due to unfortunate wavelength bins being impacted by reduced atmospheric transmissions in these wavelength regions.

4.4.2 Survey Simulation

4.4.2.1 Survey Simulation Setup

One of the key benefits of SuperSmart, with its individual telescopes, is their ability to operate independently. To investigate this, parameters need to be defined to estimate SuperSmart's performance for specific sets of objects or individual science cases. Firstly, the duration required for sets of objects with SuperSmart is defined as the number of nights needed. Here, a single night is defined as 8 hours, an average duration for nighttime throughout the year.

The time required to move the telescopes between objects is also necessary. The use of small telescopes allows for quick repositioning across the sky. An estimate of 30 seconds between objects was used because with driver slew speeds available on the market at 40 degrees/second*, the movement between objects can be rapid. GOTO is able to begin observing a target within 30 seconds of receiving the command†. MINERVA can also lock onto a target object in approximately 20 seconds (Swift et al., 2014).

The survey example used here was the GAIA follow-up survey containing 100,000 objects at $m_V < 19$ (Gilmore et al., 2012). Data was used from the GAIA Archive ‡, containing stars from DR2 (Brown et al., 2018). This gave a distribution of stars with varying magnitudes, shown in Fig. 4.4.

*`https://astelco.com/products.htm`
†(Steeghs et al., 2022)
‡`https://gea.esac.esa.int/archive/`

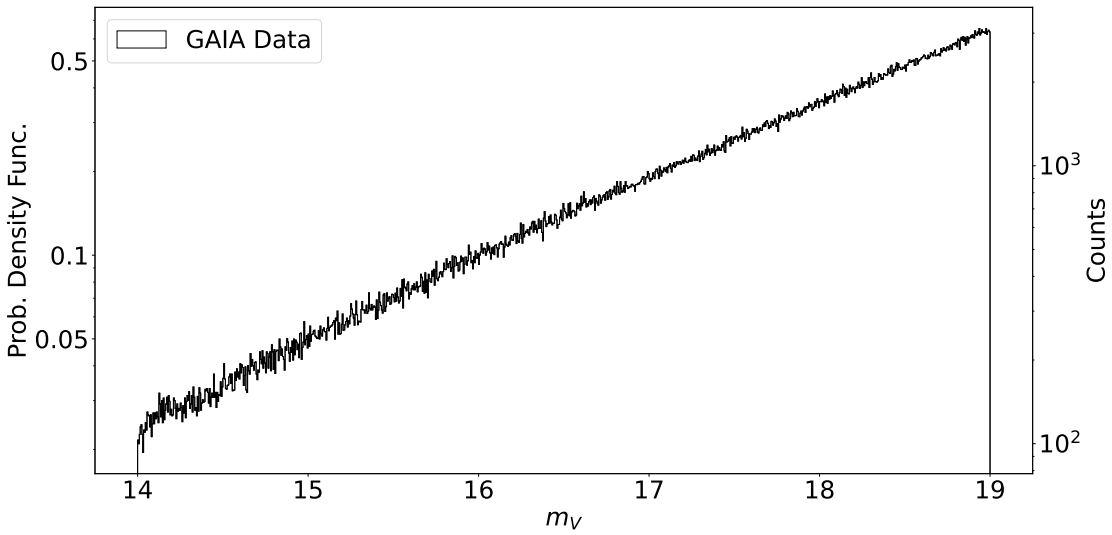

Figure 4.4: Star data obtained from the GAIA Archive. Shown is the histogram of the number of stars at varying magnitudes, with 1000 bins in the magnitude range $\approx 14 < m_V < 19$.

This data is used to create a function for the number of stars vs. a given magnitude. A probability density function is also calculated for the histogram shown using the Matplotlib library of Python. This is used to predict how many of each magnitude would be present in a 100,000 stellar object set. It should be noted that the magnitudes provided in Tables 4.3 to 4.5 do not directly correspond to the magnitudes simulated in subsequent Sections. To approximate the limiting magnitudes for different exposure times, additional KSIM simulations were conducted to determine the magnitudes achievable with varying exposure times. KSIM simulations were run to determine the required exposure times for an SNR>5, for 60, 80, and 100cm telescopes. The results of this are shown in Table 4.6. These values were then interpolated using SciPy for any magnitudes which lay between the data points shown.

With the exposure times required for the varying telescopes in SuperSmart and the calculated number of objects to observe, a simulation of the survey observation of 100,000 objects was conducted using these KSIM results. This simulation configured a desired number of telescopes, and when they were ready, i.e., not ob-

Table 4.6: KSIM rerun simulations to determine exposure times in seconds for the telescope diameters 60, 80, and 100cm at m_V 14-19, with an SNR>5.

m_V	Exposure time (s)		
	100cm	80cm	60cm
19	3200	5000	9000
18	1031	1611	2900
17	391	611	1100
16	146	228	410
15	57	89	160
14	23	36	64

serving an object, one of a particular magnitude was assigned to each telescope. The object was randomly assigned based on the probability density function created using GAIA star data, as shown in Fig. 4.4. The time required to observe each assigned object was tracked until completion, at which point the telescope was set to 'ready' for a new assignment. The total time taken for all objects to be observed was tracked and then converted into the number of nights required. An outline of this process is shown in Fig. 4.5. It is noted that certain error sources were not included in detail because they were outside the scope of this initial concept simulation. These include effects such as the residual atmospheric dispersion and fibre coupling efficiency. These error sources can be explored in more detail with a purpose built simulation instead. As with the simulations in Chapter 3, error sources such as the loss from the optics involved are considered.

4.4.2.2 Results

Considering the GAIA follow-up survey of approximately 100,000 stars with magnitudes $\approx 14 < m_V < 19$. For the estimation as discussed in Sec. 4.4.2.1, an average of 8 hours was assumed for observations in a single night, a movement time of 30s between objects was used, and all objects had magnitudes assigned to them from the probability density function shown previously.

Different total effective diameter SuperSmarts were simulated to determine the

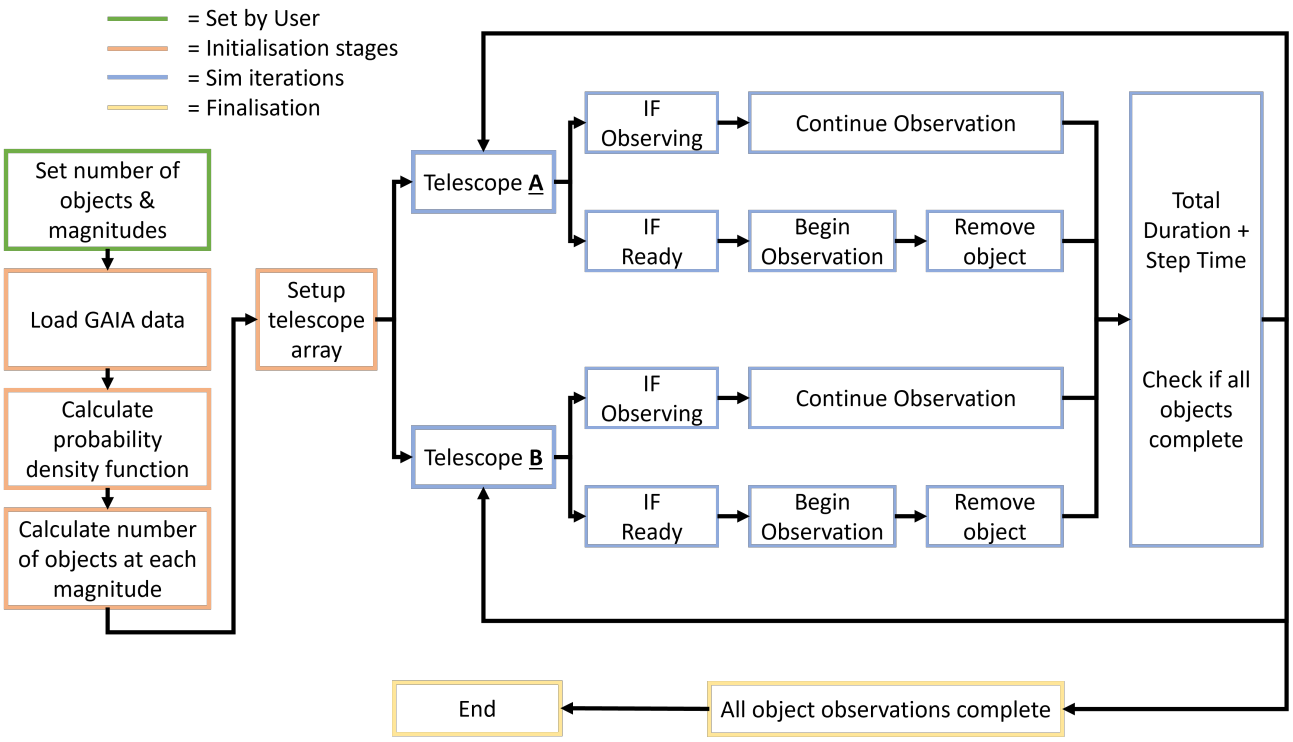

Figure 4.5: A block diagram of the Survery simulation used to determine the number of nights required for a SuperSmart design to observe a set number of objects. The observation durations were set by previously determined exposure times from KSIM. Two telescopes (A and B) are shown here as an example but this can be any number of telescopes.

number of nights required, using the simulation outlined in the previous Section. These SuperSmarts consisted of varying amounts of 0.6m telescopes, from 17 (2.0m effective diameter) to 69 (4.0m effective diameter). Fig. 4.6 contains the results of the simulations.

As expected, the number of nights required decreases with a higher total effective diameter. This was also simulated with the telescopes all acting independently, a key feature of any SuperSmart design. The benefit of this approach is that, for example, with a 4.0m effective diameter, the number of nights required was 190. However, when the telescopes were also set to wait for all telescopes in the array to finish their current observation, having more similarity to a traditional telescope and spectrograph. Here the number of nights more than doubled, increasing to 477 nights.

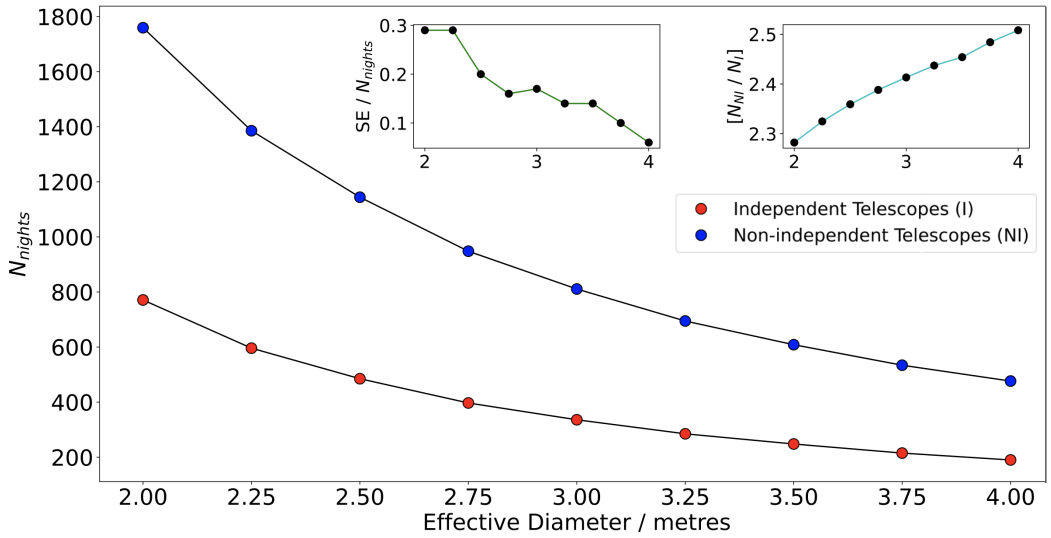

Figure 4.6: Number of nights (N_{nights}) required to observe the 100,000 object set, with varying effective diameter. The left inset contains the standard error with units of number of nights. The right inset shows the ratio of the number of nights required by a set of non-independent telescopes to the nights required by a set of independent telescopes (N_{NI}/N_I).

The other diameters were also tested with non-independence. The simulation was used to represent how a single larger telescope of diameter 2.0-4.0m with many fibres would operate, where to move the single telescope all of the fibres would need to finish their observation. These are displayed in Fig. 4.6, along with the standard error of the simulations and the ratio of the non-independent number of nights to the independent number of nights. This ratio illustrates how the gains evolve, with the benefit of using them independently increasing as the number of telescopes grows.

Because of the random assignment of objects, the calculated number of nights varied slightly in each simulation, typically by approximately one night. To determine the mean average of the required number of nights, we conducted ten repetitions for each diameter. We then calculated the mean average and determined the standard error. This repetition process was not applied to the independent telescopes simulation because, as all objects would be observed independently, the order of selection for faint objects did not impact the results.

As shown in the left inset of Fig. 4.6, the error in the average number of nights was found to be negligible when compared to the actual values of the number of nights, even at its highest value of 0.29 for the lowest number of telescopes, which was 17. Fig. 4.6 also indicates that increasing the number of telescopes reduces this error. Despite the larger number of telescopes being restricted to the longest exposure, the increased number of observations at once still leads to an improved spread in the resulting number of nights.

4.4.3 LISA sources

As discussed in Section 4.2, UCBs play a crucial role in the context of LISA. In this analysis, we consider two magnitudes: the faintest magnitude of the UCBs described in Kupfer et al. (2018) and Section 3.6, which is approximately 24, and the magnitude of the double white dwarf binary system ZTF J153932.16+502738.8 described in Burdge et al. (2019), which is $\approx$ 20.4 at a wavelength of $\approx$ 467nm. Due to the faintness of these objects, we reran KSIM simulations to provide a more accurate prediction of SuperSmart's potential performance.

The reran limiting magnitudes at 538nm were used for comparison with a magnitude of 24. To observe a system with a magnitude of 24 at a medium spectral resolving power in a single night, it would be necessary to combine enough telescopes to form an effective telescope diameter greater than 4m. Specifically, a 2m effective diameter telescope would only be capable of observing an object with a magnitude of 22.1 at SNR>5 within a single night, assuming a spectral resolving power of 6000. However, if the spectral resolving power is rebinned to 1420, as described in Section 3.6, a 2m effective diameter telescope could observe an object with a magnitude of approximately 22.7. Lastly, a single 0.8m telescope, when rebinned to a spectral resolving power of 1420, could reach a magnitude of approximately 21.6 within an 8-hour night.

In a single 8-hour observing night, a SuperSmart with a total 4m effective diameter

could reach magnitudes of approximately 22.9 at a spectral resolving power of 6000. However, if the spectral resolving power is rebinned to 1420, the limiting magnitude improves to approximately 23.5.

To observe an object with magnitude $m = 24$ and SNR>5, a 4m effective diameter SuperSmart would require 18 hours, or 2.3 nights. This would still be straightforward with SuperSmart because multiple exposures across nights can be binned together owing to the MKID's lack of read noise and photon counting capabilities.

For ZTF J153932.16+502738.8, with a magnitude of approximately 20.4 at $\approx$ 467nm, this object could be observed even with a single 0.6m telescope when rebinned to lower spectral resolving powers. Using the limiting magnitude of 18.3 in 1 hour at 484nm at medium spectral resolving power, when rebinned to a spectral resolving power of 1420, it would take almost an entire night, specifically 6 hours, to achieve an SNR>5. Alternatively, a 2m effective diameter telescope would be able to observe ZTF J153932.16+502738.8 for an SNR>5 at medium spectral resolution in 1.7 hours. With a 4m effective diameter telescope, it would take 1200s at medium spectral resolution, less than the hour required as shown in Table 4.3.

To achieve the required 9s exposures with SNR>5 for this particular system, approximately 15 hours of observation would be required. Alternatively, considering the exposure time requirement discussed in Table 4.2, observing HM Cnc instead, which has $m_B = 20.7$. For phase bins of 7s with SNR>5 with a 4m effective diameter SuperSmart, approximately 24 hours of observation would be required, but is achievable with the same capabilities mentioned for the Burdge et al. (2019) system. This would give 47 points throughout the orbit of these systems, which would reduce the error of subsequent fits of the system's S-wave. In reality this number of points may even be reduced because the orbital phase itself can be used to rebin the exposure into desired phase bins, from the MKID time stream.

4.5 Telescope Design Cost Estimation

The cost of using a large number of telescopes is now an important consideration. For 35 0.6m telescopes when all telescopes are combined, they would have an effective diameter of 2.9m. The cost of these telescopes would amount to €3.7 million. In contrast, using 20 0.8m telescopes would also result in a total effective diameter of 2.9m and cost €4.5 million for the telescopes. Thus, for a larger total effective diameter, combining 60cm telescopes is more cost-effective than using 80cm diameter telescopes.

To further illustrate this telescope cost efficiency, the area per cost of just the individual telescopes can be used as a metric. The 0.8m telescopes have an efficiency of $1.4\text{mm}^2/€$, whereas the 0.6m telescopes have an efficiency of $1.8\text{mm}^2/€$. This indicates that the 0.6m telescopes offer improved cost efficiency compared to the 0.8m telescopes, as observed above.

Using 13 1m would also result in an effective diameter of 2.9m. The total cost for these telescopes would amount to €7.1 million, with a cost efficiency of $0.9\text{mm}^2/€$. This cost efficiency here is half that of the 0.6m telescope. However, the number of dilution refrigerators required may also negatively impact some cost efficiencies when they are considered. Fig. 4.7 illustrates the cost to total effective diameter when using multiple of the same telescope.

SuperSmart could however, be a combination of different-sized telescopes. For example, by using 15 0.6m telescopes, 7 0.8m telescopes, and 3 1m telescopes, the total telescope cost for this combination would amount to €4.8 million, with a cost efficiency of $1.4\text{mm}^2/€$. This combination of telescopes would also result in an effective diameter of 2.9m. To reach an effective diameter of 3.6m with a cost efficiency of $1.4\text{mm}^2/€$, 23 0.6m telescopes, 11 0.8m telescopes, and 5 1m telescopes would be required. These setups would have a cost efficiency the same as using only 0.8m telescopes, also with the same number of dilution refrigerators for an

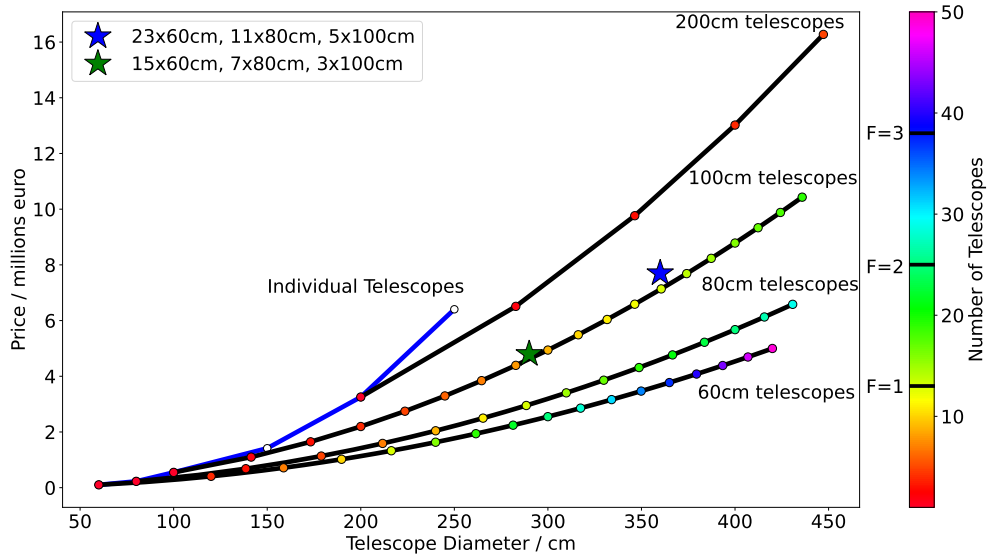

Figure 4.7: Cost of varying telescope sizes and amounts. The individual telescopes, marked with a blue line, are made up of the increasingly larger size telescopes and their cost from Astrosysteme. All other datasets are made up of one size telescope, but with their size totalled with increasing numbers of them used. The star markers represent the combination of telescopes discussed in this Section. The black bars on the colourbar indicate the number of dilution refrigerators required, with the number of telescopes underneath each bar representing the number of fridges needed. This was calculated using 2670 MKIDs per linear array, with three linear arrays per telescope.

effective diameter of 2.9m.

4.6 Future Implementation

From these results, it is clear that SuperSmart has the potential to contribute to important science cases. SuperSmart's potential to observe both sets of objects and faint single targets has been demonstrated, with independent telescopes quickly observing survey objects, doubling the rate of observation in comparison to non-independent telescopes. Medium resolution observations of ZTF J153932.16+502738.8 and HM Cnc with the required time resolution of 7s were also seen to be possible. This could be achieved using multiple smaller telescopes together, making up an effective diameter of $\approx$ 4m, and an observation of 24 hours.

To fully maximise SuperSmart's potential in these observing scenarios, the future implementation should focus on a combination of differently sized telescopes. This approach strikes a balance between having a larger total effective diameter, individual telescopes with larger diameters for individual fainter observations, and the cost of the smaller telescopes. When fully combined, this design would also have a sufficiently large effective diameter for the LISA verification systems described in Sec. 4.4.3.

The total cost of implementing 23 0.6m telescopes, 11 0.8m telescopes, and 5 1.0m telescopes would be approximately €8 million, however without an enclosure or the construction costs of the array. If the external scope for simultaneous sky subtraction is desired, this will add an estimate of €250 per scope, and therefore €500 per telescope. This price is used as a guideline from Celestron*. This would add an additional €20,000. Alternatively, by assuming a price of €20,000 to install the fibre pick-off for a single telescope, this would cost €780,000 for 39 telescopes.

Using 3 sets of 2670 MKIDs for a spectral resolving power of 6000 would require a total of 312,390 MKIDs, which could be accommodated in multiple large arrays of MKIDs. One MKID set for science, one for sky subtraction, and one for a comparison object. This would also necessitate up to 4 cryogenic refrigerators. The majority of the cost for the MKIDs would come from the cryogenic refrigerators and the detector readout. by assuming a refrigerator cost of €500,000, the use of the fibre pick-off system, and a per-pixel readout cost of ≈€10 which includes the boards and required HEMT amplifiers (discussed more in Chapter 5), the combination of differently sized telescopes design for SuperSmart would currently cost approximately €14 million, resulting in a total effective diameter telescope of 3.6m.

*https://www.celestron.com/products/c90-mak-spotting-scope

Chapter 5

MKID Operation

The readout of MKID devices broadly involves generating a set of probe signals. These signals are tuned to the resonant frequencies of the MKID devices in the array, forming a 'frequency comb' that is propagated through the devices. They modify their corresponding probe signals depending on the observed photons. Once the probe signals return, they undergo amplification with a cryogenic HEMT and are then digitised outside of the cryostat. The phase and amplitude modulation of the frequency comb are recorded using electronics at room temperature (McHugh et al., 2012).

To generate, send, and receive these signals, a Xilinx ZCU111 board[†] is used. These boards come equipped with 60.5 Mb of memory, 4272 DSP (Digital Signal Processor) slices, 16 33G transceivers responsible for data communication at a rate of up to 33 Gbps, and 371 maximum I/O pins for external connections via digital signals.

However, the resonant frequencies of MKIDs are above the range possible for the Digital-to-Analogue Converters (DACs) and Analogue-to-Digital Converters (ADCs)—the ZCU111, in particular, is equipped with 8 of each. The DAC is responsible for converting the probe signals from digital to analogue, and vice versa for the ADC. To address this limitation, a Local Oscillator (LO) is employed. The

[†] https://www.xilinx.com/products/boards-and-kits/zcu111.html#information

LO generates a continuous microwave tone frequency that closely matches the resonant frequencies of the MKID devices. This LO signal is then multiplied by a 'baseband' signal, which operates within the working range of the DAC and ADC. Each baseband signal for each device comprises two waveforms: a sine wave at the resonant frequency of the MKID minus the LO frequency (I=in-phase), and a similar wave shifted -90 degrees out of phase (Q=quadrature) (McHugh et al., 2012).

After the converted probe signal has traversed the MKID and amplifiers, it is then returned to its baseband form using the ADC. Once the data has been digitised by the ADC, the frequency comb must be separated into individual tones, a process referred to as channelisation. The bandwidth of the frequency comb is divided into equally sized bins. For each tone in the frequency comb, a low-pass filter is applied to isolate the individual tones and a narrow bandwidth around the tone frequencies (Strader, 2016). The result of the channelisation step is a complex signal of (I,Q). Fig. 5.1, as depicted in Strader (2016), provides an overview of this channelisation process.

The IQ data is then initially used to characterise the MKID. This is achieved by altering the frequency of the sent probe signal to generate the device's IQ loop. A basic outline of this readout process is shown in Fig. 5.2, with an example IQ loop. Once the IQ loop is characterised, photon data can be collected. This photon data can be used to determine the R_E of the device by exposing it to a monochromatic source. As discussed in Chapter 3, the R_E defines how many spectral orders an MKID can separate, and characterising this value determines design aspects of a constructed KIDSpec, such as the Prototype shown in Chapter 6. In this chapter, these characterisation steps will be described in more detail.

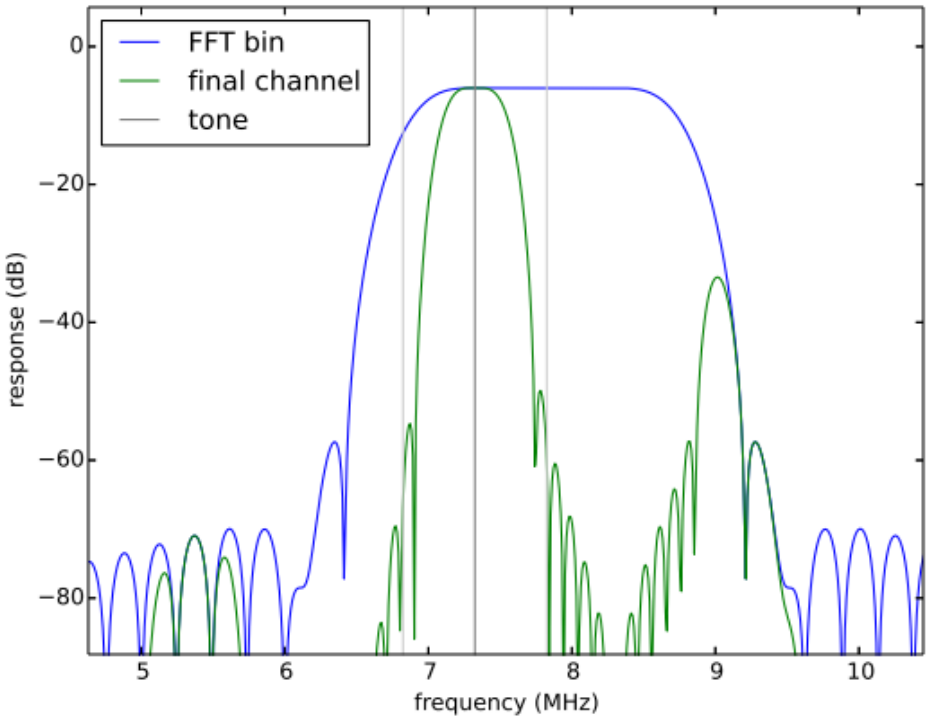

Figure 5.1: Shown from Strader (2016) is an example of the channelisation process, which separates the frequency comb into its individual tones. One of the equally sized bins in the first stage of channelisation is labelled as the Fast-Fourier Transform (FFT) bin. The 'final channel' is the result of the second stage, where the individual tone is constrained using a low-pass filter.

5.1 Device Readout

5.1.1 Overview

As described above for readout, a microwave signal passes through the MKID. The frequency comb itself is generated by the Xilinx ZCU111 board, which then sends the signal into a BlueFors cryogenic refrigerator, as shown in Fig. 5.3. Here, as described in Chapter 2, photon events cause the resonant frequency to shift, moving the resonance to a lower frequency and making the resonance dip shallower and broader. This, in turn, alters the amplitude and phase of the microwave signal (Day et al., 2003). The data received from the Xilinx board after the signal returns is in the form of points in the IQ plane, provided in arbitrary units.

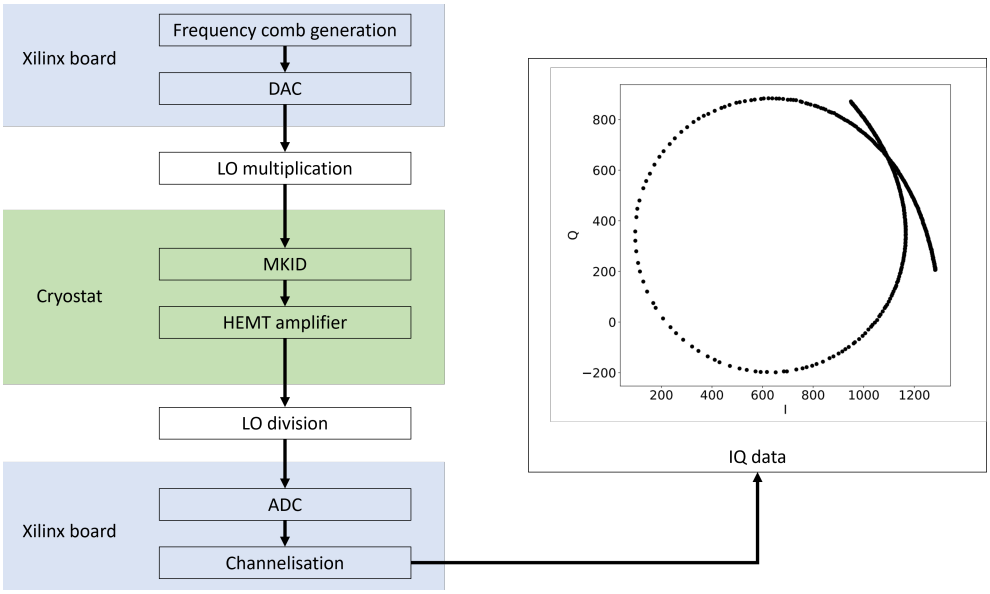

Figure 5.2: The outline of the MKID readout process from frequency comb generation to the IQ data generation. The IQ data shown in the figure is the result of altering the probe signal frequency to a single MKID, thereby generating this loop. The resonant frequency is the portion of the loop pointed at the IQ origin.

Figure 5.3: **Left** shows a BlueFors dilution refrigerator. Achieves sub-Kelvin temperatures by pumping liquid helium throughout the system to cool the MKID, as described in Sec. 2.3. **Right** shows the Xilinx board used to generate and receive the microwave tones used for reading out the MKID devices.

The following sections are responsible for analysing the data received from the readout Xilinx board. To be able to use the MKID devices for science with the layout described here, two essential characteristics are required: the center of the IQ loop and the resonant frequency of the device.

5.1.2 IQ Loop Fitting

The IQ loop centre and naturally the resonant frequency are vital for using an MKID device for science. When a photon strikes an MKID, the effect of this on the IQ loop is that the resonant frequency moves along the loop. The angle at which the resonant frequency moves around the loop describes the energy of the photon. To determine this angle the centre of the IQ loop is required for the readout used in this thesis. To generate the IQ loop, a range of frequencies surrounding the resonant frequency must be sampled. An example IQ loop from an Al-based MKID device from De Visser et al. (2021) with a resonant frequency of 4.25 GHz, sampled with +/- 1 MHz, is shown in Fig. 5.4. To characterise the loop itself for the central coordinates, a Least-Squares Approximation is used. This assumes that the loop is a circle; however, if the loop is not a circle, the response due to photons is no longer linear. If the MKID's response is not linear, it causes the photon event analysis to be less trivial and requires a more complex wavelength calibration. This non-linearity is due to the IQ loop becoming an ellipse or even bifurcating, which means that the shape cannot effectively track the changes caused by the photons.

The IQ points are first trimmed to remove the tails on either end of the loop, leaving only the loop itself. This is shown in Fig. 5.5. The Least-Squares Approximation begins with the equation of the circle, given by Eq. 5.1,

$$(I - I_c)^2 + (Q - Q_c)^2 = r^2 \tag{5.1}$$

where I_c and Q_c are the centre coordinates of the circle, r is the radius of the circle, and I and Q are the IQ coordinates of the loop. Eq. 5.1 can then be expanded to,

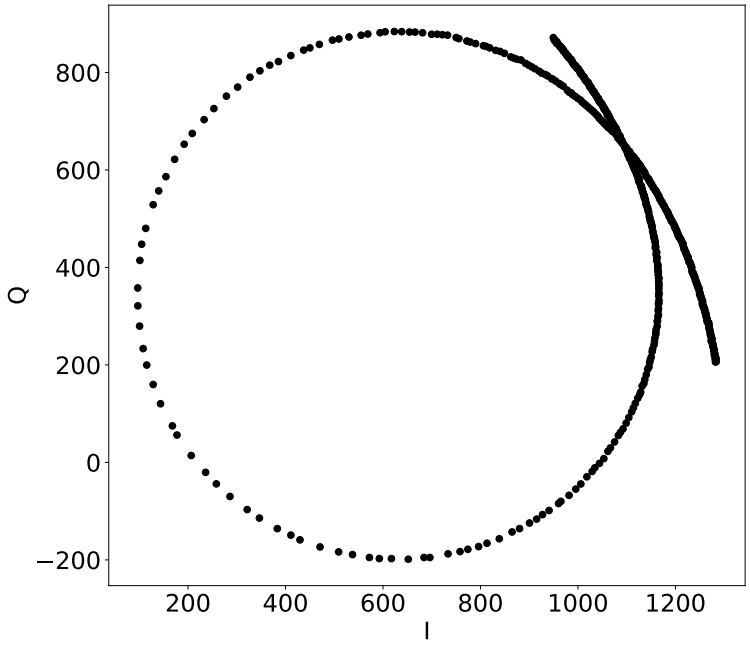

Figure 5.4: An IQ loop measured of an Al MKID, with the probe signal sweeping in frequency from $\approx 4.249 - 4.251$ GHz. Each point represents a frequency in this range. At each frequency 256 readings of I and Q are taken, and then mean averaged. The tone power used was -46dBm.

$$2II_c + 2QQ_c + r^2 - I_c^2 - Q_c^2 = I^2 + Q^2. \tag{5.2}$$

Here new variables a, b, and c are introduced, with definitions,

$$\begin{aligned} a &= 2I_c \\ b &= 2Q_c \\ c &= r^2 - I_c^2 - Q_c^2. \end{aligned} \tag{5.3}$$

Now the loops points can be written in matrix form as,

$$\begin{bmatrix} I_1 & Q_1 & 1 \\ I_2 & Q_2 & 1 \\ \dots & \dots & \dots \\ I_n & Q_n & 1 \end{bmatrix} \cdot \begin{bmatrix} a \\ b \\ c \end{bmatrix} = \begin{bmatrix} I_1^2 + Q_1^2 \\ I_2^2 + Q_2^2 \\ \dots \\ I_n^2 + Q_n^2 \end{bmatrix}. \tag{5.4}$$

From this the loop points can now be given by,

$$A \cdot X = B \tag{5.5}$$

where,

$$A = \begin{bmatrix} I_1 & Q_1 & 1 \\ I_2 & Q_2 & 1 \\ \dots & \dots & \dots \\ I_n & Q_n & 1 \end{bmatrix}, X = \begin{bmatrix} a \\ b \\ c \end{bmatrix}, B = \begin{bmatrix} I_1^2 + Q_1^2 \\ I_2^2 + Q_2^2 \\ \dots \\ I_n^2 + Q_n^2 \end{bmatrix}. \tag{5.6}$$

Following this X can be calculated using,

$$X = A^+ \cdot B \tag{5.7}$$

where A^+ is the Moore-Penrose inverse of A. This can be calculated using A^T, the transpose of A,

$$A^+ = (A \cdot A^T)^{-1} A^T. \tag{5.8}$$

From the found X, all that remains is to find the coordinates of the centre and the radius of the IQ loop as follows,

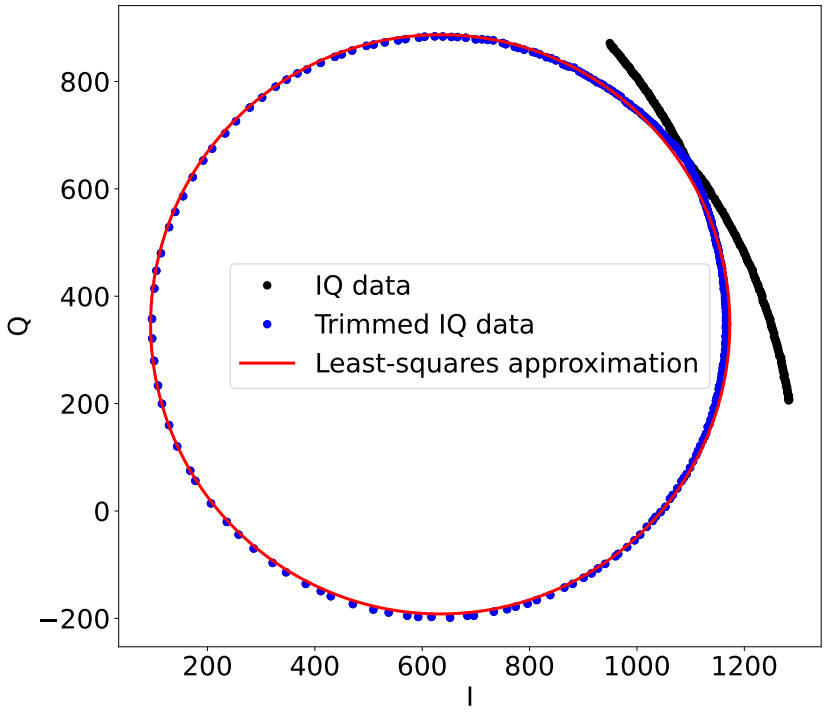

Figure 5.5: An IQ loop from an Al MKID. The IQ loop is the loop shown in Fig. 5.4. The blue points are the trimmed IQ data points which are used for characterisation. The least-squares approximation used to characterise the loop for the centre coordinates and radius is shown, resulting in central coordinates of (634,348) and a radius of 539.

$$\begin{aligned} I_c &= \frac{a}{2} \\ Q_c &= \frac{b}{2} \\ r &= \frac{\sqrt{4c + a^2 + b^2}}{2}. \end{aligned} \tag{5.9}$$

Fig. 5.5 shows a characterisation of the loop using this method (Chernov and Lesort, 2005). This method gave values for I_c, Q_c, and r of 634, 348, and 539 respectively for Fig. 5.5.

Moving on to determining the resonant frequency, when analysing the magnitude of the IQ points ($|S_{21}|$), a dip appears, as shown in the example in Fig. 5.6. At this

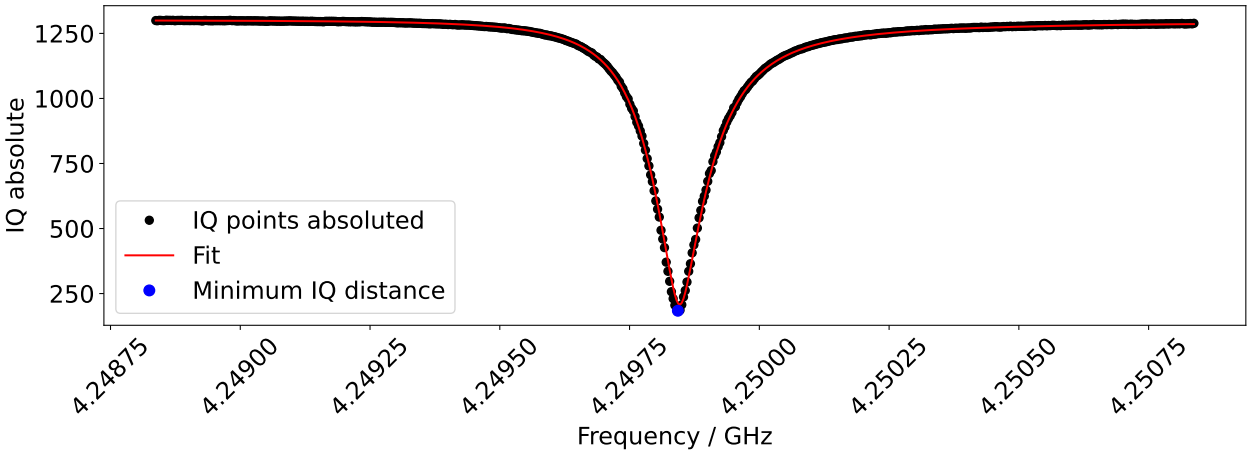

Figure 5.6: The resonance dip, obtained by taking the absolute values of the IQ points shown in Fig. 5.4, was fitted using the method described in Gao (2008). The primary goal was to find the frequency of the resonance dip. The blue point in the plot represents the absoluted IQ point with the shortest distance to the origin, thus providing the estimated resonant frequency. In this case, the resonance was found to be at 4.24985 GHz using both methods.

point, there are two options to consider. The first option is to infer the resonant frequency from the loop itself, while the second option is to fit the resonance dip.

To infer the resonant frequency from the IQ points, the distance of each IQ point to the origin is calculated. Based on the shape of the resonance dip, the IQ point with the shortest distance to the origin is identified as the minimum of the resonance dip. This provides the estimated resonant frequency because each IQ point corresponds to a known frequency, which was set before beginning the frequency sweep.

The second option involves fitting the resonant dip using Eq. 5.10 from Gao (2008),

$$S_{21}(f) = ae^{-2\pi jf\tau}\left[1 - \frac{Q_r/Q_c e^{j\psi_0}}{1 + 2jQ\frac{f-f_r}{f_r}}\right] \tag{5.10}$$

where S_{21} represents the complex transmission through the readout system, a is a complex constant representing the gain and phase shift through the system, τ represents the electronics delay, Q_r is the resonator quality factor, Q_c the coupling quality factor, Q the quality factor of the resonant circuit, f are the sampled frequencies, f_r is the resonant frequency, and ψ_0 is the rotation angle with respect

to the origin. The magnitude of S_{21} has the form of the dip shown in Fig. 5.6. The parameters shown in Eq. 5.10 are fitted using Python. The resulting fit is also shown in Fig. 5.6, with a fitted resonant frequency of 4.24985 GHz. This fit was computed for the same IQ points shown in Fig. 5.5.

The first method using the IQ points only requires the IQ loop and is faster in computation time than the fitting method. However, if extra parameters about the device or a more accurate estimate of the resonant frequency are desired, then the fitting can be used instead, as the IQ points on their own give a fast estimate of the resonant frequency.

5.2 Characterisation and Calibration

5.2.1 Power Sweep

Before being used for science, the MKID device must undergo a power sweep to find the ideal power to give the tone sent to the MKID. This is necessary to maximize the signal-to-noise ratio without applying so much power that the IQ loop appears distorted or bifurcates (Mazin, 2004).

Bifurcation is an issue because it prevents the MKID device's response to photons from being observable along the IQ loop. The distortion of the IQ loop occurs when the driving power of the probe signal, set by the readout, exceeds the power handling capacity of the superconducting transmission line, which is what couples the incoming photons to the MKID device (Mazin, 2004). For the devices used here from SRON, the power range was swept from -60 to -40 dBm. Fig. 5.7 shows IQ loops with increasing power from the same MKID device.

Initially, for each power, the IQ loop is characterised following the method shown in Sec. 5.1.2. An ellipse is also applied to the IQ data using a similar method to the one used in Sec. 5.1.2 for a circle, and the eccentricity of the ellipse is then

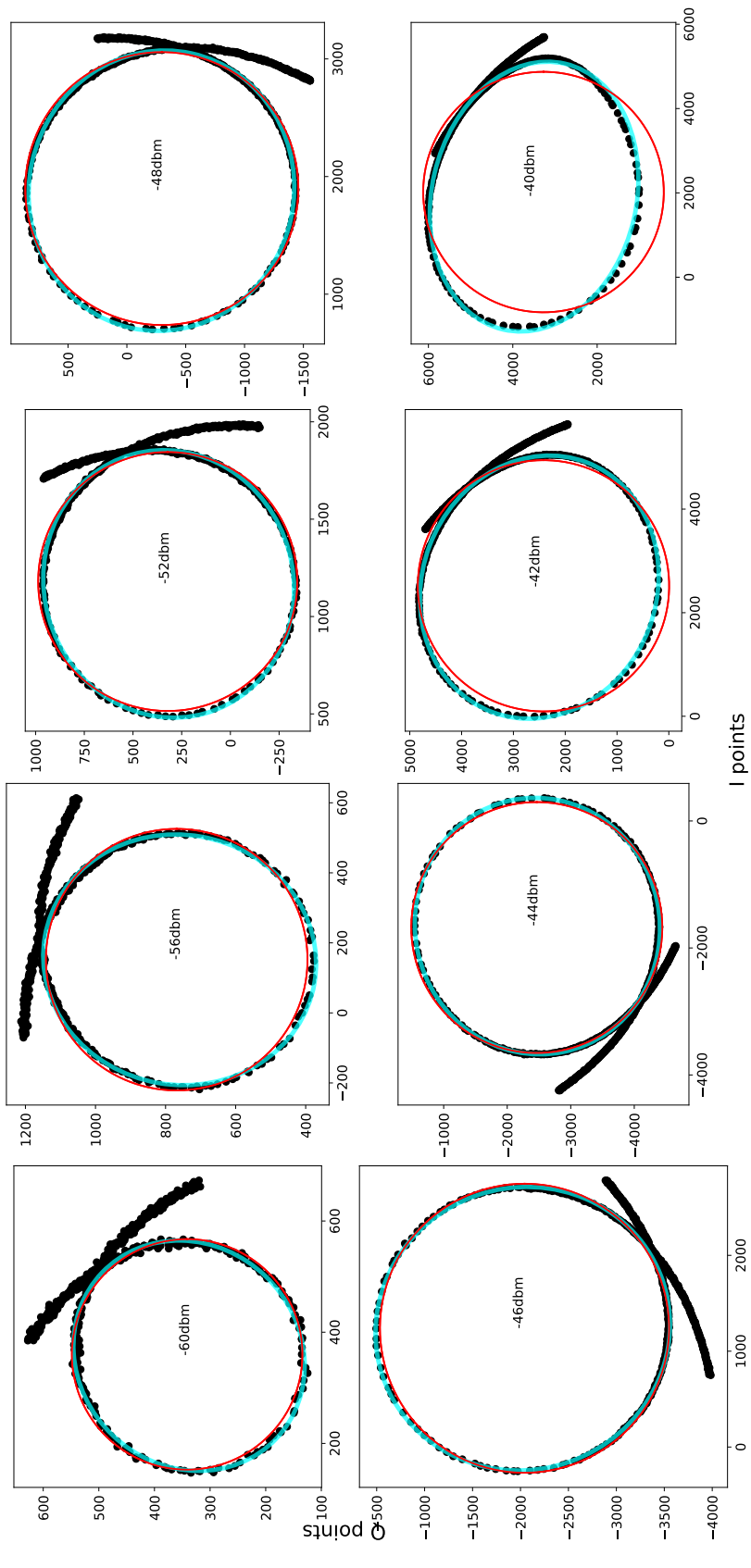

Figure 5.7: IQ loop fits for all frequency sweeps measured at increasing tone powers. In each plot, the black points represent the IQ data, the red line is the circle approximation described in Sec. 5.1.2, and the cyan line is an ellipse approximation computed similarly to the method in Sec. 5.1.2. As the tone power increases, the elliptical shape begins to form, as seen in the **Bottom Middle Right** panel, and in the **Bottom Right** panel, it has become an ellipse, so the circle shape no longer represents the loop. In a clockwise direction from the **Top Left** panel, the ellipse eccentricities were 0.44, 0.44, 0.38, 0.34, 0.30, 0.31, 0.54, and 0.66.

determined, which defines how elliptical the shape is. Eq. 5.11 and 5.12 defines the ellipse,

$$1 = \frac{I^2}{a^2} + \frac{Q^2}{b^2} \tag{5.11}$$

$$e = \sqrt{1 - \frac{b^2}{a^2}} \tag{5.12}$$

where a and b correspond to the width and height of the ellipse respectively, and e is the ellipse eccentricity. From Fig. 5.7, the eccentricities for the powers -60, -56, -52, -48, -46, -44, -42, and -40 dBm were 0.44, 0.44, 0.38, 0.34, 0.30, 0.31, 0.54, and 0.66, respectively. To calibrate the device used in this work the power -46 dBm was chosen as the optimum power due to it having the lowest eccentricity before the higher powers began experiencing greater eccentricities. Additionally, for the lower powers tested, the loops appear noisier, potentially contributing to the deformation of the IQ loop circle. As the signal power is increased, the SNR clearly increases, due to the loops appearing less noisy with higher power. For simplicity, the eccentricity is not used in subsequent sections, and a circle is assumed. While the loop does not bifurcate and the device is properly calibrated to understand it's phase response to photons, then the eccentricity will not affect future data taken. In addition the power of the probe signal used to propagate through the MKID must not be changed.

5.2.2 Photon Event Fitting

With the IQ loop centre and resonant frequency characterised, the incoming IQ data points from a photon exposure can be converted to a phase time stream in units of degrees. This is done by computing the angle of the IQ points on the loop with respect to the loop centre. This stream can then be analysed for photon events.

An example of this stream is shown in Fig. 5.8, with the IQ points from which the phase time stream originated. This phase stream had 633nm photons incident on the MKID during its recording, causing a change in the amplitude and phase of the probe signal. As a result, the IQ points appear to shift around the loop, as illustrated in the IQ data in Fig. 5.8. In a phase time stream, photons manifest as phase value peaks, as seen in the right panel of Fig. 5.8. This is due to photons causing the IQ points to shift around the loop, altering their angle relative to the centre of the IQ loop.

Because a monochromatic source was used for the data in Fig. 5.8, the heights of the phase peaks should be quite uniform. However, phase heights of approximately 92 and 98 degrees can be seen. This is due to photons arriving very closely together in time, causing photon peaks to coincide with the 'tail' of previous phase peak events. This results in a higher phase change that may not represent a separate photon event. An example of this and a single photon event is shown in Fig. 5.9. To avoid these events compromising the data by showing incorrect phase peak heights, the events are fitted, and events with poor fits are filtered.

A small MKID detector, consisting of four MKID devices from SRON in the Netherlands, as shown in De Visser et al. (2021), was used during the work in this thesis. Initially, a threshold in the phase is used to sort any potential photons. The threshold is set up by taking the mean average of a dark phase time stream, i.e., no photons exposed onto the MKID. This threshold does not require the utmost accuracy, as the photon event fitting procedure filters out any non-events. The standard deviation of this mean average is then used to determine the threshold.

Fig. 5.10 shows a phase time stream taken when the MKID was exposed to photons with wavelengths of 1000 and 500nm. Using the calculated average dark phase, the standard deviations of the phase were also calculated, resulting in the bold bars seen in Fig. 5.10. The threshold can then be set to a desired number of standard deviations above the mean average of the phase time stream. This does introduce a trade off where some low energy photons may be lost, to reduce the number of

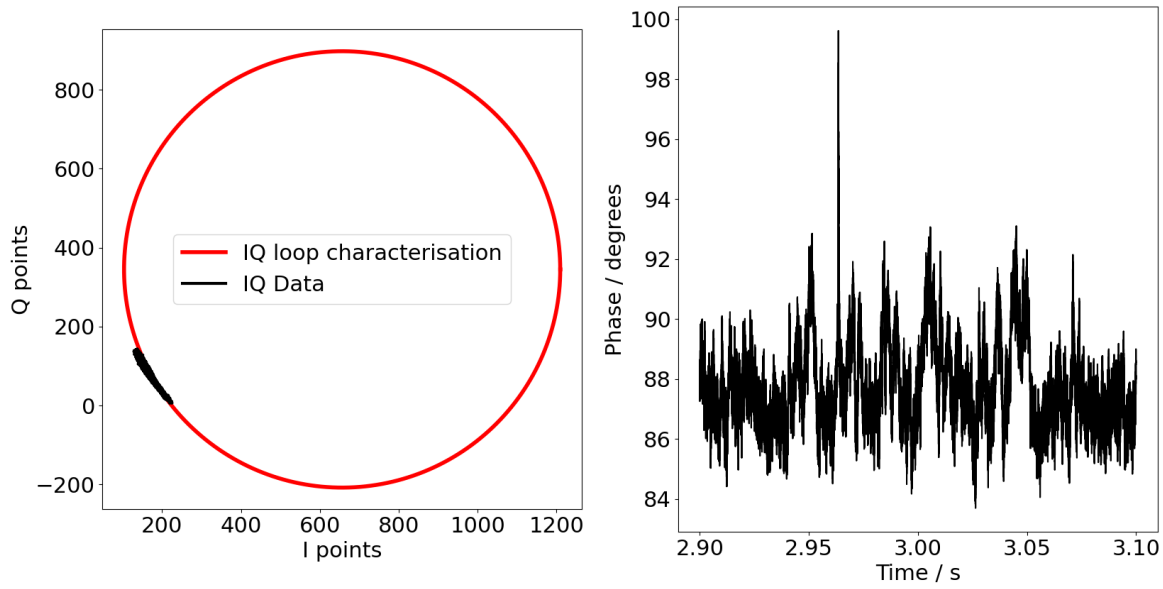

Figure 5.8: **Left** contains the IQ points from an 8s exposure using an Al-based MKID when exposed to a 633 nm source. Included is the IQ loop characterisation for this device taken before this exposure, using a tone power of -46 dBm at 4.250 GHz. **Right** shows a section in time of the phase time stream for this exposure from these IQ points shown. The peaks within the phase time stream are due to photons from the 633 nm source used. The peak reaching ≈ 100 degrees may be random noise from the electronics, as it fades too rapidly to likely be a photon event. It also is too great a reaction in phase for a single photon event.

overall photon candidates computed, because this is a process that could have the length of hours for a simply 8 second exposure. From Fig. 5.10, 4σ was used to filter out as much noise as possible while still retaining potential photon events. Once the potential events have been filtered out of the phase time stream, a section of phase approximately 300 μs before each event and approximately 800 μs after the event is used for fitting. This section is shown in Fig. 5.11.

An exponential decay is used to fit this section of data using,

$$\theta = \begin{cases} \gamma \times \exp\left(-\frac{t}{\tau}\right), & \text{if } t \geq t_{event} \\ 0, & \text{otherwise} \end{cases} \tag{5.13}$$

where θ is the phase in degrees, γ is the height of the phase peak, t_{event} is the time

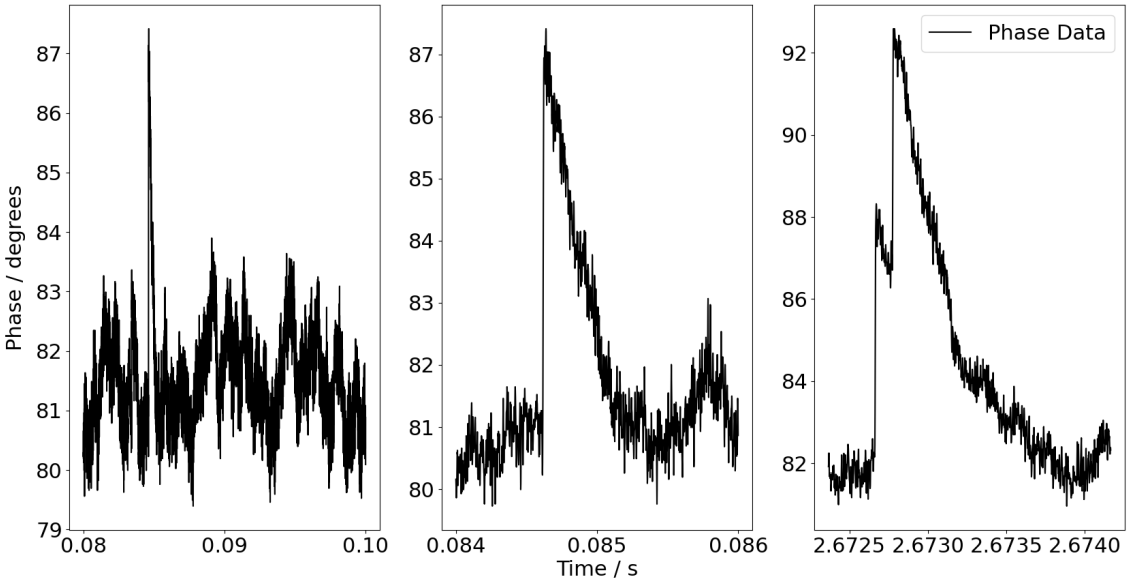

Figure 5.9: **Left** contains a mostly photon-less or 'dark' 0.02s portion of a phase time stream, but with a single photon event at ≈ 0.085 seconds. **Middle** is the zoom-in of this single photon event, an example of how photons appear in the MKID data. **Right** shows an example of when two photon events arrive within a short amount of time, on the order of hundreds of microseconds. The second photon event sits on the phase 'tail' of the first event, resulting in an apparent phase peak of ≈ 92 degrees. This data was from an 8s exposure using an Al-based MKID when exposed to a 633 nm source. A tone power of -46 dBm at 4.250 GHz was used.

of the photon arriving in seconds, t is time in seconds, and τ is the decay constant of the photon event, also in seconds. Eq. 5.13 is then used as the function for fitting using Python, with the phase and time stream data as the inputs. This returns γ, t_{event}, and τ. It should be noted that it is possible to not fit τ when using the MKID. This was not done here because the value of τ had not been determined to an acceptable confidence, and would require more data to understand this. A wide range of τ values were determined from data taken and fitted during this work, and fitting a value that would not affect future data was not within the scope of this work. Because of this the value of τ was fitted for each event to avoid this potential issue. Determining a value for τ for the device in use would however help future science uses of a particular MKID once the value of τ is suitably known,

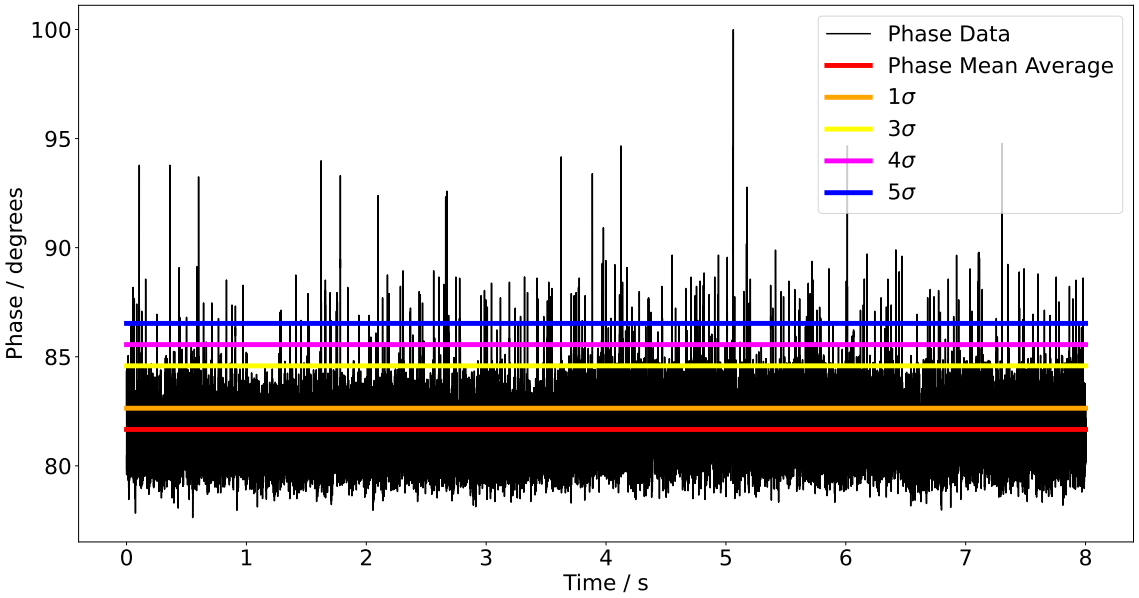

Figure 5.10: A phase time stream taken with the Al-based MKID, when exposed to photons with wavelength 1000 and 500nm. Bold bars are plotted over the phase time stream corresponding to the mean of the phase stream without any potential photon events, and increasing standard deviations of this average. Here 4σ was selected, because it was above the 'dark' phase time stream, and below the visible events.

and reduce computing time for analysis of the phase time stream. An example of a completed fit for an event from the Al-based device described in Sec. 5.1.2 is shown in Fig. 5.11.

With Eq. 5.13, this can then be used to determine how likely it is that the fitted event is as Eq. 5.13 describes. The likelihood is preferred because of factors such as detector and photon noise. Therefore after the fit has been computed, it is passed through a Reduced-Chi Squared filter to ascertain whether the event is likely due to a photon. The noise model used for this is composed of three parts. Two of them are MKID noise sources estimated using Mazin (2004), and the third uses the phase noise to represent the electronics noise. The first noise source is the Fano noise equation (Mazin, 2004),

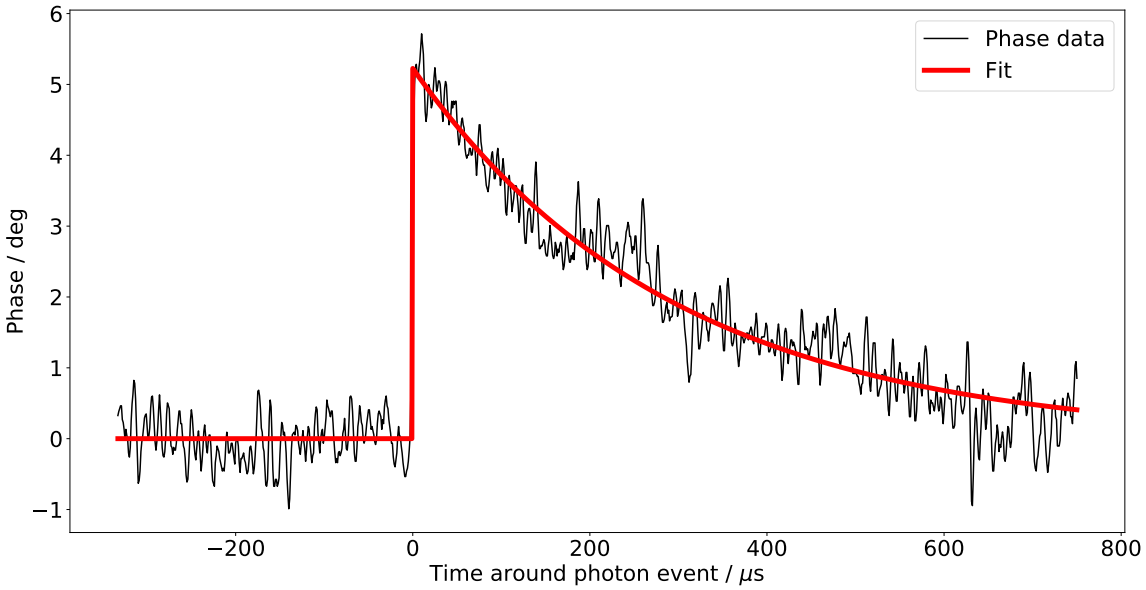

Figure 5.11: A section of a phase time stream containing a $\lambda \approx 1000$nm photon. Measured using an Al MKID at a tone frequency and power of 4.250 GHz and -46 dBm respectively. Overlaid onto the phase stream data is the resulting fit using the method described in Sec. 5.2.2. This resulted in a γ of 5.22 degrees, τ of 294μs, and t_{event} of 0.44s after the start of the exposure.

$$\sigma_N = \sqrt{F\eta h\nu/\Delta} \tag{5.14}$$

where F is the Fano factor, η is the quasiparticle generation efficiency, $h\nu$ is the energy of the incoming photon, and Δ is the gap energy of the superconductor. Fano noise describes the variation in the number of quasiparticles generated when a photon is absorbed by the MKID. However, some of the energy is lost as it is converted to phonons rather than generating quasiparticles, separating Eq. 5.14 from Eq. 2.6. The variance in the generated quasiparticle number, denoted as σ_N, is related not only to the quasiparticle population N_{qp} but also to FN_{qp}, as described in Mazin (2004).

The second noise source is the generation-recombination noise, which is caused by the random generation and recombination of thermal quasiparticles, leading to fluctuations in the kinetic inductance. This noise can be described by,

$$NEP_{gr} = 2\Delta\sqrt{N_{eq}/\tau_{qp}} \tag{5.15}$$

where NEP_{gr} is the noise equivalent power as a result of the generation recombination noise, N_{eq} is the equilibrium number of quasiparticles, and τ_{qp} is the quasiparticle lifetime. Finally, for the third component, a section of the phase time stream data without any potential photon events is taken, and the variance of that section is measured. This phase time stream section, visible in Fig. 5.11, has its continuum removed, and then the phase variance is calculated. These noise sources are then used in a Reduced-Chi Squared test, along with the photon event fit and phase time stream data shown in Fig. 5.11. After the fit has been tested with a Reduced-Chi Squared test, a Pearson Correlation Coefficient test is computed between the fit and data, as described in Sec. 3.6.2. This is done to ensure that the data does not include multiple photon events. If the data does not return a correlation score greater than 0.75, it is discarded. These values that are used are done to ensure that what is observed is indeed statistically a photon, while there is a possibility that some photons are lost, these filters prevent excess noise from tainting science data taken with the MKID.

In summary, each potential photon data segment from the phase time stream is fitted with Eq. 5.13 and subjected to a Reduced-Chi Squared test. If the resulting score is below 2.71, it passes the photon event analysis and is saved. According to Avni (1976), a score of 2.71 corresponds to a 90% confidence level when evaluating one primary parameter of interest, which, in our case, is the photon event phase height. This means that 90% of data repeats with the same height should yield a similar fit.

Several fits of varying Reduced-Chi Squared scores are shown in Fig. 5.12, as a result of 1000nm photons. The bottom-right panel with a Reduced-Chi score of 4.17 appears to have had either a large amount of noise incident or a longer, potentially NIR, wavelength photon incident on the MKID during the tail of the

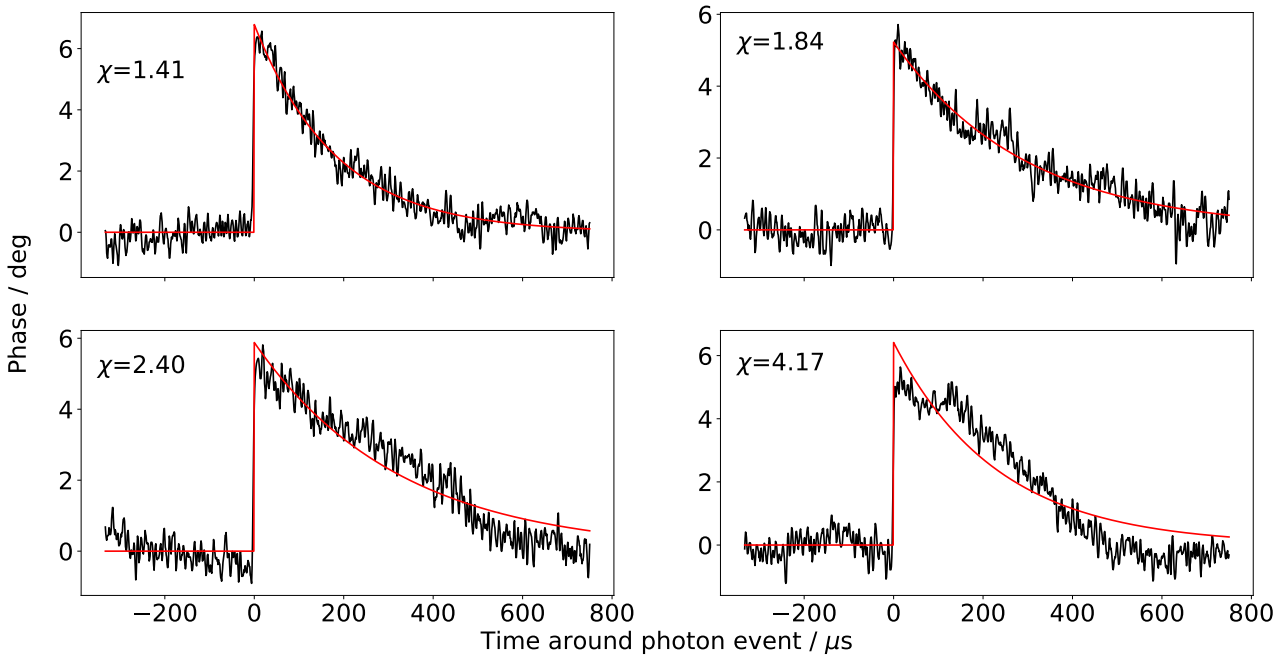

Figure 5.12: ≈ 1000nm photon events measured using an Al MKID at a tone frequency and power of 4.250 GHz and -46 dBm respectively. Each photon event was fitted using the method outlined in Sec. 5.2.2, and then passed through the Reduced-Chi testing described in the same Section. The results of each Reduced-Chi test result is shown in the top left of each panel.

photon event. Because of the Reduced-Chi Squared score exceeding 2.71, this event would be discarded. It appears to resemble a photon, but due to the shape of its decay, its height is non-trivial to determine. From this result, it can be seen how it can be a double photon event, where one photon sits on the tail of another photon event as shown in the right panel of Fig. 5.9, can be filtered out.

Due to the limited number of MKID devices available, the method of fitting the potential photon events is suitable in this context. This is because fitting each potential photon is a slow process, taking approximately 10 minutes for four resonators that may have observed on the order of a thousand photons. If there were a full instrument-level MKID array with tens of thousands of MKIDs, fitting each potential photon would become impractical due to its slowness and computational expense. An alternative approach could involve computing a correlation statistic

on the phase time stream using a photon template. Peaks in this correlation could then be used to extract photon events, significantly reducing computation time.

5.2.3 Determining Device Energy Resolution

R_E is a critical parameter for MKIDs and KIDSpec because it defines how effectively an MKID can determine the energy carried by an incoming photon. As discussed in Section 3.2, R_E for KIDSpec plays a crucial role in determining the number of spectral orders it can separate. To determine R_E, a monochromatic source is exposed to the MKID device. From this exposure, we observe a spread in photon event phase heights, as determined in Section 5.2.2.

When the photon heights are binned into a histogram, this spread takes the approximate form of a Gaussian distribution. To determine the R_E, the mean of the resulting Gaussian is divided by the FWHM (Meeker et al., 2015). This Gaussian is shown in Fig. 5.13, which displays a Gaussian distribution of photon event phase heights, generated from 633nm photons observed by the same Al device used previously and subsequently in this thesis. Potential photons were fitted using the method outlined in Section 5.2.2 and filtered using a Reduced-Chi score of ≤ 2.71. Using 5357 photons, a Gaussian distribution was fitted to a histogram of these photon's phase changes. The calculated mean and standard deviation of the Gaussian resulted in an R_E of 7.19. The appearance of a tail stretching to lower phase changes, as shown in De Visser et al. (2021), is the result of photons striking the MKID in non-inductor areas of the device, causing lower-energy events. This tail is not necessarily the result of lower energy photons being incident on the MKID, which only had 633nm photons exposed onto it (De Visser et al., 2021).

5.3 MKID devices

The MKID devices available throughout this work's duration were Al-based detectors described in De Visser et al. (2021). These are research-grade devices, which

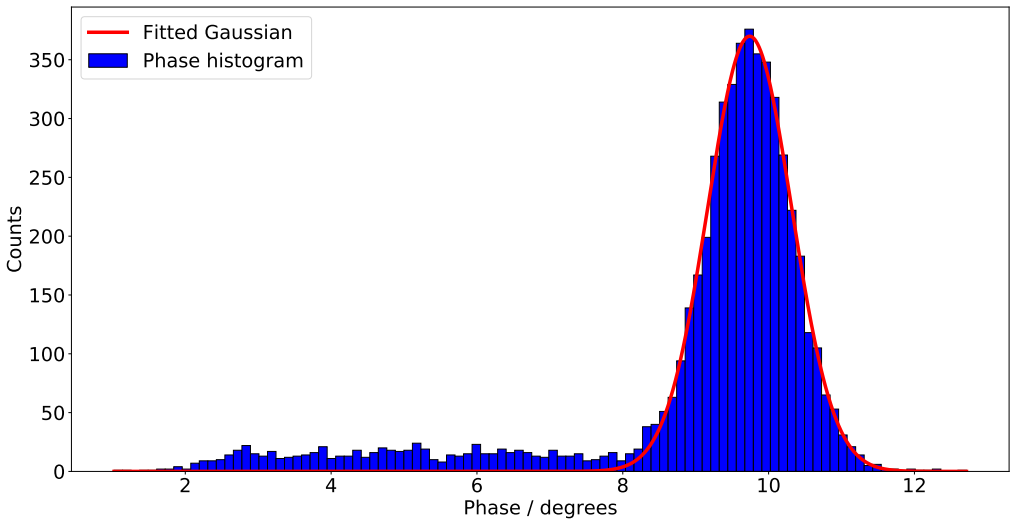

Figure 5.13: The resulting spread of wavelengths from a 633 nm laser exposed onto an Al MKID, with a tone frequency and power of 4.250 GHz and -46 dBm respectively. Each potential photons was fitted using the method in Sec. 5.2.2, and then filtered for events with a Reduced-Chi Score of ≤ 2.71. With a total of 5357 photons this resulted in an of $R_E = 7.19$.

had higher R_E values owing to a membrane used to trap phonons caused by photon absorption.

These devices cannot be fabricated into large arrays due to their architecture and design, as the silicon nitride membrane increases the fabrication time for a large array. Additionally, the use of aluminium makes the devices highly reflective in the optical, has a small area with respect to the whole device, and has low kinetic inductance, making it difficult to fabricate an MKID array with a high QE on the order of thousands or hundreds of thousands (De Visser et al., 2021; Zobrist et al., 2022).

The value of the R_E for these devices is ≈ 40 at 986nm and is also capable of $R_E \approx 52$ at 400nm. The R_E of these devices do not follow Eq. 2.6 due to them not being entirely governed by Fano statistics, due to phonon losses still occurring. As seen in Sec. 5.2.3, their maximum R_E was unable to be reproduced due to differences in readout and cryogenic refrigerator setup, such as not having a magnetic shield

for the MKIDs (De Visser et al., 2021).

Chapter 6

KIDSpec Prototype

6.1 Overview

To demonstrate the MKIDs benefit to a spectrograph, the KIDSpec Prototype was created, intended to be used with the Al-based MKID described previously in Sec. 5.3.

This therefore required the Prototype to be able to produce a spectrum with a bandpass of an MKID, $\approx 300 - 1500$nm here, with a single device.

The overall design of the prototype involved placing the grating at the centre of a rotating stage, equipped with an 'arm' for positioning the camera. This arm held the camera, which focused a portion of the spectrum dispersed by the grating into a fibre, ultimately connected to a single MKID. The arm could be rotated to gradually assemble a spectrum, covering the required bandpass. A diagram illustrating the Prototype concept can be found in Fig. 6.1.

6.2 Optical and Mechanical Design

The initial step in developing the KIDSpec Prototype was to create an optical design. The initial concept involved setting up a simple spectrograph using Off-Axis Parabola (OAP) mirrors coated with protected silver from Thorlabs for the

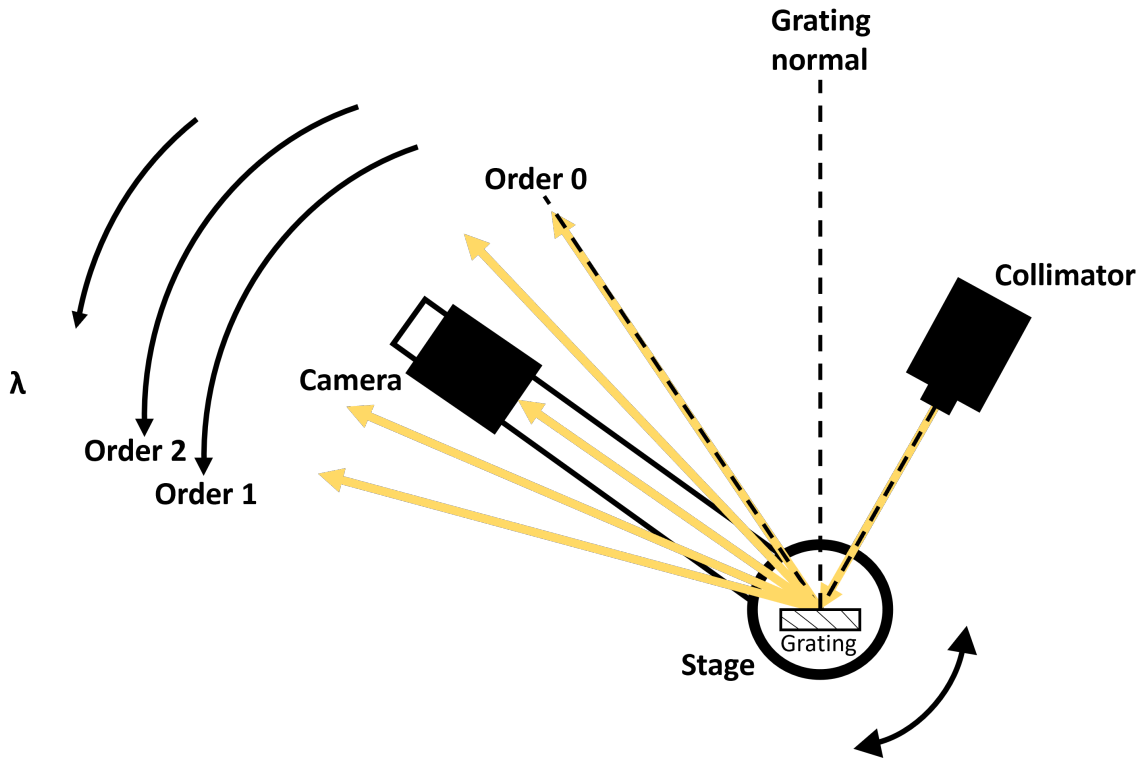

Figure 6.1: Concept diagram for the KIDSpec Prototype. The Prototype will have a rotating arm to allow the capture of a $\approx 300 - 1500$nm spectrum using a single MKID pixel. The arm rotating around the grating will pass the camera through the spectral orders, allowing for the capture of the bandpass while also demonstrating the MKID's order separation capability.

camera and collimator. The choice of mirrors over lenses was driven by the need for a wider effective wavelength range. Lenses have high efficiency only within specific narrow bands and are susceptible to chromatic aberration due to varying focal lengths over such a wide bandpass. This is not a concern for the silver-coated mirrors, which exhibit over 90% reflectance across the range of 0.4 to 20 µm, as demonstrated in Fig. 6.2 from Thorlabs. In contrast, a lens collimator system from Thorlabs guarantees over 95% efficiency only within the 350-700 nm range, as shown in Fig. 6.3 from Thorlabs*.

From this stage of the concept the final spectral resolution of the KIDSpec Prototype can be used to determine other factors of the Prototype, such as camera focal length. The predicted spectral resolution can be found from the reciprocal

*https://www.thorlabs.com/newgrouppage9.cfm?objectgroup_id=12897

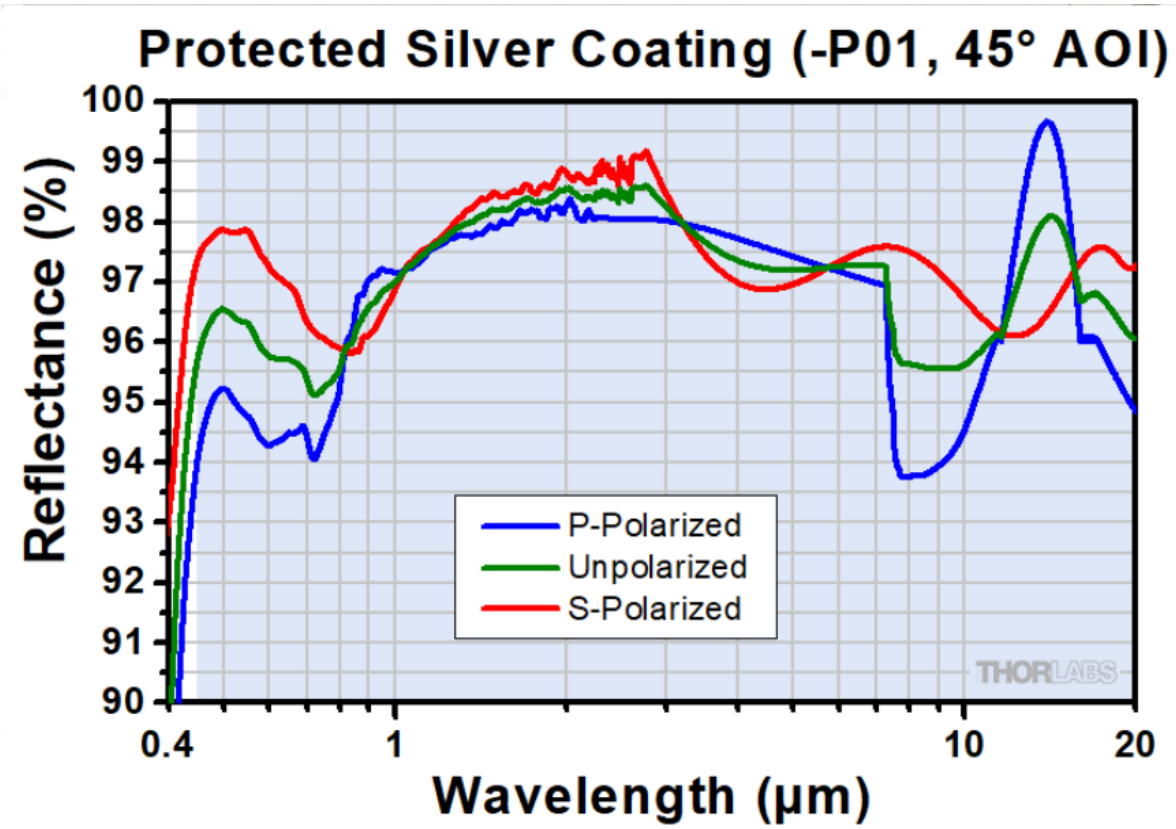

Figure 6.2: Reflectance with wavelength of the Thorlabs off-axis parabolic mirror with a protected silver coating. This is beneficial to the KIDSpec Prototype due to these mirrors having >90% efficiency across the bandpass of the single MKID detector.

dispersion defined as,

$$\Delta\Theta = \frac{\cos(\theta) \times 1e6}{gnF_{cam}} \tag{6.1}$$

where $\Delta\Theta$ is the reciprocal dispersion in units of nm/mm, θ is the angle of reflection, g is the grooves per mm, n is the order number, and F_{cam} is the camera focal length. Utilising the reciprocal dispersion, one can calculate the wavelength range focused into a $200\mu m$ diameter fibre, acting as a slit and limiting the spectral resolution of this design. From this range, $\Delta\lambda$, the resolving power can be determined using $R = \lambda/\Delta\lambda$.

For these calculations, a 300 lines/mm grating at blaze at 1000nm, $\cos(\theta) \approx 1$, and a Thorlabs mirror at the camera with a focal length of 203.2mm, the longest focal

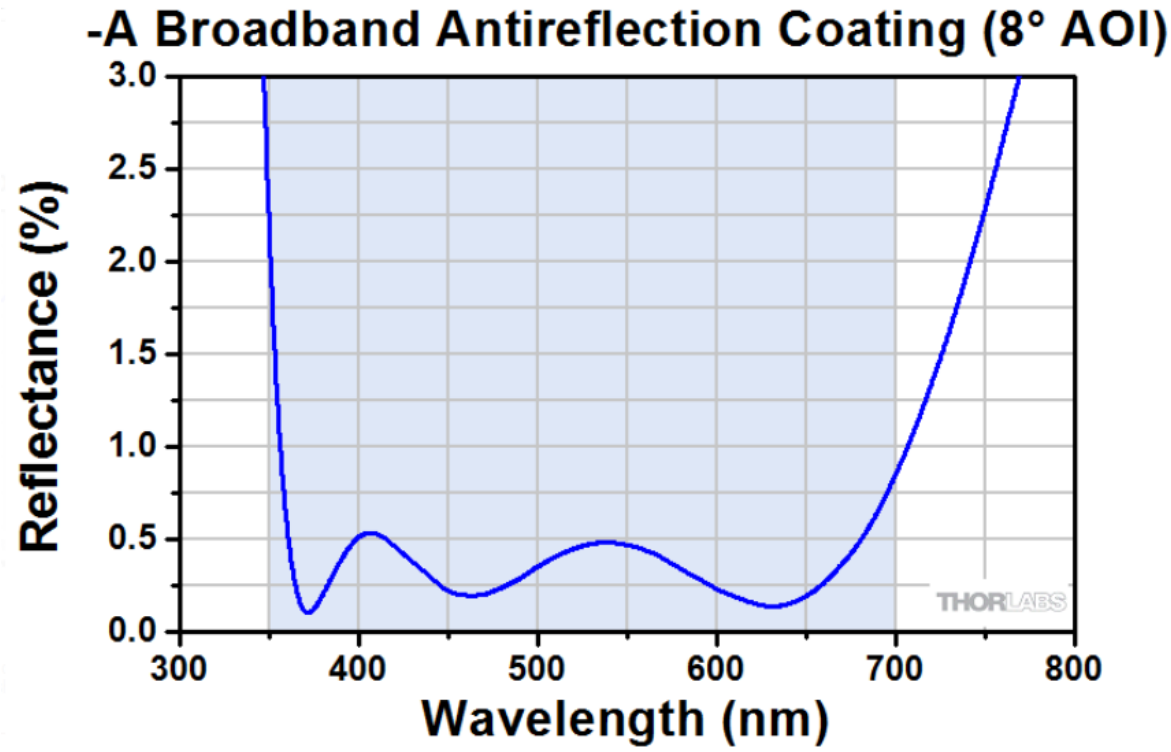

Figure 6.3: Reflectance with wavelength of the Thorlabs high-NA achromatic collimators for multimode fibres. Lens based options like these were not considered for the Prototype due to their narrow range of effectiveness, as shown here. Here this range is only guaranteed between 350-700nm.

length available, were employed. This yielded $\Delta\Theta = 8.2\text{nm/mm}$. Given a $200\mu\text{m}$ diameter fibre, $\Delta\lambda$ was approximated to be around 1.64nm for grating order 2 and approximately 3.28nm for order 1.

The resolving power at the wavelength of interest can be determined as $0.5 \times \lambda/\Delta\lambda$, where the factor of 0.5 accounts for Nyquist sampling. Finally, the resolution element for the order can be calculated by dividing the central order wavelength by the resolving power.

For order 1, with a central wavelength of 1000nm and sampling at 710nm, the expected resolution element is 9.24nm. For order 2, sampling at 550nm, the resolution element should be 2.98nm. These wavelengths were selected to test the resolution using lines from a Ne and Hg(Ar) lamp, respectively, as detailed in Sec. 6.4.3. This setup was initially chosen to start the Prototype, and after construction

and testing, improvements to the spectral resolution can be made.

To create the optical design for the Prototype, Zemax* was used. Using the parameters in Sec. 6.1, and a 24.5mm focal length collimator OAP mirror, the design shown in Fig. 6.4 was developed. To facilitate the transmission of light to and from the Prototype, a 0.22 numerical aperture (NA) 200μm diameter fibre was used. Specifically the M25 series of fibres from Thorlabs. These fibres are commonly used and have a wide wavelength range of 400-2200nm. The mirrors used as the collimator and camera were the MPD119-P01 and MPD189-P01 respectively, from Thorlabs. The mirror used for the collimator was used for its focal length of 25.4mm to fill the mirror's full circular diameter of 25.4mm, longer focal lengths would cause the light to be extended beyond the mirror's area. The mirror with the longest focal length offered by Thorlabs was used for the camera to maximise the spectral resolution, as seen in Eq. 6.1. This focal length is 203.2mm. For the grating, the GR25-0310 Thorlabs model was used, for its physical dimensions being larger than the beam diameter (of approximately 10mm) from the collimator. For this grating and a beam diameter of 10mm, this would result in a resolving power in spectral order 2 of $R = mN = 6000$ where m is order number and N is the number of grooves which are illuminated.

With the Zemax design illustrated in Fig. 6.4, we can validate the predicted spectral resolution. By focusing on the central field from the input fibre, we expect the wavelength range that covers the 200μm diameter of the output fibre to be approximately 1.64nm when considering order 2 at 700nm.

Fig. 6.5 presents a footprint diagram of a 200μm diameter aperture at the IMAGE surface in Zemax. These diagrams display optical spot sizes over a specific surface in the optical design.

The results obtained from Fig. 6.5 align with the theory presented earlier in this section, which predicted a range of approximately 1.64nm. The central spot is at

*https://www.zemax.com/

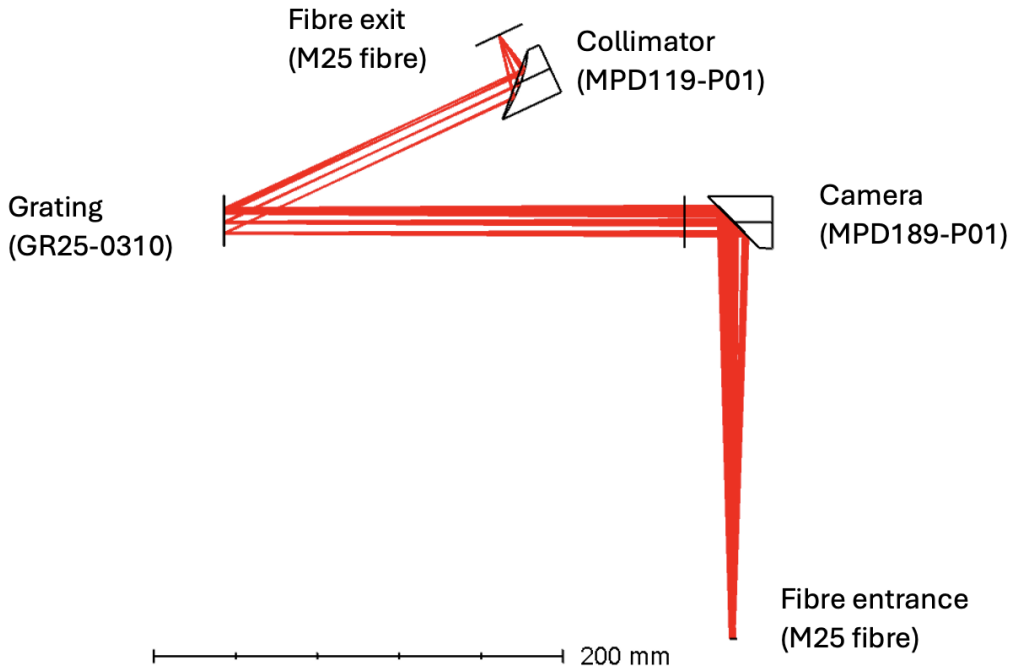

Figure 6.4: The optical design for the KIDSpec Prototype as seen within the Zemax optical simulation software. The collimator mirror (MPD119-P01) has a focal length of 24.5mm, and the camera mirror (MPD189-P01) has a focal length of 203.2mm. The grating used here is the GR25-0310 model. The M25 fibres from Thorlabs are used as the input and output of the system. The system shown is the ray path of order 2 at 700nm.

700nm, so a spot representing 700.82nm should still be visible at the diameter of the 200μm fibre. This is because a range of 1.64nm, as previously found, is covered by wavelengths ranging from $\pm$0.82nm from the central wavelength. Notably, Zemax showed that wavelengths up to 700.85nm were visible inside the fibre diameter, resulting in a focused wavelength range of 1.7nm.

Any optical system will encounter optical aberrations, and this will ultimately affect the linewidth the Prototype can produce.There are a number of optical aberrations which could affect this, and make this wavelength range larger, reducing the overall resolution of the Prototype. For example, spherical aberration caused by light focusing in different points due to the curvature of the mirrors used. The use of mirrors is also an attempt to avoid chromatic aberration, because all of the light within the bandpass wavelength here would be affected in the same way by the mirrors. If a lens was used the light would be focused differently depending on

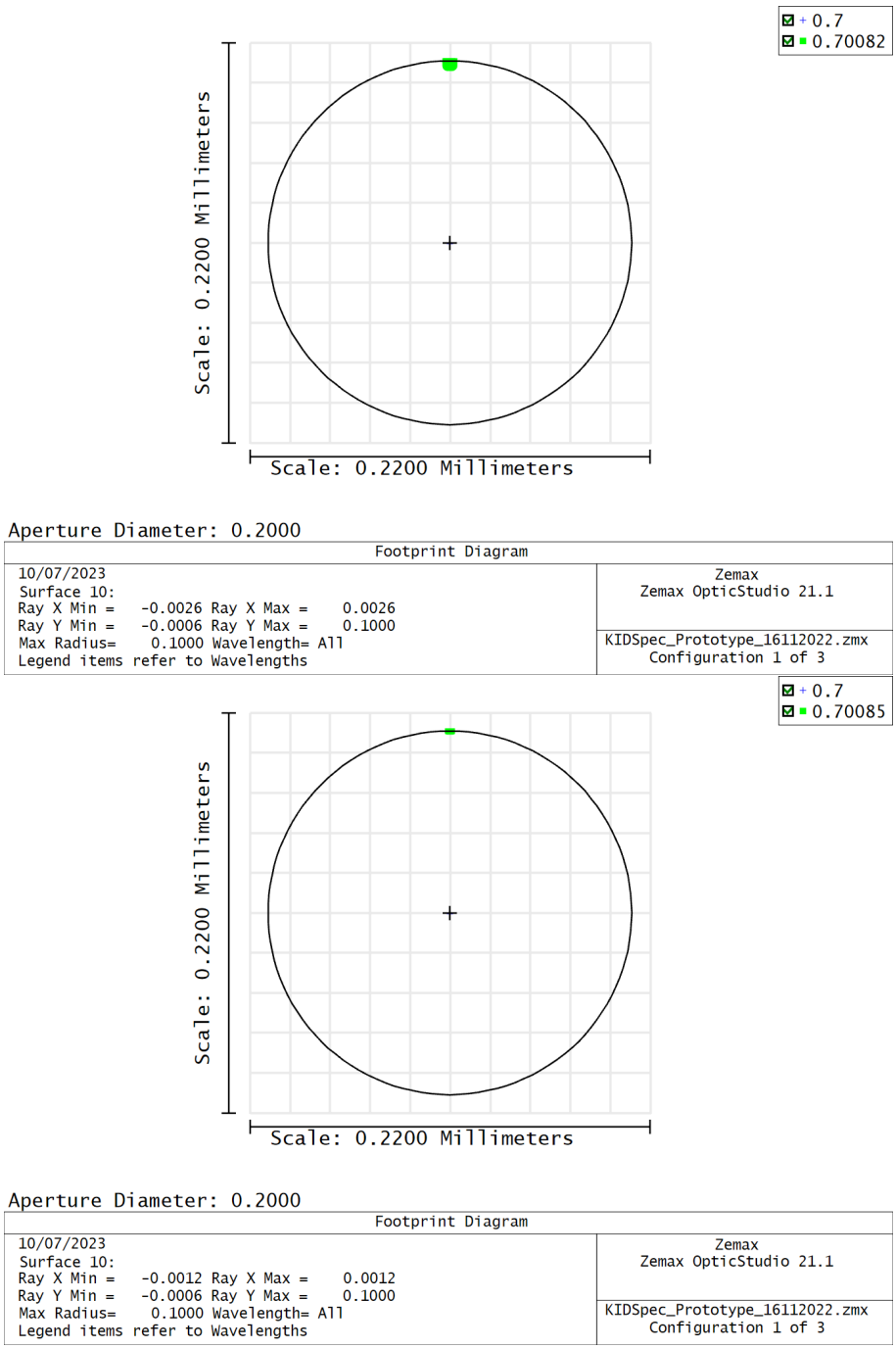

Figure 6.5: Footprint diagrams of a 200μm diameter aperture at the IMAGE plane. **Top** shows the central spot of 700nm. Due to the central wavelength being focused well it is not quite visible in the shown, in comparison to the size of the fibre. Also shown in the spot of the 700.82nm wavelength, clearly within the fibre diameter. **Bottom** shows the same as **Top**, but with 700.85nm instead, which has mostly fallen outside the fibre diameter. Any higher wavelengths would be completely outside the fibre diameter.

wavelength. Coma could also be encountered, if the beam directed at the mirrors is not collimated, some light will not be parallel to the optical axis and therefore not focus the light properly. Sec. 6.3 discusses the alignment procedure to avoid these aberrations as much as possible.

The initial mechanical design for the KIDSpec Prototype was created using Autodesk Inventor software. To enable precise wavelength adjustments, the HDR50 rotation stage was selected for its fine motion control, with a minimum motion capability of 0.8μrad and a weight capacity of 50kg. The first component designed in the Inventor software was the arm responsible for holding the camera. This arm was required to support a rail for attaching the camera, and it needed to remain rigid even when supporting the weight of the camera setup.

The camera setup consisted of several components, including the MPD189-P01 mirror, KCB1P mirror mount, PH20 post holder with TR30 post, an RLA300 dovetail rail, a BA1 with an RC1 to slide along the dovetail rail, two SM1L35 lens tubes, an adjustable SM1V15 lens tube, and the SM1SMA fibre link. The mirror mount was chosen for its ability to encase the mirror and orient it at a 45-degree angle with fine adjustment features, simplifying the alignment process. The combination of lens tubes was selected to achieve the required focal length for the camera mirror, with the adjustable lens tube allowing for precise adjustments.

6.3 Assembly and Alignment

Utilising the Thorlabs components discussed in Section 6.2, the final construction design, as depicted in Figure 6.6, was developed. The next steps involved assembly and alignment.

After the construction phase, the positions of the fibres in relation to the mirrors were fine-tuned to match the focal length using a shear plate interferometer, specifically the SI100 model from Thorlabs. The SI100 is designed to give a qualitative test the collimation of an incoming beam of light. The goal of using this equipment

was to collimate the beam as much as possible, and return to the collimation if the results in future sections were not achieved. For the collimation itself this process involved exposing a laser source to the shear plate and examining the interferometry pattern that emerged to assess the collimation of the beam. The beam was considered collimated when the pattern's lines were vertical. To achieve this, the fibre was positioned at the focal length of the mirror, and the SI100 was attached to the opposite face of the KCB1P mount using Thorlabs' 30mm cage system.

An issue arose when using the initially chosen 25.4mm focus mirror: the focus point was located at the boundary between the KCB1P mount and the lens tubes that held the fibre. Furthermore, the fine-tuning dials on the KCB1P mount had to be set to opposite extremes to align the collimated beam onto the held mirror. However, this problem did not occur when the 76.2mm mirror was used instead. In this case, the extreme dial positions were not necessary. Figure 6.7 illustrates the interferometer pattern when the beam is collimated, meaning the pattern appears vertical. If the pattern leans in either direction, it indicates that the beam is not collimated, signifying that the fibre source is not at the mirror's focus. However, as can be seen in Figure 6.7, the interferometer fringes are jagged which indicates higher order aberrations, which reduced the final spectral resolution possible when aligned in this setup. These issues with the alignment of the system were not reduced further, because the aim here was to be able to observe separate orders from an MKID, which was still ultimately achieved.

The camera mirror did not exhibit collimation issues similar to those encountered with the collimator mirror. The interferometer pattern shown in Fig. 6.7 was successfully produced. The spectral resolution was tested in Sec. 6.4.3 with the previously determined resolution elements for order 1 and 2 from Sec. 6.2. This was completed using a Hg(Ar) lamp, aiming for the expected resolving element of 2.98nm at 550nm in order 2, and a Ne lamp for the expected 9.24nm resolving element at 710nm in order 1.

To ensure that the camera and collimator were at equal heights from the bread-

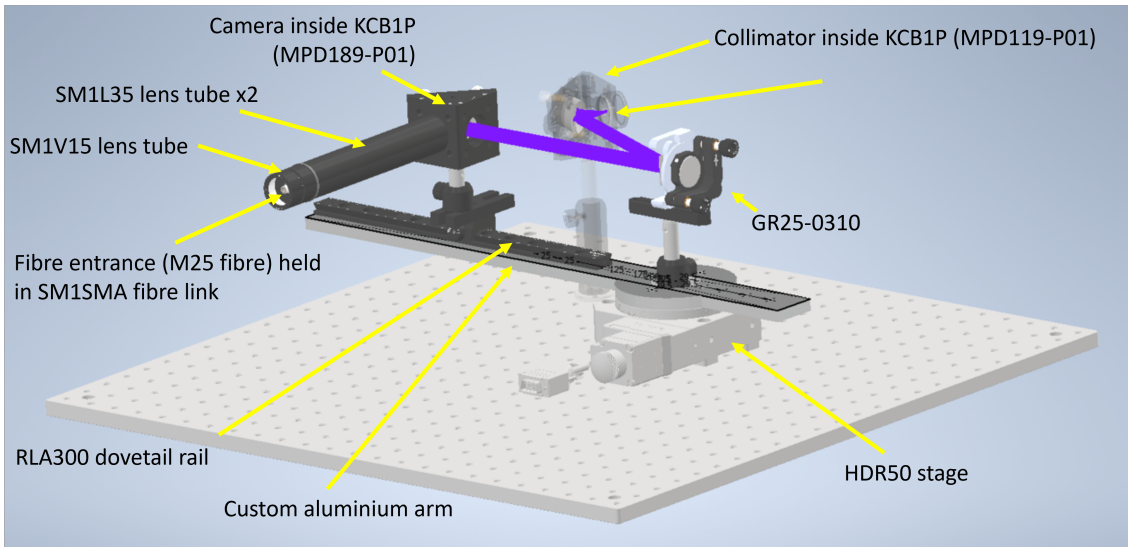

Figure 6.6: The final mechanical design for the KIDSpec Prototype, generated using the Autodesk Inventor software. Included are all parts discussed in Sec. 6.2, and the optical design imported from Zemax. The KCB1P mount with the camera inside is supported by a PH20 post holder with a TR30 post inside, mounted onto a BA1 with an RC1 to slide along the dovetail rail.

Figure 6.7: Pictures taken of the shear plate from the SI100 when a 633nm laser was used. **Left** is the collimation result for the 76.2mm focal length OAP mirror. **Right** shows the collimation for the 203.2mm focal length OAP mirror. Because the pattern is clearly vertical along the line included on the shear plate, both were assumed to be collimated.

board, a spirit level was placed on top of the two mounts. The grating was then mounted on a kinematic mount from Thorlabs and aligned after ensuring that the mounts were set to the same height.

6.4 KIDSpec Prototype Demonstration

6.4.1 Demonstration setup

For this section and the data collected within it, the KIDSpec prototype was set up as depicted in Fig. 6.8. The only modification made was to rotate the grating by 8 deg away from the collimator's normal, facing towards the grating. This adjustment was made because 8 deg corresponds to GR25-0310's blaze angle, which enhances the throughput of the KIDSpec Prototype. The chosen stage angles for this setup ranged from 38 deg to 49 deg, with Fig. 6.8 illustrating the Prototype at 38 deg. These angles covered the possible wavelength range of 1200-300nm, averaging the spectral resolution discussed in Sec. 6.3.

Using the Prototype, order separation could also be demonstrated. The initial wavelengths selected were 600nm and 1200nm for orders 2 and 1, respectively. To observe the range from 1200nm to 600nm with order 1, a range from 600nm to 300nm was required for order 2. Given a resolving power of approximately 140, a sampling element of 4nm was used. This resulted in 150 angles within the range of 38 deg to 49 deg.

Four demonstrations are presented in the subsequent sections. The first is a wavelength calibration utilising a Thorlabs SLS201L source, which covers the range of 360-2600nm. This demonstration also showcases the MKIDs' ability to separate orders. The second and third demonstrations involve spectra of a Newport Optics 6035 Hg(Ar) and 6032 Ne calibration lamp, respectively. These lamps exhibit spectral features primarily within the range of 400-900nm. Finally, a spectrum of the

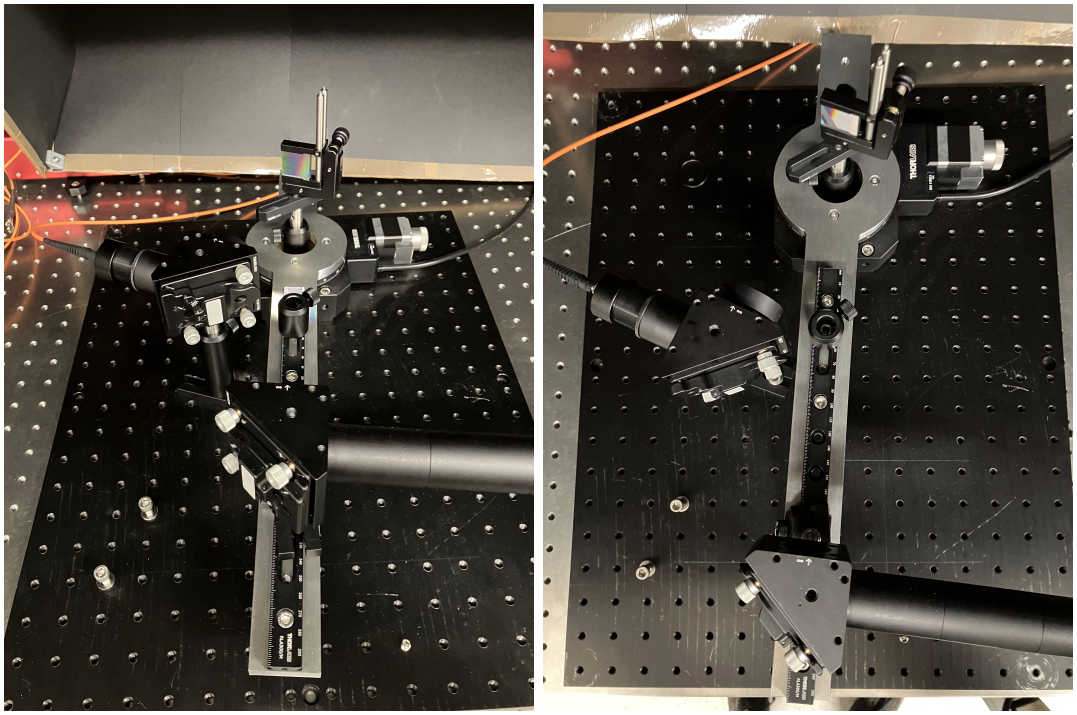

Figure 6.8: The KIDSpec prototype readied for a set of measurements covering the angle range $38 - 49$ deg. The stage is currently in the positions for 38 deg.

Sun is attempted using the Prototype. When necessary, an Ocean Optics FLAME USB spectrograph * is employed as a comparison dataset.

6.4.2 Wavelength Calibration

To ascertain the response of the MKIDs as a result of specific photon energies, the response of the devices must be calibrated. The Al devices were calibrated here, using the SLS201L source. This in combination with the KIDSpec Prototype allows for set wavelengths to be exposed onto the MKID, to observe the resulting phase change from these photons. This was done for the range of $\approx 400 - 1000$ nm, with 110 angles instead because the trends observed would all be fitted instead, in case of a change of angle number. With the HDR50 stage having an error in position of $\pm 820 \mu$rad†, this corresponded to an uncertainty in wavelength of ± 3nm for order

*https://epi-preprod.oceanoptics.com/products/spectrometers/general-purpose-spectrometer/custom-configured-flame-series-spectrometers/custom-configured-flame-spectrometer/

†https://www.thorlabs.com/newgrouppage9.cfm?objectgroup_id=1064

1, and ±1nm for order 2. However the stage was only used while moving it in the same direction, likely reducing this error since only travelling in one direction would reduce the backlash and hysteresis effects. This implies that wavelength cannot be inferred solely from the arm angle offset until after wavelength calibration has been performed using the lamp spectra. We do not consider this error further within this work.

The Al MKID was characterised and used with the method outlined in Chapter 5. The only change made between the data taken in Chapter 5 and this Chapter, is the use of a Savitsky-Golay filter (Savitzky and Golay, 1964). The filter is used to improve how low energy a photon can be, before its resulting phase change is lost beneath the phase noise. The use of this filter with a smaller window than the duration of the photon events will leave the photon event in the phase intact, while reducing the standard deviation of the phase stream by 14% with a window width of 30 microseconds. This had the additional benefit of improving the computation time for the analysis, to show this an exposure of white light was used. This was observed when considering the number of photon events passing filtering when compared to the original number of potential events. When the filter was used this value increased by 38%, in comparison to no filter. In this case the original number of potential events to analyse was also lower for the filtered phase stream, thereby reducing the computing time required for this method of readout analysis.

Spectra of the KIDSpec Prototype at each angle were taken using the FLAME USB spectrograph. From these spectra, their peaks were found using the scipy.signal.find_peaks Python method using the default values for all inputs with an exception of the 'height' parameter which was set at 1000. Fig. 6.9 shows the peak found using this setup of scipy.signal.find_peaks as a red marker. These peaks then corresponded to the wavelength observed at each angle.

Next data was taken using the MKID instead. The resulting MKID phase time streams captured for each angle were analysed using the photon fitting method shown in Chapter 5. In summary, the potential photons were fitted with an expo-

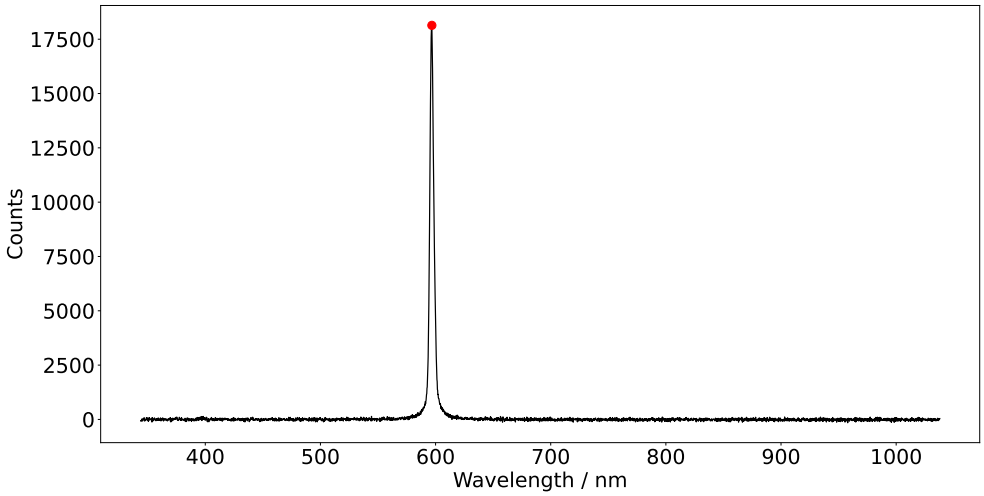

Figure 6.9: Spectrum with the KIDSpec Prototype at position 37.8 deg. The data shown was captured with the FLAME USB spectrograph fed with a fibre from the camera exit, showing order 2 at 597nm.

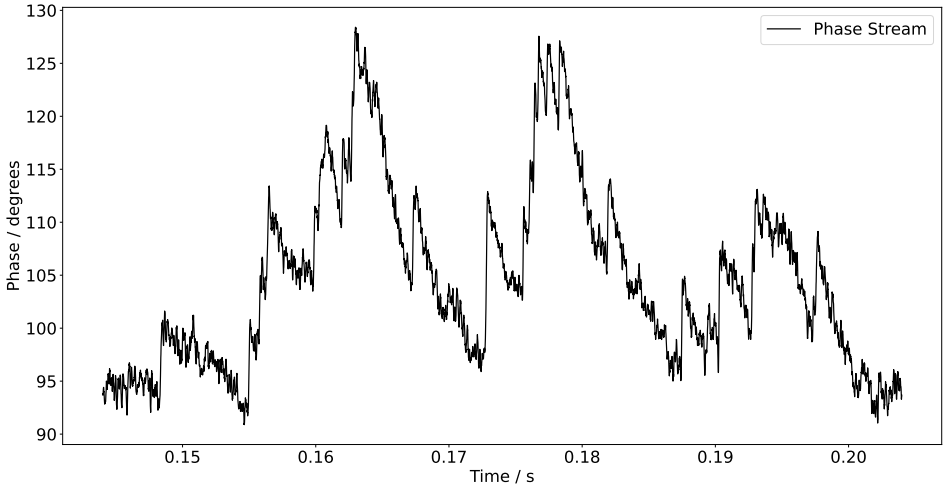

Figure 6.10: Section of an 8 second exposure taken at the 45.13 deg angle. Shown is a saturated phase time stream which caused photon events to arrive during the decay of a previous event, erroneously increasing the phase change of that incoming event.

nential and the results from the phase stream filtered using a Reduced Chi-Squared filter. From each angle's resulting observed photons, the phase change Gaussian was formed, as shown previously in Fig. 5.13 from Sec. 5.2.3.

At first 11 exposures at each angle were taken here, with an 8 second duration each. It was observed that for the angles $\approx 41 - 49$ the photon count had increased to the level where majority of the photons observed had arrived during the 'tail' of previous photons, i.e. the detector was saturated. This was because of the light source used for the experiment, the Thorlabs SLS201L tungsten lamp. This lamp has an intensity following a blackbody curve within its bandpass of 300-2600nm. From Fig. 6.11 the angles $\approx 41 - 49$ for order 1 correspond with the peak intensity of $\approx$ 900nm*, causing the observed 'hump'.

An example of this from the 45.13 deg angle is shown in Fig. 6.10. In this Figure many photon events occur, shown by a rapid rise in phase, followed by a decay. While this decay is occurring more photons arrive, resting on this decay. This caused the mean phase change to increase, causing the large 'hump' shown in Fig. 6.11 when considering the angle of the Prototype and the mean phase change. The change in phase should be not as sharp as this, and change more gradually (De Visser et al., 2021).

From Fig. 6.11, not all angles were affected. A resulting photon Gaussian from the 37.8 degree angle, thereby unaffected by the saturation issue, is shown in Fig. 6.12. This is the same angle as the USB spectrograph data shown in Figure 6.9. This MKID dataset clearly shows two separate orders, order 1 at 597nm, and order 2 at 1194nm, demonstrating the MKID's capability to separate spectral orders. Using these Gaussians the mean phase change is determined by fitting the Gaussian equation to the histogram generated from the MKID data using scipy.optimize.leastsq with default settings, with the results of these fits shown in Fig. 6.11. These Gaussians had mean phase changes of 5.50 ± 0.50 and 10.45 ± 0.51 degrees, for the 1194nm and 597nm wavelengths respectively.

*https://www.thorlabs.com/newgrouppage9.cfm?objectgroup_id=7269

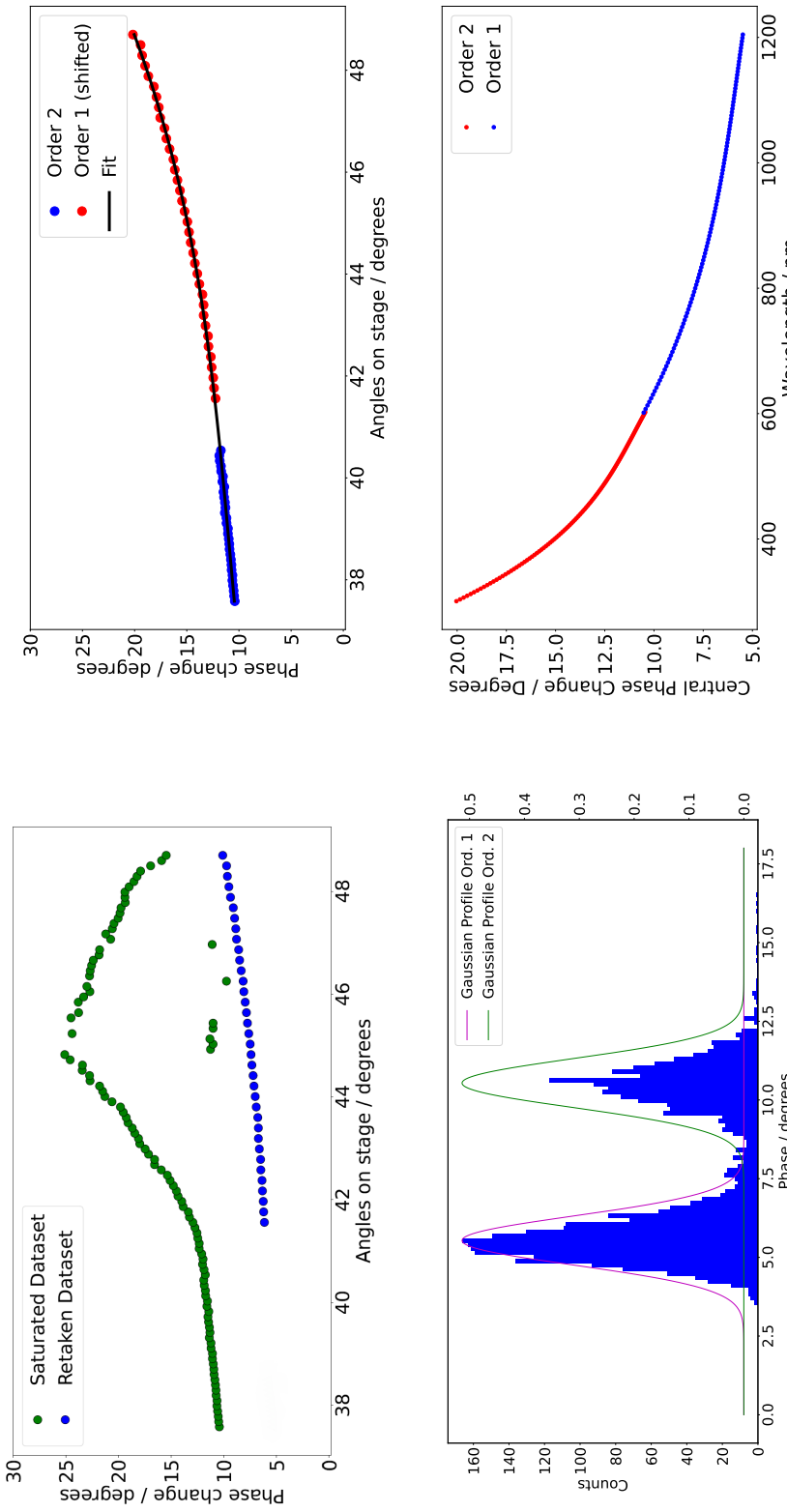

Figure 6.11: **Top Left:** shows the mean MKID phase changes found with respect to the angles sampled, with the saturated exposures causing the 'hump' between $\approx 41 - 49$ deg. These angles should have exhibited a trend seen by the retaken dataset. **Top Right:** is the trend of MKID phase change as a result of the angle observed, fitted to the order 2 and shifted order 1 data. **Bottom Left:** shows a Gaussian profile determined using the fit in the top right panel. **Bottom Right:** shows the wavelength range of the Prototype with respect to the generated Gaussian profile's mean phase change.

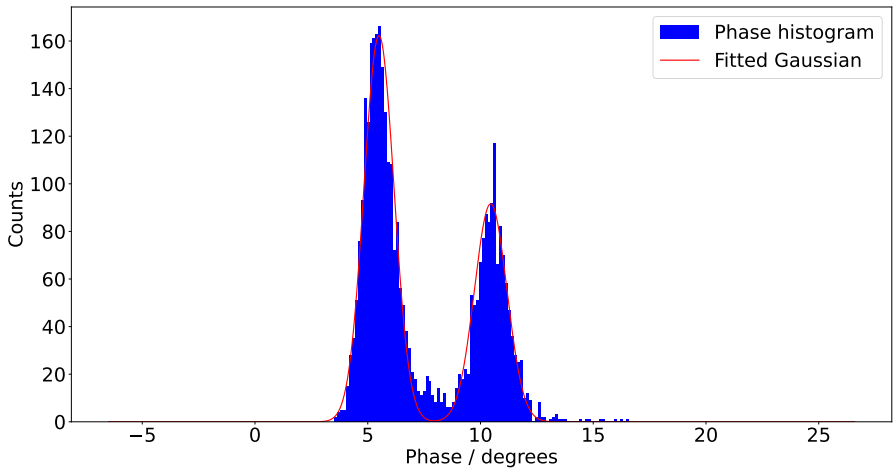

Figure 6.12: Spectrum with the KIDSpec Prototype at position 37.8 deg. The data shown was captured with the Al MKID fed with a fibre from the camera exit, showing order 2 at 597nm, and order 1 at 1194nm. 11 exposures of 8 seconds each were used for this data. These Gaussians had mean phase changes of 5.50 ± 0.50 and 10.45 ± 0.51 degrees, for the 1194nm and 597nm wavelengths respectively

The appearance of a 'hump' at $\approx$ 7.5 degrees (in the phase angle, Fig. 6.11) is caused by the Al MKID device used experiencing a 'tail' of phase events from energetic photons. This phenomenon can be seen in De Visser et al. (2021), where the 'tail' is caused by the incoming photons energy 'leaking' due to diffusion and phonon transport into the substrate of the device. This causes these lower energy results than the shown Gaussian.

To resolve the saturation issue for the angles affected, the angles were reduced to 66 total, approximately half, in an attempt to still build a model of phase shift vs angle but in half the time per full spectrum. The data up to 40 degrees in order 2 were still used, and new data was taken for the rest of the angles. The saturation of the MKID was then avoided with the use of a variable attenuator from Thorlabs (CFH2-V).

Because of the saturation issue, this reduced the number of data points for mean phase change in both order 1 and 2, at different angles. To be able to have more data points in a single order the assumption that an order 1 wavelength would have

approximately half the phase change as an order 2 wavelength was used. This would be reasonable because the order 2 wavelength here would have twice the energy of the corresponding order 1 wavelength, owing to it being half the wavelength, as in Eq. 3.9. The exact factor used was determined using the angles which were unaffected such as 37.8 degrees. This gave a factor of 1.9 between the two Gaussian peaks. This assumption was used to give more data points in order 2 so that the fitting would have points across the angles used. The mean phase changes which were computed using this assumption are shown in Fig. 6.11.

A factor of 2 between the two Gaussian peaks would be expected, but was within errors of the fit. This may have been the result of the Gaussian fitting being shifted due to the presence of the 'hump' seen in Fig. 6.12, affecting the peak fit. Alternatively this could be the result of the phonon losses in addition to the use of different equipment with the MKID devices, than what was used in De Visser et al. (2021). This could have affected the higher energy wavelengths more on these devices than lower energy wavelengths, within these device's wavelength range (De Visser et al., 2021). In this case, the experiment was continued in an attempt to still observe the Prototype in use as a spectrograph, albeit with this discrepancy. This behaviour would not affect results taken with the Prototype, due to it being calibrated for in this step. As seen here and below in this Chapter, this did not prevent the MKID from sorting the spectral orders and subsequently observing spectral features.

The reduced number of angles observed were interpolated to generate profiles for each angle discussed in the previous Section. This is appropriate because the features of the photon Gaussian depends on wavelength, and follows a trend without features, as shown in Fig. 6.11. Since each data point shown corresponds to a particular photon energy, the photon energies between the two points must follow the trend. This is because a photon energy between the two points cannot break more Cooper pairs consistently than a higher energy photon on the same MKID device, as described in Sec. 2.1.

The standard deviations of the profiles were determined from the fitted standard deviations of the fits. From these fitted Gaussian parameters, a set of Gaussian profiles can be generated for each angle observed by KIDSpec within the 38-49 degree range. The profiles for 37.8 degrees is shown in Fig. 6.11, along with the phase change with respect to wavelength, which follows a continuous trend with no sudden features.

These Gaussian profiles were then used to determine at each angle which order an incoming photon belonged to, with a 3σ maximum distance in phase shift from the mean phase shift of the profile. This also can then filter any photons which may have not originated from the source being observed, such as a torch being lit in the laboratory. Using these profiles, the spectra of various sources could be taken. It is noted that these profiles can be improved in the future with an extended repetition of this wavelength calibration phase with more angles sampled. However here the profiles were used as they still reflected the phase change range at which photons from each angle would appear.

6.4.3 Calibration Lamps

6035 Hg(Ar) and 6032 Ne spectral calibration lamps were used as a source with the KIDSpec Prototype. The aim here was to be able to discern features in this spectrum, and ensure that there was only flux observed where lines were present. This was also expected to occur for the MKID due to the throughput reduction with the addition of the Prototype and exposing the light from the fibre onto the MKID in the cryostat. Therefore the lines which were not bright enough for the USB spectrograph to detect, should not have been detected by the MKID with the KIDSpec Prototype.

4 exposures of 8 seconds each were taken, and the saturation of the MKID was not observed owing to the same use of the variable attenuator from Thorlabs (CFH2-V). After photon analysis of the phase time streams captured with the KIDSpec

Prototype, the Gaussian profiles from Sec. 6.4.2 were used to determine how many photons from each order arrived during the exposures taken at each angle.

An example of a Gaussian profile from both lamps used on an angle's total photons from all 4 exposures is shown in Fig. 6.13. The angles chosen were 44.97deg for the Hg(Ar) lamp and 46.76deg for the Ne lamp. These were chosen due to them having a high enough photon count to begin to see the Gaussian trend appear in the photon phase changes, with 1460 and 1153 respectively. It is noted that the profiles do not appear to be perfectly central on the phase changes. This is a result of the wavelength calibration needing to be altered during the process, but the profiles are still able to filter the relevant photons from Fig. 6.13, and from the results shown later, features are still observed. In particular for the Ne results shows the tail observed from De Visser et al. (2021), and the profile thereby filters it out.

Using these profiles and the photons which arrived within them, the photons observed at each wavelength was then determined, resulting in the Hg(Ar) and Ne spectra observed in Fig. 6.14 and Fig. 6.15 respectively. Each instrument had its data plotted using its own y-axis for these plots, which are then simply overlaid onto each other. By eye the Prototype successfully found features present in the calibration lamps. The relative levels of the features were not expected to be consistent because the intensities of the lines vary, as forewarned by Newport Optics*. This would, for the MKID spectrum, cause the heights to not be in agreement with a FLAME USB spectrograph because the MKID wavelengths were not taken simultaneously. For the Hg(Ar) results in Fig. 6.14 there is an interesting feature at $\approx$ 880nm which does not have a likewise FLAMES feature. This may be due to KIDSpec observing a very limited number of photons for a faint line that the FLAMES spectrograph was not able to observe due to the intensity of the other lines. However it may also be due to photons being incorrectly assigned the wrong order. There is a feature at $\approx$ 440nm which had $\approx$ 1400 photons arrive, and so this

*`https://www.newport.com/p/6032`

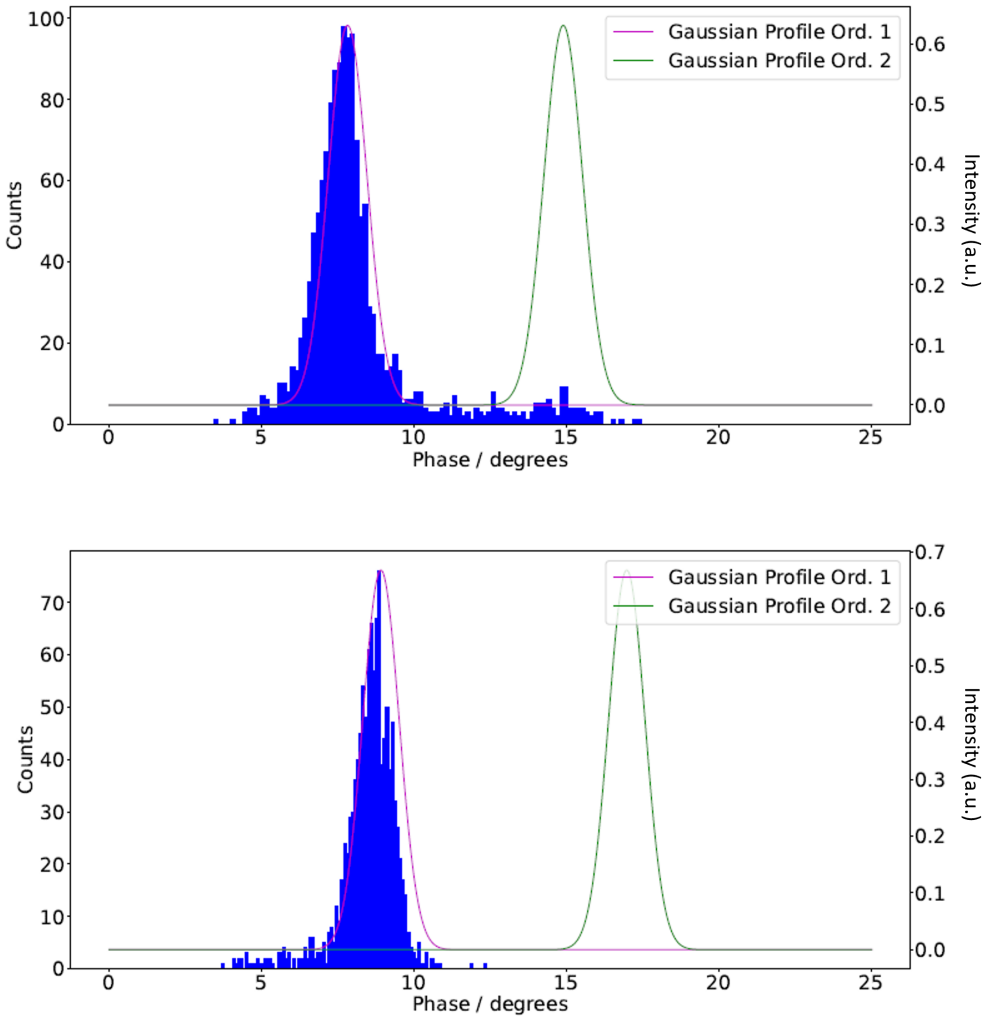

Figure 6.13: **Top** shows the Gaussian profile at an angle of 44.97deg, or 807.9 and 404.0nm for order 1 and 2 respectively. The data shown is the Hg(Ar) spectral calibration lamp at this angle, with 1460 photons. This filter passed 1223 and 94 photons for order 1 and 2 respectively. **Bottom** shows the same, but for the Ne lamp. Here this is at an angle of 46.76deg, or 708.9 and 354.4nm. This filter passed 1081 and 0 photons for order 1 and 2 respectively, from a total of 1153.

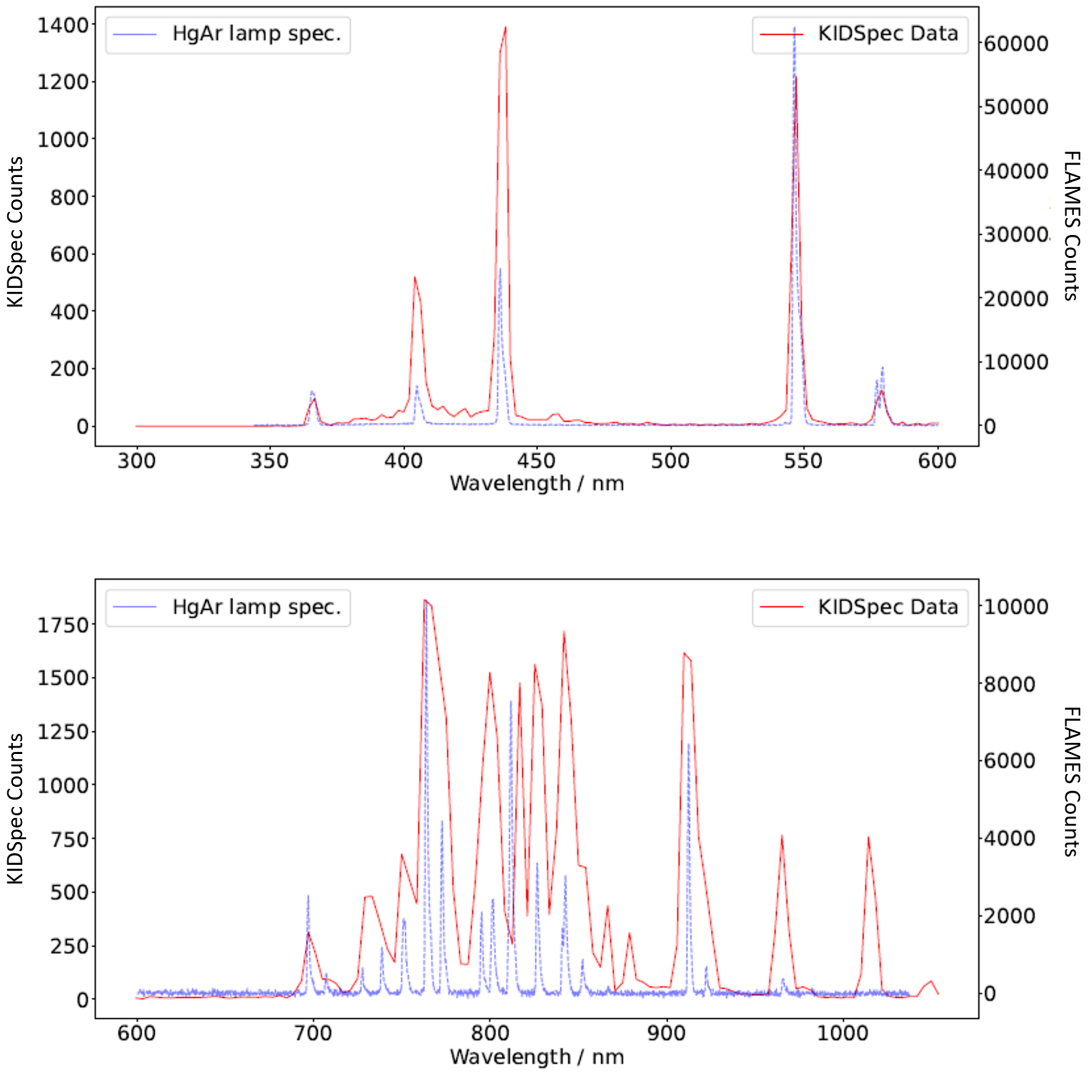

Figure 6.14: Spectrum of the 6035 Hg(Ar) calibration lamp with 4 exposures of 8s at each angle. Plotted in the top panel is order 2, and order 1 is in the bottom panel. The calibration spectrum marked with a dashed blue line was taken using the FLAME VIS USB spectrograph.

mystery feature at 880nm could be the result of some photons leaking into order 1 from order 2 here.

From the Ne spectrum results in the top panel of Fig. 6.15 were observed photons which did not appear to align with any features observed by the USB Spectrograph. However from the data sheets provided by Newport Optics*, there are 'faint' lines

*https://www.newport.com/p/6032

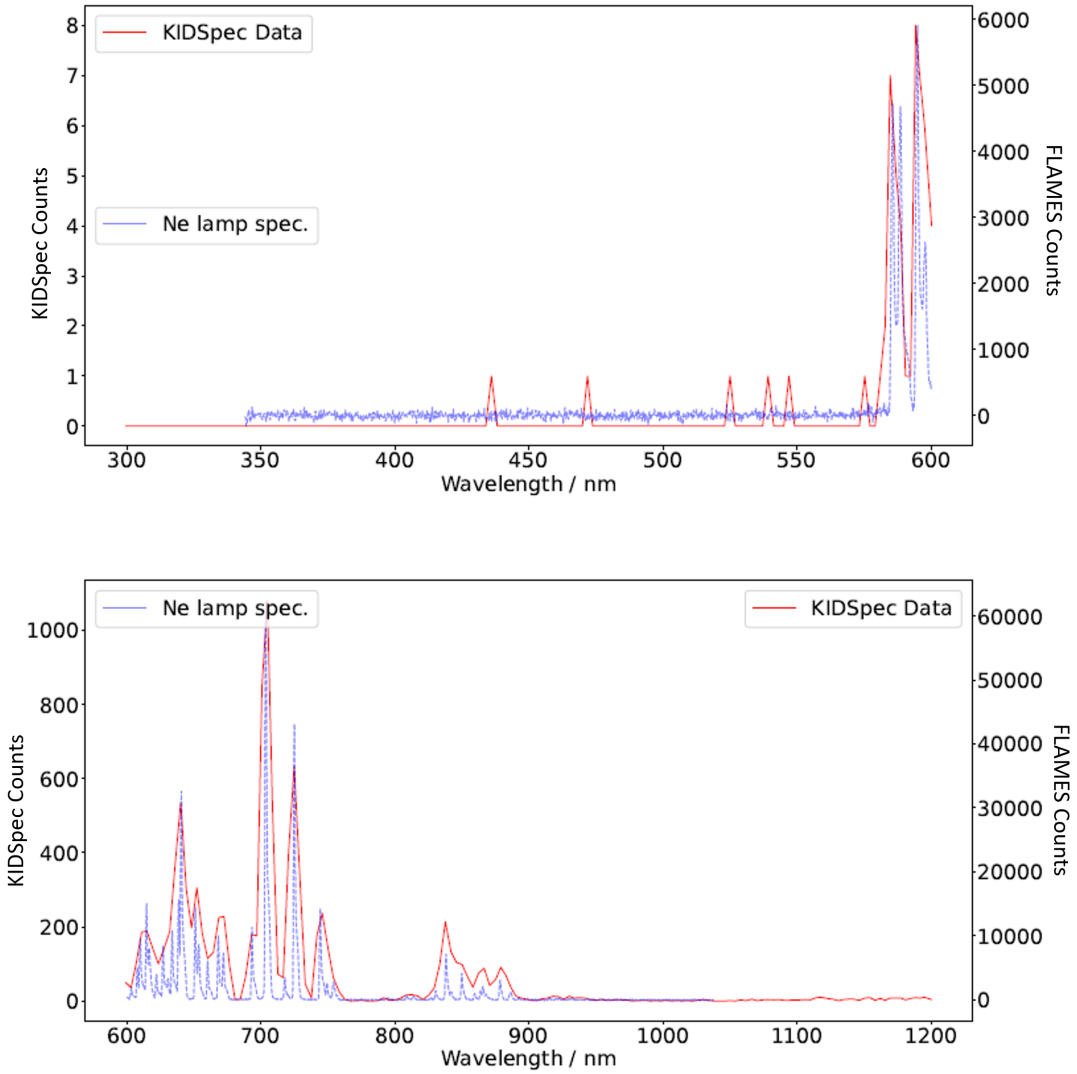

Figure 6.15: Spectrum of the 6032 Ne calibration lamp with 4 exposures of 8s at each angle. Plotted in the top panel is order 2, and order 1 is in the bottom panel. The calibration spectrum marked with a dashed blue line was taken using the FLAME VIS USB spectrograph.

present in the range 470-550nm which may have caused the single photons to reach the final stages of the analysis. These lines are shown in Fig. 6.16. The only line which may not have a source is the line at approximately 440nm. This and the other photon events could also be the result of a single noise event being able to pass through the filters, across 12586 photon events recorded. The lines with a brighter appearance at $\approx$ 540nm in Fig. 6.16 did not appear strongly in either the Prototype results or the FLAMES data. This was likely due to the lamp's lines here being of a lower intensity than the lines in the region of 600-700nm. The datasheets from Newport Optics do not state relative intensities between the two panels shown in Fig. 6.16, and warn the relative intensities may vary with operating conditions. From this it was concluded that the region of 600-700nm was a much brighter region than below 550nm, because there is a higher concentration of 'bright' lines, and the lines below 550nm were simply fainter relatively to the wavelength regions above 550nm. This outcome however does not interfere with the goal for this section, which was to observe the lamp's lines or regions with lines correctly, when considering their wavelength position only and not necessarily their brightness, when compared to the FLAMES data as shown in Fig. 6.15.

Using the feature shown at $\approx$ 550nm in the Hg(Ar) spectrum, the result shown by the KIDSpec Prototype gives a FWHM of $\approx$ 4nm here, which gives a spectral resolving power of $\approx$ 138 which is expected. This feature was fitted with a Gaussian equation using SciPy, to determine the FWHM of the feature the KIDSpec Prototype observed. The spectrum taken with the FLAME spectrograph was also rebinned to the resolving power of the Prototype and fitted. The standard deviation of the Gaussian fitted was converted to a FWHM with $\sigma \times 2\sqrt{2log(2)}$, where σ is the standard deviation. Fig. 6.17 shows the results of the fits for both the FLAME and KIDSpec data. The fits agreed, having standard deviations of 1.43 ± 0.03 and 1.47 ± 0.02nm for KIDSpec and FLAME respectively. From this it is assumed that KIDSpec did indeed observe this line as what would be expected for this resolving power, which had a FWHM of 3.36 ± 0.07nm, which approaches

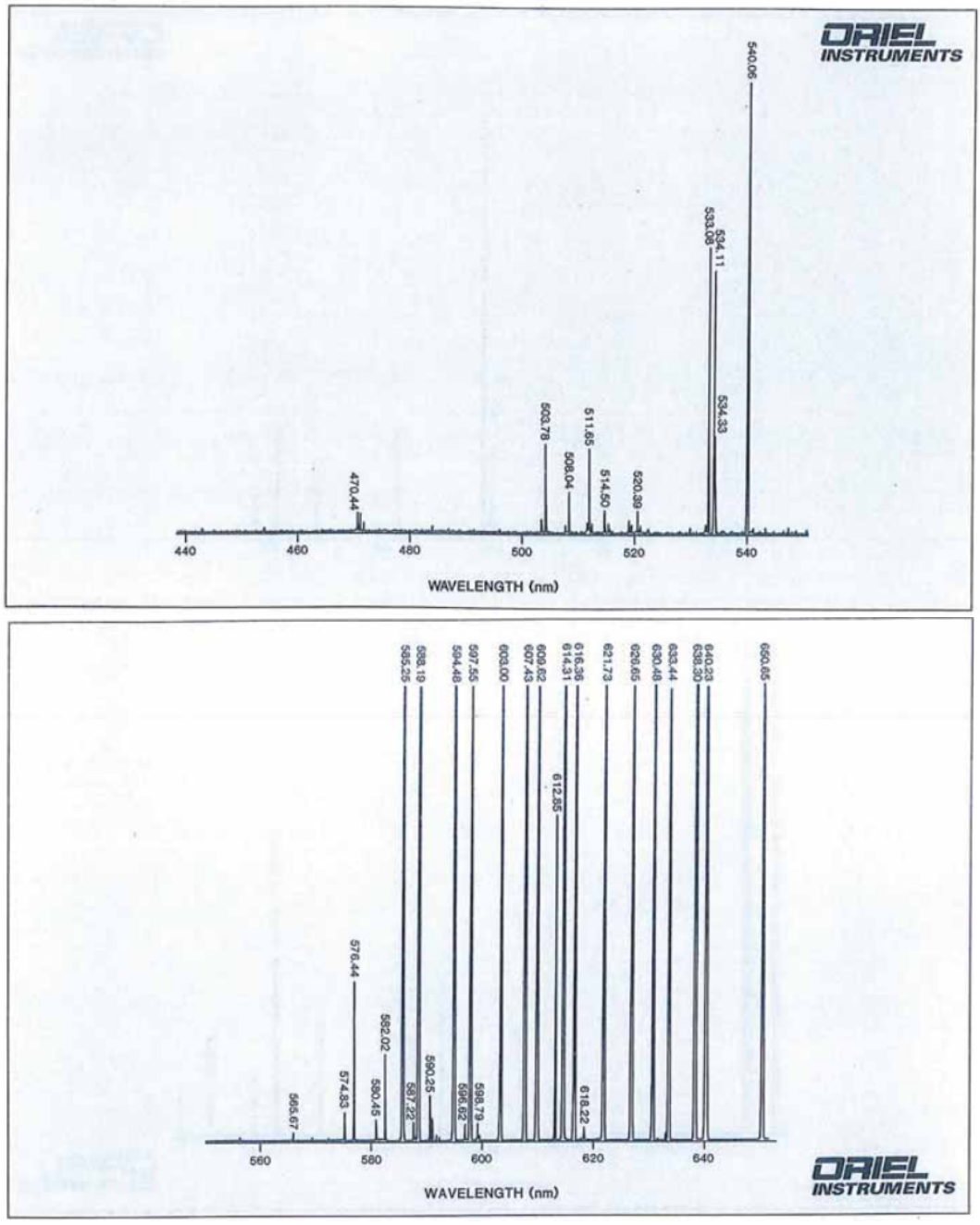

Figure 6.16: Spectrum of the 6032 Ne calibration lamp provided by Newport Optics.

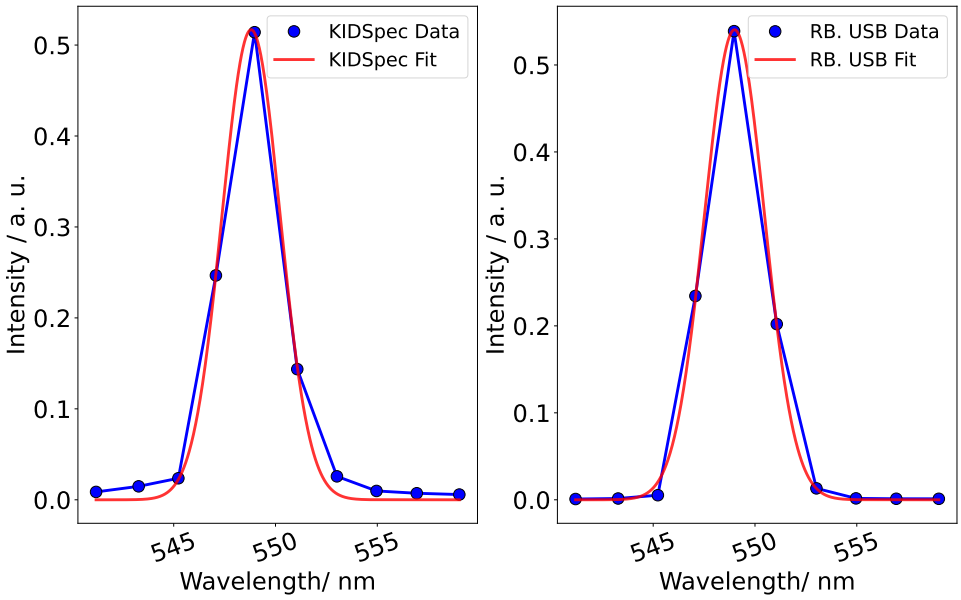

Figure 6.17: **Left** shows the Gaussian fit to the KIDSpec Prototype data of the Hg(Ar) lamp. This fit gave a standard deviation of 1.43±0.03nm. **Right** shows the Hg(Ar) lamp data captured with the FLAME spectrograph, which gave a standard deviation fit of 1.47 ± 0.02nm.

the $\Delta\lambda \approx 3$nm discussed in Sec. 6.3.

The Ne lamp was used to test the resolution at 710nm using a spectral line present. The feature was fitted in the same way as the Hg(Ar) line in Fig. 6.17, with the FLAME data rebinned to the KIDSpec Prototype data. Fig. 6.18 shows the results of the fits for both the FLAME and KIDSpec data. The fits did not agree here, having standard deviations of 3.84 ± 0.31 and 1.51 ± 0.03nm for KIDSpec and FLAME respectively. Here this may have been the result of the Prototype's resolution, causing the sharp peak which was observed by the FLAMES spectrograph to be spread out over the $\approx$ 15nm range seen in Fig. 6.17. This is because of the range of wavelengths which are able to be focused into the fibre at the focus point of the camera into the 200μm fibre which was acting as a slit. The expected wavelength range which would have been focused into the fibre would be 9.24nm, whereas this was higher for the Prototype from Figure 6.18. It is noted that the FLAME data shown does not have multiple datapoints within the feature, meaning

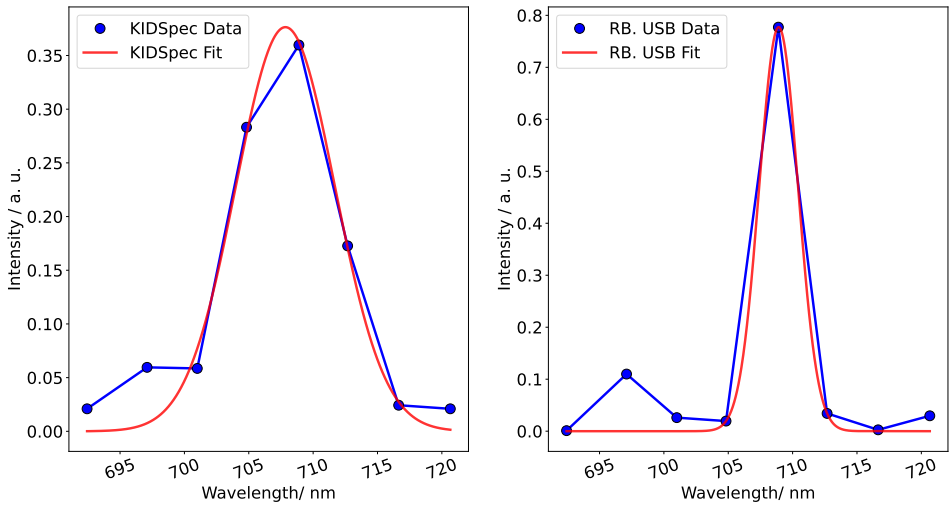

Figure 6.18: **Left** shows the Gaussian fit to the KIDSpec Prototype data of the Ne lamp. This fit gave a standard deviation of 3.84 ± 0.31nm. **Right** shows the Ne lamp data captured with the FLAME spectrograph, which gave a standard deviation fit of 1.51 ± 0.03nm.

it was not Nyquist sampled by the USB spectrograph. But the true width of the feature was not required here for further science so is still included.

However from the results shown the Prototype has shown the ability to observe spectra, with two spectral calibration lamps line features observed.

6.4.4 Solar Spectrum

A spectrum of the Sun was attempted similarly to the calibration lamps, with the aim of resolving solar absorption lines such as the Fraunhofer lines. This was done using a Celestron Nexstar Telescope with a Seymour Solar Filter attached. A SMA fibre connector was 3D printed and attached to the rear of the telescope to transfer the observed solar light to the KIDSpec Prototype using a 5m fibre fed through a window into the lab.

However a problem was encountered whereby the solar filter in combination with the transmission efficiency of the KIDSpec Prototype and the MKID setup in the Bluefors cryostat reduced the number of observed photons to a handful in an 8s

Figure 6.19: The Celestron Nexstar Telescope used to observe the Sun, with the 3D printed fibre attachment on the rear of the telescope. The orange fibre was fed from the telescope to the KIDSpec Prototype through the lab window.

exposure. The filter was recommended by the supplier not to be removed due to the intensity of the Sun, so instead, the fibre was suspended on the telescope observing the Sun directly. This gave enough photons such that the CFH2-V attenuator was required to avoid saturation. Fig. 6.19 shows the setup used. Using the Prototype in the same way as Sec. 6.4.3, angles in the range 38-49 degrees were sampled, with the telescope moved to keep track of the Sun throughout observations.

Another issue was caused by the weather for the attempted observations. These observations took place in Durham, in the North East region of England. The weather during the attempted observations was not clear enough with cloud patches consistently present. This caused unexpected reductions in the incoming flux during the observation datasets, at varying points throughout the observation. One set of angles containing 150 angles required approximately 2 hours to be completed.

Because of this a spectrum of the Sun was unable to be recreated here. In future, a alternate location would be appropriate for this experiment. Additionally, if this would be done in a location with more suitable weather, other astronomical sources could observed during the night as well.

However individual angles still had photons arrive independently. So the Gaussian profiles made in Sec. 6.4.2 would still be expected to find the correct phase changes for their given spectral orders. Fig. 6.20 shows three profiles used on the solar data gained when observing through the same set of angles used in Sec. 6.4.3. From Fig. 6.20 the profiles match the phase change Gaussians present at each angle, even for the top panel where it appears a Gaussian was beginning to take shape for order 2, but is centred on the profile for the second order. From these results and the spectra shown in Sec. 6.4.3, the Prototype would be able to recreate a solar spectrum in the range 400-1200nm, given clear weather without flux interruptions from clouds.

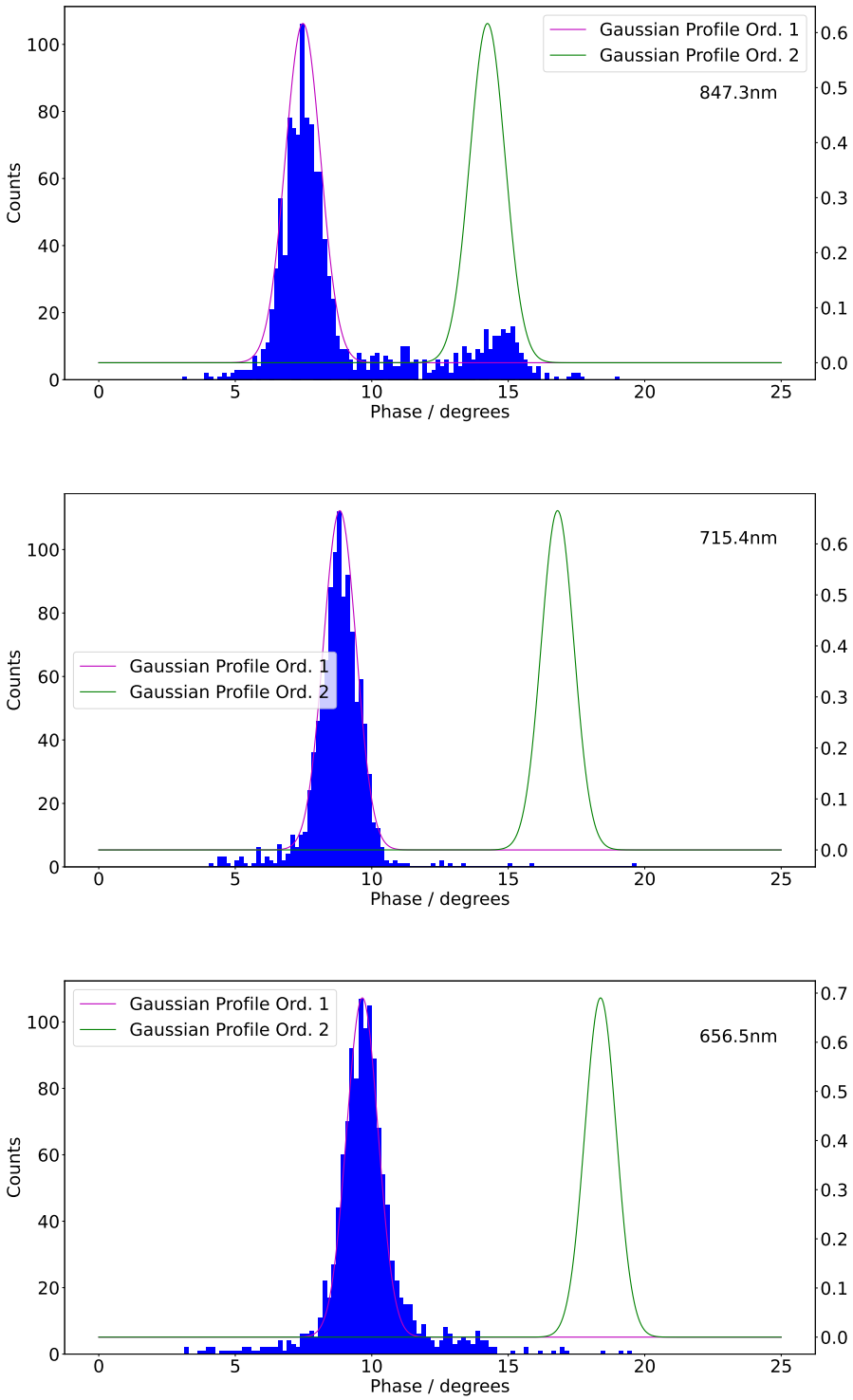

Figure 6.20: Shows the photons observed from the solar data at the angles 44.3, 46.6, and 47.7 degrees. Overlaid on each panel are the profiles for 847.3 (Top), 715.4 (Middle), and 656.5nm (Bottom) in order 1, which are expected at these angles.

Chapter 7

Conclusions

KIDSpec aims to set itself apart with its use of MKIDs. These superconducting detectors bring several benefits, including time resolution, no read noise, no dark current, and excellent cosmic ray mitigation. The intrinsic energy resolving capabilities of MKIDs mean a cross-disperser is not required, as MKIDs can separate the orders themselves, simplifying the optical layout of KIDSpec. Resolving the orders represents one of the greatest challenges for KIDSpec. Its capabilities will be limited by the R_E of its MKIDs, which limits how many orders can be observed by a single MKID. The benefits of MKIDs makes KIDSpec suitable for a growing list of science, including faint source spectroscopy and short period binaries, owing to the MKID's lack of read noise and dark current, and time resolution.

The KIDSpec Simulator (KSIM) has been developed to evaluate KIDSpec's performance, and is now in a position to test more KIDSpec parameters and new science cases. By simulating the atmosphere, telescope, grating, MKIDs, and other aspects, KSIM simulates how KIDSpec could observe a given object. Through the Order Gaussian or PTS method, KSIM can now aid the future development of the KIDSpec instrument. Using KSIM's variety of input parameters, observing scenarios, and objects can be simulated. Simulated in this work were various stars and galaxies, including comparisons with X-Shooter's ETC. It was found that for short observations involving fainter objects, KIDSpec potentially doubles the SNR of the

same simulated observation with X-Shooter.

Also discussed in Chapter 3 was the LISA verification sources which are binary systems with periods less than 30 minutes. One such system is ZTFJ1539 + 5027, a magnitude 19 system with a a period of 7 minutes. Typical CCD detector instruments struggle here with their read noise due to the short exposures required to constrain parameters of the system. A ZTFJ1539 + 5027 like system was simulated using KSIM and FORS' ETC. KIDSpec, using its read noise free MKIDs and microsecond time resolution will improve over these detectors, almost doubling the SNR of FORS for the same 10s observation simulation to 3.5 from 1.8. LSST will search in photometry for these LISA verification sources and will able to detect systems with a magnitude brighter than ≈ 24. When extending this to simulate KIDSpec on an ELT class telescope for a night of observations, KIDSpec could observe systems with up to $m_V \approx 24.3$ with an SNR>5. Here KIDSpec could build SNR in a particular orbital phase in the period of ZTFJ1539+5027 with a long continuous observation to reach these magnitudes. This work demonstrates KIDSpec's potential and flexibility for faint and short spectroscopy. KSIM can be obtained on request from the author.

MKID fabrication effects were also simulated to observe the impact they may have on observations. The dead pixels most affected the recreation of the object spectra, while R_{var} had a lower observed impact on the RCS value. Additionally, these fabrication errors will be further mitigated as the technology and fabrication continues to improve, and with testing KIDSpec's MKID array after fabrication to find the locations of any dead pixels. Multiple designs were also simulated to predict limiting magnitudes for various KIDSpecs, which found it would have comparable or fainter limiting magnitudes than X-Shooter. This work demonstrates KSIM's ability and flexibility to test a variety of science cases and KIDSpec designs, to progress the realisation of KIDSpec as a constructed instrument. To further grow the list of science cases for KIDSpec objects can be simulated using KSIM on request, or the simulation tool can also be obtained online.

Presented in Chapter 4 was the SuperSmart telescope array concept. SuperSmart would be an array of $\leq$ 1m diameter telescopes. With each telescope would be a KIDSpec-like instrument optically connected with a fibre. These telescopes would have the benefits of KIDSpec and MKIDs, namely the lack of read noise, energy resolving, and time resolution capabilities. In addition to this SuperSmart would take advantage of the flexible rebinning feature of the MKIDs, which would allow multiple telescopes to combine their observed photons, acting effectively as a larger class telescope. This flexibility will allow SuperSmart to contribute to the KIDSpec science cases but also survey follow up with its multiple telescopes, but also faint sources such as the LISA calibration sources.

From this a GAIA spectral follow up of 100,000 objects was simulated of the magnitude range $14 < m_V < 19$, using star data from GAIA DR2. These were passed to a SuperSmart telescopes simulator which determined how many nights a particular SuperSmart would require to observe a given set of objects. This simulator functioned by tracking each telescopes status in time steps, where a telescope could be observing or ready for a new object observation. It was found that if using 69 0.6m telescopes for a total effective diameter of 4m, SuperSmart could observe this set of 100,000 objects in 190 nights. This involved the telescopes all acting independently, and not requiring other telescopes to finish their observations before new ones. When this independence was not considered, the nights required over doubled to 477.

The flexibility of SuperSmart was demonstrated with this result and the LISA sources, whereby the telescopes could combine their observed photons due to the photon counting nature of the MKIDs, such as to a 4m total effective diameter. SuperSmart would be able to reduce the standard error of the radial velocity semi amplitude of ZTFJ1539+5027 by half with exposures of 9s throughout the period of the system. Multiple periods can then be observed to build the photons in these time bins. To reach an SNR>5 SuperSmart would require $\approx$ 15 hours. To observe the faintest LISA calibration sources of $m = 24$ when combined to a total effective

diameter of 4m, SuperSmart would need 18 hours of observation, or 2.3 nights. The ability for SuperSmart to be used for these varied science cases will be its strongest feature.

For implementation the telescopes used should be a mixture of differently sized telescopes. For an effective diameter of $\approx$ 4m, 23 0.6m, 11 0.8m, and 5 1m telescopes could be used. This would give a cost efficiency of 1.4mm^2/€, which is the same as only using 0.8m telescopes, while reducing the number of telescopes required for an total effective diameter of $\approx$ 4m, which reduces the number of MKIDs needed. For this combination of telescopes the hardware costs of the telescopes themselves, MKIDs, readout, and cryostats would be approximately €13 million.

The KIDSpec Prototype was demonstrated, using Al MKIDs. These MKIDs were first characterised before use to determine the MKID's IQ loop centre and resonant frequency. This was done using a least squares approximation of a circle on the IQ loop, which determined the centre of the loop. The resonant frequency of the could be inferred from the IQ loop using the point on the loop which was closest to the origin, and is the minima of the resonance dip in $|S_{21}|$ space. Alternatively, the resonance dip was fitted to determine the resonant frequency. With these characteristics determined, photons could be observed in a phase time stream. Photons take the approximate shape of an exponential decay, and to find the height and legitimacy of possible photon events, sections of phase time stream data were fitted with an sharp rise and exponential decay. These fits were filtered using a Reduced-Chi Squared and Pearson Correlation Coefficient test to retain the photon events. The KIDSpec prototype itself consisted of a fibre-fed collimator, grating, and camera focused onto another fibre. Both the collimator and camera used protected silver off-axis parabolic mirrors for a wider usable wavelength range. The camera was mounted onto an arm outstretched from the grating. The arm could then be rotated around the grating with the use of a rotating stage, to sample wavelengths in the range $\approx 300 - 1200$nm.

The broadband SLS201L source was used for the wavelength calibration of the

Prototype. Angles, or wavelengths, were sampled to generate Gaussian profiles of the MKID's response across the KIDSpec Prototypes working range. These profiles were then used for a Hg(Ar) and Ne calibration lamp, and solar data. The spectra of the calibration lamps were successfully recreated at a lower than expected spectral resolving power of KIDSpec which was ≈ 138, shown from fits to features from these calibration lamps. However this reduced spectral resolving power was sufficient to resolve features in the calibration lamps. A solar spectrum was unable to be achieved here, due to poor weather conditions in the observation location of Durham, UK. The weather included, at best, intermittent clouds which artificially reduced flux during the observations. However data at each individual angle was still taken and solar photons were still successfully observed. Additionally, from all of these samples the MKID's capability for separating orders was shown, with orders 1 and 2 separated throughout the angles of the Prototype. While there are also errors from the optical aberrations, stage alignment of $\pm 3nm$ for order 1, and MKID readout, these were not sufficient to prevent what was the primary goal of this Chapter which was to be able to separate two spectral orders using an MKID. This demonstrates the MKID's potential for spectroscopy.

Future work for the KIDSpec concept would be the observation of astronomical sources spectra using the Prototype. This would also benefit from an increased spectral resolution to ensure resolving important spectral lines such as Hα. For this a grating upgrade could be used, which could also allow for higher spectral orders to be observed and separated by the MKID, in addition to more orders at once to be separated. Alongside this, the simulation of the KIDSpec concept would continue. Specifically focusing on the short period binary systems, simulating these systems and the evolution of their spectra throughout in KSIM would be highly interesting. From these simulations their results could be analysed and fitted to determine the characteristics of the system and test the improvement KIDSpec should make over CCD based instruments.

Bibliography

B. P. Abbott, R. Abbott, T. D. Abbott, and F. Acernese. Multi-messenger observations of a binary neutron star merger. In *Proceedings of Science*, volume 362, 2017. doi: 10.3847/2041-8213/aa91c9.

R. Ahumada, C. A. Prieto, A. Almeida, F. Anders, S. F. Anderson, B. H. Andrews, B. Anguiano, R. Arcodia, E. Armengaud, M. Aubert, S. Avila, V. Avila-Reese, C. Badenes, C. Balland, K. Barger, J. K. Barrera-Ballesteros, S. Basu, J. Bautista, R. L. Beaton, T. C. Beers, B. I. T. Benavides, C. F. Bender, M. Bernardi, M. Bershady, F. Beutler, C. M. Bidin, J. Bird, D. Bizyaev, G. A. Blanc, M. R. Blanton, M. Boquien, J. Borissova, J. Bovy, W. N. Brandt, J. Brinkmann, J. R. Brownstein, K. Bundy, M. Bureau, A. Burgasser, E. Burtin, M. Cano-Díaz, R. Capasso, M. Cappellari, R. Carrera, S. Chabanier, W. Chaplin, M. Chapman, B. Cherinka, C. Chiappini, P. Doohyun Choi, S. D. Chojnowski, H. Chung, N. Clerc, D. Coffey, J. M. Comerford, J. Comparat, L. da Costa, M.-C. Cousinou, K. Covey, J. D. Crane, K. Cunha, G. d. S. Ilha, Y. S. Dai, S. B. Damsted, J. Darling, J. W. Davidson, R. Davies, K. Dawson, N. De, A. de la Macorra, N. De Lee, A. B. d. A. Queiroz, A. Deconto Machado, S. de la Torre, F. Dell'Agli, H. du Mas des Bourboux, A. M. Diamond-Stanic, S. Dillon, J. Donor, N. Drory, C. Duckworth, T. Dwelly, G. Ebelke, S. Eftekharzadeh, A. Davis Eigenbrot, Y. P. Elsworth, M. Eracleous, G. Erfanianfar, S. Escoffier,

X. Fan, E. Farr, J. G. Fernández-Trincado, D. Feuillet, A. Finoguenov, P. Fofie, A. Fraser-McKelvie, P. M. Frinchaboy, S. Fromenteau, H. Fu, L. Galbany, R. A. Garcia, D. A. García-Hernández, L. A. G. Oehmichen, J. Ge, M. A. G. Maia, D. Geisler, J. Gelfand, J. Goddy, V. Gonzalez-Perez, K. Grabowski, P. Green, C. J. Grier, H. Guo, J. Guy, P. Harding, S. Hasselquist, A. J. Hawken, C. R. Hayes, F. Hearty, S. Hekker, D. W. Hogg, J. A. Holtzman, D. Horta, J. Hou, B.-C. Hsieh, D. Huber, J. A. S. Hunt, J. I. Chitham, J. Imig, M. Jaber, C. E. J. Angel, J. A. Johnson, A. M. Jones, H. Jönsson, E. Jullo, Y. Kim, K. Kinemuchi, C. C. Kirkpatrick IV, G. W. Kite, M. Klaene, J.-P. Kneib, J. A. Kollmeier, H. Kong, M. Kounkel, D. Krishnarao, I. Lacerna, T.-W. Lan, R. R. Lane, D. R. Law, J.-M. Le Goff, H. W. Leung, H. Lewis, C. Li, J. Lian, L. Lin, D. Long, P. Longa-Peña, B. Lundgren, B. W. Lyke, J. Ted Mackereth, C. L. MacLeod, S. R. Majewski, A. Manchado, C. Maraston, P. Martini, T. Masseron, K. L. Masters, S. Mathur, R. M. McDermid, A. Merloni, M. Merrifield, S. Mészáros, A. Miglio, D. Minniti, R. Minsley, T. Miyaji, F. G. Mohammad, B. Mosser, E.-M. Mueller, D. Muna, A. Muñoz-Gutiérrez, A. D. Myers, S. Nadathur, P. Nair, K. Nandra, J. C. do Nascimento, R. J. Nevin, J. A. Newman, D. L. Nidever, C. Nitschelm, P. Noterdaeme, J. E. O'Connell, M. D. Olmstead, D. Oravetz, A. Oravetz, Y. Osorio, Z. J. Pace, N. Padilla, N. Palanque-Delabrouille, P. A. Palicio, H.-A. Pan, K. Pan, J. Parker, R. Paviot, S. Peirani, K. P. Ramŕez, S. Penny, W. J. Percival, I. Perez-Fournon, I. Pérez-Ràfols, P. Petitjean, M. M. Pieri, M. Pinsonneault, V. J. Poovelil, J. T. Povick, A. Prakash, A. M. Price-Whelan, M. J. Raddick, A. Raichoor, A. Ray, S. B. Rembold, M. Rezaie, R. A. Riffel, R. Riffel, H.-W. Rix, A. C. Robin, A. Roman-Lopes, C. Román-Zúñiga, B. Rose, A. J. Ross, G. Rossi, K. Rowlands, K. H. R. Rubin, M. Salvato, A. G. Sánchez, L. Sánchez-Menguiano, J. R. Sánchez-Gallego, C. Sayres, A. Schaefer, R. P. Schiavon, J. S. Schimoia, E. Schlafly, D. Schlegel, D. P. Schneider, M. Schultheis, A. Schwope, H.-J. Seo, A. Serenelli, A. Shafieloo, S. J. Shamsi, Z. Shao, S. Shen, M. Shetrone, R. Shirley, V. S. Aguirre, J. D. Simon, M. F. Skrutskie,

A. Slosar, R. Smethurst, J. Sobeck, B. C. Sodi, D. Souto, D. V. Stark, K. G. Stassun, M. Steinmetz, D. Stello, J. Stermer, T. Storchi-Bergmann, A. Streblyanska, G. S. Stringfellow, A. Stutz, G. Suárez, J. Sun, M. Taghizadeh-Popp, M. S. Talbot, J. Tayar, A. R. Thakar, R. Theriault, D. Thomas, Z. C. Thomas, J. Tinker, R. Tojeiro, H. H. Toledo, C. A. Tremonti, N. W. Troup, S. Tuttle, E. Unda-Sanzana, M. Valentini, J. Vargas-González, M. Vargas-Magaña, J. A. Vázquez-Mata, M. Vivek, D. Wake, Y. Wang, B. A. Weaver, A.-M. Weijmans, V. Wild, J. C. Wilson, R. F. Wilson, N. Wolthuis, W. M. Wood-Vasey, R. Yan, M. Yang, C. Yèche, O. Zamora, P. Zarrouk, G. Zasowski, K. Zhang, C. Zhao, G. Zhao, Z. Zheng, Z. Zheng, G. Zhu, and H. Zou. The 16th Data Release of the Sloan Digital Sky Surveys: First Release from the APOGEE-2 Southern Survey and Full Release of eBOSS Spectra. *The Astrophysical Journal Supplement Series*, 249(1):3, 2020. ISSN 1538-4365. doi: 10.3847/1538-4365/ab929e.

J. Allington-Smith. Basic principles of integral field spectroscopy. *New Astronomy Reviews*, 50(4-5):244–251, 2006. ISSN 13876473. doi: 10.1016/j.newar.2006.02.024.

P. Amaro-Seoane, H. Audley, S. Babak, J. Baker, E. Barausse, P. Bender, E. Berti, P. Binetruy, M. Born, D. Bortoluzzi, J. Camp, C. Caprini, V. Cardoso, M. Colpi, J. Conklin, N. Cornish, C. Cutler, K. Danzmann, R. Dolesi, L. Ferraioli, V. Ferroni, E. Fitzsimons, J. Gair, L. G. Bote, D. Giardini, F. Gibert, C. Grimani, H. Halloin, G. Heinzel, T. Hertog, M. Hewitson, K. Holley-Bockelmann, D. Hollington, M. Hueller, H. Inchauspe, P. Jetzer, N. Karnesis, C. Killow, A. Klein, B. Klipstein, N. Korsakova, S. L. Larson, J. Livas, I. Lloro, N. Man, D. Mance, J. Martino, I. Mateos, K. McKenzie, S. T. McWilliams, C. Miller, G. Mueller, G. Nardini, G. Nelemans, M. Nofrarias, A. Petiteau, P. Pivato, E. Plagnol, E. Porter, J. Reiche, D. Robertson, N. Robertson, E. Rossi, G. Russano, B. Schutz, A. Sesana, D. Shoemaker, J. Slutsky, C. F. Sopuerta, T. Sumner, N. Tamanini, I. Thorpe, M. Troebs, M. Vallisneri, A. Vecchio, D. Vetrugno, S. Vitale, M. Volonteri, G. Wanner, H. Ward, P. Wass, W. Weber, J. Ziemer,

and P. Zweifel. *Laser Interferometer Space Antenna (LISA L3 mission proposal)*. 2017. URL `http://arxiv.org/abs/1702.00786`.

I. Appenzeller, K. Fricke, W. Fürtig, W. Gässler, R. Häfner, R. Harke, H.-J. Hess, W. Hummel, P. Jürgens, R.-P. Kudritzki, K.-H. Mantel, W. Meisl, B. Muschielok, H. Nicklas, G. Rupprecht, W. Seifert, O. Stahl, T. Szeifert, and K. Tarantik. Successful commissioning of FORS1 - the first optical instrument on the VLT. *The Messenger*, 94(94):1–6, 1998. URL `http://labs.adsabs.harvard.edu/ui/abs/1998Msngr..94....1A`.

D. E. Atkinson, D. N. B. Hall, S. M. Jacobson, and I. M. Baker. Dark Current in the SAPHIRA Series of APD Arrays. *The Astronomical Journal*, 154(6):265, 2017. ISSN 00046256. doi: 10.3847/1538-3881/aa9610. URL `http://dx.doi.org/10.3847/1538-3881/aa9610`.

Y. Avni. ENERGY SPECTRA OF X-RAY CLUSTERS OF GALAXIES *. *The Astrophysical Journal*, 210:642–646, 1976.

R. Bacon, G. Adam, A. Baranne, G. Courtes, D. Dubet, and J. P. Dubois. The Integral Field Spectrograph TIGER. *Very Large Telescopes and their Instrumentation*, page 1185, 1988. URL `https://ui.adsabs.harvard.edu/abs/1988ESOC...30.1185B/abstract`.

R. Bacon, M. Accardo, L. Adjali, H. Anwand, S. Bauer, I. Biswas, J. Blaizot, D. Boudon, S. Brau-Nogue, J. Brinchmann, P. Caillier, L. Capoani, C. M. Carollo, T. Contini, P. Couderc, E. Daguisé, S. Deiries, B. Delabre, S. Dreizler, J. Dubois, M. Dupieux, C. Dupuy, E. Emsellem, T. Fechner, A. Fleischmann, M. François, G. Gallou, T. Gharsa, A. Glindemann, D. Gojak, B. Guiderdoni, G. Hansali, T. Hahn, A. Jarno, A. Kelz, C. Koehler, J. Kosmalski, F. Laurent, M. Le Floch, S. J. Lilly, J.-L. Lizon, M. Loupias, A. Manescau, C. Monstein, H. Nicklas, J.-C. Olaya, L. Pares, L. Pasquini, A. Pécontal-Rousset, R. Pelló, C. Petit, E. Popow, R. Reiss, A. Remillieux, E. Renault, M. Roth, G. Rupprecht, D. Serre, J. Schaye, G. Soucail, M. Steinmetz, O. Streicher, R. Stuik,

H. Valentin, J. Vernet, P. Weilbacher, L. Wisotzki, and N. Yerle. The MUSE second-generation VLT instrument. *Ground-based and Airborne Instrumentation for Astronomy III*, 7735:773508, 2010. ISSN 0277786X. doi: 10.1117/12.856027.

I. Baker, C. Maxey, L. Hipwood, and K. Barnes. Leonardo (formerly Selex ES) infrared sensors for astronomy: present and future. In *High Energy, Optical, and Infrared Detectors for Astronomy VII*, volume 9915, page 991505. SPIE, 8 2016. ISBN 9781510602090. doi: 10.1117/12.2231079.

M. Boer, A. Klotz, and J. L. Atteia. THE GAMMA-RAY BURST HUNT AT LA SILLA THE TAROT-S VERY FAST MOVING TELESCOPE. *The Messenger*, (September):45–48, 2003.

N. A. Bond, Ivezić, B. Sesar, M. Jurić, J. A. Munn, A. Kowalski, S. Loebman, R. Roškar, T. C. Beers, J. Dalcanton, C. M. Rockosi, B. Yanny, H. J. Newberg, C. Allende Prieto, R. Wilhelm, Y. S. Lee, T. Sivarani, S. R. Majewski, J. E. Norris, C. A. Bailer-Jones, P. R. Fiorentin, D. Schlegel, A. Uomoto, R. H. Lupton, G. R. Knapp, J. E. Gunn, K. R. Covey, J. A. Smith, G. Miknaitis, M. Doi, M. Tanaka, M. Fukugita, S. Kent, D. Finkbeiner, T. R. Quinn, S. Hawley, S. Anderson, F. Kiuchi, A. Chen, J. Bushong, H. Sohi, D. Haggard, A. Kimball, R. McGurk, J. Barentine, H. Brewington, M. Harvanek, S. Kleinman, J. Krzesinski, D. Long, A. Nitta, S. Snedden, B. Lee, J. R. Pier, H. Harris, J. Brinkmann, and D. P. Schneider. The milky way tomography with SDSS. III. Stellar kinematics. *Astrophysical Journal*, 716(1):1–29, 2010. ISSN 15384357. doi: 10.1088/0004-637X/716/1/1.

A. G. Brown, A. Vallenari, T. Prusti, J. H. De Bruijne, C. Babusiaux, C. A. Bailer-Jones, M. Biermann, D. W. Evans, L. Eyer, F. Jansen, C. Jordi, S. A. Klioner, U. Lammers, L. Lindegren, X. Luri, F. Mignard, C. Panem, D. Pourbaix, S. Randich, P. Sartoretti, H. I. Siddiqui, C. Soubiran, F. Van Leeuwen, N. A. Walton, F. Arenou, U. Bastian, M. Cropper, R. Drimmel, D. Katz, M. G. Lattanzi, J. Bakker, C. Cacciari, J. Castañeda, L. Chaoul, N. Cheek, F. De An-

geli, C. Fabricius, R. Guerra, B. Holl, E. Masana, R. Messineo, N. Mowlavi, K. Nienartowicz, P. Panuzzo, J. Portell, M. Riello, G. M. Seabroke, P. Tanga, F. Thévenin, G. Gracia-Abril, G. Comoretto, M. Garcia-Reinaldos, D. Teyssier, M. Altmann, R. Andrae, M. Audard, I. Bellas-Velidis, K. Benson, J. Berthier, R. Blomme, P. Burgess, G. Busso, B. Carry, A. Cellino, G. Clementini, M. Clotet, O. Creevey, M. Davidson, J. De Ridder, L. Delchambre, A. Dell'Oro, C. Ducourant, J. Fernández-Hernández, M. Fouesneau, Y. Frémat, L. Galluccio, M. García-Torres, J. González-Núñez, J. J. González-Vidal, E. Gosset, L. P. Guy, J. L. Halbwachs, N. C. Hambly, D. L. Harrison, J. Hernández, D. Hestroffer, S. T. Hodgkin, A. Hutton, G. Jasniewicz, A. Jean-Antoine-Piccolo, S. Jordan, A. J. Korn, A. Krone-Martins, A. C. Lanzafame, T. Lebzelter, W. Löffler, M. Manteiga, P. M. Marrese, J. M. Martín-Fleitas, A. Moitinho, A. Mora, K. Muinonen, J. Osinde, E. Pancino, T. Pauwels, J. M. Petit, A. Recio-Blanco, P. J. Richards, L. Rimoldini, A. C. Robin, L. M. Sarro, C. Siopis, M. Smith, A. Sozzetti, M. Süveges, J. Torra, W. Van Reeven, U. Abbas, A. Abreu Aramburu, S. Accart, C. Aerts, G. Altavilla, M. A. Álvarez, R. Alvarez, J. Alves, R. I. Anderson, A. H. Andrei, E. Anglada Varela, E. Antiche, T. Antoja, B. Arcay, T. L. Astraatmadja, N. Bach, S. G. Baker, L. Balaguer-Núñez, P. Balm, C. Barache, C. Barata, D. Barbato, F. Barblan, P. S. Barklem, D. Barrado, M. Barros, M. A. Barstow, S. Bartholomé Muñoz, J. L. Bassilana, U. Becciani, M. Bellazzini, A. Berihuete, S. Bertone, L. Bianchi, O. Bienaymé, S. Blanco-Cuaresma, T. Boch, C. Boeche, A. Bombrun, R. Borrachero, D. Bossini, S. Bouquillon, G. Bourda, A. Bragaglia, L. Bramante, M. A. Breddels, A. Bressan, N. Brouillet, T. Brüsemeister, E. Brugaletta, B. Bucciarelli, A. Burlacu, D. Busonero, A. G. Butkevich, R. Buzzi, E. Caffau, R. Cancelliere, G. Cannizzaro, T. Cantat-Gaudin, R. Carballo, T. Carlucci, J. M. Carrasco, L. Casamiquela, M. Castellani, A. Castro-Ginard, P. Charlot, L. Chemin, A. Chiavassa, G. Cocozza, G. Costigan, S. Cowell, F. Crifo, M. Crosta, C. Crowley, J. Cuypersy, C. Dafonte, Y. Damerdji, A. Dapergolas, P. David, M. David, P. De Laverny, F. De Luise, R. De March,

D. De Martino, R. De Souza, A. De Torres, J. Debosscher, E. Del Pozo, M. Delbo, A. Delgado, H. E. Delgado, P. Di Matteo, S. Diakite, C. Diener, E. Distefano, C. Dolding, P. Drazinos, J. Durán, B. Edvardsson, H. Enke, K. Eriksson, P. Esquej, G. Eynard Bontemps, C. Fabre, M. Fabrizio, S. Faigler, A. J. Falcão, M. Farràs Casas, L. Federici, G. Fedorets, P. Fernique, F. Figueras, F. Filippi, K. Findeisen, A. Fonti, E. Fraile, M. Fraser, B. Frézouls, M. Gai, S. Galleti, D. Garabato, F. García-Sedano, A. Garofalo, N. Garralda, A. Gavel, P. Gavras, J. Gerssen, R. Geyer, P. Giacobbe, G. Gilmore, S. Girona, G. Giuffrida, F. Glass, M. Gomes, M. Granvik, A. Gueguen, A. Guerrier, J. Guiraud, R. Gutiérrez-Sánchez, R. Haigron, D. Hatzidimitriou, M. Hauser, M. Haywood, U. Heiter, A. Helmi, J. Heu, T. Hilger, D. Hobbs, W. Hofmann, G. Holland, H. E. Huckle, A. Hypki, V. Icardi, K. Janßen, G. J. De Fombelle, P. G. Jonker, L. Juhász, F. Julbe, A. Karampelas, A. Kewley, J. Klar, A. Kochoska, R. Kohley, K. Kolenberg, M. Kontizas, E. Kontizas, S. E. Koposov, G. Kordopatis, Z. Kostrzewa-Rutkowska, P. Koubsky, S. Lambert, A. F. Lanza, Y. Lasne, J. B. Lavigne, Y. Le Fustec, C. Le Poncin-Lafitte, Y. Lebreton, S. Leccia, N. Leclerc, I. Lecoeur-Taibi, H. Lenhardt, F. Leroux, S. Liao, E. Licata, H. E. Lindstrøm, T. A. Lister, E. Livanou, A. Lobel, M. López, S. Managau, R. G. Mann, G. Mantelet, O. Marchal, J. M. Marchant, M. Marconi, S. Marinoni, G. Marschalkó, D. J. Marshall, M. Martino, G. Marton, N. Mary, D. Massari, G. Matijević, T. Mazeh, P. J. McMillan, S. Messina, D. Michalik, N. R. Millar, D. Molina, R. Molinaro, L. Molnár, P. Montegriffo, R. Mor, R. Morbidelli, T. Morel, D. Morris, A. F. Mulone, T. Muraveva, I. Musella, G. Nelemans, L. Nicastro, L. Noval, W. O'Mullane, C. Ordénovic, D. Ordóñez-Blanco, P. Osborne, C. Pagani, I. Pagano, F. Pailler, H. Palacin, L. Palaversa, A. Panahi, M. Pawlak, A. M. Piersimoni, F. X. Pineau, E. Plachy, G. Plum, E. Poggio, E. Poujoulet, A. Prša, L. Pulone, E. Racero, S. Ragaini, N. Rambaux, M. Ramos-Lerate, S. Regibo, C. Reylé, F. Riclet, V. Ripepi, A. Riva, A. Rivard, G. Rixon, T. Roegiers, M. Roelens, M. Romero-Gómez, N. Rowell, F. Royer, L. Ruiz-

Dern, G. Sadowski, T. Sagristà Sellés, J. Sahlmann, J. Salgado, E. Salguero, N. Sanna, T. Santana-Ros, M. Sarasso, H. Savietto, M. Schultheis, E. Sciacca, M. Segol, J. C. Segovia, D. Ségransan, I. C. Shih, L. Siltala, A. F. Silva, R. L. Smart, K. W. Smith, E. Solano, F. Solitro, R. Sordo, S. Soria Nieto, J. Souchay, A. Spagna, F. Spoto, U. Stampa, I. A. Steele, H. Steidelmüller, C. A. Stephenson, H. Stoev, F. F. Suess, J. Surdej, L. Szabados, E. Szegedi-Elek, D. Tapiador, F. Taris, G. Tauran, M. B. Taylor, R. Teixeira, D. Terrett, P. Teyssandier, W. Thuillot, A. Titarenko, F. Torra Clotet, C. Turon, A. Ulla, E. Utrilla, S. Uzzi, M. Vaillant, G. Valentini, V. Valette, A. Van Elteren, E. Van Hemelryck, M. Van Leeuwen, M. Vaschetto, A. Vecchiato, J. Veljanoski, Y. Viala, D. Vicente, S. Vogt, C. Von Essen, H. Voss, V. Votruba, S. Voutsinas, G. Walmsley, M. Weiler, O. Wertz, T. Wevers, Wyrzykowski, A. Yoldas, M. Žerjal, H. Ziaeepour, J. Zorec, S. Zschocke, S. Zucker, C. Zurbach, and T. Zwitter. Summary of the contents and survey properties. *Astronomy and Astrophysics*, 616, 2018. ISSN 14320746. doi: 10.1051/0004-6361/201833051.

W. R. Brown, M. Kilic, J. J. Hermes, C. A. Prieto, S. J. Kenyon, and D. E. Winget. A 12 minute orbital period detached white dwarf eclipsing binary. *Astrophysical Journal Letters*, 737(1), 8 2011. ISSN 20418205. doi: 10.1088/2041-8205/737/1/L23.

K. B. Burdge, M. W. Coughlin, J. Fuller, T. Kupfer, E. C. Bellm, L. Bildsten, M. J. Graham, D. L. Kaplan, J. v. Roestel, R. G. Dekany, D. A. Duev, M. Feeney, M. Giomi, G. Helou, S. Kaye, R. R. Laher, A. A. Mahabal, F. J. Masci, R. Riddle, D. L. Shupe, M. T. Soumagnac, R. M. Smith, P. Szkody, R. Walters, S. R. Kulkarni, and T. A. Prince. General relativistic orbital decay in a seven-minute-orbital-period eclipsing binary system. *Nature*, 571 (7766):528–531, 2019. ISSN 14764687. doi: 10.1038/s41586-019-1403-0. URL `http://dx.doi.org/10.1038/s41586-019-1403-0`.

J. Caruana, A. J. Bunker, S. M. Wilkins, E. R. Stanway, S. Lorenzoni, M. J. Jarvis,

and H. Ebert. Spectroscopy of z ˜ 7 candidate galaxies: Using Lyman α to constrain the neutral fraction of hydrogen in the high-redshift universe. *Monthly Notices of the Royal Astronomical Society*, 443(4):2831–2842, 2014. ISSN 13652966. doi: 10.1093/mnras/stu1341.

R. Casini and P. G. Nelson. On the intensity distribution function of blazed reflective diffraction gratings. *Journal of the Optical Society of America A*, 31(10): 2179, 2014. ISSN 1084-7529. doi: 10.1364/josaa.31.002179.

F. J. Castander, R. C. Nichol, A. Merrelli, S. Burles, A. Pope, A. J. Connolly, A. Uomoto, J. E. Gunn, J. E. Anderson, J. Annis, and N. A. Bahcall. THE FIRST HOUR OF EXTRAGALACTIC DATA OF THE SLOAN DIGITAL SKY SURVEY SPECTROSCOPIC COMMISSIONING : THE COMA CLUSTER. Technical report, 2001. URL `www.astro.princeton.edu/PBOOK/welcome.html`.

N. Chernov and C. Lesort. Least Squares Fitting of Circles. *Journal of Mathematical Imaging and Vision*, 23:239–252, 2005. doi: https://doi.org/10.1007/s10851-005-0482-8.

M. Cirasuolo and t. M. Consortium. MOONS: The New Multi-Object Spectrograph for the VLT. *The Messenger*, 180:10–17, 2020. doi: 10.18727/0722-6691/5195. URL `http://arxiv.org/abs/2009.00628%0Ahttp://dx.doi.org/10.18727/0722-6691/5195`.

C. F. Claver, T. Sandrine, K. Reil, and K. Bechtol. Overview and status of Vera C Rubin Observatory system integration, test and commissioning. *SPIE Modeling, Systems Engineering, and Project Management for Astronomy X*, 12187, 2022. doi: https://doi.org/10.1117/12.2630643. URL `https://www.spiedigitallibrary.org/conference-proceedings-of-spie/12187/121870G/Overview-and-status-of-Vera-C-Rubin-Observatory-system-integration/10.1117/12.2630643.full`.

Y. Clénet, E. Gendron, D. Gratadour, G. Rousset, and F. Vidal. Anisoplanatism effect on the E-ELT SCAO point spread function. A preserved coherent core across the field. *Astronomy and Astrophysics*, 583:1–10, 2015. ISSN 14320746. doi: 10.1051/0004-6361/201425469.

R. Content. New design for integral field spectroscopy with 8-m telescopes. *Optical Telescopes of Today and Tomorrow*, 2871(March 1997):1295–1305, 1997. ISSN 0277786X. doi: 10.1117/12.269020.

C. M. Copperwheat, T. R. Marsh, V. S. Dhillon, S. P. Littlefair, R. Hickman, B. T. Gänsicke, and J. Southworth. Physical properties of IP pegasi: An eclipsing dwarf nova with an unusually cool white dwarf. *Monthly Notices of the Royal Astronomical Society*, 402(3):1824–1840, 2010. ISSN 13652966. doi: 10.1111/j.1365-2966.2009.16010.x.

R. Cornelisse, J. Casares, T. Muñoz-Darias, D. Steeghs, P. Charles, R. Hynes, K. O'Brien, A. Barnes, R. M. Bandyopadhyay, S. Wachter, D. Gelino, and C. R. Gelino. An Overview of the Bowen Survey: Detecting Donor Star Signatures in Low Mass X-ray Binaries. In *AIP Conference Proceedings*, volume 148, pages 148–152, 2008. ISBN 9780735405301. doi: 10.1063/1.2945024.

G. Courtes. AN INTEGRAL FIELD SPECTROGRAPH (IFS) FOR LARGE TELESCOPES. *Instrumentation for Astronomy with Large Optical Telescopes*, pages 123–128, 1982. URL `https://www.cambridge.org/core/journals/international-astronomical-union-colloquium/article/an-integral-field-spectrograph-ifs-for-large-telescopes/ED8A8E6B4EB9CEFD3F5E019F8C74723A`.

R. D. Cowan. *The Theory of Atomic Structure and Spectra*. University of California Press, Los Angeles, 1981. ISBN 0520038215, 9780520038219.

M. Cropper, M. Barlow, M. A. Ferryman, K. Horne, R. Bingham, M. Page, P. Guttridge, A. Smith, A. Peacock, D. Walker, and P. Charles. A concept

for a superconducting tunnelling junction based spectrograph. *Monthly Notices of the Royal Astronomical Society*, 344(1):33–44, 2003. ISSN 00358711. doi: 10.1046/j.1365-8711.2003.06772.x.

E. Da Cunha, A. M. Hopkins, M. Colless, E. N. Taylor, C. Blake, C. Howlett, C. Magoulas, J. R. Lucey, C. Lagos, K. Kuehn, Y. Gordon, D. Barat, F. Bian, C. Wolf, M. J. Cowley, M. White, I. Achitouv, M. Bilicki, J. Bland-Hawthorn, K. Bolejko, M. J. Brown, R. Brown, J. Bryant, S. Croom, T. M. Davis, S. P. Driver, M. D. Filipovic, S. R. Hinton, M. Johnston-Hollitt, D. H. Jones, B. Koribalski, D. Kleiner, J. Lawrence, N. Lorente, J. Mould, M. S. Owers, K. Pimbblet, C. G. Tinney, N. F. Tothill, and F. Watson. The taipan galaxy survey: Scientific goals and observing strategy, 2017. ISSN 14486083.

M. Dai, W. Guo, X. Liu, M. Zhang, Y. Wang, L. F. Wei, G. C. Hilton, J. Hubmayr, J. Ullom, J. Gao, and M. R. Vissers. Measurement of Optical Constants of TiN and TiN/Ti/TiN Multilayer Films for Microwave Kinetic Inductance Photon-Number-Resolving Detectors. *Journal of Low Temperature Physics*, 194(5-6): 361–369, 2019. ISSN 15737357. doi: 10.1007/s10909-018-2095-9. URL `https://doi.org/10.1007/s10909-018-2095-9`.

G. Dalton, S. C. Trager, D. C. Abrams, D. Carter, P. Bonifacio, J. A. L. Aguerri, M. MacIntosh, C. Evans, I. Lewis, R. Navarro, T. Agocs, K. Dee, S. Rousset, I. Tosh, K. Middleton, J. Pragt, D. Terrett, M. Brock, C. Benn, M. Verheijen, D. Cano Infantes, C. Bevil, I. Steele, C. Mottram, S. Bates, F. J. Gribbin, J. Rey, L. F. Rodriguez, J. M. Delgado, I. Guinouard, N. Walton, M. J. Irwin, P. Jagourel, R. Stuik, G. Gerlofsma, R. Roelfsma, I. Skillen, A. Ridings, M. Balcells, J.-B. Daban, C. Gouvret, L. Venema, and P. Girard. WEAVE: the next generation wide-field spectroscopy facility for the William Herschel Telescope. In *Ground-based and Airborne Instrumentation for Astronomy IV*, volume 8446, page 84460P. SPIE, 9 2012. ISBN 9780819491473. doi: 10.1117/12.925950.

B. Davies, R. P. Kudritzki, B. Plez, S. Trager, A. Lançon, Z. Gazak, M. Bergemann,

C. Evans, and A. Chiavassa. The temperatures of red supergiants. *Astrophysical Journal*, 767(1), 2013. ISSN 15384357. doi: 10.1088/0004-637X/767/1/3.

P. K. Day, H. G. LeDuc, B. A. Mazin, A. Vayonakis, and J. Zmuidzinas. A broadband superconducting detector suitable for use in Large Arrays. *Nature*, 425 (October):12–14, 2003. doi: 10.1038/nature01981.1.

P. J. de Visser, V. Murugesan, D. Thoen, and B. Jochem. Experimental demonstration of a resolving power of 25-55 at 1545-402 nm wavelengths with photon-counting MKIDs. *SPIE 11454 X-Ray, Optical, and Infrared Detectors for Astronomy IX*, IX, 2020. doi: https://doi.org/10.1117/12.2561523.

P. J. De Visser, S. A. De Rooij, V. Murugesan, D. J. Thoen, and J. J. Baselmans. Phonon-Trapping-Enhanced Energy Resolution in Superconducting Single-Photon Detectors. *Physical Review Applied*, 16(3):1–14, 2021. ISSN 23317019. doi: 10.1103/PhysRevApplied.16.034051.

V. S. Dhillon, T. R. Marsh, C. Copperwheat, N. Bezawada, D. Ives, A. Vick, and K. O'Brien. ULTRASPEC: High-speed spectroscopy with zero readout noise. In *AIP Conference Proceedings*, volume 984, pages 132–139, 2008. ISBN 9780735405035. doi: 10.1063/1.2896922.

V. S. Dhillon, N. Bezawada, M. Black, S. D. Dixon, T. Gamble, X. Gao, D. M. Henry, P. Kerry, S. P. Littlefair, D. W. Lunney, T. R. Marsh, C. Miller, S. G. Parsons, R. P. Ashley, E. Breedt, A. Brown, M. J. Dyer, M. J. Green, I. Pelisoli, D. I. Sahman, J. Wild, D. J. Ives, L. Mehrgan, J. Stegmeier, C. M. Dubbeldam, T. J. Morris, J. Osborn, R. W. Wilson, J. Casares, T. Muñoz-Darias, E. Pallé, P. Rodríguez-Gil, T. Shahbaz, M. A. P. Torres, A. d. U. Postigo, A. Cabrera-Lavers, R. L. M. Corradi, R. D. Domínguez, and D. García-Alvarez. HiPERCAM: a quintuple-beam, high-speed optical imager on the 10.4-m Gran Telescopio Canarias. 7 2021. doi: 10.1093/mnras/stab2130. URL `http://arxiv.org/abs/2107.10124http://dx.doi.org/10.1093/mnras/stab2130`.

S. D'Odorico, M. I. Andersen, P. Conconi, V. De Caprio, B. Delabre, P. Di Marcantonio, H. Dekker, M. D. Downing, G. Finger, P. Groot, H. H. Hanenburg, F. Hammer, D. Horville, J. Hjorth, L. Kaper, J. Klougart, P. Kjaergaard-Rasmussen, J.-L. Lizon, M. Marteaud, R. Mazzoleni, N. Michaelsen, R. Pallavicini, F. Rigal, P. Santin, A. Norup Soerensen, P. Spano, L. Venema, P. Vola, and F. M. Zerbi. X-shooter: UV-to-IR intermediate-resolution high-efficiency spectrograph for the ESO VLT. *Ground-based Instrumentation for Astronomy*, 5492(September 2004): 220, 2004. ISSN 0277786X. doi: 10.1117/12.550005.

G. Dubus. Gamma-ray binaries and related systems, 2013. ISSN 09354956.

D. Dussault and P. Hoess. Noise performance comparison of ICCD with CCD and EMCCD cameras. *Infrared Systems and Photoelectronic Technology*, 5563 (October 2004):195–204, 2004. ISSN 0277786X. doi: 10.1117/12.561839.

H. Gao and Y. P. Jing. Universal conditional distribution function of [OII] luminosity of galaxies, and prediction for the [OII] luminosity function at redshift $z<3$. *Astrophysical Journal*, 2020. URL `http://arxiv.org/abs/2007.12878`.

J. Gao. The Physics of Superconducting Microwave Resonators Thesis by. 2008, 2008.

G. Gilmore, S. Randich, M. Asplund, J. Binney, P. Bonifacio, J. Drew, S. Feltzing, A. Ferguson, R. Jeffries, G. Micela, I. Negueruela, T. Prusti, H.-W. Rix, A. Vallenari, E. Alfaro, C. Allende-Prieto, C. Babusiaux, T. Bensby, R. Blomme, A. Bragaglia, E. Flaccomio, P. François, M. Irwin, S. Koposov, A. Korn, A. Lanzafame, E. Pancino, E. Paunzen, A. Recio-Blanco, G. Sacco, R. Smiljanic, S. Van Eck, and N. Walton. The Gaia-ESO Public Spectroscopic Survey. *The Messenger*, 147(March):25–31, 2012. URL `http://adsabs.harvard.edu/abs/2012Msngr.147...25G`.

S. B. Goebel, D. N. B. Hall, O. Guyon, E. Warmbier, and S. M. Jacobson. Overview of the SAPHIRA Detector for AO Applications. 5 2018. doi: 10.1117/1.JATIS.

4.2.026001. URL http://arxiv.org/abs/1805.08419http://dx.doi.org/10.1117/1.JATIS.4.2.026001.

C. Hagmann and P. L. Richards. Adiabatic demagnetization refrigerators for small laboratory experiments and space astronomy. *Cryogenics*, 35(5):303–309, 1995. ISSN 00112275. doi: 10.1016/0011-2275(95)95348-I.

F. Hamann and G. Ferland. Elemental abundances in quasistellar objects: Star formation and galactic nuclear evolution at high redshifts. *Annual Review of Astronomy and Astrophysics*, 37(1):487–531, 1999. ISSN 00664146. doi: 10.1146/annurev.astro.37.1.487.

T. Hamaoka, K. K. McCully, M. Niwayama, and B. Chance. The use of muscle near-infrared spectroscopy in sport, health and medical sciences: Recent developments. *Philosophical Transactions of the Royal Society A: Mathematical, Physical and Engineering Sciences*, 369(1955):4591–4604, 2011. ISSN 1364503X. doi: 10.1098/rsta.2011.0298.

R. J. Harms, R. Angel, F. Bartko, E. Beaver, W. Bloomquist, R. Bohlin, E. M. Burbidge, A. F. Davidsen, J. C. Flemming, H. Ford, and B. Margon. Faint-Object Spectrograph For Space Telescope. *Space Optics II*, 0183(September 1979):74–87, 1979. doi: 10.1117/12.957398.

T. Hashimoto, T. Garel, B. Guiderdoni, A. B. Drake, R. Bacon, J. Blaizot, J. Richard, F. Leclercq, H. Inami, A. Verhamme, R. Bouwens, J. Brinchmann, S. Cantalupo, M. Carollo, J. Caruana, E. C. Herenz, J. Kerutt, R. A. Marino, P. Mitchell, and J. Schaye. The MUSE Hubble Ultra Deep Field Survey: X. Ly α equivalent widths at $2.9 < z < 6.6$. *Astronomy and Astrophysics*, 608(2003), 2017. ISSN 14320746. doi: 10.1051/0004-6361/201731579.

J. Hearnshaw. *The historical development of astronomical spectroscopes and spectrographs*. Cambridge University Press, Christchurch, 2009. ISBN 9780511735288. doi: 10.1017/cbo9780511735288.002.

J. Heidt, I. Appenzeller, R. Bender, and K. J. Fricke. The FORS Deep Field. 2001. doi: 10.1007/978-94-017-3313-7{_}139.

F. Henault, R. Bacon, C. Bonneville, D. Boudon, R. L. Davies, P. Ferruit, G. F. Gilmore, O. LeFevre, J.-P. Lemonnier, S. Lilly, S. L. Morris, E. Prieto, M. Steinmetz, and P. T. de Zeeuw. MUSE: a second-generation integral-field spectrograph for the VLT. *Instrument Design and Performance for Optical/Infrared Ground-based Telescopes*, 4841(March 2003):1096, 2003. ISSN 0277786X. doi: 10.1117/12.462334.

V. B. Hofmann and K. O'Brien. KSIM: simulating KIDSpec, a Microwave Kinetic Inductance Detector spectrograph for the optical/NIR. *RAS Techniques and Instruments*, 2(1):278–292, 1 2023. doi: 10.1093/rasti/rzad018.

V. B. Hofmann, K. O'Brien, and D. Geng. What could KIDSpec, a new MKID spectrograph, do on the ELT? page 329. SPIE-Intl Soc Optical Eng, 8 2022. doi: 10.1117/12.2628889.

C. Howlett, A. S. G. Robotham, C. D. P. Lagos, and A. G. Kim. Measuring the Growth Rate of Structure with Type IA Supernovae from LSST. *The Astrophysical Journal*, 847(2):128, 2017a. ISSN 15384357. doi: 10.3847/1538-4357/aa88c8. URL `http://dx.doi.org/10.3847/1538-4357/aa88c8`.

C. Howlett, L. Staveley-Smith, and C. Blake. Cosmological forecasts for combined and next-generation peculiar velocity surveys. *Monthly Notices of the Royal Astronomical Society*, 464(3):2517–2544, 2017b. ISSN 13652966. doi: 10.1093/mnras/stw2466.

K. D. Irwin, G. C. Hilton, and C. E. Ed. *Transition-Edge Sensors*, volume 99. 2005. ISBN 3540201130. doi: 10.1007/10933596{_}3.

D. Ives, N. Bezawada, V. Dhillon, and T. Marsh. ULTRASPEC: an electron multiplication CCD camera for very low light level high speed astronomical spec-

trometry. *High Energy, Optical, and Infrared Detectors for Astronomy III*, 7021 (July 2008):70210B, 2008. ISSN 0277786X. doi: 10.1117/12.790376.

Ivezić, S. M. Kahn, J. A. Tyson, B. Abel, E. Acosta, R. Allsman, D. Alonso, Y. AlSayyad, S. F. Anderson, J. Andrew, J. R. P. Angel, G. Z. Angeli, R. Ansari, P. Antilogus, C. Araujo, R. Armstrong, K. T. Arndt, P. Astier, Aubourg, N. Auza, T. S. Axelrod, D. J. Bard, J. D. Barr, A. Barrau, J. G. Bartlett, A. E. Bauer, B. J. Bauman, S. Baumont, E. Bechtol, K. Bechtol, A. C. Becker, J. Becla, C. Beldica, S. Bellavia, F. B. Bianco, R. Biswas, G. Blanc, J. Blazek, R. D. Blandford, J. S. Bloom, J. Bogart, T. W. Bond, M. T. Booth, A. W. Borgland, K. Borne, J. F. Bosch, D. Boutigny, C. A. Brackett, A. Bradshaw, W. N. Brandt, M. E. Brown, J. S. Bullock, P. Burchat, D. L. Burke, G. Cagnoli, D. Calabrese, S. Callahan, A. L. Callen, J. L. Carlin, E. L. Carlson, S. Chandrasekharan, G. Charles-Emerson, S. Chesley, E. C. Cheu, H.-F. Chiang, J. Chiang, C. Chirino, D. Chow, D. R. Ciardi, C. F. Claver, J. Cohen-Tanugi, J. J. Cockrum, R. Coles, A. J. Connolly, K. H. Cook, A. Cooray, K. R. Covey, C. Cribbs, W. Cui, R. Cutri, P. N. Daly, S. F. Daniel, F. Daruich, G. Daubard, G. Daues, W. Dawson, F. Delgado, A. Dellapenna, R. d. Peyster, M. d. Val-Borro, S. W. Digel, P. Doherty, R. Dubois, G. P. Dubois-Felsmann, J. Durech, F. Economou, T. Eifler, M. Eracleous, B. L. Emmons, A. F. Neto, H. Ferguson, E. Figueroa, M. Fisher-Levine, W. Focke, M. D. Foss, J. Frank, M. D. Freemon, E. Gangler, E. Gawiser, J. C. Geary, P. Gee, M. Geha, C. J. B. Gessner, R. R. Gibson, D. K. Gilmore, T. Glanzman, W. Glick, T. Goldina, D. A. Goldstein, I. Goodenow, M. L. Graham, W. J. Gressler, P. Gris, L. P. Guy, A. Guyonnet, G. Haller, R. Harris, P. A. Hascall, J. Haupt, F. Hernandez, S. Herrmann, E. Hileman, J. Hoblitt, J. A. Hodgson, C. Hogan, J. D. Howard, D. Huang, M. E. Huffer, P. Ingraham, W. R. Innes, S. H. Jacoby, B. Jain, F. Jammes, J. Jee, T. Jenness, G. Jernigan, D. Jevremović, K. Johns, A. S. Johnson, M. W. G. Johnson, R. L. Jones, C. Juramy-Gilles, M. Jurić, J. S. Kalirai, N. J. Kallivayalil, B. Kalmbach, J. P. Kantor, P. Karst, M. M. Kasliwal, H. Kelly, R. Kessler, V. Kinnison,

D. Kirkby, L. Knox, I. V. Kotov, V. L. Krabbendam, K. S. Krughoff, P. Kubánek, J. Kuczewski, S. Kulkarni, J. Ku, N. R. Kurita, C. S. Lage, R. Lambert, T. Lange, J. B. Langton, L. L. Guillou, D. Levine, M. Liang, K.-T. Lim, C. J. Lintott, K. E. Long, M. Lopez, P. J. Lotz, R. H. Lupton, N. B. Lust, L. A. MacArthur, A. Mahabal, R. Mandelbaum, T. W. Markiewicz, D. S. Marsh, P. J. Marshall, S. Marshall, M. May, R. McKercher, M. McQueen, J. Meyers, M. Migliore, M. Miller, D. J. Mills, C. Miraval, J. Moeyens, F. E. Moolekamp, D. G. Monet, M. Moniez, S. Monkewitz, C. Montgomery, C. B. Morrison, F. Mueller, G. P. Muller, F. M. Arancibia, D. R. Neill, S. P. Newbry, J.-Y. Nief, A. Nomerotski, M. Nordby, P. O'Connor, J. Oliver, S. S. Olivier, K. Olsen, W. O'Mullane, S. Ortiz, S. Osier, R. E. Owen, R. Pain, P. E. Palecek, J. K. Parejko, J. B. Parsons, N. M. Pease, J. M. Peterson, J. R. Peterson, D. L. Petravick, M. E. L. Petrick, C. E. Petry, F. Pierfederici, S. Pietrowicz, R. Pike, P. A. Pinto, R. Plante, S. Plate, J. P. Plutchak, P. A. Price, M. Prouza, V. Radeka, J. Rajagopal, A. P. Rasmussen, N. Regnault, K. A. Reil, D. J. Reiss, M. A. Reuter, S. T. Ridgway, V. J. Riot, S. Ritz, S. Robinson, W. Roby, A. Roodman, W. Rosing, C. Roucelle, M. R. Rumore, S. Russo, A. Saha, B. Sassolas, T. L. Schalk, P. Schellart, R. H. Schindler, S. Schmidt, D. P. Schneider, M. D. Schneider, W. Schoening, G. Schumacher, M. E. Schwamb, J. Sebag, B. Selvy, G. H. Sembroski, L. G. Seppala, A. Serio, E. Serrano, R. A. Shaw, I. Shipsey, J. Sick, N. Silvestri, C. T. Slater, J. A. Smith, R. C. Smith, S. Sobhani, C. Soldahl, L. Storrie-Lombardi, E. Stover, M. A. Strauss, R. A. Street, C. W. Stubbs, I. S. Sullivan, D. Sweeney, J. D. Swinbank, A. Szalay, P. Takacs, S. A. Tether, J. J. Thaler, J. G. Thayer, S. Thomas, A. J. Thornton, V. Thukral, J. Tice, D. E. Trilling, M. Turri, R. V. Berg, D. V. Berk, K. Vetter, F. Virieux, T. Vucina, W. Wahl, L. Walkowicz, B. Walsh, C. W. Walter, D. L. Wang, S.-Y. Wang, M. Warner, O. Wiecha, B. Willman, S. E. Winters, D. Wittman, S. C. Wolff, W. M. Wood-Vasey, X. Wu, B. Xin, P. Yoachim, and H. Zhan. LSST: From Science Drivers to Reference Design and Anticipated Data Products. *The Astrophysical Journal*, 873(2):111, 2019. ISSN 15384357.

doi: 10.3847/1538-4357/ab042c.

E. Jehin, M. Gillon, D. Queloz, P. Magain, J. Manfroid, V. Chantry, M. Lendl, D. Hutsemekers, and S. Udry. TRAPPIST: TRAnsiting Planets and PlanetesImals Small Telescope. *The Messenger*, 145(September): 2–6, 2011. URL `http://adsabs.harvard.edu/cgi-bin/nph-data_query?bibcode=2011Msngr.145....2J&link_type=ABSTRACT%0Apapers3://publication/uuid/5C1C5EB6-BC04-42D7-8313-A8E87788BF9D`.

N. Kaiser. Astronomical redshifts and the expansion of space. *Monthly Notices of the Royal Astronomical Society*, 438(3):2456–2465, 2014. ISSN 13652966. doi: 10.1093/mnras/stt2362.

N. Kaiser, W. Burgett, K. Chambers, L. Denneau, J. Heasley, R. Jedicke, E. Magnier, J. Morgan, P. Onaka, and J. Tonry. The Pan-STARRS wide-field optical/NIR imaging survey. In *Ground-based and Airborne Telescopes III*, volume 7733, page 77330E. SPIE, 7 2010. ISBN 9780819482235. doi: 10.1117/12.859188.

L. Kaper, S. D'Odorico, F. Hammer, R. Pallavicini, and P. K. Rasmussen. X-shooter: a medium-resolution, wide-band spectrograph for the VLT. In *Science with the VLT in the ELT era*, number January. 2008. ISBN 9781402091902. doi: 10.1007/978-1-4020-9190-2{_}53. URL `http://arxiv.org/abs/0803.0609%0Ahttp://dx.doi.org/10.1007/978-1-4020-9190-2_53`.

C. Knigge, K. S. Long, R. A. Wade, R. Baptista, K. Horne, I. Hubeny, and R. G. M. Rutten. HUBBL E SPACE T EL ESCOPE ECLIPSE OBSERVATIONS OF THE NOVA-LIKE CATACLYSMIC VARIABLE UX URSAE MAJORIS1. Technical report, 1998.

V. Korol, E. M. Rossi, P. J. Groot, G. Nelemans, S. Toonen, and A. G. Brown. Prospects for detection of detached double white dwarf binaries with Gaia, LSST and LISA. *Monthly Notices of the Royal Astronomical Society*, 470(2):1894–1910, 2017. ISSN 13652966. doi: 10.1093/mnras/stx1285.

K. Kouwenhoven, I. Elwakil, J. van Wingerden, V. Murugesan, D. J. Thoen, J. J. A. Baselmans, and P. J. de Visser. Model and Measurements of an Optical Stack for Broadband Visible to Near-IR Absorption in TiN KIDs. *Journal of Low Temperature Physics*, (0123456789), 2021. ISSN 1573-7357. doi: 10.1007/s10909-022-02774-0. URL `http://arxiv.org/abs/2110.05787`.

A. G. Kozorezov, J. K. Wigmore, D. Martin, P. Verhoeve, and A. Peacock. Phonon noise in thin metal films in an advanced energy down-conversion stage. *Journal of Low Temperature Physics*, 151(1-2 PART 1):51–57, 2008. ISSN 00222291. doi: 10.1007/s10909-007-9612-6.

T. Kupfer, V. Korol, S. Shah, G. Nelemans, T. R. Marsh, G. Ramsay, P. J. Groot, D. T. Steeghs, and E. M. Rossi. LISA verification binaries with updated distances from Gaia Data Release 2. *Monthly Notices of the Royal Astronomical Society*, 480(1):302–309, 2018. ISSN 13652966. doi: 10.1093/mnras/sty1545.

M. Kurakado. Developments in superconducting tunnel junction detectors. *Nuclear Inst. and Methods in Physics Research, A*, 314(2):252–262, 1992. ISSN 01689002. doi: 10.1016/0168-9002(92)90968-A.

E. V. Linder and R. N. Cahn. Parameterized beyond-Einstein growth. *Astroparticle Physics*, 28(4-5):481–488, 2007. ISSN 09276505. doi: 10.1016/j.astropartphys.2007.09.003.

P. Magnan. Detection of visible photons in CCD and CMOS: A comparative view. *Nuclear Instruments and Methods in Physics Research, Section A: Accelerators, Spectrometers, Detectors and Associated Equipment*, 504(1-3):199–212, 2003. ISSN 01689002. doi: 10.1016/S0168-9002(03)00792-7.

D. W. Marsden, B. A. Mazin, K. O'Brien, and C. Hirata. Giga-z: A 100,000 object superconducting spectrophotometer for lsst follow-UP. *Astrophysical Journal, Supplement Series*, 208(8):15, 2013. ISSN 00670049. doi: 10.1088/0067-0049/208/1/8.

C. Martayan, T. Rivinius, D. Baade, A. M. Hubert, and J. Zorec. Populations of Be stars: Stellar evolution of extreme stars. *Proceedings of the International Astronomical Union*, 6(S272):242–253, 2011. ISSN 17439221. doi: 10.1017/S1743921311010489.

D. D. Martin, A. Peacock, P. Verhoeve, A. Poelaert, and R. Venn. Matrix readout scheme for Superconducting Tunnel Junction arrays. *Nuclear Instruments and Methods in Physics Research, Section A: Accelerators, Spectrometers, Detectors and Associated Equipment*, 444(1):115–119, 2000. ISSN 01689002. doi: 10.1016/S0168-9002(99)01341-8.

F. Martin, G. Vermeulen, P. Camus, and A. Benoit. A closed cycle 3He-4He dilution refrigerator insensitive to gravity. *Cryogenics*, 50(9):623–627, 2010. ISSN 00112275. doi: 10.1016/j.cryogenics.2010.02.014. URL `http://dx.doi.org/10.1016/j.cryogenics.2010.02.014`.

B. A. Mazin. *Microwave Kinetic Inductance Detectors*. PhD thesis, California Institute of Technology, 2004.

B. A. Mazin. Superconducting Materials for Microwave Kinetic Inductance Detectors. pages 1–19, 2020. URL `http://arxiv.org/abs/2004.14576`.

B. A. Mazin, K. O'Brien, S. McHugh, B. Bumble, D. Moore, S. Golwala, and J. Zmuidzinas. ARCONS: a highly multiplexed superconducting optical to near-IR camera. *Ground-based and Airborne Instrumentation for Astronomy III*, 7735 (805):773518, 2010. ISSN 0277786X. doi: 10.1117/12.856440.

B. A. Mazin, B. Bumble, S. R. Meeker, K. O'Brien, S. McHugh, and E. Langman. A superconducting focal plane array for ultraviolet, optical, and near-infrared astrophysics. *Optics Express*, 20(2):1503, 2012. ISSN 1094-4087. doi: 10.1364/oe.20.001503.

B. A. Mazin, S. R. Meeker, M. J. Strader, P. Szypryt, D. Marsden, J. C. van Eyken, G. E. Duggan, A. B. Walter, G. Ulbricht, M. Johnson, B. Bumble, K. O'Brien,

and C. Stoughton. ARCONS: A 2024 Pixel Optical through Near-IR Cryogenic Imaging Spectrophotometer. *Publications of the Astronomical Society of the Pacific*, 125(933):1348–1361, 2013. ISSN 00046280. doi: 10.1086/674013.

B. A. Mazin, G. D. Becker, G. Cancelo, K. France, W. C. Fraser, T. Jones, S. R. Meeker, K. O'Brien, J. X. Prochaska, S. Tendulkar, and G. Vasisht. KRAKENS: a superconducting MKID integral field spectrograph concept for the Keck I telescope. In *SPIE Astronomical Telescopes + Instrumentation*, number July 2018, page 16, 2018. ISBN 9781510619579. doi: 10.1117/12.2312221.

B. A. Mazin, J. Bailey, J. Bartlett, C. Bockstiegel, B. Bumble, G. Coiffard, T. Currie, M. Daal, K. Davis, R. Dodkins, N. Fruitwala, N. Jovanovic, I. Lipartito, J. Lozi, J. Males, D. Mawet, S. Meeker, K. O'Brien, M. Rich, J. Smith, S. Steiger, N. Swimmer, A. Walter, N. Zobrist, and J. Zmuidzinas. Optical and Near-IR Microwave Kinetic Inductance Detectors (MKIDs) in the 2020s. *Astro2020 APC*, (805), 2019. URL `http://arxiv.org/abs/1908.02775`.

S. McHugh, B. A. Mazin, B. Serfass, S. Meeker, K. O'Brien, R. Duan, R. Raffanti, and D. Werthimer. A readout for large arrays of microwave kinetic inductance detectors. *Review of Scientific Instruments*, 83(4), 2012. ISSN 00346748. doi: 10.1063/1.3700812.

G. A. McLoughlin, M. Dan, T. M. Tsang, D. N. Jones, J. Cilia, M. D. Hill, M. J. Robbins, I. M. Benzel, P. R. Maycox, E. Holmes, and S. Bahn. Analyzing the effects of psychotropic drugs on metabolite profiles in rat brain using 1H NMR spectroscopy. *Journal of Proteome Research*, 8(4):1943–1952, 2009. ISSN 15353893. doi: 10.1021/pr800892u.

S. R. Meeker, B. A. Mazin, R. Jensen-Clem, A. B. Walter, P. Szypryt, M. J. Strader, and C. Bockstiegel. Design and development status of MKID integral field spectrographs for high contrast imaging. *Adaptive Optics for Extremely Large Telescopes 4 - Conference Proceedings*, 2015. doi: 10.20353/K3T4CP1131701.

S. R. Meeker, B. A. Mazin, A. B. Walter, P. Strader, N. Fruitwala, C. Bockstiegel, P. Szypryt, G. Ulbricht, G. Coiffard, B. Bumble, G. Cancelo, T. Zmuda, K. Treptow, N. Wilcer, G. Collura, R. Dodkins, I. Lipartito, N. Zobrist, M. Bottom, J. C. Shelton, D. Mawet, J. C. Van Eyken, G. Vasisht, and E. Serabyn. DARKNESS: A microwave kinetic inductance detector integral field spectrograph for high-contrast astronomy. *Publications of the Astronomical Society of the Pacific*, 130(988), 2018. ISSN 00046280. doi: 10.1088/1538-3873/aab5e7.

F. A. Merchant and K. R. Castleman. *Microscope Image Processing, Second Edition*. Academic Press, 2 edition, 2022. ISBN 9780128210499. doi: 10.1016/C2019-0-01813-4.

A. Modigliani, P. Goldoni, F. Royer, R. Haigron, L. Guglielmi, P. François, M. Horrobin, P. Bristow, J. Vernet, S. Moehler, F. Kerber, P. Ballester, E. Mason, and L. Christensen. The X-shooter pipeline. *Observatory Operations: Strategies, Processes, and Systems III*, 7737(July 2010):773728, 2010. ISSN 0277786X. doi: 10.1117/12.857211.

R. P. Naidu, J. Matthee, P. A. Oesch, C. Conroy, D. Sobral, G. Pezzulli, M. Hayes, D. Erb, R. Amorín, M. Gronke, D. Schaerer, S. Tacchella, J. Kerutt, A. Paulino-Afonso, J. Calhau, M. Llerena, and H. Röttgering. The synchrony of production and escape: half the bright Lyα emitters at z 2 have Lyman continuum escape fractions 50. *Monthly Notices of the Royal Astronomical Society*, 510(3):4582–4607, 2021. ISSN 13652966. doi: 10.1093/mnras/stab3601.

I. Newton. A letter of Mr. Isaac Newton, Professor of the Mathematicks in the University of Cambridge; containing his new theory about light and colors: sent by the author to the publisher from Cambridge, Febr. 6. 1671/72; in order to be communicated to the R. Society. *Philosophical Transactions of the Royal Society of London*, 6(80):3075–3087, 1672. doi: 10.1098/rstl.1671.0072. URL `https://royalsocietypublishing.org/doi/abs/10.1098/rstl.1671.0072`.

S. Noll, D. Mehlert, I. Appenzeller, R. Bender, A. Böhm, A. Gabasch, J. Heidt, U. Hopp, K. Jäger, S. Seitz, O. Stahl, C. Tapken, and B. L. Ziegler. The FORS deep field spectroscopic survey. *Astronomy and Astrophysics*, 418(3):885–906, 2004. ISSN 00046361. doi: 10.1051/0004-6361:20034434.

K. O'Brien, N. Thatte, and B. Mazin. KIDSpec: an MKID based medium resolution integral field spectrograph. In *Ground-based and Airborne Instrumentation for Astronomy V*, volume 9147, page 91470G, 2014. ISBN 9780819496157. doi: 10.1117/12.2056297.

J. B. Oke, J. G. Cohen, M. Carr, J. Cromer, A. Dingizian, F. H. Harris, S. Labrecque, R. Lucinio, and W. Schaal. The Keck Low-Resolution Imaging Spectrometer. *Astronomical Society of the Pacific*, 105:375–385, 1995.

M. Onodera, R. Shimakawa, T. L. Suzuki, I. Tanaka, Y. Harikane, M. Hayashi, T. Kodama, Y. Koyama, K. Nakajima, and T. Shibuya. Broad-band selection, spectroscopic identification, and physical properties of a population of extreme emission line galaxies at 3<z<3.7. *Astrophysical Journal*, 904:23, 2020. doi: https://doi.org/10.3847/1538-4357/abc174. URL `http://arxiv.org/abs/2010.07545`.

K. O'Brien. KIDSpec: An MKID-Based Medium-Resolution, Integral Field Spectrograph. *Journal of Low Temperature Physics*, 199(1):537–546, 2020. ISSN 15737357. doi: 10.1007/s10909-020-02347-z. URL `https://doi.org/10.1007/s10909-020-02347-z`.

L. Pasquini, G. Avila, A. Blecha, and C. Cacciari. Installation and Commissioning of FLAMES, the VLT Multifibre Facility. *The Messenger*, 110:9, 2002. URL `https://ui.adsabs.harvard.edu/abs/2002Msngr.110....1P/abstract`.

E. Pian, P. D'Avanzo, S. Benetti, M. Branchesi, E. Brocato, S. Campana, E. Cappellaro, S. Covino, V. D'Elia, J. P. Fynbo, F. Getman, G. Ghirlanda, G. Ghisellini, A. Grado, G. Greco, J. Hjorth, C. Kouveliotou, A. Levan, L. Limatola,

D. Malesani, P. A. Mazzali, A. Melandri, P. Møller, L. Nicastro, E. Palazzi, S. Piranomonte, A. Rossi, O. S. Salafia, J. Selsing, G. Stratta, M. Tanaka, N. R. Tanvir, L. Tomasella, D. Watson, S. Yang, L. Amati, L. A. Antonelli, S. Ascenzi, M. G. Bernardini, M. Boër, F. Bufano, A. Bulgarelli, M. Capaccioli, P. Casella, A. J. Castro-Tirado, E. Chassande-Mottin, R. Ciolfi, C. M. Copperwheat, M. Dadina, G. De Cesare, A. Di Paola, Y. Z. Fan, B. Gendre, G. Giuffrida, A. Giunta, L. K. Hunt, G. L. Israel, Z. P. Jin, M. M. Kasliwal, S. Klose, M. Lisi, F. Longo, E. Maiorano, M. Mapelli, N. Masetti, L. Nava, B. Patricelli, D. Perley, A. Pescalli, T. Piran, A. Possenti, L. Pulone, M. Razzano, R. Salvaterra, P. Schipani, M. Spera, A. Stamerra, L. Stella, G. Tagliaferri, V. Testa, E. Troja, M. Turatto, S. D. Vergani, and D. Vergani. Spectroscopic identification of r-process nucleosynthesis in a double neutron-star merger. *Nature*, 551(7678): 67–70, 2017. ISSN 14764687. doi: 10.1038/nature24298.

P. Prugniel and C. Soubiran. ASTRONOMY AND ASTROPHYSICS A database of high and medium-resolution stellar spectra . Technical report, 2001. URL `http://www.obs-hp.fr`.

C. Ramos Almeida, A. M. García, and J. A. Acosta-Pulido. Near-infrared spectroscopy of seyfert galaxies. Nuclear activity and stellar population. *Astrophysical Journal*, 694(2):1379–1394, 2009. ISSN 15384357. doi: 10.1088/0004-637X/694/2/1379.

R. Roelfsema, M. Klein Wolt, S. Bloemen, P. Groot, F. Bettonvil, H. Balster, P. Dolron, A. van Elteren, A. Engels, M. de Haan, R. ter Horst, J. Kragt, R. Navarro, G. Nelemans, W. J. Paalberends, S. Pal, G. Raskin, H. Rutten, B. Scheers, M. Schuil, and P. Sybilski. The BlackGEM array in search of black hole mergers: integrated performance modelling. *Integrated Modeling of Complex Optomechanical Systems II*, 10012(July 2016):1001206, 2016. ISSN 1996756X. doi: 10.1117/12.2204767.

G. H. Roelofs, A. Rau, T. R. Marsh, D. Steeghs, P. J. Groot, and G. Nele-

mans. Spectroscopic evidence for a 5.4 minute orbital period in HM cancri. *Astrophysical Journal Letters*, 711(2 PART 2), 2010. ISSN 20418213. doi: 10.1088/2041-8205/711/2/L138.

A. Rogalski. *HgCdTe photodetectors*. Elsevier Ltd., 2019. ISBN 9780081027097. doi: 10.1016/B978-0-08-102709-7.00007-3. URL `https://doi.org/10.1016/B978-0-08-102709-7.00007-3`.

W. Saunders, T. Bridges, P. Gillingham, R. Haynes, G. A. Smith, J. D. Whittard, V. Churilov, A. Lankshear, S. Croom, D. Jones, and C. Boshuizen. AAOmega: a scientific and optical overview. In *Ground-based Instrumentation for Astronomy*, volume 5492, page 389. SPIE, 9 2004. doi: 10.1117/12.550871.

A. Savitzky and M. J. E. Golay. Smoothing and Differentiation of Data by Simplified Least Squares Procedures. *American Chemical Society*, 36(8):1627–1639, 1964. ISSN 0003-2700. doi: https://doi.org/10.1021/ac60214a047. URL `https://pubs.acs.org/sharingguidelines`.

J.-T. Schindler, E. P. Farina, E. Bañados, A.-C. Eilers, J. F. Hennawi, M. Onoue, B. P. Venemans, F. Walter, F. Wang, F. B. Davies, R. Decarli, G. D. Rosa, A. Drake, X. Fan, C. Mazzucchelli, H.-W. Rix, G. Worseck, and J. Yang. The X-SHOOTER/ALMA Sample of Quasars in the Epoch of Reionization. I. NIR Spectral Modeling, Iron Enrichment, and Broad Emission Line Properties. *The Astrophysical Journal*, 905(1):51, 2020. ISSN 15384357. doi: 10.3847/1538-4357/abc2d7.

B. Sesar, Ivezić, R. H. Lupton, M. Jurić, J. E. Gunn, G. R. Knapp, N. De Lee, J. A. Smith, G. Miknaitis, H. Lin, D. Tucker, M. Doi, M. Tanaka, M. Fukugita, J. Holtzman, S. Kent, B. Yanny, D. Schlegel, D. Finkbeiner, N. Padmanabhan, C. M. Rockosi, N. Bond, B. Lee, C. Stoughton, S. Jester, H. Harris, P. Harding, J. Brinkmann, D. P. Schneider, D. York, M. W. Richmond, and D. Vanden Berk. Exploring the Variable Sky with the Sloan Digital Sky Survey. *The Astronomical Journal*, 134(6):2236–2251, 2007. ISSN 0004-6256. doi: 10.1086/521819.

P. Shirron, E. Canavan, M. DiPirro, J. Tuttle, and C. Yeager. A MULTI-STAGE CONTINUOUS-DUTY ADIABATIC DEMAGNETIZATION REFRIGERATOR. In *1999 Cryogenic Engineering Conference*, volume 552, pages 36–54, 1999. ISBN 9280717669.

D. Sobral, J. Matthee, B. Darvish, D. Schaerer, B. Mobasher, H. J. Röttgering, S. Santos, and S. Hemmati. EVIDENCE for PopIII-LIKE STELLAR POPULATIONS in the MOST LUMINOUS Ly EMITTERS at the EPOCH of REIONIZATION: SPECTROSCOPIC CONFIRMATION. *Astrophysical Journal*, 808(2), 2015. ISSN 15384357. doi: 10.1088/0004-637X/808/2/139.

D. Steeghs, D. K. Galloway, K. Ackley, M. J. Dyer, J. Lyman, K. Ulaczyk, R. Cutter, Y. L. Mong, V. Dhillon, P. O'Brien, G. Ramsay, S. Poshyachinda, R. Kotak, L. K. Nuttall, E. Pallé, R. P. Breton, D. Pollacco, E. Thrane, S. Aukkaravittayapun, S. Awiphan, U. Burhanudin, P. Chote, A. Chrimes, E. Daw, C. Duffy, R. Eyles-Ferris, B. Gompertz, T. Heikkilä, P. Irawati, M. R. Kennedy, T. Killestein, H. Kuncarayakti, A. J. Levan, S. Littlefair, L. Makrygianni, T. Marsh, D. Mata-Sanchez, S. Mattila, J. Maund, J. McCormac, D. Mkrtichian, J. Mullaney, K. Noysena, M. Patel, E. Rol, U. Sawangwit, E. R. Stanway, R. Starling, P. Strøm, S. Tooke, R. West, D. J. White, and K. Wiersema. The Gravitational-wave Optical Transient Observer (GOTO): Prototype performance and prospects for transient science. *Monthly Notices of the Royal Astronomical Society*, 511(2):2405–2422, 2022. ISSN 13652966. doi: 10.1093/mnras/stac013.

M. J. Strader. Digital Readout for Microwave Kinetic Inductance Detectors and Applications in High Time Resolution Astronomy. Technical report, 2016.

M. J. Strader, M. D. Johnson, B. A. Mazin, G. V. Spiro Jaeger, C. R. Gwinn, S. R. Meeker, P. Szypryt, J. C. Van Eyken, D. Marsden, K. O'Brien, A. B. Walter, G. Ulbricht, C. Stoughton, and B. Bumble. Excess optical enhancement observed with arcons for early Crab giant pulses. *Astrophysical Journal Letters*, 779(1), 12 2013. ISSN 20418205. doi: 10.1088/2041-8205/779/1/L12.

J. J. Swift, M. Bottom, J. A. Johnson, J. T. Wright, N. McCrady, R. A. Wittenmyer, P. Plavchan, R. Riddle, P. S. Muirhead, E. Herzig, J. Myles, C. H. Blake, J. Eastman, T. G. Beatty, S. I. Barnes, S. R. Gibson, B. Lin, M. Zhao, P. Gardner, E. Falco, S. Criswell, C. Nava, C. Robinson, D. H. Sliski, R. Hedrick, K. Ivarsen, A. Hjelstrom, J. de Vera, and A. Szentgyorgyi. Miniature Exoplanet Radial Velocity Array (MINERVA) I. Design, Commissioning, and First Science Results. 11 2014. doi: 10.1117/1.JATIS.1.2.027002. URL `http://arxiv.org/abs/1411.3724http://dx.doi.org/10.1117/1.JATIS.1.2.027002`.

R. Szczerba, M. Hajduk, Y. V. Pavlenko, B. J. Hrivnak, B. Kaminsky, K. Volk, N. Siódmiak, I. Gezer, L. Začs, W. Pych, and M. Sarna. Validating post-AGB candidates in the LMC and SMC using SALT spectra. *Astronomy & Astrophysics*, 2020. doi: 10.1051/0004-6361/201935392. URL `http://arxiv.org/abs/2007.14739%0Ahttp://dx.doi.org/10.1051/0004-6361/201935392`.

P. Szypryt, G. E. Duggan, B. A. Mazin, S. R. Meeker, M. J. Strader, J. C. van Eyken, D. Marsden, K. O'Brien, A. B. Walter, G. Ulbricht, T. A. Prince, C. Stoughton, and B. Bumble. Direct detection of SDSS J0926+3624 orbital expansion with ARCONS. *Monthly Notices of the Royal Astronomical Society*, 439(3):2765–2770, 2014. ISSN 13652966. doi: 10.1093/mnras/stu137.

P. Szypryt, S. R. Meeker, G. Coiffard, N. Fruitwala, B. Bumble, G. Ulbricht, A. B. Walter, M. Daal, C. Bockstiegel, G. Collura, N. Zobrist, I. Lipartito, and B. A. Mazin. Large-format platinum silicide microwave near-IR astronomy. *Optical Society of America*, 2017.

R. Tamai, B. Koehler, M. Cirasuolo, F. Biancat-Marchet, M. Tuti, and J.-C. González-Herrera. The ESO's ELT construction progress. *SPIE Ground-based and Airborne Telescopes VIII*, (December 2020):254, 2020. ISSN 1996756X. doi: 10.1117/12.2562828.

R. G. Tull, P. J. MacQueen, C. Sneden, and D. L. Lambert. The High-Resolution Cross-Dispersed Echelle White-Pupil Spectrometer of the McDonald Observat-

ory 2.7-m Telescope. *Journal of Chemical Information and Modeling*, 53(9): 1689–1699, 2019. ISSN 1098-6596. doi: 10.1017/CBO9781107415324.004.

S. M. Tulloch and V. S. Dhillon. On the use of electron-multiplying CCDs for astronomical spectroscopy. *Monthly Notices of the Royal Astronomical Society*, 411(1):211–225, 2011. ISSN 13652966. doi: 10.1111/j.1365-2966.2010.17675.x.

T. Urrutia, L. Wisotzki, J. Kerutt, K. B. Schmidt, E. C. Herenz, J. Klar, R. Saust, M. Werhahn, C. DIener, J. Caruana, D. Krajnović, R. Bacon, L. Boogaard, J. Brinchmann, H. Enke, M. Maseda, T. Nanayakkara, J. Richard, M. Steinmetz, and P. M. Weilbacher. The MUSE-Wide Survey: Survey description and first data release. *Astronomy and Astrophysics*, 624, 2019. ISSN 14320746. doi: 10.1051/0004-6361/201834656.

M. E. van den Ancker, D. Asmus, C. Hummel, H.-U. Käufl, F. Kerber, A. Smette, J. Taylor, K. Tristram, J. Vinther, and B. Wolff. Investigating the effect of atmospheric turbulence on mid-IR data quality with VISIR. *Observatory Operations: Strategies, Processes, and Systems VI*, 9910(July 2016):99102T, 2016. ISSN 1996756X. doi: 10.1117/12.2233701.

P. Verhoeve, R. H. den Hartog, D. D. E. Martin, N. Rando, A. J. Peacock, and D. J. Goldie. Development of distributed readout imaging detectors based on superconducting tunnel junctions for UV/optical astronomy. *Optical and IR Telescope Instrumentation and Detectors*, 4008(August 2000):683, 2000. ISSN 0277786X. doi: 10.1117/12.395548.

J. Vernet, H. Dekker, S. D'Odorico, L. Kaper, P. Kjaergaard, F. Hammer, S. Randich, F. Zerbi, P. J. Groot, J. Hjorth, I. Guinouard, R. Navarro, T. Adolfse, P. W. Albers, J. P. Amans, J. J. Andersen, M. I. Andersen, P. Binetruy, P. Bristow, R. Castillo, F. Chemla, L. Christensen, P. Conconi, R. Conzelmann, J. Dam, V. De Caprio, A. De Ugarte Postigo, B. Delabre, P. Di Marcantonio, M. Downing, E. Elswijk, G. Finger, G. Fischer, H. Flores, P. François, P. Goldoni,

L. Guglielmi, R. Haigron, H. Hanenburg, I. Hendriks, M. Horrobin, D. Horville, N. C. Jessen, F. Kerber, L. Kern, M. Kiekebusch, P. Kleszcz, J. Klougart, J. Kragt, H. H. Larsen, J. L. Lizon, C. Lucuix, V. Mainieri, R. Manuputy, C. Martayan, E. Mason, R. Mazzoleni, N. Michaelsen, A. Modigliani, S. Moehler, P. Møller, A. Norup Sørensen, P. Nørregaard, C. Péroux, F. Patat, E. Pena, J. Pragt, C. Reinero, F. Rigal, M. Riva, R. Roelfsema, F. Royer, G. Sacco, P. Santin, T. Schoenmaker, P. Spano, E. Sweers, R. Ter Horst, M. Tintori, N. Tromp, P. Van Dael, H. Van Der Vliet, L. Venema, M. Vidali, J. Vinther, P. Vola, R. Winters, D. Wistisen, G. Wulterkens, and A. Zacchei. X-shooter, the new wide band intermediate resolution spectrograph at the ESO Very Large Telescope. *Astronomy and Astrophysics*, 536:15, 2011. ISSN 14320746. doi: 10.1051/0004-6361/201117752.

A. B. Walter, B. A. Mazin, N. Fruitwala, S. Steiger, J. Bailey, N. Zobrist, N. Swimmer, I. Lipartito, J. P. Smith, S. R. Meeker, C. Bockstiegel, G. Coiffard, R. Dodkins, K. K. Davis, M. Daal, B. Bumble, O. Guyon, J. Lozi, and S. Vivard. The MKID Exoplanet Camera for Subaru SCExAO. *Publications of the Astronomical Society of the Pacific*, 132(1018):13, 2020. doi: https://ui.adsabs.harvard.edu/link{_}gateway/2020PASP..132l5005W/doi:10.1088/1538-3873/abc60f.

C. C. Williams, E. Curtis-Lake, K. N. Hainline, J. Chevallard, B. E. Robertson, S. Charlot, R. Endsley, D. P. Stark, C. N. A. Willmer, S. Alberts, R. Amorin, S. Arribas, S. Baum, A. Bunker, S. Carniani, S. Crandall, E. Egami, D. J. Eisenstein, P. Ferruit, B. Husemann, M. V. Maseda, R. Maiolino, T. D. Rawle, M. Rieke, R. Smit, S. Tacchella, and C. J. Willott. The JWST Extragalactic Mock Catalog: Modeling Galaxy Populations from the UV through the Near-IR over 13 Billion Years of Cosmic History . *The Astrophysical Journal Supplement Series*, 236(2):33, 2018. ISSN 00670049. doi: 10.3847/1538-4365/aabcbb.

G. G. Williams, P. A. Milne, H. S. Park, S. D. Barthelmy, D. H. Hartmann, A. Up-

dike, and K. Hurley. The Robotic Super-LOTIS Telescope: Results & Future Plans. *AIP Conference Proceedings*, 1000(May):535–538, 2008. ISSN 0094243X. doi: 10.1063/1.2943525.

H. Yang, L. Infante, J. E. Rhoads, W. Hu, Z. Zheng, S. Malhotra, J. Wang, L. F. Barrientos, W. Kang, and C. Jiang. Ly α Galaxies in the Epoch of Reionization (LAGER): Spectroscopic Confirmation of Two Redshift 7.0 Galaxies . *The Astrophysical Journal*, 876(2):123, 2019. ISSN 1538-4357. doi: 10.3847/1538-4357/ab16ce. URL `http://dx.doi.org/10.3847/1538-4357/ab16ce`.

S. J. Yates, J. J. Baselmans, A. Endo, R. M. Janssen, L. Ferrari, P. Diener, and A. M. Baryshev. Photon noise limited radiation detection with lens-antenna coupled microwave kinetic inductance detectors. *Applied Physics Letters*, 99(7), 2011. ISSN 00036951. doi: 10.1063/1.3624846.

N. L. Zakamska, F. Hamann, I. Pâris, W. N. Brandt, J. E. Greene, M. A. Strauss, C. Villforth, D. Wylezalek, R. M. Alexandroff, and N. P. Ross. Discovery of extreme [O III] λ5007 Å outflows in high-redshift red quasars. *Monthly Notices of the Royal Astronomical Society*, 459(3):3144–3160, 2016. ISSN 13652966. doi: 10.1093/mnras/stw718.

A. Ziad. Review of the Outer Scale of the atmospheric turbulence. *SPIE Astronomical Telescopes + Instrumentation*, AO V(July 2016), 2016. doi: 10.1117/12.2231375.

N. Zobrist, W. H. Clay, G. Coiffard, M. Daal, N. Swimmer, P. Day, and B. A. Mazin. Membrane-less phonon trapping and resolution enhancement in optical microwave kinetic inductance detectors. *American Physical Society*, 017701(129): 1–6, 2022. doi: 10.1103/PhysRevLett.129.017701. URL `http://arxiv.org/abs/2204.13669`.